Synthesis and Characterisation of Chiral Nanomaterials and their Influence on Stem Cell Differentiation

by

Gregor Kemper

A thesis
presented to the University of Waterloo
in fulfilment of the
thesis requirement for the degree of
Doctor of Philosophy
in
Pharmacy

Waterloo, Ontario, Canada, 2017

Examining committee membership

The following served on the Examining Committee for this thesis. The decision of the Examining Committee is by majority vote.

External Examiners	Véronique MIGONNEY Professor
Supervisors	Marie-Christine DURRIEU DR INSERM
	Shawn WETTIG Associate Profesor
Internal Member	Praveen NEKKAR RAO Associate Professor
Internal/External Member	Eric PROUZET Associate Professor
Other Members	Marie-Claire DEPAUW-GILLET Chargée de cours adjointe
	Reiko ODA DR CNRS
	Hiroyuki MIYAKE Associate Professor

Author's declaration

I hereby declare that I am the sole author of this thesis. This is a true copy of the thesis, including any required final revisions, as accepted by my examiners. I understand that my thesis may be made electronically available to the public.

Sommaire

Introduction

Un patient peut souffrir d'une perte de substance osseuse de taille critique suite à des accidents ou des pathologies. Aujourd'hui, le traitement le plus fréquent consiste en la greffe du tissu osseux (autogreffe ou allogreffe). Compte tenu des complication rencontrées (réponse immunologique, morbidité du site donneur), la recherche actuelle s'inscrit dans la recherche de synthèse d'un biomatériau bioactif favorisant la régénération osseuse. Ces matériaux devraient imiter les qualités de la matrice extracellulaire osseuse pour stimuler la formation osseuse. Les cellules souches mésenchymateuses jouent un rôle important du fait de leur capacité de prolifération et différentiation en ostéoblastes. Pour profiter de ce potentiel des cellules souches, il est nécessaire de comprendre comment contrôler leur comportement et mesurer l'impact du microenvironnement cellulaire sur la différenciation ostéogénique de ces cellules. Comme les cellules souches mésenchymateuses sont capables de différencier en plusieurs phénotypes différents, il est indispensable de les diriger dans la direction désirée. Plusieurs facteurs qui influencent le devenir cellulaire ont été identifiés, comme certains peptides bioactifs, des facteurs mécaniques comme la rigidité, ou la topographie de surface de matériaux.

Dans la matrice extracellulaire naturelle du tissu osseux, les cellules souches mésenchymateuses sont entourées d'une variété de principes actifs, dont le plus abondant est le collagène I. Cette protéine s'assemble pour former des nanofibres qui présentent une nanomorphologie périodique avec une périodicité bien définie. La question posée au début de ce travail était: Cette structure a-t-elle un impact sur la différenciation des cellules souches?

Pour étudier l'impact de la périodicité nanofibrillaire, nous proposons dans ce travail de recherche l'utilisation d'hélices modèles qui miment en partie la morphologie du collagène. Les hélices nanomètriques auto-assemblées des surfactants gemini peuvent avoir un pas d'hélice et un diamètre similaires à ceux du collagène. La modulabilité de ces paramètres et la possibilité de modifier ces structures par des molécules bioactives permettent de moduler les caractéristiques des nanoobjets et d'étudier l'impact de ces nanomatériaux sur les cellules souches mesenchymateuses.

Procédure expérimentale

Les surfactants gemini sont synthétisés par réaction entre le tétraméthyléthylènediamine et la bromohexadécane. Le produit de cette réaction est un bromide qui est transformé en acétate par réaction avec de l'acétate d'argent. Ensuite, le produit obtenu réagit avec de l'acide tartrique (l'utilisation de l'éantiomère *L* ou *D* produit des hélices avec des orientations différentes). Le produit final, le tartrate gemini 16-2-16, est dissous dans l'eau et chauffé à 60 °C pour initier la formation des hélices organiques. La durée de ce procédé de viellissement est de 48 heures pour les hélices qui miment le collagène; un changement de ce temps entraîne une morphologie différente des nanoobjets finaux. A la fin du développement des hélices, une solution préhydrolysée d'orthosilicate de tétraéthyle (TEOS) est ajoutée pour initier une condensation sol-gel. La morphologie des nanohélices en silice ainsi obtenues est vérifiée par microscopie électronique en transmission (MET).

La modification bioactive des hélices en silice commence par la réaction des hélices avec des molécules de 3-aminopropyltriéthoxysilane (APTES), qui permettent l'introduction de groupements amines en surface des nanomatériaux. Le 3-(maleimido)propionate de succinimidyle (SMP) sert de lien moléculaire entre l'APTES et les peptides. Suite à la liaison covalente du SMP et les groupements amines, une solution de peptide est ajoutée, ce qui mène à une liaison covalente du peptide avec les hélices. Les peptides utilisés dans cet étude sont les séquences KRGDSPC

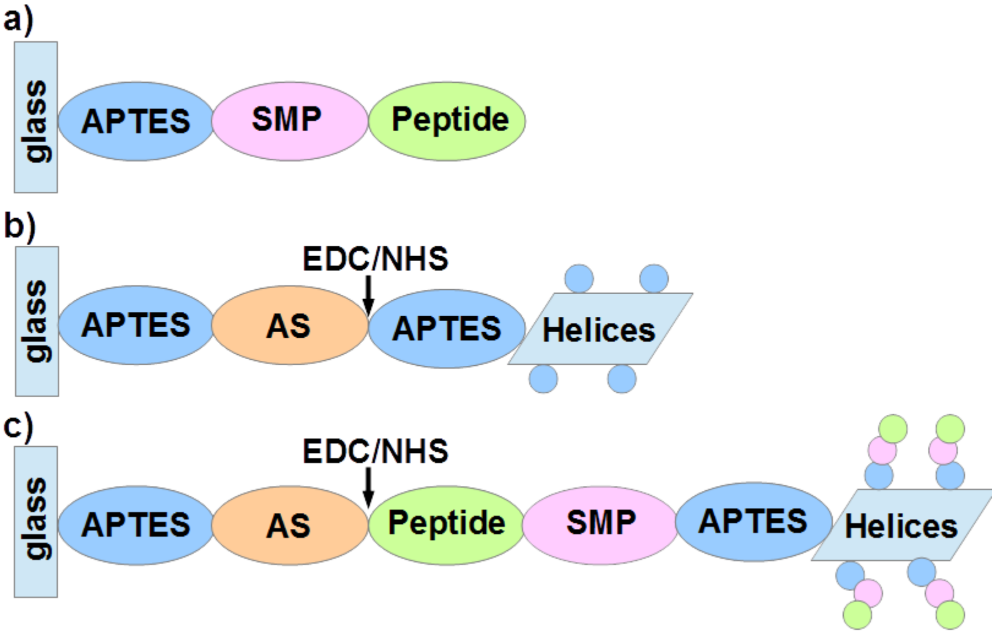

Figure 1: Schéma de préparation des a) matériaux de peptide homogène, b) matériaux avec nanohélices, et c) matériaux avec nanohélices modifiées de peptide. Les réactifs utilisés sont APTES (3-aminopropyltriéthoxysilane), SMP (3-(maleimido)propionate de succinimidyle) et AS (anhydride succinique). Comme indiqué par les boules autour des hélices, la surface des hélices est fonctionnalisée avec les peptides partout, mais seulement une partie d'eux fait partie de la liaison covalente avec la surface de verre.

(RGD), qui facilite l'adhésion cellulaire, et KRKIPKASSVPTELSAISMLYLC (BMP), un peptide mimétique de la protéine BMP-2, qui est connu pour son effect ostéogénique.

Afin de créer un environnement de culture cellulaire en 2D, les hélices avec ou sans modification peptidique sont liées aux surfaces en verre de manière covalente (voir schéma Figure 1.). Premièrement, les matériaux en verre sont traités avec l'APTES pour introduire des groupements amines; cette réaction et la suivante ont lieu sous une atmosphère contrôlée d'argon. Les matériaux ainsi préparés réagissent avec une solution d'anhydride succinique (AS) pour créer une couche de groupements carboxyles, qui est ensuite couplée avec les N-terminaux des peptides sur les hélices en utilisant la technique de couplage EDC/NHS.

On a également préparé des surfaces homogènes fonctionnalisées avec des peptides pour comparer leur effet à celui des matériaux avec les hélices. Ce greffage est effectué en utilisant APTES et SMP comme décrit plus haut.

La présence des peptides sur les matériaux est vérifiée en utilisant la spectroscopie photoélectronique X (XPS) et la microscopie à fluorescence. Des peptides couplés avec un fluorochrome comme l'isothiocyanate de fluorescéine sont employés pour rendre les molécules greffées visibles en fluorescence. Les peptides greffés sur les hélices sont quantifiés par leur absorption UV/Vis.

Le degré de couverture de surface d'hélice des matériaux greffés d'hélices est estimé en utilisant la microscopie électronique à balayage (MEB). Cette méthode sert aussi à vérifier la morphologie des nanoobjets après le greffage. Par ailleurs, l'orientation chirale des hélices est observée par la microscopie à force atomique (AFM). La MEB est une technique de microscopie où un faisceau d'électrons est accéléré vers une surface à examiner. Les électrons secondaires ainsi générés sont recueillis par un détecteur pour obtenir un image de la surface. Dans l'AFM, la surface à examiner est balayée par une sonde qui est déviée par l'interaction attractive ou répulsive avec la surface.

Avec le protocole décrit plus haut, des matériaux en verre modifiés ont été préparés:

- nanohélices *L* et *D*
- nanohélices *L* et *D*, modifiées du peptide RGD
- nanohélices *L* et *D*, modifiées du peptide BMP
- nanohélices *L* et *D*, modifiées des peptides RGD et BMP
- peptide RGD (homogène)
- peptide BMP (homogène)
- peptides RGD et BMP (homogènes)
- APTES
- verre

Des cellules souches mésenchymateuses humaines issues de la moelle osseuse sont cultivées sur ces matériaux pendant quatre semaines. Ces cellules sont ensuite fixées et marquées avec des anticorps pour l'immunofluorescence. Dans cette étude, deux marqueurs sont utilisés: Runx2 et OCN, qui sont des marqueurs ostéoblastiques.

Paralèllement, une expérience de protéomie a été effectuée avec le lysat cellulaire des cellules souches mésenchymateuses cultivées sur trois conditions pendant quatre semaines. Les conditions choisies sont: Le verre nettoyé et le verre fonctionnalisé avec des hélices vierges et le verre fonctionnalisé avec des hélices modifiées par des peptides mimétiques de la BMP-2. Les protéomes de ces échantillons ont été comparés pour identifier des différences d'expression de protéines.

Résultats et Discussion

La morphologie des hélices et leur similarité au collagène ont été vérifiées à l'aide de MET. Pour les hélices *L* du type 16-2-16, une périodicité de 64 ± 7nm et un diamètre de 29 ± 3nm ont été trouvés. Comme l'équipe de Dr. Reiko Oda[1] a découvert, la longueur et la morphologie des hélices (c'est-à-dire le pas d'hélice et le diamètre) peuvent être modifiées par fragmentation des hélices et par un changement de la composition chimique.

Les hélices, qui sont obtenues avec des aggrégats emmêlées, peuvent être homogénéisées par sonication. Pour cette technique, les nanohélices en silice sont lyophilisées, et la poudre est resuspendue dans un solvant et dispersée à l'aide d'ultrasons. Suite à ce traitement, elles sont dénouées et plus courtes, et la suspension d'hélices est plus homogène avec moins d'aggrégats.

La variation de l'excès énantiomérique du tartrate change la morphologie aussi. Les images obtenues par microscopie électronique à balayage (MEB) et par microscopie à force atomique (AFM) montrent que si l'acide tartrique *D* est utilisé pour la synthèse au lieu de l'acide tartrique *L*, le sens de rotation des hélices est inversé. Si un mélange du tartrate gemini *L* et *D* est utilisé, les nanomatériaux obtenus présentent des morphologies différentes. Il y a des hélices avec la

---

[1] IECB Bordeaux, 2 rue Robert Escarpit, 33607 Pessac, France

forme observée pour le tartrate *L* pur, mais aussi avec des périodicités et diamètres plus larges. Comme l'excès énantiomérique du tartrate gemini diminue, la proportion des nanoobjets dont la morphologie ressemble aux rubans torsadés plutôt qu'aux hélices augmente. La distribution des morphologies devient plus étroite si le tartrate gemini est synthétisé avec un excès énantiomérique bien défini de l'acide tartarique, comparé à la méthode où les tartrates de deux énantiomères sont mélangés sous forme de poudre. Pour ces nanoobjets aussi, on observe plus que l'excès énantiomérique diminue, moins les rubans en silice sont tordus. Pour les excès énantiomériques très bas, la morphologie hélicoïdale n'est plus visible.

Après le greffage des peptides bioactifs sur les hélices, la présence des peptides modifiés avec FITC a été vérifiée par leurs spectres d'absorption. La croissance du pic d'absorption autour de 490nm pour les hélices fonctionnalisées montre que les peptides sont bien liées en surface. Des matériaux greffés avec des peptides ont été préparés pour avoir un échantillon de référence qui peut être comparé aux matériaux fonctionnalisés avec les nanomatériaux. La présence des peptides sur ces matériaux a été validée par deux méthodes: XPS et microscopie de fluorescence. Les résultats XPS montrent que le greffage des peptides s'est bien réalisé en surface de verre. Les pourcentages atomiques expérimentaux restent en accord avec les pourcentages théoriques attendus théoriquement au cours des différents étapes de fonctionnalisation. Les analyses des spectres "haute-résolution" du Carbone et de l'Azote permettent de confirmer la présence des groupements N-C=O présents après greffage des crosslinkers, et l'augmentation des groupements C-O après greffage des peptides.

L'observation par microscopie de fluorescence des matériaux modifiés avec des peptides fluorescents confirme que la fluorescence des telles surfaces est homogène. La quantité de peptides greffés a été déterminée par des gammes étalons. Ces résultats obtenus par microscopie à fluorescence permettent de confirmer que les peptides sont présents en surface des matériaux de façon homogène avec une densité de 1.4 pmol/mm^2 pour RGD et 1.2 pmol/mm^2 pour BMP.

La présence et la morphologie des hélices greffées sur les matériaux en verre ainsi que la densité d'hélices immobilisées ont été évaluées par MEB et AFM. Les résultats AFM montrent que les hélices *L* et *D* ont effectivement des orientations chirales opposées. Les images SEM montrent que des hélices greffées sont présentes sur les surfaces, mais leur quantité est basse et varie beaucoup entre les échantillons. Le pourcentage de surface qui est couverte d'hélices est entre 9% et 29%, déterminé par analyse des images MEB.

Dans les manipulations de culture cellulaire, les intensités de deux marqueurs, OCN et Runx2, ont été quantifiées pour les cellules cultivées après un ensemement de quatre semaines sur les matériaux énumerés. Runx2 est un marqueur précoce de la différenciation ostéoblastique alors que OCN est un marqueur tardif de la différentiation ostéoblastique.

Les résultats de l'immunofluorescence montrent que Runx2 et OCN sont surexprimés sur les matériaux fonctionnalisés avec BMP, ce qui indique une stimulation ostéogénique. Sur les échantillons avec RGD et BMP ensemble, OCN est même plus abondant, alors que Runx2 reste stable. Il n'y a pas de différence significative entre les résultats pour les hélices *L* and *D*.

Compte tenu de manque de réproductibilité au niveau du recouvrement des hélices fonctionnalisées ou non en surface, les résultats obtenus manquent de réproductibilté. Comme une partie des matériaux n'est pas couverte des hélices, quelques cellules ne sont pas exposées aux hélices, ces dernières sont seulement en contact avec une la surface de verre fonctionnalisée d'APTES. L'importance de cet effet peut varier entre les échantillons à cause de la variation entre les matériaux, ce qui expliquerait les observations.

Dans la manipulation de protéomie, des expressions différentielles de plusieures protéines ont été identifiées. La comparaison avec trois autres études protéomiques referéncées dans la littérature montre que des protéines qui sont exprimées lors la différenciation ostéogénique présentent des abondances plus hautes surtout dans les cellules cultivées sur les hélices modifiées avec BMP. En plus, on a montré quelles protéines différentiellement exprimées sont associées par fonction en utilisant la base de données STRING. Les protéines identifiées dans cette expérience, comme Annexin A1, pourraient servir comme pistes d'investigation pour la recherche future.

Conclusions

Un biomatériau avec une morphologie hélicoidale qui imite celle du collagène a été synthétisé. On a montré comment ces hélices peuvent être modifiées avec des peptides bioactifs, et comment leur morphologie peut être changée pour obtenir des matériaux avec une orientation ou un pas d'hélice différent. Ces nanohélices ont été greffées sur des surfaces de verre de manière covalente afin de préparer des matériaux biomimétiques pour la culture des hMSCs. Les résultats préliminaires obtenus après quatre semaines de culture de MSCs sur les différents matériaux ne permettent pas de dégager une conclusion quant à l'impact des surfaces sur la différenciation ostéoblastique.

Les résultats montrent que plusieurs matériaux ont un niveau d'expression de marqueurs ostéogéniques significativement élevée comparé aux matériaux homogènes, mais aucune dépendance systématique de l'orientation ou la biofonctionnalisation n'est visible. Une raison possible de cette inconsistance est le fait que les quantités d'hélices attachées aux matériaux - et donc l'exposition des cellules aux bionanomatériaux - varie entre les échantillons.

Mots-clés: Biomatériaux, cellules souches mésenchymateuses, nanostructures en silice, différenciation de cellules, nanopériodicité.

Abstract

Tissue engineering is a field related to regenerative medicine which aims at replacing or regenerating a patient's tissue, usually using a combination of cells and a bioactive material which is designed to influence cell behaviour in a desired way. In approaches for bone regeneration, human mesenchymal stem cells (hMSCs) are a common choice of cells because of their ability to proliferate and differentiate into osteoblasts. Harnessing this potential requires biomaterials which promote osteoblastic differentiation, for example by mimicking the conditions in natural bone. Collagen I is a common protein in human bone; it forms fibrils with a characteristic periodic structure, which raises the question whether this particular morphology has in impact on stem cell fate. Artificial collagen-mimicking nanomaterials can help to investigate this question: Gemini surfactants with chiral counterions form twisted bilayers the morphology of which can be tuned by variation of experimental parameters like enantiomeric excess, time and temperature. The self-assembled helical nanoribbons which are obtained by this process can be transformed by a sol-gel condensation to form silica nanohelices the size and twist pitch of which resembles that of collagen fibres. The objective of this study is to prepare 2D culture environments featuring these nanomaterals (with and without bioactive peptide functionalisation) in order to explore the effect of these materials on hMSC differentiation.

Silica helices are fabricated by synthesis of surfactants with tartrate as counterion, and organic-inorganic transcription using a silica precursor compound. They can be modified by reaction with APTES and an N-hydroxysuccinimide ester and subsequent covalent immobilisation of a peptide. Two peptides were used in this study, one adhesion-promoting peptide featuring the RGD sequence and the active domain of the osteogenesis-inducing peptide BMP2. Helices with or without this bioactive functionalisation were covalently grafted to glass substrates using APTES and EDC/NHS-coupling. The presence of peptides on helices was shown by the absorption of helix-grafted peptides bearing the FITC-fluorophore. The successful peptide grafting onto glass surfaces was verified by XPS and fluorescence microscopy. The morphology of helices was monitored with TEM before helix immmobilisation on surfaces, and with SEM afterwards. SEM images were used to determine the amount of helices grafted to surfaces.

HMSCs were cultivated for four weeks on surfaces modified with APTES, peptide(s) or nanohelices, the latter being either left- or righthanded and functionalised or not with bioactive peptide(s). After fixation, the quantities of the osteogenic markers Runx2 and Osteocalcin (OCN) in the cells were evaluated. The results show that BMP2-functionalised surfaces did indeed exhibit an elevated level of Runx2 and OCN expression. A cooperative osteogenic effect of RGD and BMP2 grafted together could be observed in terms of OCN, but not with Runx2. Some helix-grafted materials exhibited a significantly higher Runx2 and/or OCN expression than the corresponding homogeneous materials, but these differences were not consistent across samples of the same chiral orientation or bioactive functionalisation. Therefore, conclusive general statements about differences in osteogenic effect between helix functionalisations and handednesses are difficult to make. A potential reason for this is the variability of surface coverage of helix-grafted materials: As the quantity of helices that are immobilised onto the surfaces is lower than expected and varies greatly between the samples, the number of cells that are not in contact with the helices might change as well, which can lead to false negatives.

The results of a proteomic experiment have shown which proteins are differentially expressed in cells cultured on helices with or without BMP-functionalisation, compared to bare glass. Comparison with other proteomic studies shows that proteins which are known to be upregulated during osteogenic differentiation are overexpressed most frequently in cells cultured on BMP-modified helices. The proteins that were identified with this method might serve as starting point for future investigations.

Keywords: Biomaterials, mesenchymal stem cells, silica nanostructures, cell differentiation, nanoperiodicity.

Acknowledgements

A phD thesis is usually a group effort, but this is even more the case for a project like this which includes several research groups and fields of science. I would like to thank the numerous people who helped in the work for this thesis, be it through active help with experiments, competent advice or other forms of support. Without them, this project would not have been possible. Firstly, I would like to express my gratitude to my supervisors, Dr. Marie-Christine Durrieu and Dr. Shawn Wettig, for their support, guidance and patience during the past years.

I thank Dr. Reiko Oda for her advice, encouragement and instruction on everything related to Gemini surfactants and for receiving me at her laboratory. Moreover, I would like to thank Dr. Laurent Plawinski, who provided immense support with cell culture and biological questions, and Dr. Emilie Pouget, who helped me with many experiments, especially with SEM. Furthermore, I would like to thank Dr. Guillaume Le Saux, whose experience with research and glovebox operation helped me to overcome countless difficulties. The support by Christel Chanseau, who lent me a hand in the preparation and characterisation of materials, is greatly appreciated. A further acknowledgement goes to the people who provided support with instrumental surface characterisation techniques, namely Dr. Christine Labrugère and the members of the research group of Dr. Leonenko in Waterloo.

Of course, I would also like to thank my fellow phD students: Especially Jiaji Cheng, who not only helped me with TEM experiments, but taught me most of what I know about nanohelix synthesis as well. Moreover, I would like to thank Laurence Padiolleau and Caroline Royer for their help and advice at the CBMN, and all my other colleagues at the Bio^3 group, the Oda group and the Wettig group who not only provided valuable by lending a helping hand, but also created an environment I enjoyed working in. I would like to acknowledge in particular the colleagues at the School of Pharmacy who enabled me to find my way around Waterloo University.

Finally, I would like to appreciate the colleagues who told me there was hope when I thought there was not; my parents, who supported my work abroad not only logistically but also emotionally; and my fiancée Tianjiao Cai, who was always there for me to help me carry on.

IDS
FUNMAT

Erasmus
Mundus

This phD project was funded by and carried out in the framework of the International Doctoral School for functional materials (IDSfunmat) of the Erasmus Mundus program, as a cooperation between the Universities of Bordeaux and Waterloo. The work was carried out under the supervision of Dr. Marie-Christine Durrieu and Dr. Shawn Wettig at the IECB and CBMN of the University of Bordeaux, the School of Pharmacy of the University of Waterloo, and the Department of Chemistry at the University of Liége. Specific experiments were performed at the Plateforme Aquitaine de Caractérisation des Matériaux and the Departments of Physics and Biology of Waterloo University.

Table of Contents

List of Figures

List of Tables

List of abbreviations

AFM	Atomic force microscopy
a.u.	arbitrary unit(s)
APTES	3-Aminopropyl triethoxysilane
AS	Succinic anhydride
BMP	Bone morphogenetic protein
BSA	Bovine serum albumin
CPS	Counts per second
DAPI	4,6-Diamidine-2-phenylindole
DMF	Dimethylformamide
DMSO	Dimethylsulfoxide
DTT	Dithiothreitol
ECM	Extracellular matrix
EDC	1-ethyl-3-(3-dimethylaminopropyl)carbodiimide
ee	Enantiomeric excess
FITC	Fluorescein isothiocyanate

(h)MSC	(human) mesenchymal stem cells
MES	2-(N-morpholino)ethanesulfonic acid
NHS	N-hydroxosuccinimide
NP	Nanoparticle
OCN	Osteocalcin
OD	optical density
PBS	Phosphate buffered saline
PDMS	Polydimethyl siloxane
PEG	Polyethylene glycol
PFA	Paraformaldehyde
SEM	Scanning electron microscopy
SMPB	Succinimidyl 4-(*p*-maleimidophenyl)butyrate
TA	Tartaric acid
SMP	3-(maleimido)propionic acid N-hydroxysuccinimid ester
TEM	transmission electron microscopy
TGM2	Protein-glutamine gamma-glutamyltransferase 2
ToF-SIMS	time of flight - Secondary ion Mass spectrometry
UV/Vis	Ultraviolet and visible light

Chapter 1

Background and Motivation

1.1 Bone defects: Clinical and economic importance

A bone fracture is a common injury, and its treatment is normally not an extraordinary procedure. However, depending on the extent of the bone damage, recovery may be hindered: In 5% of fractures, delayed healing or non-union occurs; in case of high-impact fractures, this rate even increases to 20% [1]. In this case, the body's natural healing mechanism fails and requires therapeutic intervention. This condition is named critical sized bone defect [2] . Apart from the trauma-related fracture mentioned above, it can also be caused by congenital disorders or tumour resection [3] The most common treatment in order to restore the structural function is a bone graft, an operation which is performed about one million times a year in Europe. The worldwide market value for bone grafting is estimated to be 5 billion Euro, with an annual growth rate of 10% [4]. As the risk of bone injury increases with age, it can be assumed that the importance of bone restoration in ageing western societies is going to increase in the next decades [5]. To address the challenges associated with this development, the European Union created the REBORNE project to find solutions for regenerating bone defects and conduct clinical trials.

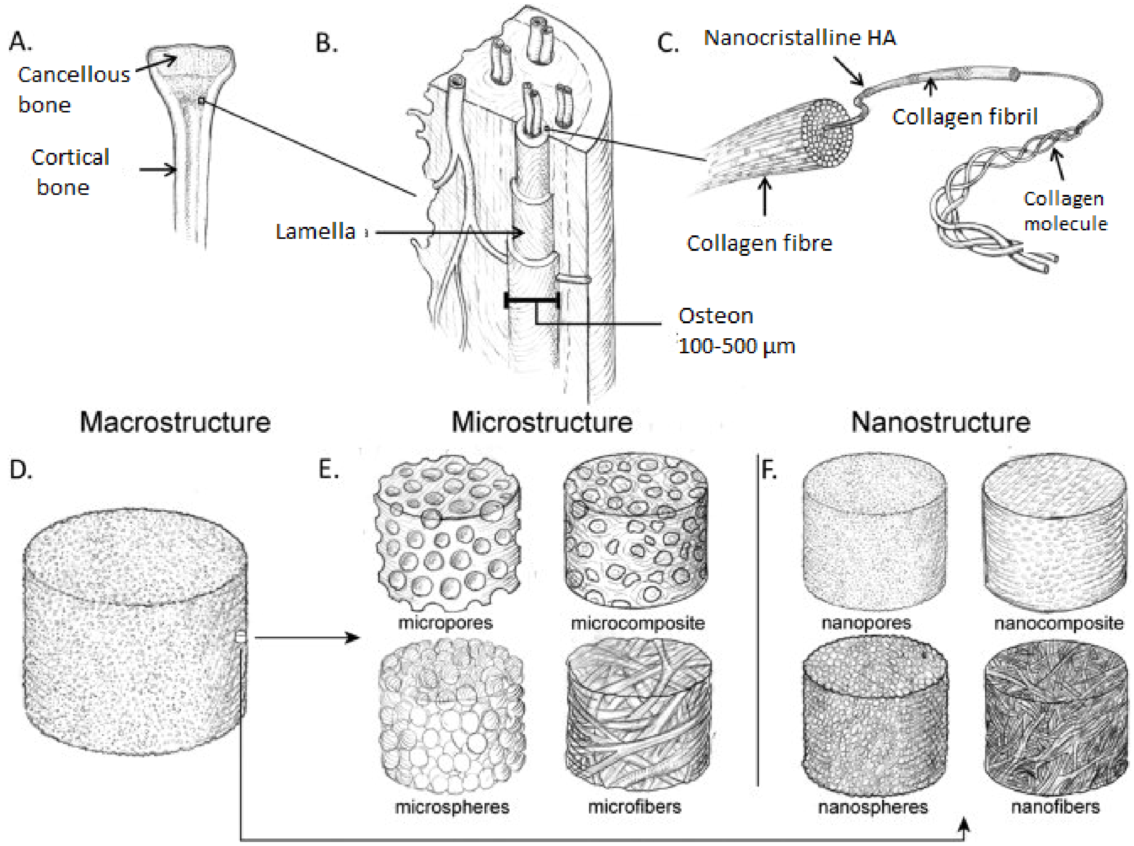

Figure 1.1: Hierarchical structure of bone (A-C) and a selection of micro-and nanostructured material types aiming at imitating bone properties [6].

1.2 Natural bone healing and the extracellular matrix

Bone is a composite material containing (inorganic) hydroxyapatite and (organic) collagen I. Osteoblasts take part in building up this structure by producing a matrix of collagen I and mineralising it [3]. As the bone is simultaneously resorbed by osteoclasts, it is a dynamic structure which undergoes a constant remodeling process. We distinguish between cancellous bone, a porous structure at the core of the bone, and cortical bone, which form the outer shell of the bone and provides structural integrity (cf. Figure 1.1, A-C).

In case of small bone defects, the human body is able to restore structural function without medical intervention. One distinguishes between primary and secondary bone healing, the former taking place only if the distance between the bone fragments is very low. Secondary bone healing

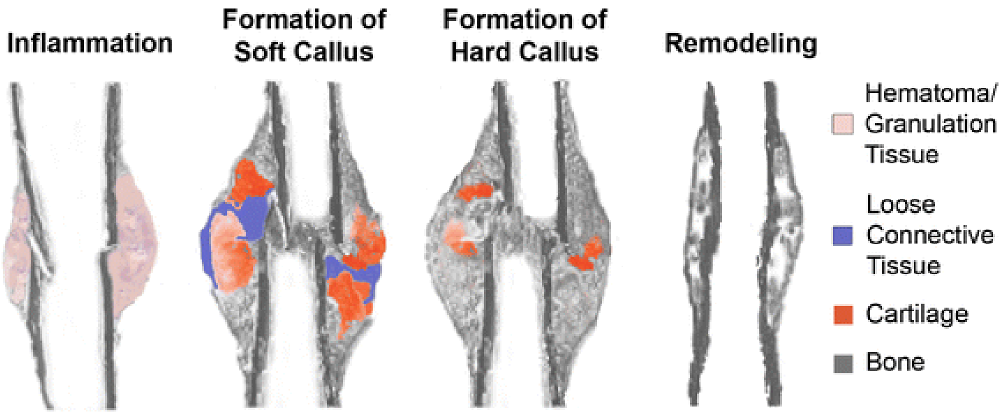

Figure 1.2: Illustration of the steps of bone healing process, [7].

consists of four steps: Firstly, a hematome is formed at the site of the injury. Secondly, a callus of cartilaginous tissue is formed, and thirdly, woven bone tissue (which consists primarily of collagen I [3]) forms a hard callus, a process which is called ossification. Ultimately, lamellar bone tissue replaces the callus. In this process, the vital role of cells is the deposition of structural biomolecules: Fibroblasts form a matrix of mainly collagen III at the defect site at the early stage of the healing process, and osteoblasts lay down the final compact bone. Mesenchymal progenitor cells can either differentiate directly into osteoblasts to form bone (intramembranous ossification) or into chondrocytes, which build up a cartilaginious matrix (endochondral ossification). In the latter case, the cartilage matrix is later replaced by woven bone [7]. The regenerative process is shown in Figure 1.2. Both osteoblasts and chondrocytes synthesise proteins which belong to the bone matrix [8].

1.3 Traditional therapeutic approaches and their shortcomings

Traditionally, the medical approach to dealing with loss or nonfunctionality of tissues or organs is transplantation medicine: If an organ or tissue is lost or damaged due to an accident or a disease or congenital condition, it can replaced by a transplant from a donor. There are two types of transplant to distinguish between: In an allotransplantation, the donor belongs to the same species as the patients, whereas a xenotransplantation is an interspecies tissue transplantation, e.g. from animal to human. If the transplant originates from the patient himself, the term autotransplant is used. The patient's immune response to the transplant is in many cases the limiting factor for transplantation medicine. Their immune system will react to the genotypic difference between donor and patient and reject the organ. The vehemence of this response depends on the genetic similarity, which is a major obstacle for xenotransplantation [9]. In order to enable transplantation of e.g. heart valves from pigs to humans without provoking a potentially lethal rejection, human genes can be inserted into the porcine germ line [10]. However, this does not solve the problem of transmission of diseases from the donor organism to humans: A virus which might be harmless to an animal might be pathological in humans.

In the case of allotransplantations, similar limitations apply, but their severity is mitigated by the genetic similarity of donor and patient: The probability of rejection is lower, and there is no risk of infection by pathogens from other species. If donor and patient are compatible, the immunogenicity can be diminished even further. On the negative side, for ethical reasons, removal of tissue or organs from a human donor is only appropriate if this intervention doesn't overly interfere with his health. A removal of vital organs is hence impossible.

Tissue engineering is a possible approach to overcome these limitations [11]. In this technique, cells are removed from the patient and expanded *in vitro* in order to obtain a graft to be re-implanted. As the expansion step requires high proliferation activity in order to obtain a significant amount of tissue, the use of the patient's fully differentiated primary cells is difficult because of their limited ability to proliferate. Instead, stem cells can be used. These cells have the ability to undergo numerous replication steps, but they bring along the challenge that they can differentiate into several different cell types. As the graft which is implanted must consist of cells of the same type as the tissue to be replaced, it is necessary to control their differentiation. For bone defects, the current gold standard in regenerative medicine is autologous transplantation. In this method, a piece of bone is removed from the patient himself and implanted into the defect site. This approach can heal bone defects which are too big for natural bone regeneration (named ”critial sized bone defects”) [12] and does not lead to immunogenicity, but there is a risk of donor site morbidity or paresthesia [13].

1.4 Biomaterials

1.4.1 Material types

Numerous studies have been dedicated to the development of methods in tissue engineering which improve the performance of bone regeneration by combining cells (usually stem cells) and cell recipient materials, which are referred to as scaffolds or matrices. These materials are required to be biocompatible to avoid adverse reactions to their implantation, porous, bioresorbable and matching the mechanical properties of bone - the latter is challenging, because the mechanics of bone are not the same throughout the bone [14]. In some cases, bioactive molecules are added as a third component in order to influence cell proliferation and/or differentiation: Growth factors like TGF-β (transforming growth factor β), BMP (bone morphogenetic protein), IGF (insulin-like growth factor) and FGF (fibroblast growth factor) are some examples. Mesenchymal stem cells (MSCs) are a standard cell type for this approach when dealing with bone regeneration, because they are capable of differentiating into osteoblasts. Frequently used scaffold materials are inorganic compounds like calcium phosphate, or polymers of synthetic or biological origin [15].

The popularity of calcium phosphate is due to its similarity to the hydroxy apatite of natural bone; several different compositions were tested. Another inorganic material of interest is bioglass, which is porous, degradable and available on the market. Studies refined this strategy by using hydroxyl apatite nanoparticles instead of a bulk material, or by incorporating strontium into the inorganic matrix to enhance proliferation and osteogenic commitment [16]. Porous metallic scaffolds are not biodegradable, but have high mechanic strength. Silica scaffolds show good biocompatibility; their bioactivity can be enhanced by incorporation of BMP and other biomolecules [17]. As to organic compounds, natural polymers are commonly used in the form of hydrogels: collagen, fibrin, alginate, silk, hyaluronic acid and chitosan are some examples [14].

Artificial polymers are equally employed, especially hydrophilic ones like polylactic acid (PLA), polyglycolic acid (PGA), polycaprolactone (PCL), or blends thereof [14]. Composite materials of organic and inorganic components received a share of attention because bone consists not only of hydroxyl apatite, but also collagen and other proteins and is thus also a composite material [18]. Another approach is the use of actual bone material which is seeded with MSCs to achieve a high level of similarity between the graft and the surrounding tissue [19]. A large variety of manufacturing techniques have been used for the fabrication of these materials. Apart from approaches like sol-gel reactions to obtain porous silica scaffolds, 3D printing techniques also gained some importance [20]: In solid free form fabrication (SFF), a powder and a binder component are applied to a surface in an alternating and locally controlled fashion . The powder can be based on ceramics, metals or polymers [14]. Similarly, laser engineered net shaping (LENS) is a layer-by-layer technique where a metal powder is locally molten by laser irradiation. Repeated addition of powder permits the fabrication of porous 3D matrices. For polymer materials, electrospinning is a popular technique, but it can also be applied to polymer/ceramic composites [14]. One advantage of silica is that it can be formed by sol-gel condensation in a matter of hours [**?**]. In the present study, the assembly of nanomaterials needs to happen quickly, which is why silica was choosen as material.

1.4.2 Biomimetic strategies

Many approaches for biomaterials are based on the idea that the desired cellular behaviour - stem cells undergoing the right differentiation at the appropriate time and location - takes place in nature as a part of tissue maintenance and repair. Therefore, it is attractive to try to mimic and recreate biological conditions *in vitro* in order to make cells behave the way they would *in vivo*. This strategy of imitating an *in vivo* situation is referred to as biomimetic. Due to the complexity of natural systems, studies to investigate biomimetic matrices are often limited to imitating one aspect of the natural extracellular matrix (ECM). Some studies focus on the chemical aspect and employ biological or bioinspired macromolecules as scaffold materials. Çelebi *et al.* [21] used

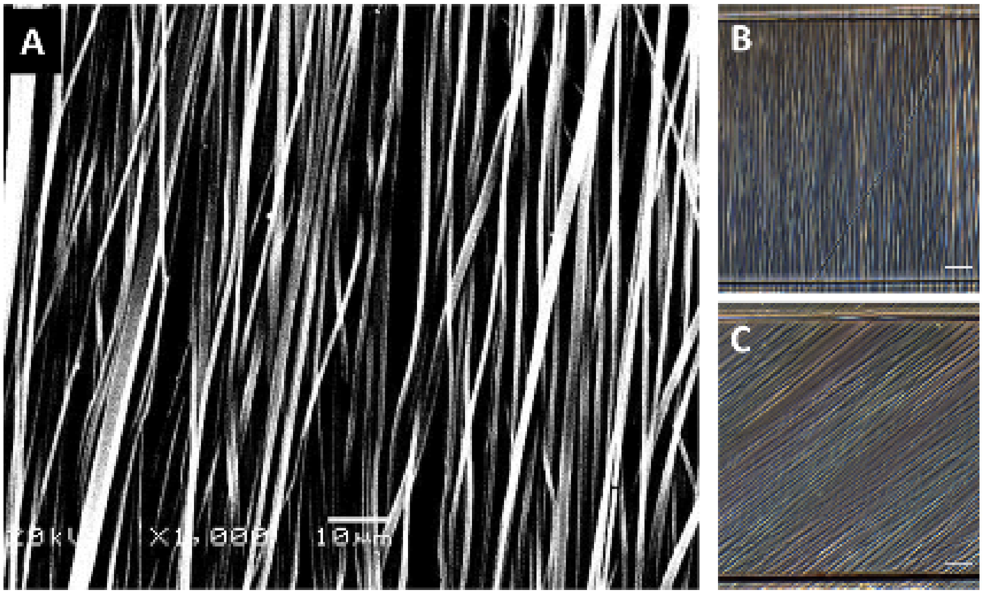

Figure 1.3: SEM images of aligned PLGA nanofibres as described in [23]. Scale bar in B and C: 50μm.

polymers inspired by elastin, a fibrillar structural protein which occurs in most vertebrates, to coat surfaces for hMSC culture. Their results indicate that this kind of environment might possibly stimulate osteogenic differentiation. Instead of picking specific proteins from the ECM, it is also possible to use, for example, the entire matrix taken from dental pulp, embedded in a scaffold consisting of collagen and chitosan [22]. This approach may yield only limited insight because the resulting cell culture scaffold is too diverse to pin down what causes its bioactivity, but these materials are interesting for applications because of their low immunogenicity and natural content of growth factors. Other studies concentrate on the impact of mechanical properties on cells in a given tissue. In native cartilage, for example, cells are exposed to the flow of interstitial fluid. It was attempted [23] to mimic the interplay of this flow stimulus and a nanofibrous matrix by culturing hMSCs in a microfluidic device with aligned nanofibres. The alignment of the fibres is shown in Figure 1.3. Varying the angle between nanofibres and flow direction showed that cells which experienced a perpendicular angle between flow and fibre alignment exhibited the highest degree of fibrochondrogenesis. This effect is hypothesised to be mediated by the RhoA/ROCK-pathway, which also mediates the cellular response to substrate stiffness. Spatial properties of bone

ECM as a possible regulating factor in tissue formation: As bone is a hierarchical structure with micro- and nanofeatures, biomimetic materials are often designed to have micro- and/or nanoscale dimensions (cf. Figure 1.1).

Another characteristic of natural tissues is their high water content, which is why many synthetic scaffolds are hydrogels. Scaffolds of polycaprolactone, polyvinylalcohol and gelatin were freezedried to obtain porous, highly hydrated matrices for the culture of MSCs [24]. Gelatin is of special interest because while it is hydrolysed collagen without any fibrillar shape, it retains the adhesive sequence of collagen. This cartilage-mimicking biomaterial was shown to support the chondrogenic differentiation of MSCs. A further aspect of the properties of cartilage is its composite character. In another study [25], electrospun polycaprolactone microfibres were combined with incorporated graphene nanoplatelets and carbon nanotubes. This scaffold, which mimics the mechanical properties of the composite cartilage ECM, was shown to promote chondrogenesis more than microfibres without carbon nanomaterials. A third defining feature of the ECM is geometry, the nature of its spatial characteristics. For example, Shukla *et al.* [26] used laser scanning lithography to create patterns of the adhesion-promoting protein fibronectin on surfaces in order to control the differentiation of MSCs. The patterns mimic the characteristic shapes of adipocytes in order to stimulate stem cells to differentiate in this direction. Indeed, MSCs cultured on adipocyte-shaped, oval shapes exhibited a higher tendency towards adipogenic differentiation than cells on different shapes, as depicted in Figure 1.4. Another group [27] used photochemistry to reproduce the dynamic character of the ECM: Vitronectin was grafted to a 3D scaffold by a light-induced coupling reaction; this technique made it possible to change the protein adhesion pattern even after the start of cell culture on these substrates. Using this technique, osteogenesis of hMSCs was selectively promoted in defined zones of the scaffold by spatially controlled biofunctionalisation.

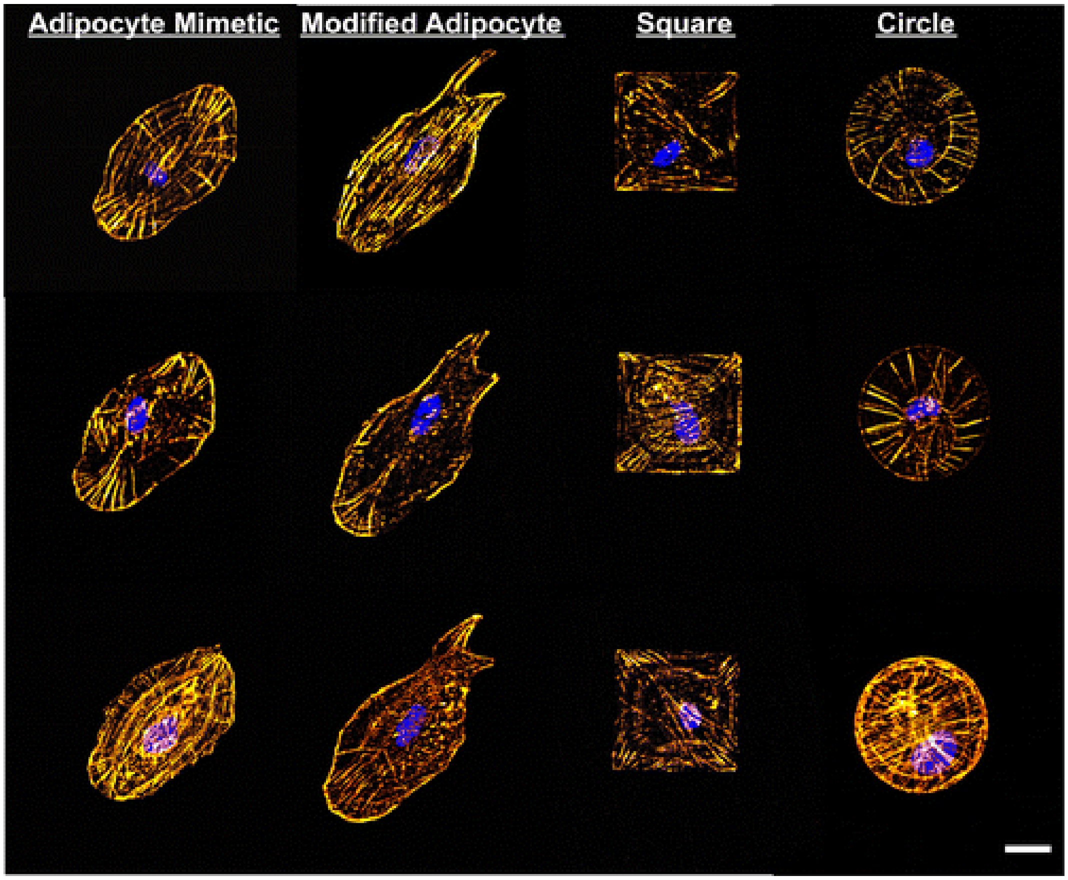

Figure 1.4: Fluorescence microscopy images of hMSCs that assume the shapes of adhesive islands on the substrate they are cultured on. Three cells per type are shown: adipocyte mimetic, modified adipocyte, square and circle shaped (from left to right). Scale bar 25μm, F-actin and nucleus stained in gold and blue. The island-induced shape was shown to influence cell fate [26].

1.4.3 ECM and bone regeneration

In order to achieve a successful reproduction of this process by means of tissue engineering, a high level of control over cell behaviour and differentiation is required. As chapter 2 will elaborate in detail, cells sense the properties of their environment in a variety of ways and respond via biochemical pathways. Designing the ECM in order to steer cell behaviour in the desired direction is hence a key strategy in regenerative medicine using tissue engineering.

In order to achieve controlled differentiation, the *in vitro* proliferation of cells for the creation of a graft should take place in an environment which provides optimal conditions for cell survival, but also sets cues to influence cell behaviour and especially differentiation of stem cells. The relevance of these effects should not be underestimated, or as it is phrased in [28]: ”Phenotype can supersede genotype”.

Natural ECM is a complex material consisting primarily of proteins, carbohydrates and growth factors, it is heterogeneous and undergoes dynamic change [15]. Unlike other tissues, bone consists of $43\ Vol\%$ mineral material, namely apatite [29]. At the microscale, the structure is organised in osteons, a long concentric substructure which surrounds the blood vessels inside the bone (cf. Figure 1.5). Its main organic component is collagen, which accounts for about 30% of the proteins in the human body and 90% of matrix proteins in bone [**?**]. It forms a network of aligned fibril arrays on which apatite crystals deposit and thereby provides structural support by giving tensile strength and elasticity to the matrix. Tropocollagen, the base unit of collagen, forms triple helices [29]. There are as well soluble components in the ECM, such as multiadhesive matrix proteins, which are vital for attachment of cells to their surroundings. The peptide sequence RGD (arginin-glycin-aspartic acid), often used for surface coatings to promote cell adhesion, was originally identified as the cell attachment-promoting domain of the multiadhesive protein fibronectin. The mechanical interactions between the ECM and the cell are primarily mediated by the fibronectin-binding transmembrane protein integrin: Its extracellular part binds to the surface, whereas the intracellular part is anchored to actin filaments [29]. The resulting stress on the cytoskeleton leads to the cellular response in the form of conversion of mechanical to chemical

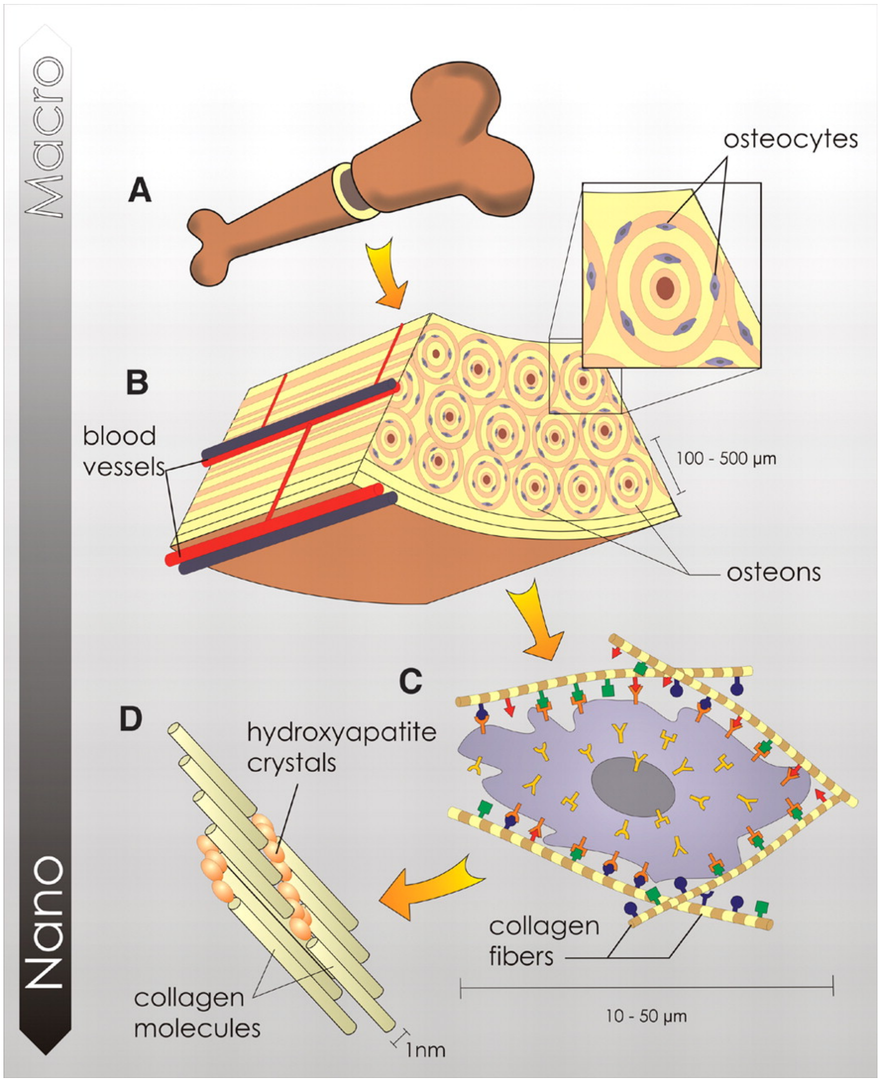

Figure 1.5: Illustration of bone structure from the macro- to the nanoscale. Osteons are cylindrical microstructures which surround the bone's blood vessels [30].

signals.

For the design of artificial ECMs for tissue engineering purposes, biocompatible hydrogels are commonly used [31]. They are polymer networks swollen by water and show similarity with natural ECM due to their softness and hydration. Common (polar) polymers for hydrogels are PEG, which can be crosslinked and functionalised, a number of other synthetic polymers [32] and several biopolymers like hyaluronan, alginate and chitosan. Hyaluronan can be found in connective tissue and is relevant for morphogenesis, *i.e.* the development of the shape of tissues and organisms. Polymer hydrogels tend to have a nanoscale mesh structure, whereas cells have micrometre scale dimensions. This potential drawback for scaffold permeability can be addressed by using hydrogels with either microporous or fibrous structure [33].

Being a ubiquitous component of natural ECM, collagen is often used in applications for regenerative medicine. For instance, in oral surgery, barrier membranes are used to cover an area where bone regeneration should take place. Due to its biocompatibility and degradability, collagen is a suitable material for this device. Its degradation time is adjusted by introducing crosslinkers [34]. Combination of collagen scaffolds with cells require a certain degree of scaffold porosity: Porous collagen sponges can be made from enzymatically digested collagen. Their crosslinked structure and interconnected pores make them suitable as scaffolds for histogenesis. They were used as biomaterials for cartilage regeneration involving chondrocytes. Cartilage is a promising starting point for tissue engineering because of its lack of blood vessels, the low cell-to-scaffold ratio and the absence of cells other than chondrocytes. Tissue generated this way exhibits good biocompatibility, and its regenerative performance can be further improved by addition of hyaluronan or growth factors. *In vivo* animal studies showed promising results. In order to mimic the composite nature of bone, layers of this collagen scaffold can be combined with demineralised bone powder. This powder has been shown to induce the formation of bone tissue and is therefore used in reconstructive surgery [35]. This principle can also be applied to bone tissue engineering: Biomaterials for bone regeneration can be composed of collagen fibrils in combination with hydroxyl apatite to imitate the mechanical properties of bone [36]. In these biomimetic composite structure, the inorganic fraction can be located embedded inside the collagen fibrils, between the tropocollagen helices or on the outside of the fibres [37].

Furthermore, in the field of cardiovascular medicine, collagen-based acellular scaffolds for reconstructive surgery are commercially available. Collagen matrices are also used (both with and without cells) in urogenital and neural tissue engineering [38]. Collagen-based materials are used as surgical wound dressings for (burn) injuries, as skin replacement for regular and diabetic wounds and as adhesives to seal damages lungs. Their advantage is the increased ease of handling compared to cellularised materials [39]. Collagen and gelatin, the hydrolysis product of collagen, are used as hemostatic agents in surgery: As they gelate, they form a clot which stops the bleeding of a wound [40].

1.4.4 The role of stem cells

As to the role of stem cells in the bone regeneration process, a study [41] suggested that the formation of new bone does not happen simply by proliferation of the seeded cells inside and around the scaffold, because the newly formed tissue turned out to consist mainly of the host organism's cells. The fact that the presence or absence of MSCs was shown to have a significant impact on bone formation nonetheless suggests that the seeded MSCs promote the migration of the body's cells into the scaffold, rather than repopulating it themselves.

Different cell sources for bone tissue engineering have been explored. A comparison [42] between MSCs which had been harvested from umbilical cord or bone marrow showed little difference between these cell origins. Moreover, embryonic and adult stem cells perform similarly on a polymer scaffold [43]. Human induced pluripotent stem cells the pluripotency of which is induced by retroviruses were compared with MSCs [44] and exhibited a similar performance. There is little evidence in literature suggesting that other cell lines are significantly superior to adult MSCs, which is why they are going to be used in this project. Moreover, adult stem cells are advantageous

as they are relatively easy to obtain and have a lower risk of tumour formation compared to embryonic stem cells [45].
It is also possible to administer hMSCs directly by intramuscular injection without a scaffold. It has been demonstrated that in spite of the short post-injection lifespan of these cells, this therapy has beneficial effects [46], but this matrix-free method is not appropriate for the treatment of bone defects because a solid support is needed to bridge the defect in the first place. The results of clinical application of MSCs in bone repair are promising: Numerous medical interventions to restore bone function using hMSCs in a scaffold material have shown good outcomes, also during the follow-up period [47].

Apart from hMSCs, several other cells are conceivable candidates for bone regeneration. Differentiated osteoblasts already have a defined phenotype and thus don't need to be directed towards a defined lineage, but their proliferation potential is not high enough to obtain a sufficient amount of cells. Embryonic stem cells (ESCs) have a very high self-renewal capability and they are pluripotent. However, their high proliferative activity produces the risk of teratoma formation. Besides, their source being embryos, their use is limited by ethical reservations and regulatory constraints. Induced pluripotent stem cells (iPSCs), which can be obtained by overexpression of the appropriate genes in differentiated cells, share many properties of ESCs. Their use requires the additional step of reprogramming (i.e. resetting them to pluripotency), but they are less ethically problematic than ESCs, which makes them interesting candidates. Adult stem cells (ASC) are undifferentiated cells which reside in tissue along with differentiated cells. ASC include mesenchymal stem cells (MSCs) which can be obtained from different origins: Umbilical cord, bone marrow and adipose tissue. MSCs harvested from umbilical cord tissue are safer than ESCs and iPSCs in terms of teratogenicity, but the body of research about them is small at present. Bone marrow derived MSCs are less easily available, but easier to isolate, and have been extensively studied. Their osteogenic potential is high, and they are currently the most common cell source for bone regeneration despite their low abundance. MSCs derived from adipose tissue present a more recent option: Their properties resemble those of bone marrow derived MSCs, but the harvest of cells from adipose tissue is easier than from bone marrow. The state of research about this cell source is less developed than that about bone marrow derived cells, but in the long run, adipose-derived MSCs can be considered a promising option [48].

Tissue engineering is not the only field of medicine where stem cells hold considerable promise. hMSCs have been explored as therapeutic agents for a number of pathologies [49]: As MSCs can differentiate into neurons, their injection can be a method of addressing neurodegenerative diseases. Symptoms of these conditions were mitigated by hMSCs in mice, and studies in humans showed that transplantation of *ex vivo* expanded hMSCs into the spinal cord did not have major adverse side effects [50]. The neuroprotective effect of injected hMSCs is due to the secretion of VEGF and other factors, which counteracts diseases like Parkinson's. Genetic modification of the patient's hMSCs can improve the possibilities to express beneficial proteins after administration of the modified cells. In a similar gene therapy approach, Alzheimer's disease - a neurodegenerative condition chracterised by a progressive loss of brain functionality - was tackled in animal models via two mechanisms: MSCs stimulate the expression of amyloid beta-degrading enzymes and have an antiinflammatory effect. The immunomodulation capacity of hMSCs also makes them an interesting candidate for the therapy of autoimmune diseases. Their administration was shown to suppress the production of cytokines, which is helpful for the treatment of rheumatoid arthritis. As hMSCs can differentiate into insulin producing cells, they can also be administered against type 1 diabetes. Furthermore, injection of hMSCs has been found to fight cardiovascular diseases in rodents if the addition of growth factors permits the transdifferentiation of the stem cells in cardiomyocytes.

1.4.5 Need for comprehension of regulation of differentiation

We have seen that the proliferative activity of hMSCs makes them an attractive choice for combined cell/scaffold approaches in regenerative medicine. Due to their ability to differentiate into several cell lineages, tissue engineering implants need to provide appropriate cues to induce formation of the desired tissue/organ type and avoid differentiation into other directions. The use of soluble induction media for systemic administration is problematic because its lack of local specificity may cause ectopic formation of the desired tissue. Therefore, the development of biomaterials which control cell behaviour and especially differentiation at the implantation site is required for the advancement of regenerative medicine.

Chapter 2

State of the Art

2.1 Stem cells

2.1.1 General behaviour

Differentiation of stem cells

Different tissues and organs in an organism fulfil different roles. Cells which undergo apoptosis need to be replaced to maintain tissue homeostasis. The balance between cell death and regeneration is kept by cell division, but cells lose their ability to divide as they differentiate and mature. Stem cells are essential for tissue maintenance because they provide fresh cells for renewal. They do this by undergoing an asymmetric cell division, which gives rise to two different daughter cells: One of them is a stem cell, one is differentiated [51] Stem cells are unspecialised cells, i.e. they do not have specific functions like differentiated cells. They are capable of sustained self-renewal by proliferation for many months and of differentiation into specialised cells. There are embryonic and adult stem cells (ESCs and ASCs): ESCs occur in blastocysts, which are cell balls in embryos, where they give rise to the formation of specialised tissues which constitute the organs. ESCs can be maintained undifferentiated *in vitro* by cultivation of a feeder layer, i.e. a coating of cells which do not divide. The factors which trigger and regulate ESC differentiation are for the

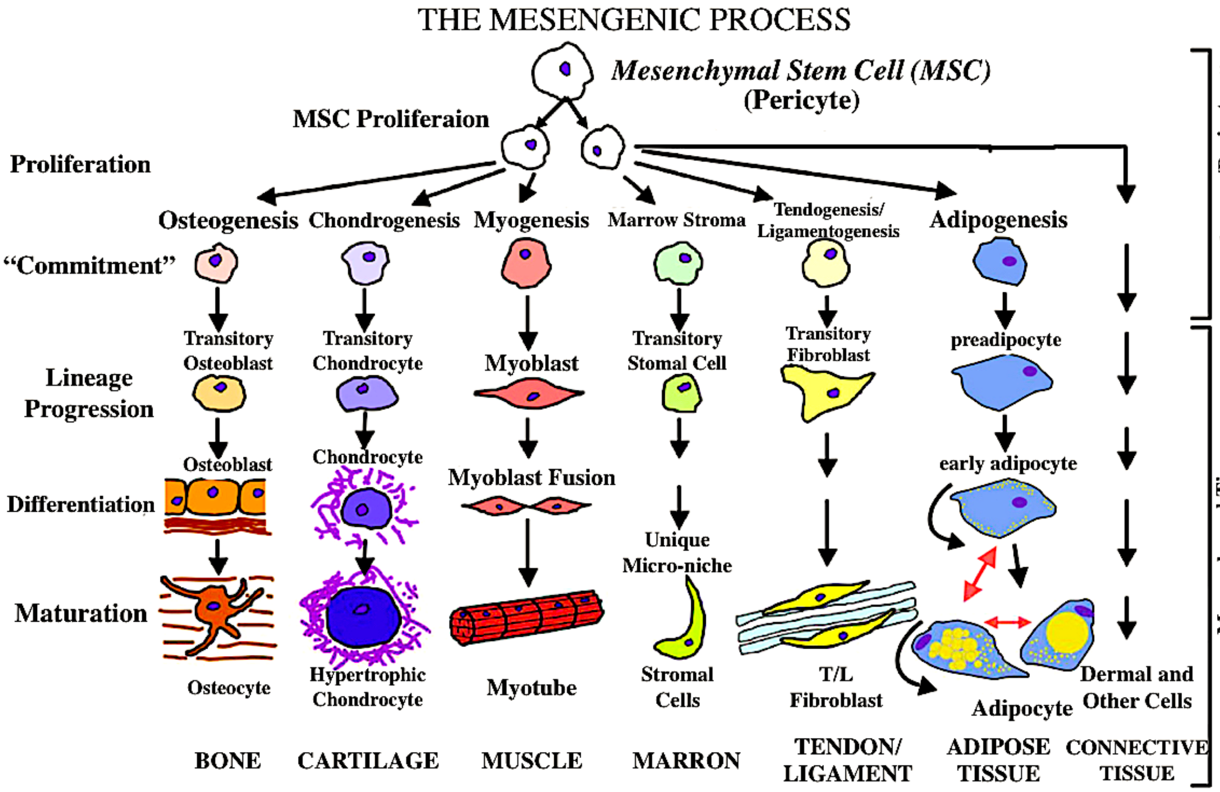

Figure 2.1: Illustration of the differentiation options of hMSCs and the steps they involve, [54].

most part elusive, but they are thought of as an interplay between regulated cellular gene expression and external stimuli. ASCs are also undifferentiated cells, but they reside between differentiated cells and are vital for their maintenance. They are also referred to as somatic stem cells. Their *in vivo* environment is called the stem cell niche, a matrix which provides appropriate cues to keep cells in a quiescent state and maintain the undifferentiated character of ASCs. Although ASCs tend to differentiate into the tissue types which they reside in, they can also undergo transdifferentiation and give rise to different cells - this property is known as plasticity [52]. Many ASC types are multipotent, they can differentiate into more than one cell type, whereas ESCs are pluripotent and able to differentiate into all somatic tissues (*i.e.* nearly all cell types of the body). Mesenchymal stem cells, for example, can differentiate into osteoblasts, osteocytes, chondrocytes and more, as shown in Figure 2.1. [53].

Human mesenchymal stem cells

Human mesenchymal stem cells can originate from various different tissues, the most typical source being bone marrow. Adipose tissue, blood and neonatal tissues like the umbilical cord are also known origins of hMSCs. The tissue of origin is of some importance because the cells' properties may vary depending on the source: For example, a study of MSCs of adipose origin in comparison to bone marrow derived MSCs revealed that the former exhibit a superior performance in terms of immunomodulation, angiogenesis and promotion of osteogenesis [55] [56]. HMSCs are characterised as stem cells due to their continuous cell cycle progression and their ability to differentiate into osteoblasts (bone cells), myocytes (muscle cells), chondrocytes (cartilage cells), adipocytes (fat cells), tendon and connective tissue [54] [57], as shown in Figure 2.1. Their mean doubling time is, depending on the tissue of origin, 24h to 40h [58]. They are able to form endo- meso- and ectodermal tissue types. Their proliferative capacity is not infinite, and their multipotency decreases with increasing number of passages [59]. Osteoblastic differentiation can be induced by addition of ascorbic acid, dexamethason and β-glycerophosphate [60]. The differentiation process involves several stages, some of which express characteristic proteins, which can serve as biomarkers for the early or late steps of the commiment process (cf. Figure 2.2).

It should be noted that the description of hMSCs can be based on its stem cell-specific self-renewal and differentiation capacity, or rather based on its *in vivo* behaviour [62]. MSCs are known not only as mesenchymal stem cells, but also under the names multipotent stromal cells, mesenchymal stromal cells or medicinal signaling cells - fortunately, the acronym MSC fits all of them.

Characteristic protein markers

hMSCs have been shown to have a protein profile similar to pericytes, and research suggests that both of them contribute to tissue regeneration [63]. They can be identified by the expression of a number of markers: CD105, CD73 and CD90 and lack of expression of CD45, CD34, CD14 or

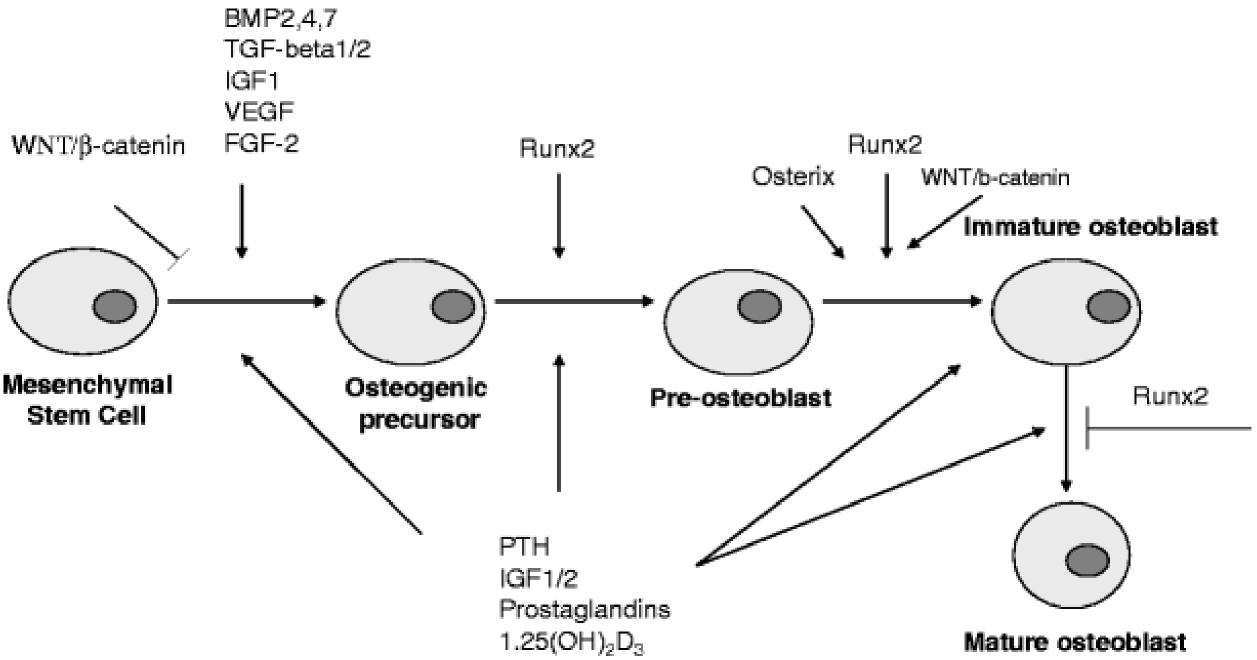

Figure 2.2: Illustration of the stages of osteogenic differentiation and a selection of the proteins involved therein, [61].

CD11b, CD79a or CD19 and HLA-DR surface markers are characteristic of mesenchymal stem cells [64]. The entirety of MSC surface markers was gleaned by Mafi *et al.* [65]. MSCs can be identified by their expression of the marker STRO-1. Although there is evidence that this antigen is also found in endothelial cells, it is commonly used to distinguish stem cells [66] [67].

The differentiation of hMSCs to osteoblasts is a complex process which involves a number of pathways. Amongst these, one protein stands out: Runx2, a transcription factor also known as runt related gene 2, regulates the development of osteogenic precursor cells to preosteoblasts and later to osteoblasts [61] [68]. It can be thought of as a master regulator of osteogenesis, because its expression preceeds and induces the activity of many other factors [69]. Osterix is a rare example of an osteogenic transcription factor that is Runx2-independent. The Runx gene is the target of several signalling pathways of relevance to osteogenic differentiation, including Wnt, TGF-β, Hedgehog and BMP [70]. Wnt signalling has a proosteogenic effect, it includes β-catenin dependent and β-catenin independent pathways. Its signalling mechanisms are visualised in Figure 2.3. In the former, activation of Wnt receptors causes accumulation of β-catenin by inhibiting its degradation, which causes this protein to unfold its transcriptional activity in the

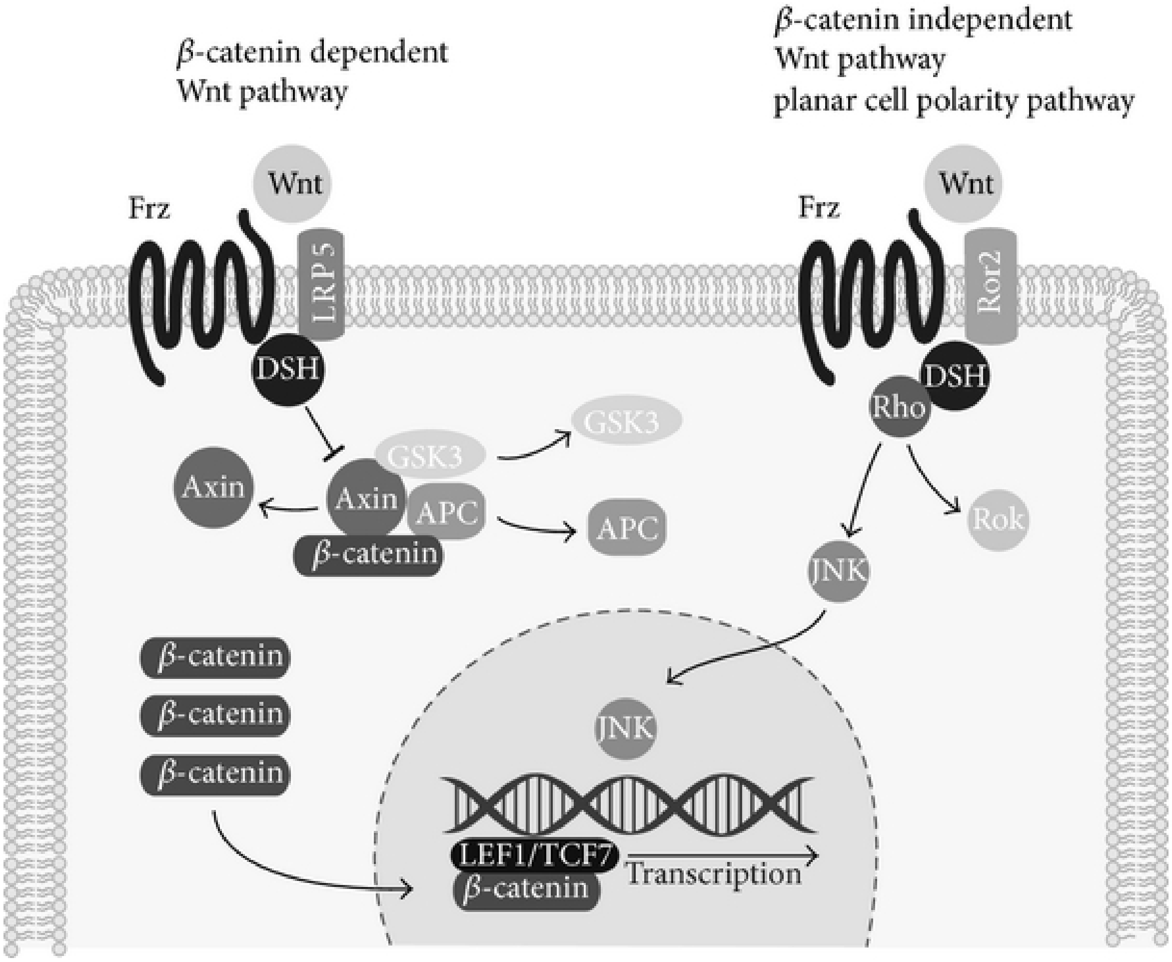

Figure 2.3: Illustration of the Wnt-signalling pathway [70].

nucleus. Hedgehog (HH) binds to cell membranes receptors which then release osteogenic lineage commitment inducing proteins of the Gli family. One of them, Gli2, also increases the expression of BMP2, initiating a feedback loop. BMPs are cytokines and belong to the TGF-β family. They can promote osteogenic differentiation through a mechanism of action that includes the Smad-pathway and MAPK. BMP2 is osteogenic, but can also have an adipogenic effect - the details of these effects are not fully understood. NELL-1 and IGF-1 are two pathways which also contribute to osteogenesis [70]. Collagen I is sometimes used as a marker for osteogenesis. It is expressed by osteoblasts even earlier on than the early bone marker Runx2 [71]. Unlike Runx2, the osteogenic markers Osteopontin (OPN) and Osteocalcin appear at a late stage of osteoblast development [72]. Rat osteoblasts were shown to be OPN-positive, whereas stem cell-like cells are OPN-negative [73]. OPN exists as secreted and intracellular protein; the latter is involved in cell migration. The expression of OPN takes place 14-28 days after osteogenic induction; at its peak, the marker is overexpressed sevenfold in comparison to stem cells [74] [75]. Osteocalcin (OCN), a calcium binding protein, is expressed mainly during the phase of the mineralisation of osteoids, i.e. of the nonmineralised bone matrix. It is released from cells and incorporated in the ECM, where it constitutes about 15% of the protein fraction which is not collagen [76] [77]. OCN is upregulated 14-28 days after osteogenic induction like OPN, but its overexpression factor is considerably lower . Alkaline phosphatase (ALP) plays a role in bone mineralisation. There are several isoforms of it, and about half of an adult's ALP originates from bones. Its expression is upregulated early in the osteogenic process and peaks 21 days after osteoinduction or earlier. ALP activity in serum can be measured with commercially available assays, and increases by the factor 80 in MSCs undergoing osteogenic dfferentiation [74].

Osterix has been shown to be essential in the formation of bone in mice. In the signalling cascade of osteogenesis, it is located downstream of Runx2 [78] [79].

The extracellular matrix

The ECM is what fills the space between cells of a tissue. It consists mainly of glycosaminoglycanes, fibrillar proteins and water. The ECM is not static but undergoes dynamic remodelling, partly by enzymes; its functions include structural support, binding of growth factors and receptors and buffering the tissue. Four of the most important proteins are collagen, elastin, fibronectin and laminin. Fibronectin is crucial for cell adhesion, and elastin influences the mechanical functions of the matrix [80]. Collagen is the most abundant protein in animals. Many different variations of it exist; the most common one is named collagen I and represents more than 90% of the body's collagen [81]. The simple polymer is called α-chain, these chains self-assemble into triple helices, which are called tropo- or procollagen and normally consist of two strands of one sequence and one of another. The sequences of collagen are continuous repeats of Gly-X-Pro

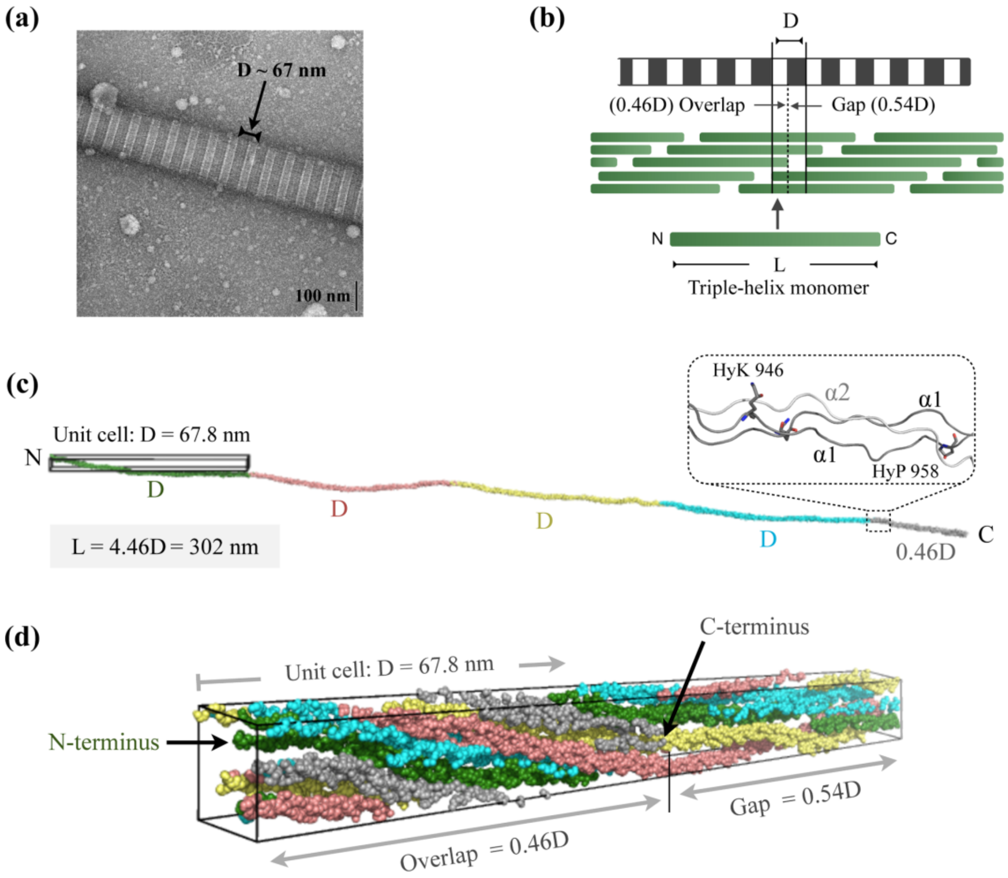

Figure 2.4: (a) TEM image of a collagen fibre, pointing out the D-band length of 67nm. (b) Visualisation of the origin of collagen nanoperiodicity. (c) Structure of tropocollagen. As the coulouring indicates, its length is not a multiple of the collagen fibre's unit cell length, which results in gaps in the fibre. (d) 3D representation of tropocollagen within a collagen fibre [82].

and Gly-Hyp-X, where Gly is glycine, Pro is proline, Hyp is hydroxyproline and X is another amino acid. The period length of tropocollagen is 86Å. Due to lateral interactions between these fibrils, they form collagen fibres of about 50nm diameter. Due to the staggered arrangement of tropocollagen in these fibres, they feature a periodicity of 67nm which can be observed as dark and bright bands [82]. Factors like salt concentration and hydration level can make this band length shrink. The periodic bands and the underlying structure are shown in Figure 2.4. Attempts were made to reproduce the two-step self-assembly behaviour of collagen. Rele *et al.* [83] synthesised collagen-mimicking fibres of 12-15nm diameter by self-assembly of synthetic peptides. Molecular dynamics calculations show that electrostatic interactions and hydrogen bonds are the driving forces for their assembly. The effect which gives rise to the band pattern is the same as in the

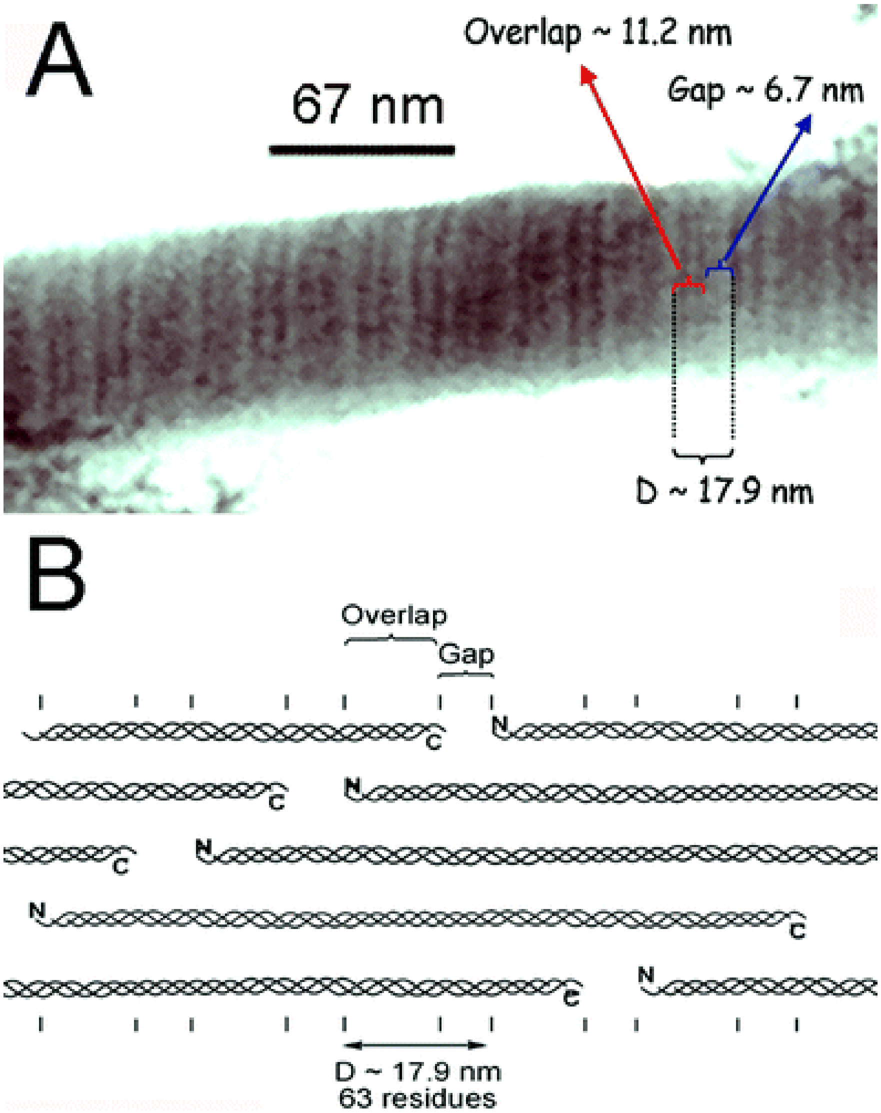

Figure 2.5: TEM image (A) and schematic representation (B) of synthetic peptide-based collagen-mimicking nanofibres [83].

case of collagen: Gaps in the staggered array occur are equidistant, as Figure 2.5 illustrates. In bone regeneration, collagen plays a role not only as a scaffold with structural function but also as nucleation point for bone mineralisation. The formation of hydroxylapatite takes place when collagen is exposed to a concentrated calcium phosphate solution. It was demonstrated that the periodic structure of collagen is also reflected in the resulting inorganic matrix [84] and that the hydroxylapatite which is deposited on demineralised collagen-rich tissue in an appropriate solution matches the mineralisation pattern of natural hydroxyapatite [85]. This raises the question how collagen is involved in the bone formation process and in which ways is interacts with its cellular aspects. He *et al.* [86] studied the behaviour of MSCs on a composite matrix consisting of hydroxyl apatite and collagen I. Cells on this scaffold exhibited an increased osteogenic commitment, as evidenced by ALP, osteopontin and osterix. This effect was not found with materials where collagen I was replaced by a synthetic hydrogel.

2.1.2 Impact of chemical and mechanical factors

In order to harness the potential of MSCs for regenerative medicine and (bone) tissue engineering, it is vital to understand their interactions with their environment, be it a natural extracellular matrix or an artificial scaffold. Of particular interest are the cues which direct cell differentiation. A large body of literature covers the impact of chemical and mechanical factors on mesenchymal stem cells.

Peptides and Proteins

Natural proteins which stimulate cellular proliferation and/or differentiation are called growth factors (GFs), e.g. BMP, TGF-β and FGF. Basic Fibroblast growth factor (bFGF or FGF2) binds heparin and as an angiogenic factor, it is important in wound healing, but was also found to be beneficial for bone regeneration in rats [87]. The glycoprotein VEGF, vascular endothelial growth factor, stimulates the proliferation of various cell lines. Platelet derived growth factor (PDGF) is a regulator of cell divison and angiogenesis; it is related to VEGF. Nerve growth factor beta (NGF-β) is primarily relevant for neuronal development, but it has also been shown to reduce the apoptosis of osteoblasts. Transforming growth factors beta 1, 2 and 3 are important factors in proliferation, adhesion and differentiation [87]. VEGF and Insulin-like growth factor 1 (IGF-1) are upregulated during the cells' proliferation stage, whereas the late growth factors FGF2 and BMP-2 are upregulated during the differentiation and maturation stage. All of them generally promote osteogenic commitment, but their exact effect depends on time and concentration [88].

Bone morphogenetic protein (BMP) is one of the growth factors that regulate the equilibrium between bone formation and resorption. There are 15 types of BMP, which are expressed at different stages of osteogenic differentiation. Some evidence suggests that BMP-2 is the most important of them. [89]. BMP-7, which is also known as osteogenic protein 1, is also used in medical applications, e.g. the treatment of tibial nonunion [90]. Many of the peptides which can influence MSC differentiation have mechanisms of action that involve the Wnt pathway. Signalling proteins in this pathway are bound to a receptor related protein complex named ”Frizzled” at the cell surface. This receptor transduces the signal to a number of intracellular proteins, including the transcriptional regulator β-catenin, the degradation of which is inhibited upon transduction of a Wnt signal [91]. The subsequent increase in β-catenin levels triggers several effects; some of them are relevant for stem cell differentiation. For example, Wnt signalling has been shown to inhibit adipogenic differentiation of hMSCs [92], whereas overexpression of microRNA-499 led to formation of cardiac cells in rat MSCs [93]. You *et al.* found that the protein Foxc2 stimulates osteogenic differentiation at the expense of adipogenesis in rabbit MSCs, possibly under involvement of the Wnt/β-catenin pathway [94]. This finding is of potential clinical relevance, because age-related loss of bone matrix is associated with an expansion of adipose tissue in the bone marrow.

Another pathway of interest is the extracellular regulated kinase (ERK)-pathway, which belongs to the mitogen-activated protein kinase (MAPK) family. When treated with mechano-growth factor, rat MSC *in vitro* exhibited stronger migration, regulated by the ERK pathway and cellular mechanotransduction [95]. Other pathways which have been shown to influence osteoblastic differentiation are the TGF-β, BMP, Notch, Hedgehog and FGF pathway.

mTOR, a kinase and target of rapamycine, has been demonstrated to have an effect of osteogenesis, but there is no consensus as to whether it enhances or inhibits it [96]. Runx2, which was mentioned earlier as a marker for osteogenesis, is known to induce osteogenic differentiation in MSCs [97]. The transcription factor, which belongs to the Runt family and occurs in three isoforms, activate a number of genes related to osteogenesis, including osterix and

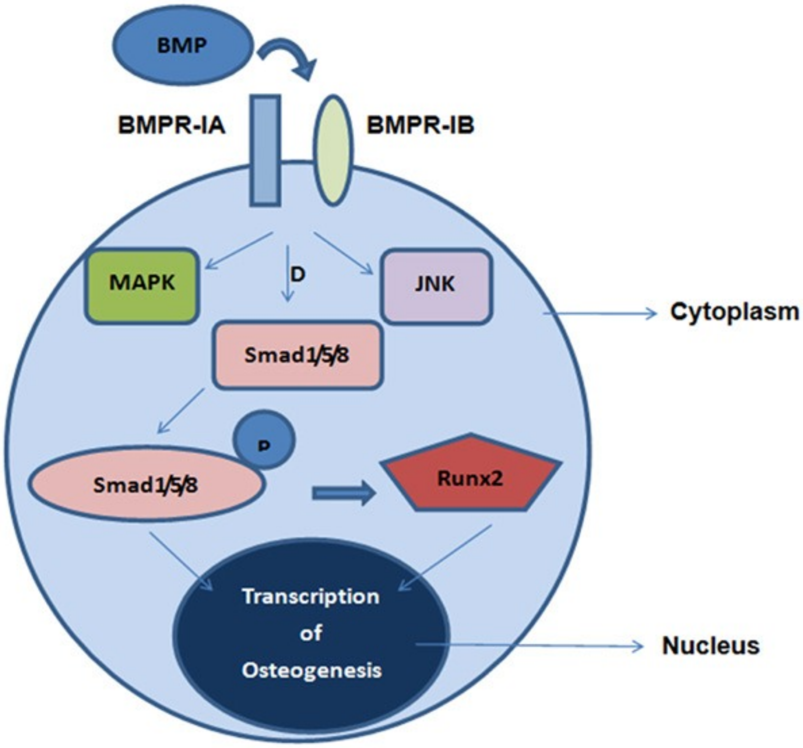

Figure 2.6: Signaling pathways involved in the BMP induced osteogenesis. BMPs bind to receptors on cells to activate downstream signal molecules such as Smad, MAPK and JNK. In the classic Smad signaling pathway, Smad protein is phosphorylated, leading to its activation. Activated Smads cooperate with Runx2 and then translocate into the nucleus to induce the transcriptional expression of osteogenesis related genes. [97].

OPN (osteopontin). After the differentiation, the Runx2 concentration decreases again; this event is vital for osteoblast maturation. The expression of Runx2 is promoted by Bone Morphogenetic Protein (BMP) via the Smad pathway, which is shown in Figure 2.6 [97].

Some peptides or proteins influence (stem) cells indirectly, e.g. by facilitating cell adhesion [99]. It is well known that peptides featuring the RGD-sequence, which is derived from the ECM protein fibronectin, is involved in integrin-mediated cell-matrix binding (cf. Figure 2.7) [100]. RGD-peptides are the most widely used adhesion promoting peptides because they are highly effective, extensively studied, bind to several integrin species and are easy to synthesise [**?**]. Other cell adhesion promotiong peptide sequences are listed here:

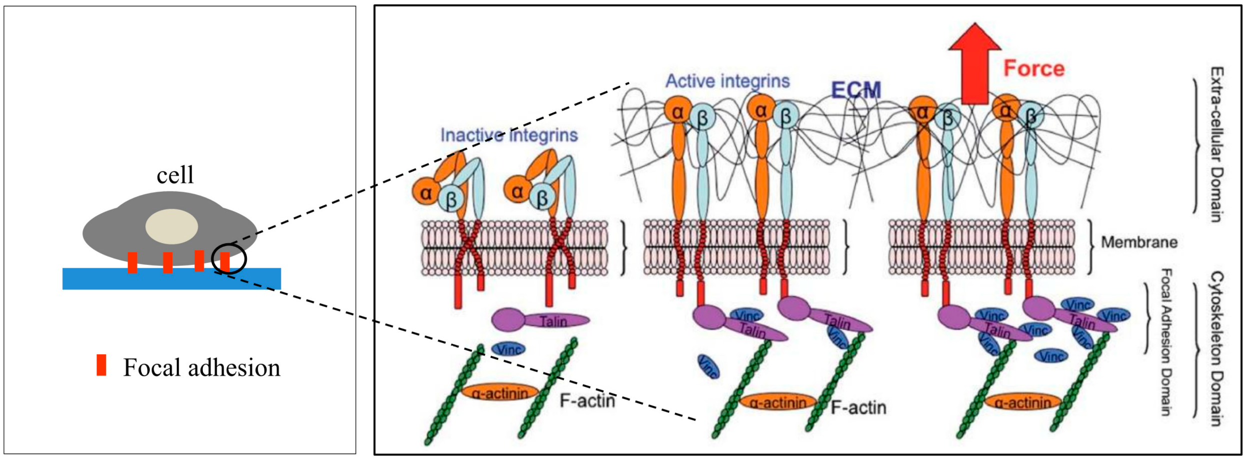

Figure 2.7: Scheme of cell-surface binding *via* focal adhesions: Cells adhere through Integrins, a transmembrane protein, which forms focal adhesions by binding to ECM molecules. [98].

- RGD
- FHRRIKA
- YIGSR
- REDV
- VAPG
- VGVAPG
- KQAGDV
- KREDVY
- KSRS
- GVKGDKGNPGWPGAP

Along with RGD, FHRRIKA is also a peptide with can support cellular adhesion: Both of these peptides can enhance cell attachment to surfaces they are grafted onto [101]. There are numerous examples of other adhesive peptides: YIGSR is an integrin receptor ligand which is derived from laminin and promotes adhesion of some cell lines. REDV is fibronectin-derived and helps endothelial cells to adhere. VAPG, VGVAPG and KQAGDV were also shown to promote cell adhesion, e.g. for vascular smooth muscle cells [100] [102]. Furthermore, peptides with the sequence KREDVY enhance the adhesion of HUVEC (Human umbilical vein endothelial cells) when covalently grafted to surfaces [103]. The sequence KRSR is interesting in the context of osteogenic differentiation, because it selectively binds to osteoblasts more strongly than to fibroblasts [104]. One of the reasons why RGD still stands out from this variety of peptides is its ability to promote the proliferation of adherent cells better than other sequences [105].

The effect of two peptides together was investigated by Ibrahim Bilem [106]: In his work, the adhesion-promoting peptide RGD and the osteogenesis-promoting BMP were grafted with a density of a few pmol/mm^2. The data show that the stem cell marker STRO-1 is expressed more on RGD-modified surfaces than on surfaces with BMP or both peptides together. The protein Runx2, which is a marker for osteogenic differentiation, is found on RGD-surfaces in similar quantities as on reference surfaces without peptide. However, the expression of Runx2 is significantly higher for BMP-surfaces, and even further elevated for samples featuring RGD and BMP together. These results suggests there is a cooperative effect between the adhesive RGD- and the osteoinductive BMP-peptide, i.e. cells cultivated on both peptides together exhibit a higher degree of osteogenic differentiation than one would expect from summing up the effects of the individual peptides alone.

Other molecules and surface types

As introduced above, osteogenic differentiation of hMSCs can be efficiently induced *in vitro* by addition of ascorbic acid, β-glycerophosphate and dexamethasone [60]. The use of osteoinductive media in clinical applications is limited due to the undesirable possibility of ectopic bone formation. Some lipids have been reported to exhibit osteoinductive behaviour. Kin *et al.* showed that gangliosides, a class of glycosphingolipids, promote osteogenic differentiation, possibly by interaction with epidermal growth factors [107]. Phosphatitylserine, a phospholipid which occurs in cell membranes, stimulates osteogenic differentiation of hMSCs [108]. This effect is assumed to be mediated through the ERK pathway. Furthermore, hints have been found that the non-neuronal cholinergic system might be a pathway which is involved in mechanisms related to osteogenesis and bone regeneration [109].

A number of studies indicated that matrix-bound bioactive proteins tend to have the same effect as proteins in solution [110].

Effect of stiffness

Early experiments to explore the impact of matrix rigidity on cells and osteogenesis showed that osteoblasts exhibited stronger bone formation and mineralisation when they were subjected to mechanical tension or compression, respectively [111]. This and the observation that lack of adjacent musculature hinders bone regeneration raised the question how mechanical factors like stiffness, tension and movement can influence cell behaviour. Engler *et al.* [112] were the first to find a connection between matrix stiffness and MSC fate: They found out that MSCs on substrates of different stiffness showed different commitments. The elasticity of a material can be quantified using the Young's modulus, which is the ratio between the force of applied stress and the resulting deformation. Soft matrices with a Young's modulus of 1kPa or less induced the formation of neuronal precursor cells, substrates of intermediate stiffness of 8-17kPa underwent myogenic differentiation and hard surfaces (25-40kPa) resulted in osteoblastic formation. One can observe that cells which naturally form hard/soft tissues were induced by a hard/soft matrix. These experimental findings where backed by computational results by Mousavi *et al.* [113], whose numerical model predicted a very similar relationship between substrate stiffness and stem cell fate. However, there are also contradictory results [114]: The aforementioned relationship between stiffness and differentiation can only be generalised for substrates which permit cell adhesion, e.g. surfaces grafted with ECM molecules which the cells can bind to. Moreover, substrates of a relatively stiff material can have the same effect as a soft surface if its surface features are more flexible than the bulk material, as it is the case with polymer nanopillars: Although they are made of a stiff material, the pillars may bend due to their low diameter, which causes the substrate to appear soft [115] (cf. Figure 2.8). It is noteworthy that the mechanical signal causes not only a biochemical but also a mechanical response in cells. AFM measurements revealed that as stem cells undergo osteogenic differentiation, their Young's modulus decreases, i.e. they become softer [116]. A possible explanation for this might be that as the cytoskeleton reorganises

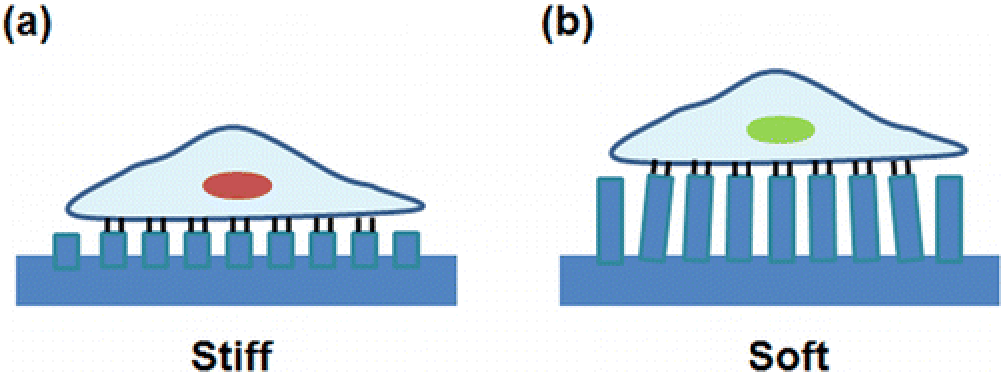

Figure 2.8: Schematic representation of cells on polymer nanopillars of different lengths. Increasing length of the features makes the material appear softer for cells [115].

to form focal adhesions at the cell-substrate interface, the quantity of actin in the upward facing part of the cell is decreased. The causal connection between matrix rigidity and the resulting stem cell commitment implies that there must be a mechanism to convert a mechanical input to a biochemical response. This mechanism is believed to rely on ion-channels, integrins and cadherins. Ion channels are required to permit transport of ions through the cell membrane. They can be activated or deactivated by mechanical stretch: The formation of stress fibres was found to transmit a mechanical tension to the plasma membrane and activate ion channels. This mechanism might be dependent on the ROCK-pathway (Figure 2.9, a). Integrins form a link between the extracellular matrix and the cytoskeleton. They consist of α- and β-subunits, and the composition defines which proteins the integrins bind to. Integrins can transmit mechanical signals to the cell, which evokes a biochemical reaction (cf. Figure 2.9, b). The function of cadherins is to establish cell-cell-bindings. Intracellularly, they are anchored to catenins, which in turn are bound to the cytoskeleton. β-Catenin is known to promote osteogenic differentiation. Focal adhesions, the intracellular anchorage point for integrins, consist of β-integrin subunits, vinculin, talin and actin. Depending on substrate stiffness, they can generate mechanical tension and thereby influence MSC differentiation [117]. Interestingly, the effect of substrate stiffness appears to last beyond the exposure to this condition. It has been reported that hMSCs which were cultured on hard substrates and were transferred to soft ones showed signs of osteogenesis, like Runx2 expression and alkaline phosphatase activity. The extent of this effect increased with the time the cells previously spent on

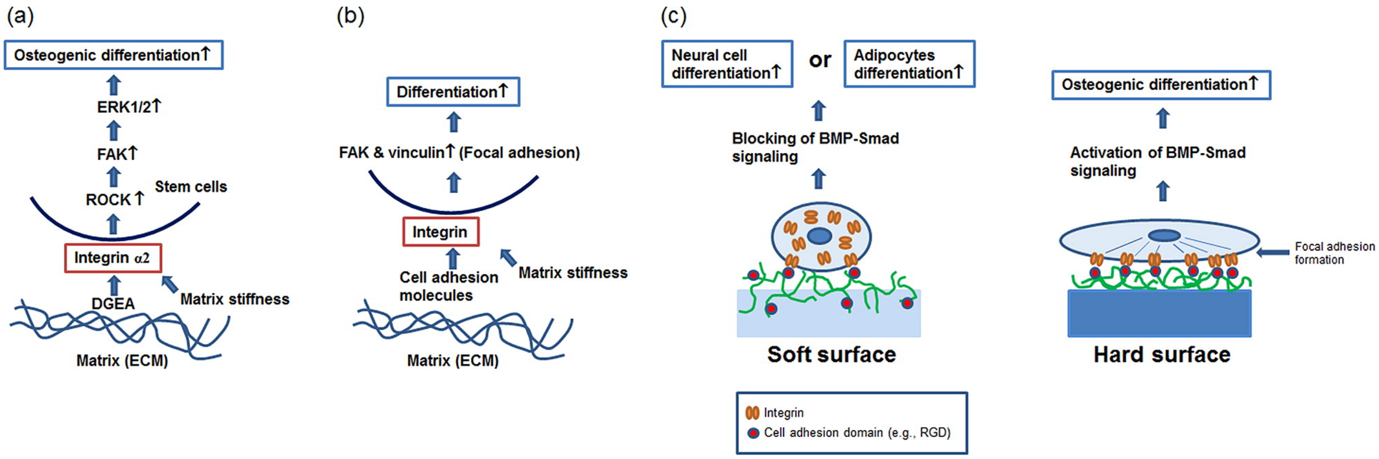

Figure 2.9: Different ways in which substrate stiffness can act on cell behaviour and differentiation: *Via* activation of the ROCK-pathway (a), *via* modification of growth and shape of focal adhesions (b) or by regulation of the BMP/Smad-pathway [115].

hard substrates [118].

It should be noted that the impact of stiffness needs to be examined differently in the case of surfaces featuring nanoobjects. If these objects are not tethered to the surface, the cells will not perceive them as a rigid substrate even if their elastic modulus is high [110].

Dynamic stress response

Mechanical force can be applied to cultured cells in two ways: By physically deforming the cells or their substrate, or by exposing the cells to fluid dynamics. Either way, the cells will be exposed to shear stress or other deformations. Yamada *et al.* cultivated murine MSCs in a porous composite scaffold and applied cyclic longitudinal compression force to it. For moderate compression loads, this treatment resulted in an increased expression of osteopontin and osteocalcin. However, this outcome was not observed for high loads [119]. Tension on cell-seeded collagen 3D matrices was shown to induce BMP-expression, which induces osteogenic differentiation [111]. Another study [120] stretched MSCs daily for up to five days using a flexible substrate. With all cells being cultivated in adipogenic medium, those that were exposed to stretching showed less markers of adipogenic differentiation than the control group. It was proposed that this mechanical influence is mediated by the TGFβ1/Smad2 pathway.

There are examples of oscillatory flow activating the RhoA and ROCKII pathway, which leads to a higher level of proliferation and expression of osteoblastic genes. Not all studies exploring the effect of dynamic mechanical stress point in the osteoinductive direction, though: Cyclic compressive loading of rabbit MSCs suspended in hydrogels caused a chondrogenic effect resembling the effect of addition of TGF-β [111].

2.1.3 Impact of geometrical factors and nanomaterials

Molecular chirality

The concept of chirality is of high relevance for biological systems, as the enantioselectivity of many natural enzymes exemplifies. Much research has been dedicated to the origin of handedness in embryonal development: How do tissues and organs in a developing foetus know which side they are on? Results suggest that the expression of certain genes provides left/right-specific cues to tissues and organs [121]. This raises the question of whether stereoselectivity is also relevant for stem cell behaviour and differentiation. Yi *et al.* synthesized polylactide films of enantionerically pure L- or D monomer or a racemic mixture. Osteoblasts which were cultivated on these films showed better adhesion and higher proliferation rates on the L-films compared to the D-films [122]. Instead of polymerising chiral monomers, chiral features can also be introduced to the surface by formation of a self-assembled monolayer (SAM). Because of its thiol groups, cystein can form SAMs on gold coated surfaces. When SAMs of L- or D-cystein are exposed to a culture medium, L-surfaces were shown to adsorb higher quantities of serum protein. Rat MSCs on these substrates were cultured with both osteo- and adipogenic medium and responded differently to the enantiomers: Cells on D-surfaces tended to undergo osteogenesis, whereas cells on L-surfaces were more prone to adipogenic differentiation. When MSCs were confined to microscale cystein-microislands, the effect of chirality disappeared and the differentiation behaviour turned out to be influenced by microisland size. The reason for the different reaction to L- and D-cystein is believed to be the different extent to which the monolayers permit the adsorption of serum protein [123]. A similar study [124] came to a matching result: Monolayers of L- or D-tartaric acid were found to adsorb insulin differently, depending on the enantiomer. Insulin adsorbed to D-surfaces retained its bioactivity, but insulin on L-surfaces formed fibrils without activity. Not surprisingly, PC12 cells - a murine cell line of embryonic origin - exhibited contrasting proliferation and differentiation behaviour after culture on these surface types.

These studies suggest that molecular chirality does have an impact on cell differentiation, but this influence might be an indirect one and mediated by surface-bound molecules interacting with serum proteins rather than with the cells themselves. This raises the question whether the nanometric chirality of e.g. proteins with a helical secondary structure can also influence cell fate.

Surface topographies

The topography of a culturing surface or scaffold is of interest in that it defines the shapes which cells can assume, which in turn influences the cytoskeletal rearrangement and evokes biochemical responses. This term covers a wide range of surface properties, some of which are shown in Figure 2.10. The range of possible techniques to introduce topographic features is large, and the choice of methods depends on the material the surface of which is to be altered. For example, the popular implant material titanium can modified in terms of surface topography by plasma-spraying a molten metal onto it, resulting in a roughened layer of a thickness on the micrometer scale. Grit-blasting is a somewhat similar approach, except that instead of liquid metal droplets, solid particles are accelerated towards the surface. Their impact as hard enough to let them stick to the surface. Etching the titanium substrate with strong, oxidising or non-oxidising acid also produces a rough surface. The etching process can also be based on the application of a potential to the metal (anodisation) [125] [126]. A simple form of topography alteration is the creation of gratings on a flat surface. Chan *et al.* [127] heat-embossed a 2μm wide grating in polystyrene culture dishes to explore the effect of this geometry on human pluripotent stem cells. The cells were found to elongate along the grating and exhibit more neurogenic differentiation in the absence of induction medium. Further experiments [128] with murine neural progenitor cells on a grating showed that

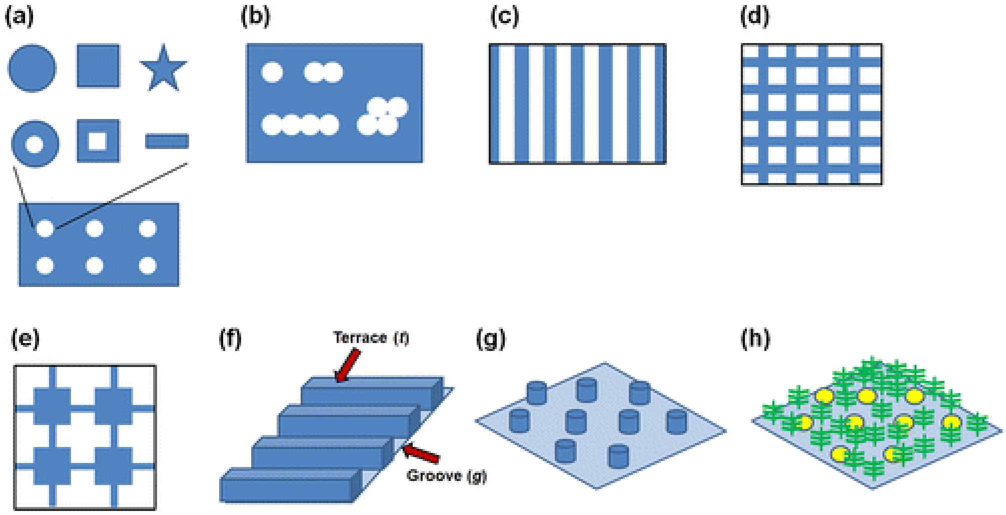

Figure 2.10: A brief visual summary of topographical features for cell differentiation studies: Nanoisland shape (a) and number (b), modified stripes (c) or grids (d), combination of grids and shapes (e), nanogrooves (f), nanopillars (g) and combination of nanoshapes and polymer brushes. [115].

elongation, alignment and neuronal differentiation increases with increasing depth of the grating features. Topographical features in combination with other, e.g. biochemical cues are hypothesised to show synergisms. A study explored the response of murine C2C12 myoblasts to polystyrene substrates featuring grooves with a width of 900nm and an adhesion-promoting RGD-peptide grafting. After myogenic induction, cells on grooves showed a more myogenic character than those on flat surfaces, but this phenomenon could not be observed for unfunctionalised samples [129]. (The grafting of RGD-peptide alone also had an effect, which was further enhanced by the presence of grooves.) A group from Aachen [130] prepared alternating grooves and ridges at the micro- and nano-scale by etching and multi beam laser interference. Cultivation of MSCs on features with varied sizes revealed that the highest level of osteogenesis was observed at 2μm width, whereas 15 μm features increased adipogenic differentiation. However, this difference was only observed in differentiation medium, which led the authors to the conclusion that nanotopography does not *per se* induce osteogenic differentiation, but supports it if other conditions are met. Comparable caveats were issued in a study that examined the combined effects of nanotopography and stiffness by culturing neuronal progenitor cells on nanopatterned PDMS-surfaces with controlled stiffness, made by interference lithography. It turned out that cell behaviour was much more influenced by mechanical properties than by topography [131]. Besides gratings and grooves, other topographies like pores and nanoarrays were also explored. Wang *et al.* [132] cultivated human osteoblasts on micro- and nanotextured topographies made of titania nanotube arrays with different tube sizes. Results showed that larger tubes induced a stronger expression of Runx2, collagen I, OPN and ALP-activity, indicating a more osteoblastic phenotype. Gene-silencing revealed that this effect is mediated by the ILK/β-catenin pathway. ILK (Integrin-linked kinase) is part of focal adhesions and binds to the cytoplasmic domain of specific beta-subunits of integrin. Due to its kinase function, it can cause an increase of β-catenin in the cytoplasm, similar to the Wnt/β-catenin-pathway. A recent study prepared titanium-niob-aluminium alloy implants with a thin nanoporous layer made by anodisation. This electrochemical method resulted in a pore size of 10-100nm. This surface type was shown to lead to an increased Runx2 expression and ALP activity of hMSCs.

Bioactive micro- and nanopatterning

Micro- and nano-lithography is a technique for the facile and spatially well-defined modification of surfaces. It includes several different appoaches, like photolithography, where a predefined part of a surface is irradiated (e.g. by UV light) through a mask, or imprint lithography, where a stamp is inked and put on a surface, similar to a conventional printing press [133]. Having taken into account how surface topography can affect cell and especially stem cell behaviour, one should also consider the effect of bioactive patterning, i.e. topographies which don't manifest as 3D-features on the surface, but rather as a chemical modification of a substrate. A common approach in this field is the lithographic preparation of defined shapes of RGD-peptides on surfaces. The RGD-sequence originates from fibronectin and facilitates cell adhesion. Peng *et al.* [134] created adhesive microislands on PEG-substrates by using photolithography to obtain gold islands. Subsequently, the thiol-terminated RGD-peptide could bind to the gold surfaces. Rat MSCs which were seeded on microislands of varied shape, yet constant area, exhibited differences in differentiation behaviour: Cells on rectangular shapes with an aspect ratio (i.e. length to width ratio) of 1 tended to undergo adipogenic differentiation, whereas an aspect ratio of 2 was more likely to induce osteogenesis. Moreover, cells cultivated on star-shaped adhesive islands were more prone to osteogenic differentiation than cells on circular shapes. Instead of microislands, RGD-peptides can also form adhesive spots with a constant spacing between them. In a number of studies [123] [135] [136], such a pattern was obtained by deposition of gold nanoparticles on a substrate, followed by thiol-mediated binding of the peptide to these nanoparticles. In a range of 37-124nm spacing for these patternings, it was shown that both osteogenic and adipogenic lineage commitment of hMSCs was increased on larger nanospacings (in the presence of osteo- and adipogenic medium). Further experiments demonstrated that this effect did not depend on the stiffness of the substrate. This patterning strategy could be useful for the design of implants which need to be osteoinductive. For example, RGD arrays with a defined nanospacing at the surface of a titanium-niobium-alloy (the stiffness of which resembles bone) were found to modulate adhesion of hMSCs [137]. Not only RGD-peptides, but also various proteins from the extracellular matrix can be attached or deposited onto surfaces in a patterned manner. A common method is microcontact printing, where a stamp (often made of a polymer like PDMS) is covered with a protein solution and brought in contact with the future culture substrate. In an effort to facilitate the study of limited numbers of neurons *in vitro*, Ricoullt *et al.* [138] printed microcircles on glass surfaces with different ECM proteins, including fibronectin and laminin. The area outside the printed features was covered with PEG, which does not encourage cell adhesion, in order to accumulate seeded cells in the desired zones. Just like RGD nanospacing patterns, ECM protein patterns may also influence cell differentiation. ESCs cultured on patterned hydrogels made by direct microcontact printing of Matrigel, gelatin and other ECM proteins were demonstrated to exhibit a cardiac phenotype more quickly than cells on nonpatterned surfaces [139]. In another study [39], human cardiomyocytes were seeded onto lithography-printed surfaces featuring different rectangular shapes of different sizes. Fibronectin and Matrigel (a commercially available basement membrane ECM protein mixture) were adsorbed to gold-coated substrates. Results of cell culture experiments with cardiomyocytes showed little impact of nanofeature aspect ratio on cell behaviour. However, it was shown that features with a width of 30-80 μm and a constant length of 1cm induced a high level of alignment with the features and an increased formation of sarcomeres. Finally, bioactive agents can also be distributed on a surface using inkjet printing, similar to a conventional printer. Phillippi *et al.* [140] used this approach to create a periodic pattern of 750 μm squares of BMP2. This group demonstrated that under myogenic conditions, cells in contact with the microfeatures exhibited increased osterix expression, whereas cells outside the squares would undergo myogenic differentiation.

Nanoobject morphologies

As we saw in the second to last section, the topographies of 2D culturing environments can be relevant for cell behaviour and stem cell differentiation. This concept can be considered in a broader way by extending it from the forms of flat surfaces to the shape of objects in general, including 3D structures. This section sometimes overlaps with the section on topography, because nanoobjects can occur both as a 3D-environment and as a surface coverage material.

A common type of nanomaterials in biological applications are polymer-based nanofibres, the morphology of which comes closest to the structure of the ECM. Hydrogels can be formed from hydrophilic polymers, e.g. polylactic-*co*-glycolic acid (PLGA), which was used by Ebrahimi-Barough *et al.* [141] to steer the neuronal differentiation of endometrial stem cells. Nanofibres made from PLGA by electrospinning and measured 400-500nm in diameter on average. They formed a substrate which led to a higher degree of differentiation into motor neuron-like cells compared to flat control substrates, as evidenced by the expression of relevant genes. An alternative to electrospinning is the use of an airbrush technique, which functions similar to a spraycan: A polymer solution is pressed through a nozzle using a compressed gas to form fibres. The fibres obtained this way are more loosely packed and exhibit higher porosity, but lower stiffness than electrospun fibres. Airbrush fibres of different polymers were shown to support osteogenic differentiation of hMSCs [142]. The complexity of nanofibrous materials can be augmented by combining it with other fabrication techniques. Cheng *et al.* [143] created a hierarchical scaffold structure featuring both nanofibres and micropores by fabricating the polymer scaffold by phase separation in the presence of NaCl template particles. Removal of the templates led to the formation of a porous matrix which combines the advantages of fibres and pores regarding proliferation, adhesion and differentiation: Human neural stem cells showed more differentiation into neurons when they were cultured on this hierarchical structure. The effect of the morphology of nanofibres can be combined with other cues to control cell behaviour, e.g. stiffness. A study [144] examined the effect of polyethylene glycol dimethacrylate nanofibre 3D hydrogels made by electrospinning and subsequent photopolymerisation on MSCs. Nanofibre mechanical properties were varied by modifying the degree of polymer crosslinking. Cells cultured on fibres with a stiffness of 8kPa or above showed larger adhesion surface areas and differences in vascular marker expression after 24h already, indicating a tendency towards vascular commitment. The relevance of nanofibres for osteogenesis was recently pointed out by Sonomoto *et al.* [145], who cultured hMSCs on a PLGA-nanofibre scaffold. The cells expressed Runx2 and the chondrogenic marker Sox9 after seven days without stimulation. Change of shape and occurrence of dentin matrix protein-1 (DMP-1) and matrix extracellular phosphoglycoprotein (MEPE) showed that cells had undergone osteogenic differentiation. In some cases, the impact of fibrous materials is not directly related to their morphology but rather to nanoobject surface modification. For example, [146], electrospun polycaprolactone nanofibres measuring 200-300nm in diameter were modified with graphene oxide, which had been shown to promote differentiation of hMSCs and other cell lines. The degree of neural stem cell differentiation into oligodendrocytes after culture on these nanofibres increased with the amount of graphene oxide coating on the scaffold.

Some fibrous matrices for cell culture applications are commercially available. Matrigel is a hydrogel which solidifies at body temperature by polymerisation. It has been shown that stromal cells encapsulated in this matrix could achieve higher degrees of neural differentiation using neural differentiation medium, compared to conventional 2D substrates. This also led to better neuronal regeneration *in vivo* in rats [24]. So-called free forming scaffolds consist of crossed 288μm struts and were shown to promote cell proliferation because of their high surface area. Kumar *et al.* [147] found that after increasing its scaffold roughness by solvent etching, this matrix type can guide

MSCs towards osteogenesis.

Biomacromolecules are an alternative source of nanomaterials for cell culture. As a later section will explore in more detail, certain peptides can self-assemble into nanofibres. Sever *et al.* [148] incorporated fibronectin into peptide nanofibres (10-20nm) and cultivated rat MSCs on them. In the absence of osteogenic induction, the cells exhibited an increased ALP activity and expression of other osteoblastic markers. Moreover, increased mineralisation was observed. Similar experiments were carried out by Fukunage *et al.* [149]. Another example of fibrillar proteins of potential use as a stem cell environment is silk fibroin, which can be freezedried in order to manufacture a porous 3D scaffold [150]. It was shown to induce preferential differentiation into muscle and endothelial cells in rat MSCs. As shown in section 2.1.1, collagen fibrils exhibit a periodic band structure, and understanding the impact of this periodicity on stem cells is a key objective of this work. Therefore, collagen is of particular interest in the context of this study. Sefcik *et al.* [151] prepared a 3D collagen fibre matrix by electrospinning and compared its influence on human adipose cells to a 2D collagen-coated substrate. After three weeks of culture, a range of osteogenic genes including collagen I, osteopontin and ALP were found to be upregulated in the nanofibre scaffold samples compared to the 2D environments.

While fibrillar matrices appear to be the most common type of nanomorphology in this context, other morphologies were also investigated: Lipski *et al.* [152] spincoated surfaces with silica nanoparticles of different sizes (50, 100 and 300nm diameter) to tune their roughness. Murine preosteoblasts cultured on materials with higher roughness (i.e. higher particle diameter) showed strong actin fibre formation, which might indicate osteogenic differentiation. A possible explanation for this is that rough surfaces arrest cellular locomotion, thereby favouring differentiation. Another study [129] explored the effect of nanoparticles on cardiomyocyte development. 5-Azacytidine is known to induce cardiomyogenic differentiation. The effect of this induction could be enhanced by culturing the cells on collagen nanoparticles or fibrils.

Order and disorder

The last aspect of ECM to be discussed in this section is the degree of order in a cellular microenvironment. This parameter can be expressed in several ways, such as a regular nanospacing between adhesion spots, or the alignment of high aspect ratio nanomaterials.

A number of studies exploring the significance of nanofibre alignment on cell behaviour found some effects of nanomaterial orientation, but in most cases cell differentiation was not affected. Yang *et al.* [153] used electrospinning to fabricate a scaffold of aligned or unaligned poly-*L*-lactic acid (PLLA) micro- and nanofibres and varied the fibre diameter by altering the concentration of the polymer solution. Cell culture experiments showed that neural stem cells grew neurites parallel to the aligned nanofibres, but differentiation was shown to be influenced by fibre size, not alignment. In a similar study [154], PLLA fibres were similarly aligned by electrospinning on a rotating receiver, followed by hot stretching, a process which caused the fibre diameter to decrease from 450nm to 275 nm compared to unaligned fibres. Osteoblast-like MG63 cells on the parallel scaffold exhibited an elongated, shuttle-like shape and a decreased ALP-activity and expression of collagen I and osteocalcin. Other groups used aligned or unaligned, electrospun fibres of PLGA, polycaprolactone and polycarbonate-urethane as substrates for porcine tooth bud cells and adipose-derived stem cells, respectively [155] [156]. Both of them found no substantial change in differentiation behaviour which could be attributed to fibre alignment.

There are as well examples of non-fibrillar objects which can be used for ordered microenvironments. Namgung *et al.* [157] prepared substrates of aligned and unaligned carbon nanotubes by spincoating. hMSCs were shown to align along the ordered tubes and to exhibit more osteogenic commitment on aligned nanotubes. Another study using the same material [158] cultured myoblasts on hierarchical nano- and microscale carbon nanotube scaffolds with two different structures: microporous foams or bundles of aligned nanofibres. It was shown that aligned scaffolds promoted the formation of multinucleated myotubes in cells. Instead of exploiting spinning techniques, ordered nanoobject arrangements can also be achieved by using microfluidics. Zan *et al.* [159] aligned rod-shaped NPs, including gold nanorods and viruses, by a flow assembly method which relies on the shear force of a fluid to control the degree of alignment. When C2C12 myoblasts were cultured on surfaces coated with these one-dimensional nanoobjects, their behaviour was shown to be guided by nanorod alignment.

As mentioned earlier, understanding the role of collagen in the ECM is an important motivation in this work. Kishore *et al.* [160] mimicked the ECM geometry by electrochemically aligning collagen using isoelectric focussing. HMSCs which were cultured on either aligned nanofibres or on disordered collagen threads exhibited stronger proliferation ability on unaligned threads, but expressed more tendon specific markers on aligned collagen. Interestingly, however, the marker protein Osteocalcin was suppressed on aligned collagen.

2.2 Nanomaterials

2.2.1 Amphiphiles and self-assembly

Gemini surfactants

The term ”surfactant” is short for ”**surf**ace-**act**ive **a**ge**nt**” and denotes compounds that adsorb onto surfaces or interfaces, altering their surface or interface free energies. In other words, surfactants lower the amount of work required to enlarge the area of an interface. They feature a lyophilic ”head” and a lyophobic ”tail”. In the case of the water/air interface, surfactants form a single layer at the interface; the hydrophobic domain facing towards the water. The hydrophobic head group can be cationic, anionic, zwitterionic or nonionic [161].

In gemini (from Lat. *gemini*: twins) surfactants, at least two surfactant units are covalently bound head to head [162]. A common notation to classify the structures of gemini consisting of two surfactants is the format x-y-z, where x and z represent the length of the two apolar tails, and y describes the length of the spacer which connects the polar head (counted in methylene units) [163]. As regular surfactants, gemini amphiphiles can undergo temperature induced phase transitions, e.g. from solution to micelles [164]. The phase transition behaviour depends on various parameters such as chain lengths or the nature of the head groups [165]. An important parameter to characterise surfactant compounds is the critical micelle concentration (CMC). This threshold is more or less sharp, depending on the number of molecules per micelle, and represents the concentration above which a solution of a surfactant starts to form micelles. The critical micelle concentrations (CMC) of gemini surfactants are much lower than the CMCs of their monomeric counterparts, even if the higher number of head groups is accounted for. The CMC generally changes with varying length of both tails and spacer (i.e. x, y and z in the aforementioned notation) because large aliphatic chains decrease solubility in a polar medium and hence promote aggregation [163]. Accordingly, gemini surfactants have a surface activity which is about three orders of magnitude higher than the activity of their monomeric counterparts [166], which corresponds to the aforementioned lower CMC compared to their monomeric counterparts. The shape of amphiphiles is of high importance for the formation of supramolecular structures, as the next section will elaborate. Depending on the size of head and tail group, the molecule's overall geometry is either conical or cylindrical, which results in preferential formation of micelles or bilayers from these amphiphiles. This means that the nature of the polar moieties and especially the length of tail and spacer chains of gemini surfactants can be tuned to influence the shape of supramolecular assemblies.

Amphiphile self-assembly

There are numerous examples of amphiphilic molecules (both gemini and standard) assembling into supramolecular structures with often interesting morphologies, like micelles and nanofibres. In most cases, the principal forces which hold the supramolecular structure together are the hydrophobic interaction between the apolar chains and the (attractive and repulsive) interactions between the polar head groups [167]. Due to their high hydrophobicity, lipids can be used as apolar groups of amphiphiles. Voronin *et al.* [168] coupled isosteviol, a molecule that has been found to exhibit an antihypertension, antihyperglycemic, insulinotropic, glucanostatic, cardio- and neuroprotective effect, to a cationic group to form micelles the properties of which depended on the counterion that was used for the cationic moiety. It is also possible that the polar and apolar groups of the amphiphile are not one molecule but rather a host-guest complex of two molecules held together by interaction between an anion and the π-system of an aromatic ring [169]. This two-part amphiphile is nevertheless capable of assembling into micelles.

Amphiphile-based self-assembled structures are 0-dimensional (micelles), 1-dimensional (fibres) or 2-dimensional (vesicles). Another type of amphiphile are peptides with an added hydrophobic domain. In terms of applicability, an advantage of this approach is that the peptides may contain a bioactive sequence called epitope, which will be located on the surface of any nanomaterials formed be these amphiphile in aqueous medium, which is a facile way of preparing bioactive nanomaterials. As the secondary structure of the peptide depends on its amino acid sequence, the choice of the sequence also influences the size and shape of the polar head and therefore the self-assembly behaviour of a peptide-based amphiphile. However, molecular simulations show that the most important factor in determining the shape of supramolecular assemblies are the relative strengths of the driving forces mentioned earlier, hydrophobic interaction and hydrogen bonding [167]. If the intermolecular hydrogen bonds between the peptide domains are weak compared to the hydrophobic interaction between the tails, the amphiphile is more prone to forming spherical micelles, given a sufficient concentration. If the opposite is the case, one-dimensional cylindrical fibres will form. In these nanofibres, the hydrophobic tail forms the core of the high aspect ratio structure, whereas the peptide moieties are located at the outside, often assuming a β-sheet organisation [170]. The molecular design of the amphiphile is not the only parameter to define assembly behaviour. For example, as peptides can be protonated, the pH value can affect their folding and thus self-assembly behaviour. Ghosh *et al.* [171] synthesised peptide amphiphiles which assemble into nanofibres with about 12nm diameter at a pH value lower than 6.6. At higher pH, the fibres disassemble reversibly (cf. Figure 2.11).

The possibility to modify nanofibre formation by tweaking molecular architecture and experimental conditions makes amphiphile self-assembly a suitable tool for the creation of biomimetic systems. Luo *et al.* [172] devised an approach to mimic collagen using a single-

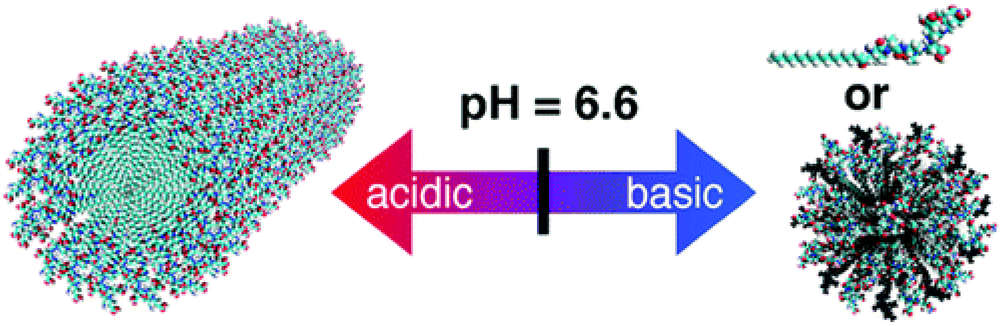

Figure 2.11: Illustration showing the pH-dependent morphology change of amphiphile nanoassemblies described in [171].

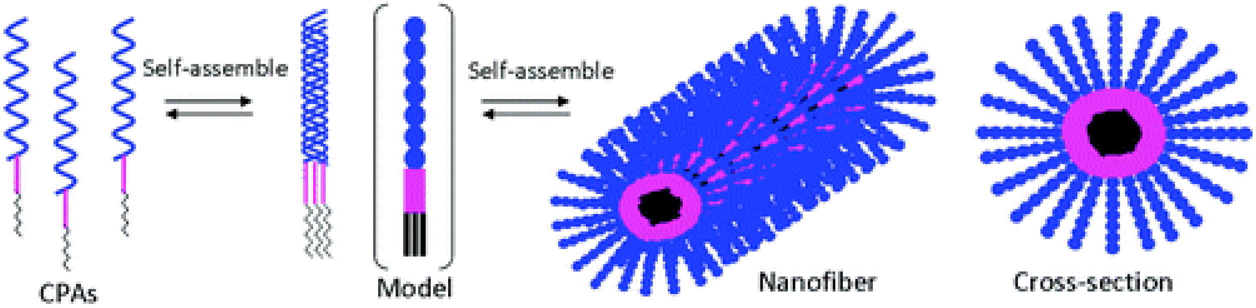

Figure 2.12: Scheme of the two-step self-assembly process of amphiphile-based collagen-mimicking nanostructures [172].

tail amphiphile the polar domain of which is a collagen-mimicking peptide. These molecules self-assemble into a triple helix, which in turn self-assembles into nanofibres with a diameter of 16nm. These nanomaterials mimic collagen in two different way: Chemically, because of the peptide sequence; and structurally, because the two-step self-assembly process, which is illustrated in Figure 2.12, strongly resembles the formation of collagen fibrils from the single biopolymer via a triple helix intermediate.

2.2.2 Chiral nanomaterials

Chirality (from Greek $\chi\epsilon\iota\rho$, hand) is a common phenomenon in nature: Both at the macroscale, where gastropod shells have a mostly dextral orientation, and at a molecular and supramolecular level, where the handedness of nucleotides and amino acids leads to chiral DNA and protein α-helices. In the following section, we will go through different strategies to obtain nanomaterials with chiral morphology.

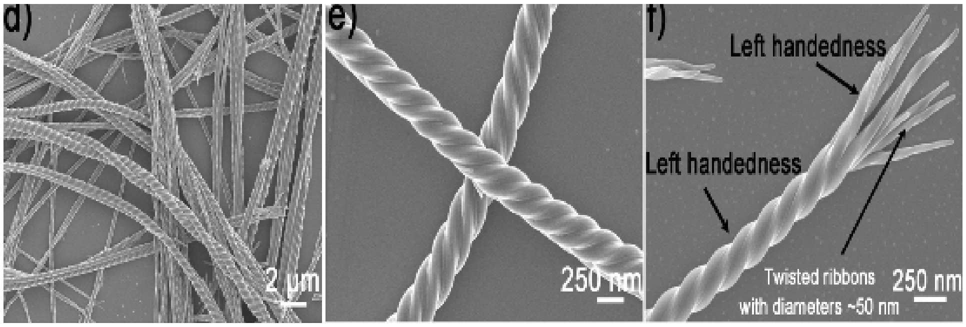

Figure 2.13: SEM images of Helices formed by modified diphenylalanine, different magnifications. The rightmost image shows how the helical morphology of the nanofibre is consistent with the chiral orientation of the smaller fibres which it is composed of [175].

Amphiphiles and Biomolecules

When examining organic nanohelices, it is logical to think first about the helical systems that are present in nature, especially DNA and protein helices. Researchers can either fall back on sequences of natural source, or engineer DNA or protein sequences in order to obtain helical structures with the desired properties as building blocks in supramolecular architectures [173]. A number of other peptide-based structures are summarised in [174], including peptide assemblies with helical features.

Even very short peptides can form complex, well defined helical structures by self-assembly, as shown by a recent study [175]: Ferrocene-modified diphenylalanine self-assembles into β-sheet structure which forms helical nanostructures, depending on its counterions (cf. fig 2.13). The reason for this is that counter(cat)ions control secondary structure of the dipeptide, and therefore the way they self-assemble. The resulting nanostructures are well-defined helical or twisted ribbons with diameters of tens to hundreds of nanometers. Morphological parameters like diameter, pitch and chiral orientation can be controlled by modification of counterions, temperature and solvent. Natural polysaccharides occurs in a helical form; for example, α-D-Glucose forms the helical polymer amylose. This natural source of chirality inspired Numata *et al.* [176] to self-assemble helical structures from synthetic polymers or carbon nanotubes and polysacharides which wrap around them in a helical fashion (Figure 2.14). The resulting 1D materials could be crosslinked at well-defined spots to combine them to 2D-materials.

Polar biomolecules can be functionalised with apolar, aliphatic moieties to obtain amphiphiles, which opens routes to prepare self-assembled nanomaterials. For example, Kira *et al.* [177] aminoalkylated *L*-glutamic acid to synthesise amphiphiles which can form nanofibres and nanotubes by self-assembly. This type of one-headed, two-tailed surfactant forms fibres of up to 25nm in diameter in both polar and apolar media. Although the fibres look symmetrical in EM images (cf. Fig. 2.15), Circular Dichroism (CD) experiments reveal a chiral ordering of amphiphiles within them, the orientation of which depends on the solvent and the molecular structure.

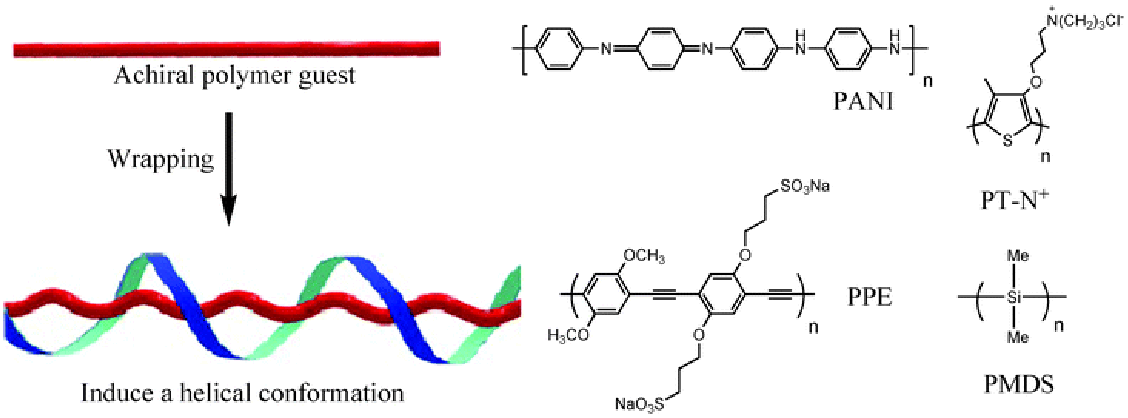

Figure 2.14: Illustration of host/guest-helices and a selection of possible host-polymers [176].

The same approach was applied to other biomolecules [178]: Disaccharides were alkylated using click chemistry; the resulting amphiphiles can self-assemble to fibrillar hydrogels consisting of fibrillar ribbons. (The aromatic triazole ring which is formed in the click reaction supports this aggregation process due to its π-π-stacking.) Due to the arrangement of amphiphiles, these ribbons are twisted, and the chiral orientation depends on the choice of head group (cf. Fig. 2.16). As a further example, certain gluconamides, i.e. sugars modified with hydrophobic chains, form bilayers which in turn assemble into helices with very regular periodicity and morphology [179].

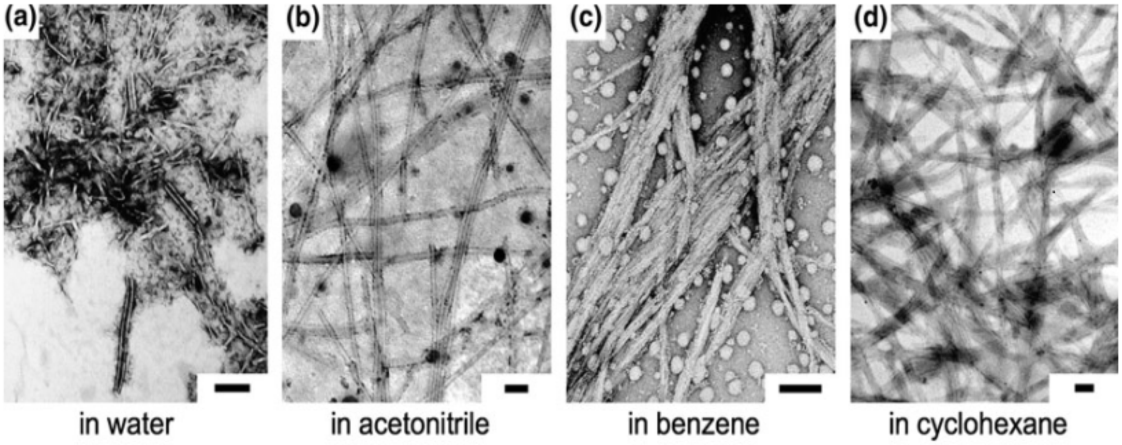

Figure 2.15: Electron microscopy images of the nanotubes described in [177] in different solvents: Water, acetonitrile, benzene and cyclohexane (from left to right).

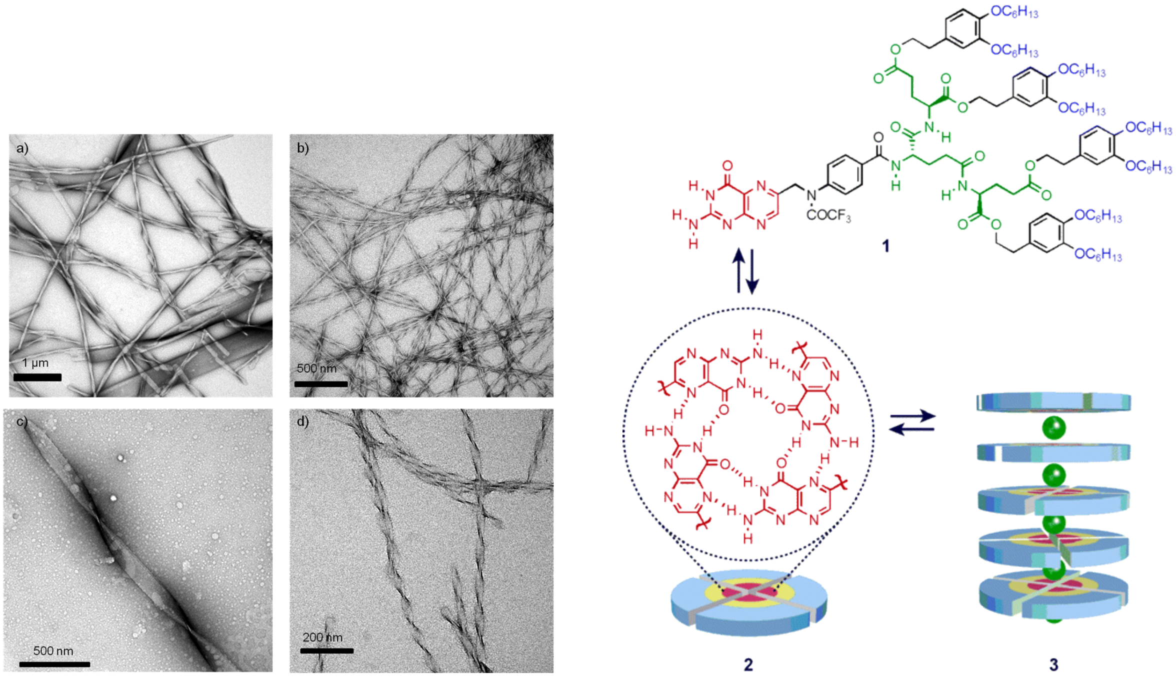

Figure 2.16: Left: TEM images of twisted ribbons as described in [178], made with two different disaccharide-based amphiphiles (a/c and b/d). Right: Structural formula of the modified folate used in [180]. The interactions between the folate moieties (in red)) which lead to the formation of tetramers (bottom left) and stacks (bottom right) are shown.

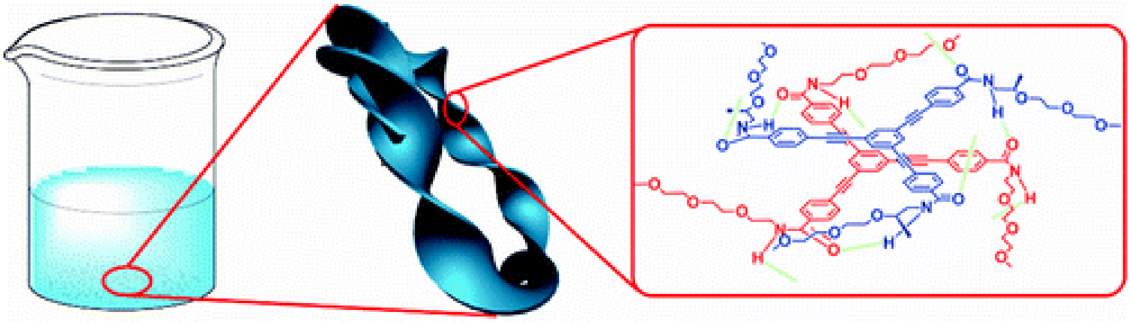

Figure 2.17: Visualisation of helix formation principle of C_3-symmetric Trisamides [181].

Stack approaches

There have been numerous approaches to manufacturing nanometre scaled helical materials, often relying on the principle of self-assembly. Some of them are based on molecules with planar geometry, which can stack to form chiral high aspect ratio nanomaterials. For example, Sánchez *et al.* [181] formed organic helices by using π-π-stacking to self-assemble trisamides with C_3-symmetry. The conformation of the molecules is maintained by hydrogen bonding, so that the molecular symmetry translates to a preferential orientation of the supramolecular structure (cf. Figure 2.17).

The repeating unit of "stack"-type helical nanomaterials can consist of more than one molecule. Derivatives of the nucleoside guanosine form planar tetramers through Hoogsteen bonding, i.e. the type of hydrogen bonding which also causes the base pairing in nucleic acids. These tetramers stack to form rod-shaped aggregates with chiral character. CD measurements show that the handedness of these supramolecular structures depends on the substituents of the guanosine moieties [182] [183]. A similar study had been carried out before with guanylic acid [184].

Aromatic folate with sterically demanding substituents can give rise to similar assemblies. The folate units form cyclic oligomers held together by hydrogen bonding, and stacked due to $\pi-\pi$-interactions between the aromatic systems (cf. Fig. 2.16). Due to the shape of the oligomers (with a hole in the centre), the stacking of these planar units results in the formation of a channel-like construct, and they exhibit properties similar to ion channels [180].

As $\pi-\pi$-stacking is often the primary factor in the formation of "stacked" high aspect ratio,

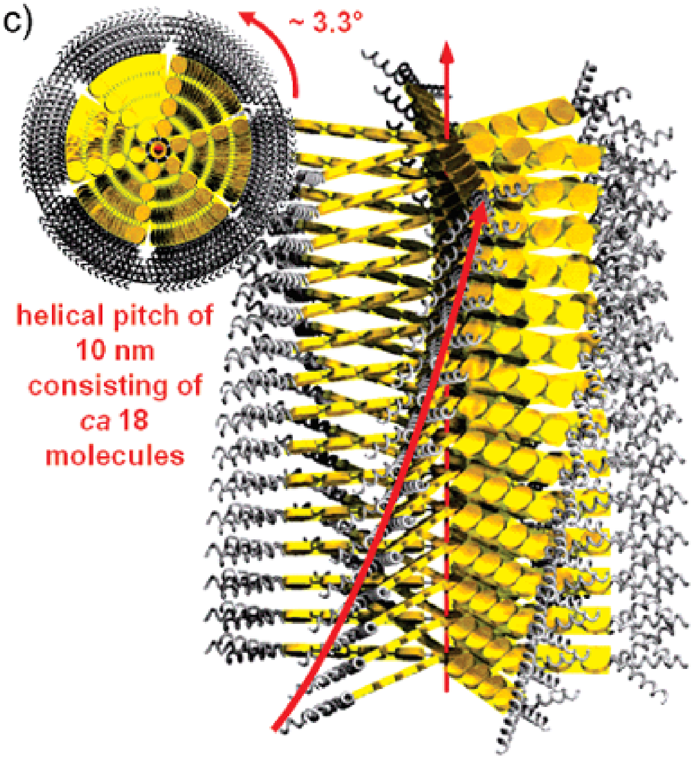

Figure 2.18: Schematic representation of how the star-shaped aromatic molecules from [185] stack in a way which leads to a helical twist with a pitch length of 10nm. Steric factors make a fully ecliptic conformation unfavourable.

the size of the π-electron system is critical to the stability of the resulting supramolecular structure. The importance of this factor was demonstrated by Tomović *et al.* [185], who synthesised a large aromatic system, *para*-substituted hexaarylbenzene. This compound with star-like geometry self-assembles in stacks to form nanowires in apolar solvents. Each molecule is rotated by a certain angle with respect to the adjacent one, which leads to a chiral structure with a pitch of 10nm as visualised in Figure 2.18. The columnar nanowires are remarkably stable at high temperatures (up to 90°C).

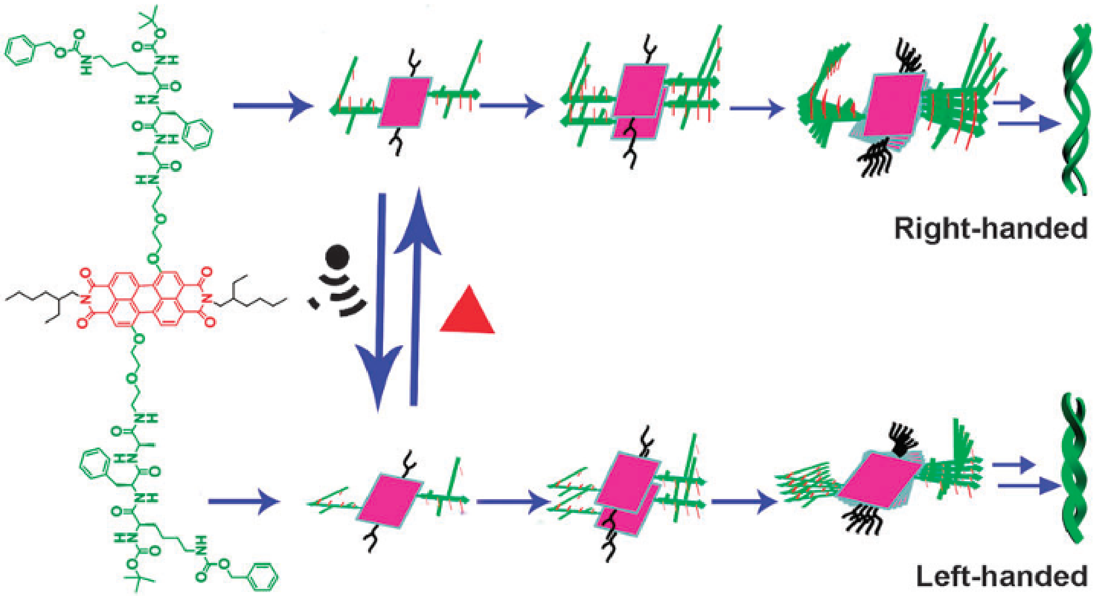

Figure 2.19: Schematic representation of the compound described in [186] visualising its principle of assembly by interactions between π-electron system (purple) and peptide arms (green).

A compound synthesised by Ke *et al.* [186] consists of a planar, aromatic moiety and two peptide arms at opposite end. π-π-interactions between the aromatic systems and hydrogen bonding between the peptide groups cause these molecules to stack, but steric factors prevent them from assuming an eclipsed conformation (Figure 2.19), which results in the formation of nanohelices. These examples show how asymetric substituents of the building blocks of nanomaterials create a preferential orientation of adjacent molecules, ultimately resulting in the creation of a chiral pattern at a supramolecular scale.

Inorganic materials

Chiral nanomaterials with helical morphology have been synthesised from a variety of starting materials, including noble metals, semiconductors, silicon dioxide, carbon nanotubes, and organic molecules and supramolecular assemblies of biologic or synthetic origin [187]. Chemical vapour deposition is a very common method to generate nanohelices and other nanostructures from their educts. In this procedure, a reaction takes place in the gas phase and the solid products are deposited on a substrate. Nath *et al.* [188] obtained magnesium boride (MgB_2) by a combination of physical and chemical vapour deposition from the gas phase reaction of magnesium and diborane. The resulting solid had a helical shape, with a helix diameter of 100-600nm (depicted in Figure 2.20). It is uncertain whether the coiling mechanism is driven by the same polar surface principle as the coiling of the aforementioned zinc oxide nanohelices. Possible metals as starting materials are platinum [189] or gold. Arrays of gold nanohelices can be created by cutting helical cavities into a polymer matrix using direct laser writing. Subsequent filling of these helix negatives with gold by electrochemical deposition results in an array of short, yet ordered gold helices [187]. This is one of the few methods for nanohelix fabrication which does not rely on self-assembly, but rather creates the helical morphology by manual intervention. Similarly, Gibbs *et al.* [190] prepared very short helices (Figure 2.21) by exploiting the shadowing effect: When a solid is cast (e.g. by chemical vapour deposition) on a surface with topographical features at an oblique angle, the solid cannot be deposited on the spots on the surface which are shielded by the features. In the described study, gold nanoparticles were deposited on a flat surface and a solid was deposited at an oblique, dynamically adjusted angle. As the substrate was rotated during this process, short helices of about two period lengths were formed. This technique can be applied to different starting materials.

Other

When we talk about chiral molecules, we usually think of molecules with stereogenic centres. However, helical compounds like helicene can also be sources of handedness. Nuckolls *et al.*

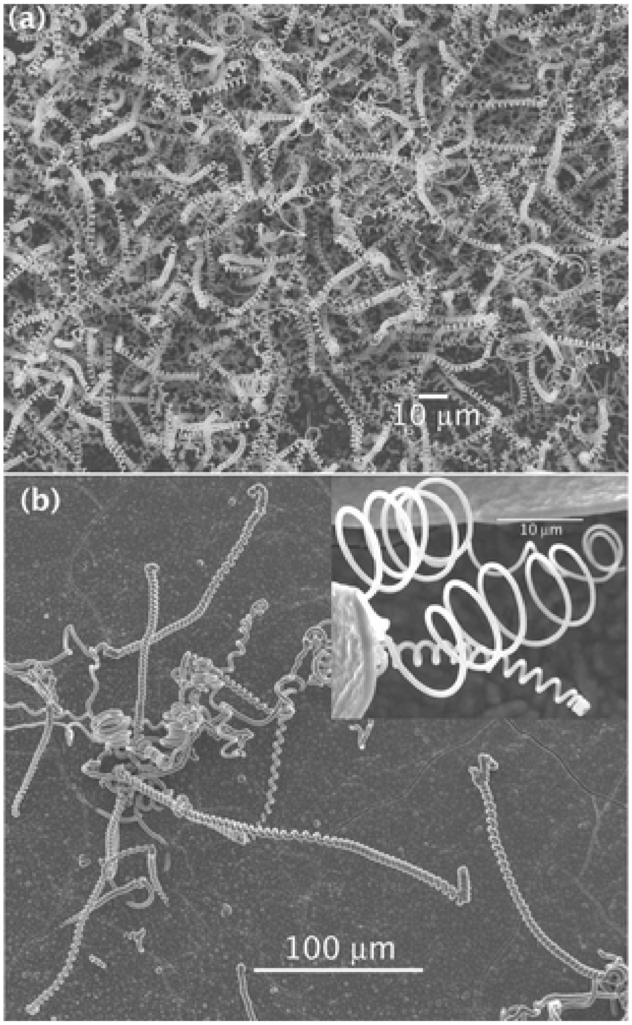

Figure 2.20: TEM images of magnesium boride helices described in [188].

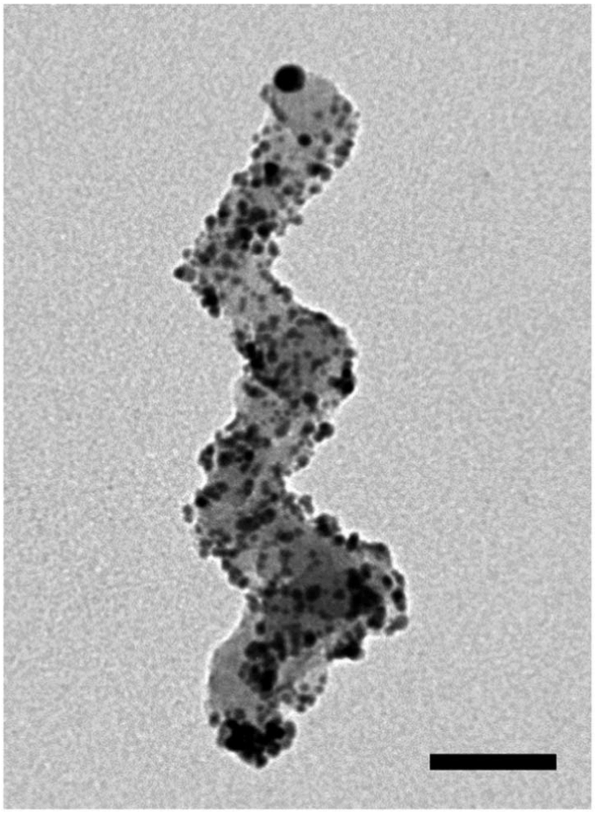

Figure 2.21: TEM image of short silica nanohelix made by shadowing technique and decorated with gold NPs; Scaling bar 50nms [190].

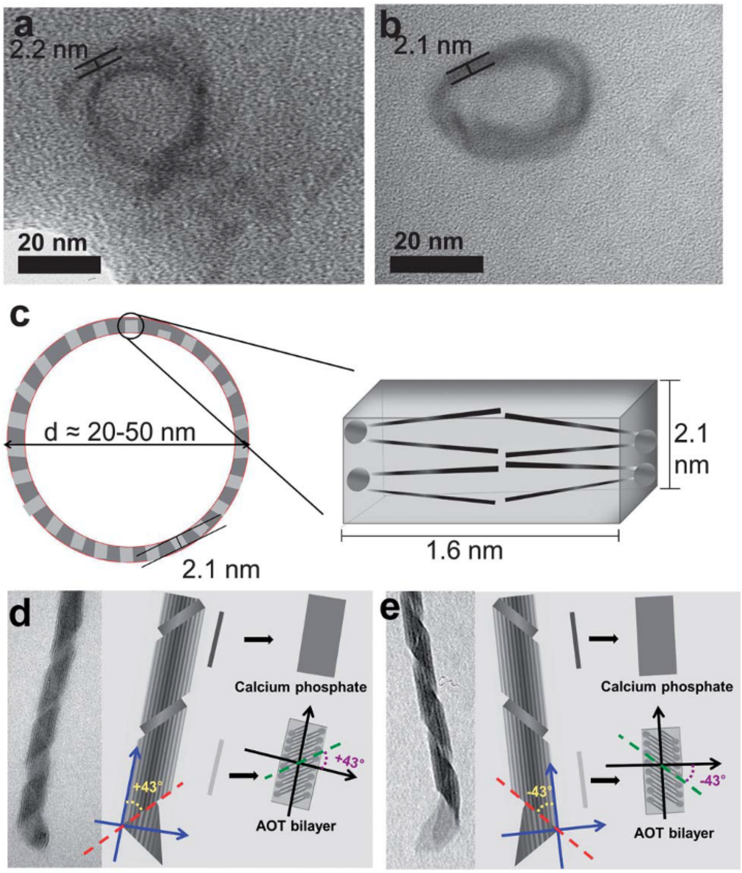

Figure 2.22: Nanohelices obtained from racemic solutions [191]: SEM images of their cross-section (a and b), schematic representation of the structure of amphiphiles in the bilayer (c), and TEM images showing their helical pitch (d and e).

showed that derivatives of helicene can assemble to aggregates, and that CD experiments indicate that these aggregates are chiral in nature, given the helicene-derivative is non-racemic [192] [193]. One study even obtained monochiral nanomaterials without any chiral compounds as starting materials: Zhai *et al.* [191] obtained homochiral helices from a racemic solution of the asymetric double-chain amphiphile (bis-(2-ethylhexyl)) sodium sulfosuccinate in a concentrated calcium nitrate solution with BSA (Figure 2.22). Characterisation experiments show that the resulting helices consist partly of organic matter, but are mostly composed of calcium salts which is believed to have formed by mineralisation of organic helices. The reason for the monochirality of these helices is the slow formation process: All helices in one batch of a solution stem from one mother helix the chiral orientation of which is passed on to all others. This way, a batch of monochiral helices can be formed even from racemic molecules.

Annealing carbon nanotubes is another approach to generate supramolecular chirality without any chiral input, but the resulting nanomaterials are racemic in this case. Carbon nanotubes, which are normally achiral, can be bound together by catalytic reaction with hydrogen. The resulting sheafs exhibit a helical morphology and show a large variety of different diameters, ranging from 10 to

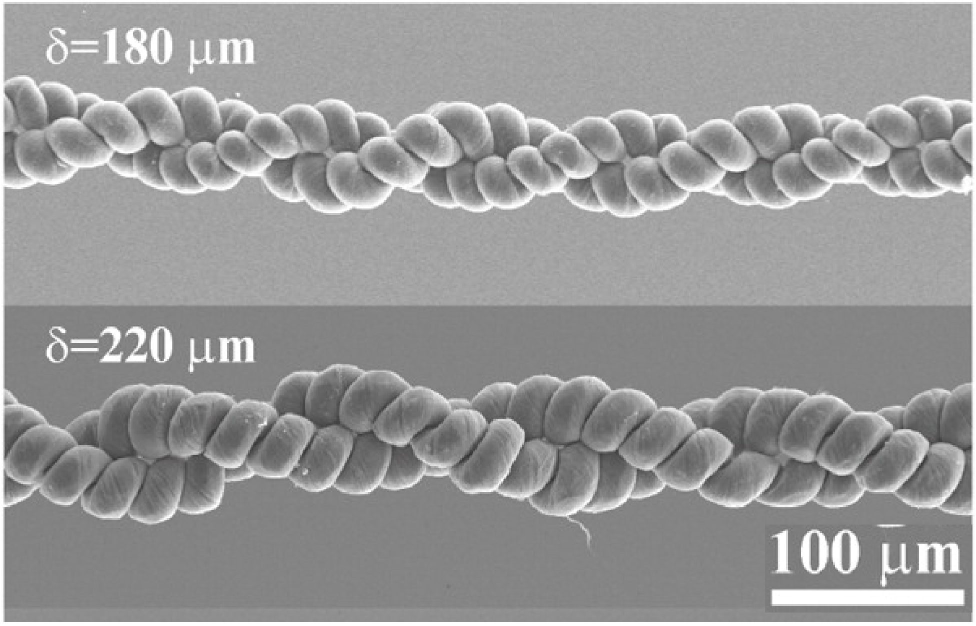

Figure 2.23: SEM images of double-helical carbon nanotube ”ropes” with two different period lengths [194].

250 nm [195]. Carbon nanotube helices [194] can be assembled into double-helices by depositing a nanotube film using chemical vapour deposition and spinning the resulting helices manually like macroscopic rope (Figure 2.23). These hierarchically organised structures are technically not nanoscale objects, because their diameters are larger than one micrometer, but the helical features of the individual strands are nanometric in size.

Artificial double-helices can be made not only by pyrolysis of small organic molecules to helical carbon nanotubes, but also by self-assembly and subsequent silanisation of organic nanohelices, e.g. proteins [196]. Similar to ropes, they are exhibit a high tensile strength.

2.3 Silica nanohelices

Considering the variety of shapes which high-aspect ratio nanomaterials can come in, we want to exploit the favourable properties of self-assembled nanohelices for the preparation of biomimetic materials. The possibility to vary their morphology provides an amply stocked toolbox to obtain a nanostructure which resembles the morphological features which stem cells encounter in their natural matrix. Silica is a suitable material for biological applications because it can exhibit biocompatibiliy and nontoxicity. (In the case of silica nanoparticles, biocompatibility depends on particle size and other factors [**?**].)

2.3.1 Synthesis

The Oda group found a class of self-assembling nanomaterials with unique properties in 1999 [197]: Dicationic gemini surfactants with certain chiral counterions like tartrate form supramolecular structures in water. When an enantiomerically pure counterion is used, they assemble into bilayers which change their shape over time: They form twisted ribbons at first, later helical ribbons and finally tubules. The enantiomeric excess of the tartrate counterions influences the morphological properties of this system: Higher enantiomeric excess leads to a smaller periodicity (i.e. period length), which shows the connection between the molecular chirality of the tartrate and the supramolecular twist of the nanomaterials. Hydrogen bonding of tartrate anions between the bilayers is thought of as an important factor for the expression of supramolecular chirality [197].

The development of nanoscale morphology depends on the conformation of amphiphiles in the bilayer, which in turn is controlled by stereoselective recognition. Indeed, an ensemble of techniques such as circular dichroism (CD), Vibrational circular dichroism (VCD) and NMR indicate that the macroscopic chirality arises from strong tartrate-surfactant-interaction [198]. Hydrogen bonding between the tartrate groups and interdigitation of the hydrophobic chains have been shown [199] to be essential forces in the formation of the assembly of the surfactants into homochiral monolayers, heterochiral bilayers and heterochiral adjacent bilayers (Figure 2.24).

Gemini surfactants can form chiral ribbons or helices with other counterions such as oligoalanins

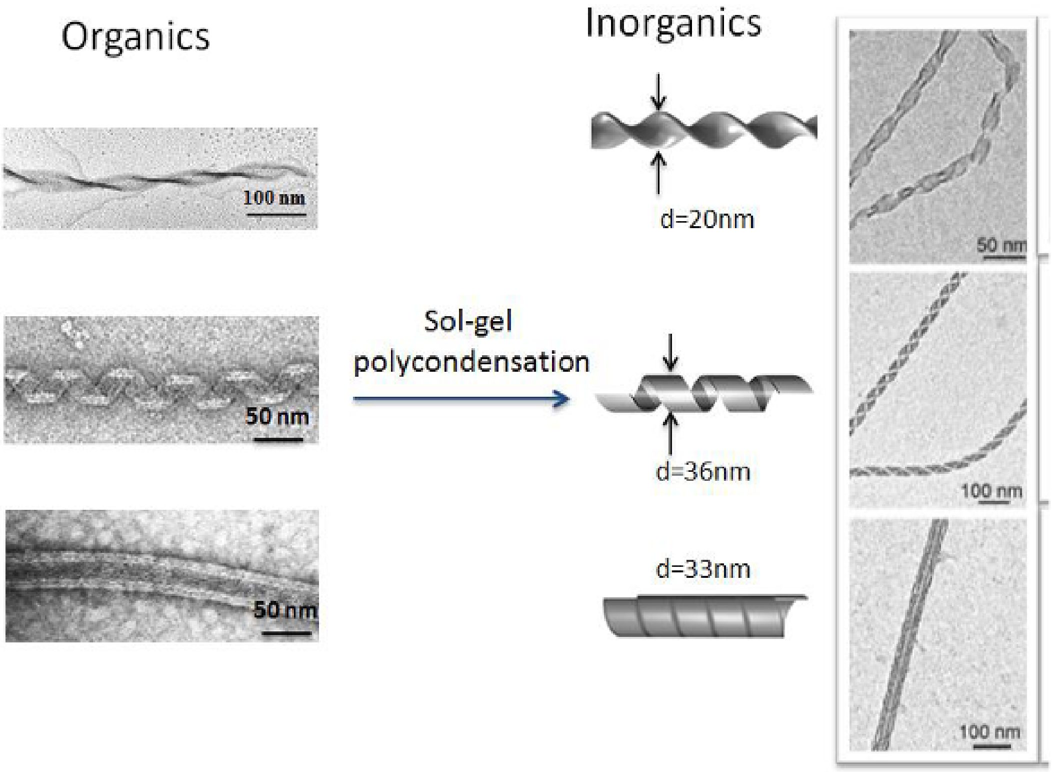

Figure 2.24: TEM images of organic (left) and inorganic (right) nanohelices. The different morphologies can be obtained by variation of the gel ageing time: 2h for twisted ribbons, 2-3 days for helices and 30-40 days for tubules (top to bottom) [200]

or nucleotides. In the following, we will focus on diammonium gemini surfactants with tartrate as counterion.

2.3.2 Tunability and Transcription

The shape of chiral self-assemblies from gemini tartrate can be adjusted via a variety of factors, including time, temperature, enantiomeric and additives. Gemini gels in water form twisted ribbons within hours which transform to helices after a few days, then to tubules with longer ageing times (Figure 2.25). The exact speed of this development depends on the concentration of gemini tartrate in water: Higher concentrations accelerate the process. The presence of alternative counterions affects morphological development as well: Substitution of less than 5% of tartrate ions by bromide slows the gel ageing process or halts it at twisted ribbon stage or even leads to the formation of flat ribbons, depending on the quantity of added bromide. Similarly, a decrease of the *ee* leads to unwinding of the structures and pitch increase. This behaviour is dynamic: For example, even after tubules formed from gemini tartrate with an *ee* of 1, they can be reversed to twisted ribbons or helices in a matter of hours by adding the appropriate amount of opposite enantiomer. CD experiments show that an inversion of TA chirality leads to a quick exchange of counterions, but the gemini surfactant cations take more time to adapt their organisation [202].

Changes in temperature can dynamically induce morphology shifts: Higher temperatures favour more unwound states, e.g. above 40°C, gels will form twisted ribbons, but no helices or tubules. This effect is reversible, tubules can turn to twisted ribbons and back again [203].

The versatile surfactant helices are of interest for biomimetic materials design due to their structural flexibility, but their lack of biocompatibility and stability makes them unsuitable for biological studies. This issue is adressed by silanisation of the helices: Silica precursor compounds like Tetraethyl orthosilicate (TEOS) in solution can undergo a sol-gel process to form a silicon oxide gel, a process described by Brinker and Scherer [204]. It consists of two steps: Hydrolysis and condensation. First, the alkoxy groups of the silane precursor are replaced by hydroxyl groups, i.e. silicic acid species are formed. This step is accelerated by a low pH value and slowed down

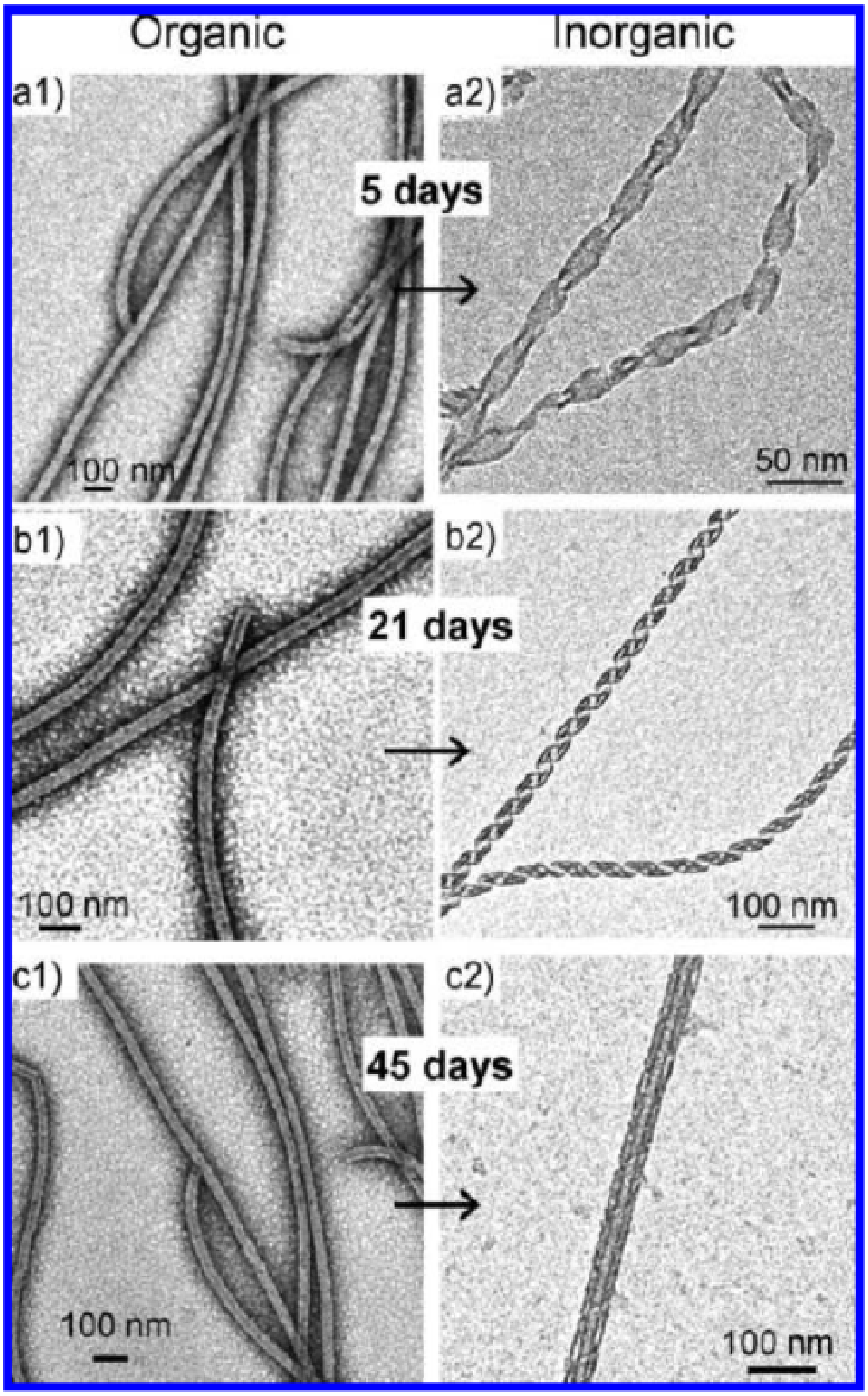

Figure 2.25: TEM images showing the tunability of helix morphology by means of varied ageing times: Ageing of 16-2-16 gemini tartrate gels for 5, 21 or 45 days leads to the formation of nanotubes (a1, b1, c1). Silica transcription of these tubes of different age results in the formation of objects of different morphologies: Twisted ribbons, nanohelices or nanotubes [201]. Changing the transcription method speeds this process up.

by steric hindrance by large alkoxy substituents. Condensation of these hydroxyl groups with either alkoxyl or hydroxyl groups under elimination of ethanol or water, respectively, results in the formation of a silica network. This behaviour is exploited to perform an organic-inorganic transcription where the organic helices or twisted ribbons serve as templates: TEOS which was prehydrolysed in water condensates preferentially at the surface of the nanomaterials thanks to the attraction of the silane precursors by the positively charged quaternary ammonium. This process is called transcription and stops further morphology change due to ageing, temperature or change in enantiomeric excess [205].

The shape of the nanoobjects after transcription depends on the reaction conditions. If the prehydrolysis of TEOS takes place in water, a partial unwinding of the ribbons takes place during the reaction, so that silica helices are obtained from organic tubules, for example [201]. Alternatively, TEOS prehydrolysis can be accelerated by lowering the pH with tartaric acid; with this method, the reaction will be completed in a shorter time, and the morphology after the transcription will be the same as before [206]. The reason for the different outcomes of these protocols is that after being hydrolysed, silicate ions compete with tartrate at the surface of the bilayers, which causes unwinding of the helical structures unless the condensation of silica happens fast.

Silica formation is affected by pH in three different ways: A low pH value catalyses the hydrolysis of the silane by facilitating the leaving of the alkoxy moiety, which is why the hydrolysis rate increases linearly with acid concentration [207]. On the other hand, the condensation reaction slows down with increasing pH (except for very high or low pH). In the basic pH range, TEOS hydrolysis is also accelerated, and its rate is proportional to the concentration of hydroxide ions. Under these conditions, the surfaces of aggregated particles are negatively charged and repel each other, which results in the formation of bigger particles. Lastly, a high pH also promotes the dissolution of silica [208]. These factors need to be taken into account when trying to efficiently synthesise nanohelices which preserve their morphology.

Using this method, helices with a period length of 63nm(±5nm) could be obtained, which matches the period length of collagen I fibres and marks these nanohelices as an appropriate model system to explore the effect of this morphology on stem cell development.

2.3.3 Modification of length and surface-chemistry

The aforementioned silica nanohelices have a high aspect ratio and are therefore normally entangled and partly sometimes aggregated. This makes them difficult to handle due to their heterogeneity. Inspired by the fragmentation of carbon nanotubes by ulttrasound, the Oda group developed a way to fragment silica helices using ultrasonic treatment in order to obtain disentangled, homogeneous colloidal solutions of shortened helices [206].

Our approach is based on the fact that ultrasound of appropriate volume creates bubbles in solvents, which rupture silica helices. For this fragmentation process which is called cutting herein, the choice of solvent is critical: When the sonication takes place in apolar, water-immiscible solvents, helices aggregate, probably because of residual water on their surfaces which makes them stick together. If polar solvents like water are used, helices take damage. This challenge can be circumvented by increasing the stability of the helices: Freeze-drying them before cutting increases the stability of the Si-O bonds. After this consolidation step, we redispersed the materials with ultrasound to obtain shortened and disentangled helices of relatively homogeneous length distribution.

The surface properties of silica helices can be modified by grafting of various molecules such as bioactive peptides. In order to perform coupling reactions on the helix surface, it is advisable to introduce a functional group first, which is achieved by reaction with APTES. The preparation of a self-assembled APTES layer on hydroxyl-terminated surfaces like silica or glass includes two steps: Firstly, hydrolysis of the ethoxy groups exposes silanol functionalities; secondly, APTES binds to the surface by intermolecular interactions. After this, covalent bonds are formed between silanes and surface hydroxyl groups under elimination of water [209]. Their stability and structure can be enhanced by thermal treatment [210] [211], which reduces the amount of unreacted ethoxy groups. The reaction can also be carried out under anhydrous conditions, but in this case longer reaction times and/or elevated temperature is required and the resulting APTES layer is thinner. The surface coverage of APTES depends on the exact reaction conditions, new strategies can reach more than 13 molecules per nm^2 on nanoparticles [169].

2.3.4 Bioactivity

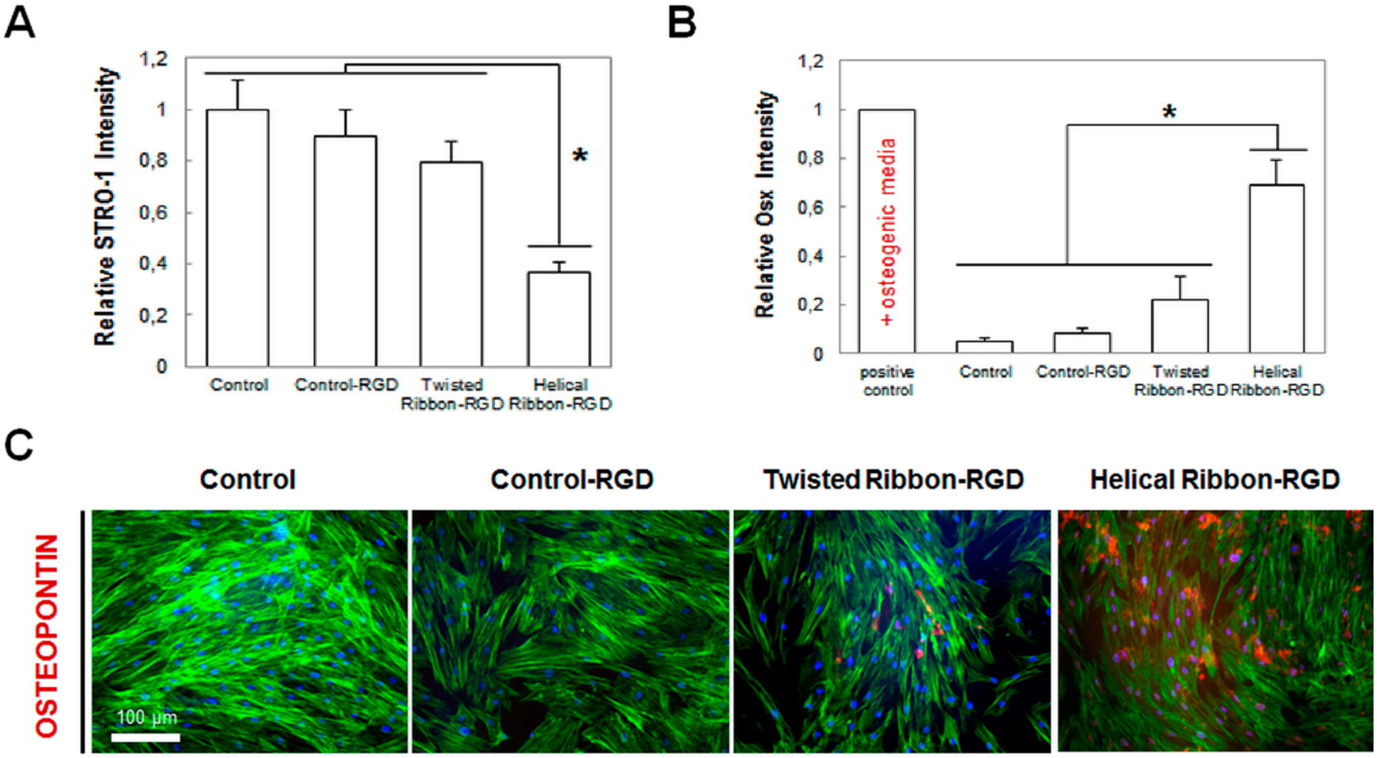

Figure 2.26: Key results obtained by R. Das and O.Zouani [212]: Relative expressions of STRO-1 and Osterix on different materials (A and B) and Fluorescence images of these conditions (C; blue staining: DAPI, green: actine, red: Osteopontin).

The previous sections have given an idea of how stem cell behaviour and differentiation can be controlled by the properties of their microenvironment, of the particular importance of collagen regarding the bone ECM, and of the possibility to create collagen-mimicking materials using amphiphile self-assembly. The tunability of these nanomaterials leads to the question whether this system can be a suitable model to help understand the role of nanoscale morphology on hMSCs. A recent work by our group [212] explored this question by grafting collagen-mimicking nanohelices onto glass surfaces and assess the expression of osteogenic markers in hMSCs cultured thereon.

Helices with a collagen-like periodicity of 63nm (herein referred to as ”helices”) were compared to twisted ribbons with a pitch of 100nm. All nanomaterials were functionalised with a cell adhesion promoting RGD-peptide. Results show that cells cultured on helices show more focal adhesions not only compared to control surfaces, but also to twisted ribbons. Furthermore, they exhibit a strongly decreased expression of STRO-1 and massively increased expression of osterix (Figure 2.26). Cells cultured on twisted ribbons showed the same tendency, but to a lesser extent. This raises the question whether cells recognise the collagen-like nanomorphology and interpret it as a cue to undergo osteogenic differentiation.

2.4 Bioactive functionalisation

2.4.1 Grafting reactions

Peptide grafting

As we have seen in many of the examples in the previous chapters, combining multiple cues to control cell differentiation may lead to synergistic effects because e.g. chemical and mechanical factors often go hand in hand. In order to achieve a bioactive functionalisation, it is helpful to covalently graft bioactive agents, e.g. peptides, to surfaces or nanomaterials to ensure that their localisation does not change when in contact with cells. There is a variety of possible approaches to perform this immobilisation: One strategy is based on coating the intended culture substrate with a polymer by submersion. This techniques enables facile subsequent functionalisation reactions if the polymer features any functional groups; on the other hand, it complicates the experimental setting because coating thickness and homogeneity need to be controlled. For example, de Giglio *et al.* [213] coated titanium substrates with polypyrrol. As thiol groups can undergo addition reactions with pyrrole in high yields (thiol-ene-reaction), peptides containing cystein can efficiently be linked to this polymer. Another study employed a method which is also available for peptides without cystein: Substrates are coated by polycaprolactone, which features ester groups. By performing an aminolysis with ethylene diamine on the polymer, amine groups are introduced. After this, different homobifunctional crosslinkers can be introduced: Glutaraldehyde can be bound to the amine groups of polymer and peptide by reductive amination, a method developed by Miller and Robyt [214]. Alternatively, a diepoxide like diethyleneglycol diglycidyle can crosslink the two amine groups. In situations where the deposition of a polymer on the substrate is not desired, functional groups can be introduced to glass or silica surfaces using APTES. Due to its ability to form self-assembled layers on silicon oxide by undergoing condensation reactions, it can modify glass objects with amine functionality in an anhydrous solvent. To perform the final grafting step between peptide and surface-bound amine groups, it is a common approach to activate the acid moieties to introduce a suitable leaving group and enable the formation of a peptide bond. For example, El Khoury *et al.* [215] linked the C-termini of peptides to an APTES-modified surface using N-hydroxysuccinimide (NHS) and N,N'-diisopropylcarbodiimide (EDC or DIC). The mechanism includes an addition of the organic acid moiety to the EDC imide bond, which creates a good leaving group which is substituted by the succinimide. The latter is eventually replaced by the APTES amine groups. If the peptide is supposed to bind via the N-terminus rather than the C-terminus, a crosslinker is necessary. For example [216], an APTES-modified glass surface can be reacted with glutaric aldehyde or other dialdehydes or cyclic anhydrides under basic conditions to expose carbonyl groups at the surface. This moiety can be bound to the peptide's amine group either using EDC/NHS coupling as described above, or via O-benzotriazole-N,N,N,N-tetramethyl-uroniumhexafluoro-phosphate (HBTU), a coupling agent for peptides which creates an activated ester that is susceptible to nucleophilic attack by amines. An alternative method for APTES-modified surfaces is to react them with a crosslinker that binds to a side chain instead of a terminus. For example, succinimidyl 6-(3-(2-pyridyldithio)propionamido)hexanoate contains a succimidyl group which permits binding to the surface amine groups. It also features a dithio-moiety which thiol groups of peptides containing cystein can bind to [217]. The crosslinker can also be homobifunctional and undergo nuccleophilic substitution by amine groups at both ends, like Disuccinimidyl suberate (DSS) [218]. Hydroxy-terminated surfaces can also be functionalised with peptides. trifluorotriazine can bind both to amine and hydroxyl groups, allowing to graft peptides to OH-terminated membranes [219]. Peyre *et al.* [220] used a two-step process to graft peptides to hydroxyl-terminated titanium oxide: First, the catechol derivative 3,4-dihydroxyphenylacetic acid binds to the surface as primary crosslinker. After that, its acid moiety is activated with NHS/EDC and linked to a secondary, homobifunctional diamine crosslinker. Finally, the peptide's C-terminus is equally activated by NHS/EDC and reacts with the free end of the secondary crosslinker. A last strategy to be mentioned in this chapter is the option to use the affinity of sulphur to gold. Thiols like cystamine can bind to gold coated surfaces to introduce functional groups, which can be anchoring points for further modification. In the given example, amine groups on the surface can form imines with aldehydes under acidic catalysis.

Nanomaterials grafting

Attaching nanomaterials to surfaces is different from peptide grafting, mainly because nanoparticles don't offer as much of a variety of functional groups as peptides, and because their diffusion is slowed down by their weight. Nonetheless, when including nanomaterials in a 2D cell culturing environment, it is advisable to link them to the substrate in order to maintain control over their position. A simple method to cover a substrate in nanoparticles is spincoating. It doesn't include chemical agents, but relies on physical principles to deposit the material to a surface. Lipski *et al.* [152] used this technique to modify glass surfaces with silica NPs with diameters ranging from 50 to 300nm. After several cycles of NP deposition, spinning and drying, the substrates are heated to 80°C to anneal the particles. Other approaches use chemical bonds instead. Glass, silica and silicon surfaces can be modified with silanes like APTES to introduce functional groups, normally after cleansing and activation of the substrate. For example, the formation of a self-assembled APTES layer introduces amine groups, which can provide direct anchorage points for nanoparticles: For example [221], palladium NPs of about 6nm size can be grafted to an APTES-functionalised glass surface by dipping the substrate into a colloidal Pd(II)-solution. Coordination bonds between amine groups and palladium immobilises the NPs to the surface. This method is useful for inorganic NPs, but cannot be applied to organic particles. NPs with a negative surface charge can be grafted in a similar way. In one study [222], silica surfaces were modified with 3-(2-Aminoethylaminopropyl)trimethoxysilane in order to attach silver nanoparticles to them. The NPs are stabilised by citrate ions, which gives them a negative surface charge. If the surface-bound amine groups are protonated, electrostatic interactions will immobilise the NPs to the surface. An alternative approach [19] permits the grafting of different types of organic NPs: Surfaces are modified with a self-assembled monolayer featuring phthalimide moieties can bind organic NPs when excited by light. Upon UV irradiation, the phthalimide groups extract a hydrogen atom from organic particles, causing a radical recombination process which creates a covalent bond. The high affinity of gold to sulphur is often exploited for the grafting of gold NPs. Kvítek *et al.* [223] used dithiols to graft gold NPs to glass surfaces: After activating the substrates using plasma discharge treatment, they were treated with ethane-1,2-dithiol to form a thiol layer which gold NPs can bind to. The limitation of this method is that some dithiol molecules form two bonds with the substrate, which leaves no thiol groups available for the NPs. A following study [224] refined the procedure by using sterically more demanding bisphenyl-4,4'-dithiol as crosslinker on a gold-sputtered surface. The size and geometry of the dithiol makes them more likely to bind to the gold NPs.

High aspect ratio nanomaterials grafting

The grafting of long nanoobjects like nanofibers is analogous to the previous section, although complicated by the higher length and therefore lower mobility in liquid phase compared to other nanoparticles. A study [225] describes the covalent surface attachment of self-assembled peptide amphiphile nanofibres onto nickel/titanium-substrates. The metal surfaces were silanised by vapour deposition of an amonipropylsilane layer. After that, an aqueous solution of the fibres was dropcast on the surface and dried, followed by EDC/NHS mediated coupling. In a more recent work [226], nanofibres made of methoxy-functionalised p-quaterphenylene (MOP4) are bound to surfaces by vacuum deposition of the material on mica. These fibres were formed during the deposition process, so this procedure is not suitable for nanofibres which need to be formed in a liquid phase. Das and Zouani [212] used an approach similar to [225], except that the acid-terminated substrates were treated with an EDC/NHS solution before getting in contact with the nanomaterials. After this step, amine-terminated silica naohelices were immobilised on these surfaces by adding aqueous helix solution to the substrates. The present study requires three grafting reactions: In order to study the effect of biofunctionalised nanohelices on cells, it is necessary to immobilise bioactive agents onto nanohelices and onto substrates, and to immobilise these nanohelices onto substrate surfaces. As these bioactive nanomaterials are destined for experiments with cells, all immobilisations need to be covalent to ensure control over the location of the materials despite cellular traction forces exerted on them. For the grafting of peptides, 3-(maleimido)propionic acid N-hydroxysuccinimide ester will be used as linker because it permits fast coupling at high yields and with mild reaction conditions. For the grafting of nanohelices onto surfaces, the aforementioned EDC/NHS-coupling will be used.

Chapter 3

Materials and Methods

3.1 Synthesis and assembly of helices

Chemicals for synthesis were purchased from Sigma Aldrich France, except hydrogen peroxide solution, which was bought from Fisher scientific. Gemini surfactants were synthesised from simple starting materials in a three-step process. First, the alkyl skeleton is established by a reaction of N,N,N',N'-tetramethyl dimethylamine with an alkyl bromide (Figure 3.1). As this study deals with gemini surfactants of the type 16-2-16, hexadecyl bromide was used. The reaction is carried out in acetonitrile at 80°C during 48 hours under reflux cooling with a molar ratio of 1:3 (amine to bromide). The standard batch size were 0.823mL amine and 5g bromohexadecane. The resulting yellow solution was kept at 4°C for at least one hour before filtration. The obtained white solid was dissolved in acetonitrile by heating, recrystallised, washed with acetone and dried under vacuum. The next reaction introduces anions which can later be replaced by tartrate. Its thermodynamic

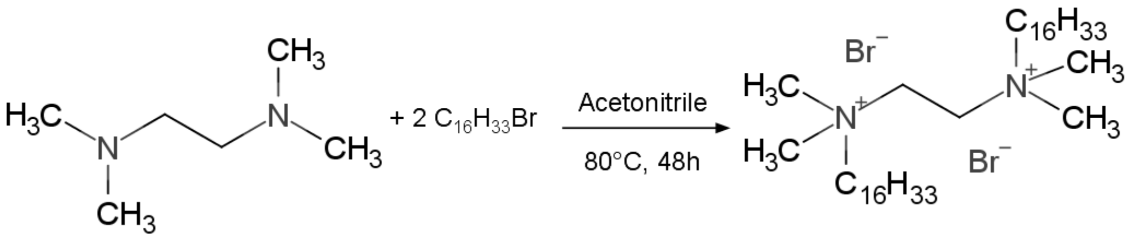

Figure 3.1: Reaction scheme of 16-2-16 gemini bromide synthesis.

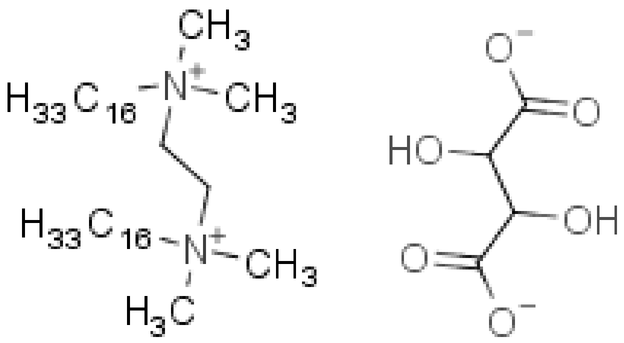

Figure 3.2: Structural formula of 16-2-16 gemini tartrate.

driving force is the elimination of silver bromide. The product of the last reaction and silver acetate were mixed in a molar ratio of 1:3 and dissolved in 100mL methanol (standard batch size: 2.01g bromide to 1.38g acetate). Due to the light sensitivity of silver salts, it is advisable to avoid prolonged exposure to light. The reaction mixture was heated to 50°C for 24h and then filtered over Celite®. The residue is discarded, the filtrate is evaporated and the remaining solid is dissolved in a minimal volume of a 9:1 chloroform/methanol. Acetone is added to precipitate the product, which is obtained by filtration after crystallisation at 4°C. 500mg of the dried gemini acetate and 220mg of enantiomerically pure tartaric acid (*L*-enantiomer by default) are dissolved separately in 50mL of 9:1 acetone/methanol each. The acetate solution is added dropwise and under vigorous stirring to the tartaric acid solution, and the reaction mixture is stirred for 20 minutes, filtered and the solid residue is dried. The final product is purified by suspending it in a solvent in a 50mL plastic tube, sonicating for 5 minutes, centrifuging at 3000g for 10 minutes and decanting the supernatant. This procedure is performed five time with cold water and twice with acetone as solvent. (The same procedure is applied later when washing silica nanohelices.) After drying under vacuum, 16-2-16 gemini tartrate (Figure 3.2) is obtained as a white powder.

Organic helices are assembled by dissolving 3.58mg of gemini tartrate in 5mL MiliQ water and heating at 60°C for 20 minutes. The handedness of the self-assembled helices is directly linked to the chirality of the counterion. Right-handed helices are formed from *L*-tartrate and left-handed helices from *D*-tartrate.

The solution ages for 48h at 20°C before the start of the silica transcription. Prior to the silanisation,

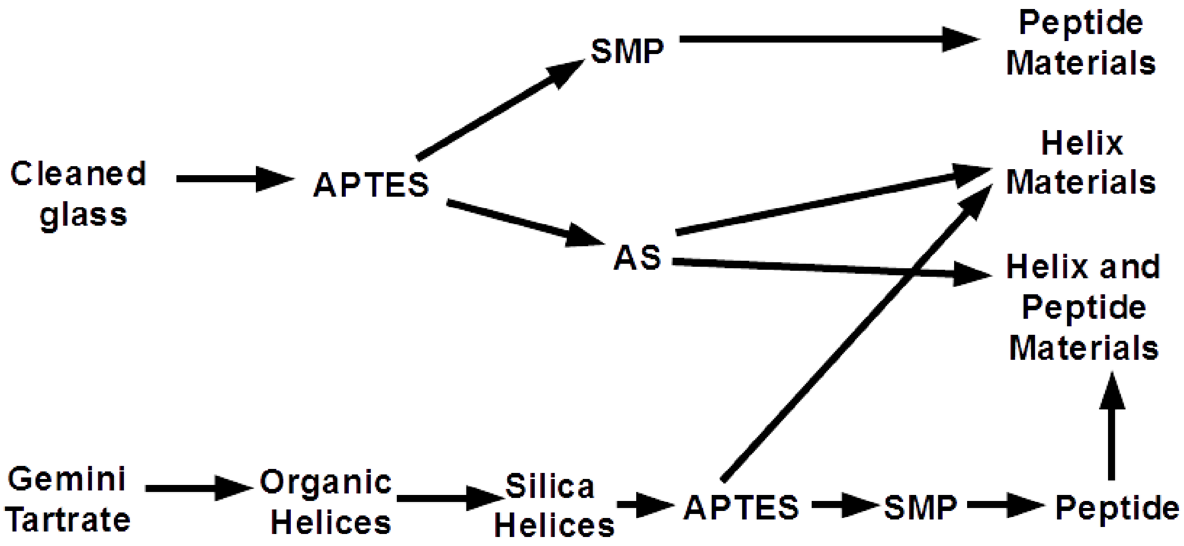

Figure 3.3: Summary of reaction steps to prepare materials. The process of gemini tartrate synthesis is not included here.

250μL of liquid tetraethyl orthosilicate are dissolved in 5mL of aqueous tartaric acid solution (0.1mM) and kept at 20°C for seven hours to prehydrolyse the silane. The two solutions are united and stored in a horizontal position for 15 hours. The product is purified the same way as the gemini tartrate, using ethanol as solvent five times and isopropanol once.

18-2-18 helices were synthesised by replacing 1-bromohexadecane by 1-bromooctadecane in the first step of the gemini surfactant synthesis *ceteris paribus*. *D*-helices are made by performing the synthesis step from gemini acetate to Tartrate with pure *D*-tartaric acid. Mixed *D/L* helices were attempted to synthesise in two ways: By mixing gemini tartrate powder of different enantiomers at a given weight ratio prior the ageing of organic helices or by using a mix of tartaric acid of both enantiomers (at a defined ratio) in the synthesis of gemini tartrate from gemini acetate.

The silica helices are dried by lyophilisation and suspended in a 1:1 ethanol/isopropanol mixture. This suspension is sonicated at 130 Watt for 15 minutes, each second of sonication being followed by a one-second pause. This process cuts the helices, removes gel lumps and yields a homogeneous solution. Figure 3.3 gives an overview over the order of the following functionalisation steps. Amine moieties are introduced to the silica helices by adding 3μL of 3-aminopropyl triethoxysilane

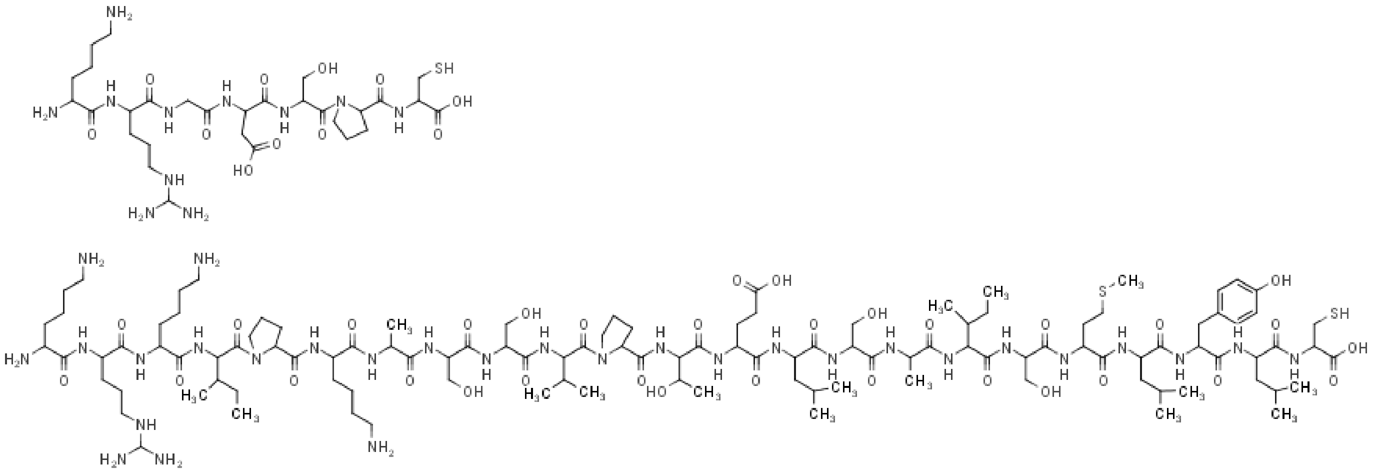

Figure 3.4: Structural formulae of RGD (top) and BMP (bottom).

to 5mL of ethanoic helix suspension. The reaction takes place at 70°C during 15 hours. The helices are rinsed with ethanol three times afterwards.

1mL of the ethanoic dispersion of APTES-treated helices was added to 1mL of ethanol containing 3mg of SMP. The reaction mixture was exposed to ultrasound for three hours, and subsequently washed with water. The two peptides used in this study (cf. Figure 3.4) are referred to as RGD (sequence KRGDSPC) and BMP, the active domain of the BMP2-protein (sequence KRKIPKASSVPTELSAISMLYLC). Both peptides were purchased from GeneCust, Luxembourg. The peptide (RGD, BMP or both together) were grafted to the helices by adding 1mL of 0.3mM aqueous solution of the peptide(s) to 1mL of aqueous helix solution and keeping it on a roller-mixer for 24 hours. After the reaction, the helices were washed with water several times. For simultaneous grafting of both peptides, the concentration of each peptide was divided by two so that the overall peptide concentration remained the same as in other samples.

3.2 Surface treatment and grafting

Borosilicate $1cm^2$ glass slides of 1mm thickness were purchased from GoodFellow SARL. Prior to functionalisation, they were cleaned with piraña solution (70% Sulfuric acid, 30% Hydrogen peroxide (35%)), rinsed extensively with MilliQ water and dried at 100%. The slides were placed

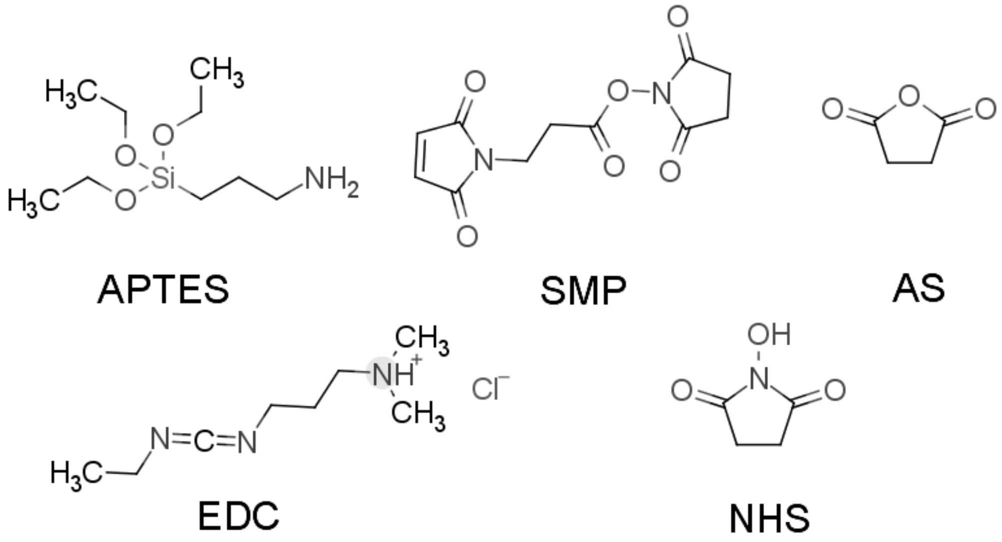

Figure 3.5: Structural formulae of all compounds used in the grafting process.

individually in snap cover glasses and transferred into a glovebox for treatment under water-free atmosphere. All materials were degassed on a heating plate (150°C) under vacuum (10^{-5} Torr) for 18 hours. After cooling, 170μL APTES in 2mL anhydrous Hexane is added to each slide, and the materials are shaken for three hours. (The molecules used in the immobilisation process are shown in Figure 3.5.) The samples are subsequently washed in Hexane three times: 30 minutes, 15 minutes in an ultrasound bath and overnight. The rinsed materials are degassed 100°C for 4 hours under vacuum.

After APTES functionalisation, a linker is introduced: Either SMP for peptide grafting or succinic anhydride (AS) (Figure 3.6) for helix immobilisation. The reaction with SMP is carried out at 2mM in DMF for two hours. In the case of AS, the materials are treated with 4mg of AS dissolved in 2mL DMF for three hours. Both crosslinker reactions take place under N_2 atmosphere and are followed by the same washing steps as for APTES (with DMF instead of Hexane), and by degassing under vacuum at 100°C for four hours. All following steps took place outside the glovebox.

Peptides (RGD, BMP or both) are grafted to the surface at 1mM in DMF for 24 hours. The structural formulae of the peptide grafting *via* SMP are shown in Figure 3.6 After immobilisation, the peptide materials are washed in DMF and ultrasound for 15 minutes. AS-functionalised

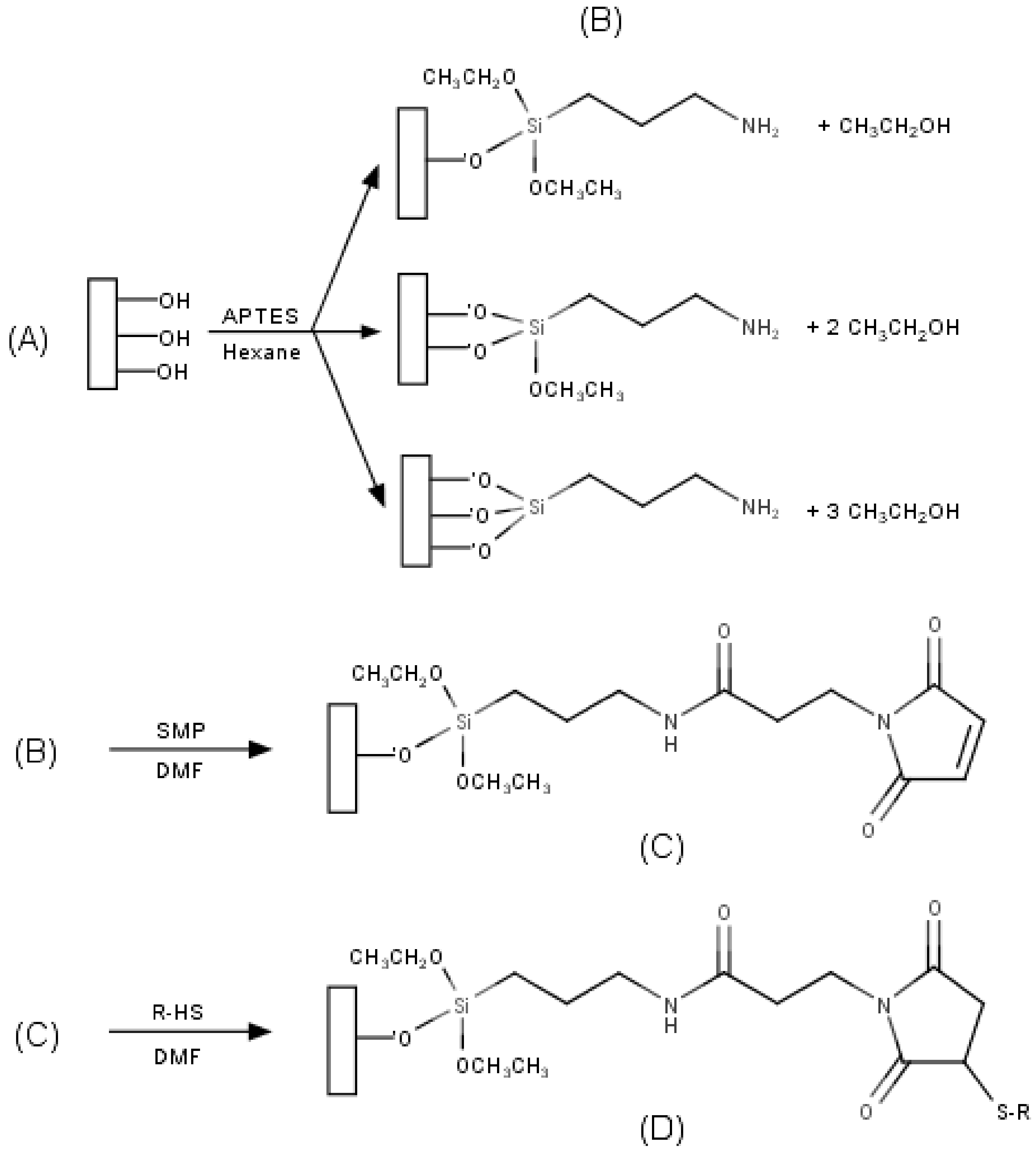

Figure 3.6: Structural formulae of the different stages of peptide functionalisations of glass surfaces: Activated glass substrate (A); APTES forming one, two or three bonds with the surface (B); SMP crosslinker introduction (C) and binding of the peptide (”R”) via the thiol group of the amino acid cystein (D).

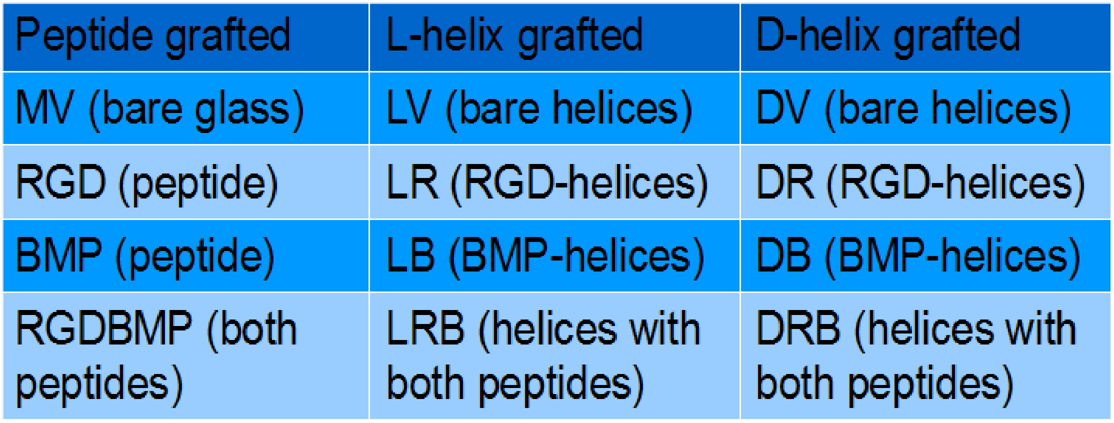

Peptide grafted	L-helix grafted	D-helix grafted
MV (bare glass)	LV (bare helices)	DV (bare helices)
RGD (peptide)	LR (RGD-helices)	DR (RGD-helices)
BMP (peptide)	LB (BMP-helices)	DB (BMP-helices)
RGDBMP (both peptides)	LRB (helices with both peptides)	DRB (helices with both peptides)

Figure 3.7: Table of modified glass surface types to be examined as cell culture substrates within this study: Homogeneously grafted peptide materials and substrates grafted with left- and right-handed silica helices.

surfaces are prepared for nanohelix grafting by EDC/NHS-chemistry): Each glass slide is treated with an aqueous solution of EDC (172mM), NHS (104mM) and MES buffer (94mM). The reaction is carried out at 4°C for 20 hours. After that, the materials are washed thoroughly with water and one mL of helix suspension is deposited on them a defined number of times. With the different types of helices and peptide modifications, twelve types of substrates for cell culture experiments were prepared (Figure 3.7).

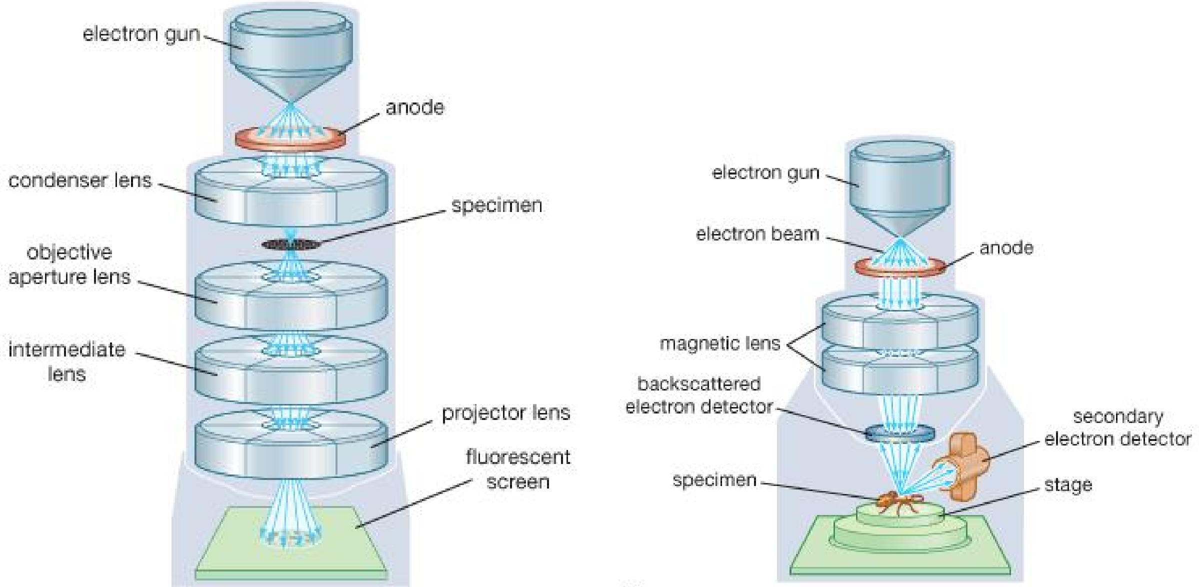

© 2008 Encyclopædia Britannica, Inc. © 2008 Encyclopædia Britannica, Inc.

Figure 3.8: Comparision of TEM (left) and SEM (right). Note that the generation of the electron beam is similar, but the methods of electron detection vary. Image source: 2008 Encyclopaedia Britannica, Inc.

3.3 Morphological characterisation

3.3.1 TEM and SEM

Electron microscopy (Figure 3.8) is a useful tool for nanomaterials imaging because the wavelength of electrons is shorter than that of visible light, which permits high magnifications. Transmission and Scanning electron microscopy (TEM and SEM) are similar methods, but they differ in how they extract information from interactions between electron and sample. In electron microscopes, a beam of electrons is created by an electron gun (filament) and focused on a sample by a condenser lens. A high tension between an anode and the filament accelerates the electrons, and a hole in the anode aligns an electron stream towards the sample. The condenser lens converges the beam on the sample, which is mounted on a support that is transparent to electrons. The image can be visualised by projecting it on a fluorescent screen or by recording it with CCD cameras [227].

Whilst TEM devices detect the electrons which pass trough the specimen, SEM detects high-energy backscattered electrons and low-energy secondary electrons. Therefore, SEM speciments do not need to be thin. They are usually covered with an electrically conductive layer to avoid charge accumulation: In the present study, metallisation with gold/palladium was performed and a conductive connection between the metallised top of the material and its bottom side was ensured. TEM was used as a routine analysis of nanohelix morphology prior to grafting them to surfaces, whereas SEM images were acquired both at low and high magnification to monitor both post-grafting helix morphology and the degree of surface coverage.

For TEM measurements, approximately 5μL helix suspension were deposited onto a 400-mesh carbon-coated copper grid and dried in air. Experiments were performed on a Philips CM120 electron microscope operating at 120 kV with a 2000x2000 Gatan ssCCD camera for image acquisition.

SEM was used for surface-grafted helices only. The prepared glass slides were fixated on SEM pin stubs using double-sided conductive adhesive. The samples were metallised and observed on a Hitachi S2500 microscope at the Plateforme Aquitaine de Caractérisation des Matériaux (CNRS) in Bordeaux (France).

3.3.2 AFM

Unlike optical and electron microscopy, Atomic force microscopy (AFM; Figure 3.9) imagery relies on the forces between the sample and a probe, called cantilever. The surface is scanned by this cantilever, which bends according to the surface topography due to repulsive interactions between cantilever tip and surface. The cantilever displacement is quantified by measuring the deflection of a laser beam which is reflected from the cantilever to a detector diode. The interactions between surface and cantilever are van der Waals forces, Coulomb forces and short-ranged forces. The latter involve a Pauli-repulsion between the electrons of probe and sample, which becomes dominant at short distances. There are different modes of data acquisition: In contact mode, either the distance between cantilever and surface or the force between them are kept constant via a feedback loop during the scanning process. In tapping or noncontact mode,

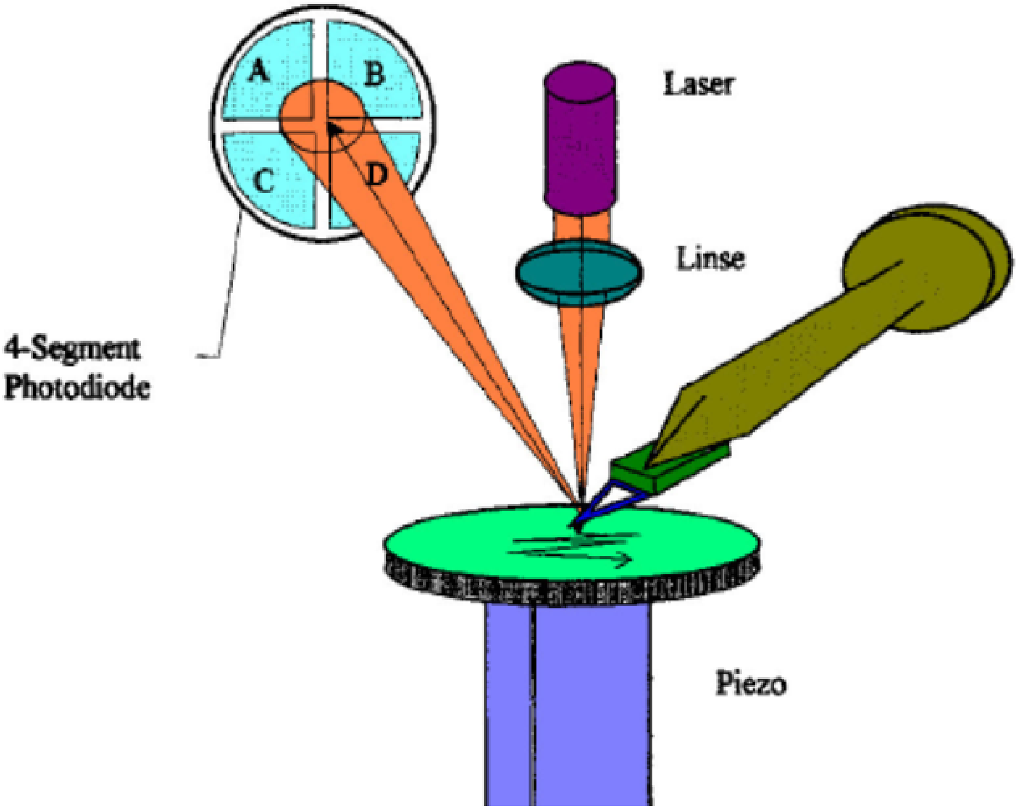

Figure 3.9: Measuring principle of AFM: Detection of cantilever movement by laser deflection [229].

the cantilever vibrates with a defined frequency as it scans the sample surface. Changes in surface topography cause alterations in amplitude and/or phase of the vibration [228]. In this study, only tapping mode is used, and surfaces are examined in air without any liquid medium. The AFM experiments in this study were carried out with the Leonenko research group at the Department of Physics and Astronomy, University of Waterloo.

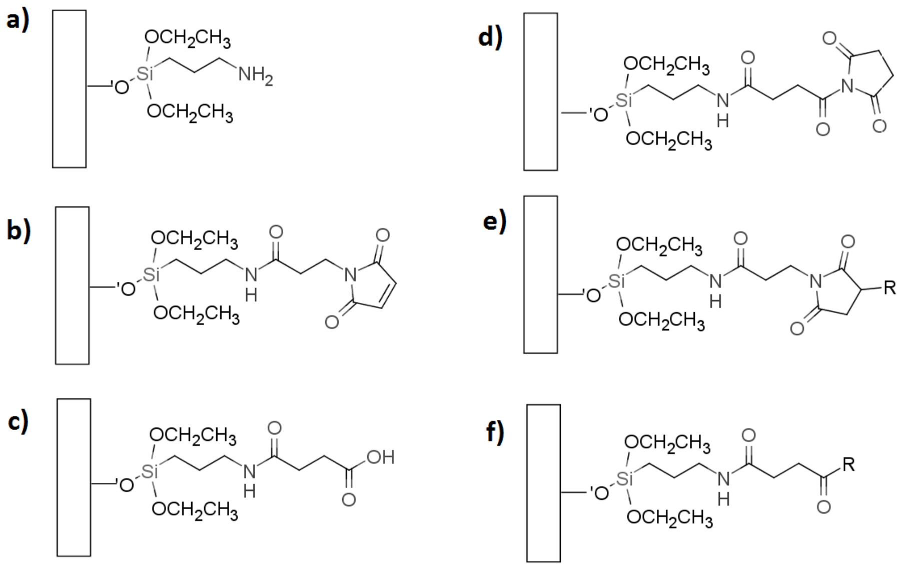

Figure 3.10: Structural formulae of the materials prepared for XPS: a) APTES, b) SMP, c) AS, d) AS/NHS, e) SMP/peptide, f) AS/peptide. Peptides are symbolised by ”R”.

3.4 Surface characterisation

3.4.1 XPS

X-ray photoelectron spectroscopy (XPS) can yield information about the chemical composition of a surface using the photoelectric effect: Excitation of matter by X-ray irradiation causes the emission of photoelectrons the energy of which permits conclusions about element-specific energy levels of electrons in the sample. This is the case because due to the conservation of energy, the difference between the irradiation energy and the energy of the detected electron is the electron binding energy of the atom which the photoelectron originates from. Therefore, XPS data can reveal the elements present in a sample, and (to some degree) the nature of their binding interactions [230].

XPS characterisations were carried out at the Plateforme Aquitaine de Caractérisation des Matériaux (CNRS) in Bordeaux (France).

A ThermoFisher Scientific K-Alpha$^{\text{TM+}}$ spectrometer was used for surface analysis. The monochromatised AlKα source (hν=1486.6eV) was activated with a spot size 200 μm in diameter.

The full spectra (0-1350 eV) were obtained with a constant pass energy of 200 eV and high resolution spectra with a constant pass energy of 40eV. The precision of the energy values is 0.2 eV, and the device FWHM is fixed between 1.4 and 1.9 eV. High resolution C1s and N1s XPS spectra were fitted and quantified using the AVANTAGE software provided by ThermoFisher Scientific. XPS was used to characterise the synthetic steps involved in the preparation of homogeneous peptide surfaces (cf. Figure 3.10): Cleaned bare glass, APTES, the two crosslinkers SMP and AS and the two peptides RGD and BMP. Both crosslinkers were used to compare their performance in covalent peptide attachment.

ToF-SIMS

ToF-SIMS stands for Time of flight - secondary ion mass spectrometry. It is a surface analysis technique which resembles XPS, but bombards surfaces with different particles: In ToF-SIMS, ions (e.g. caesium, oxygen or bismuth ions) are accelerated towards the sample surface with an energy et the keV scale. These ions, which are called primary ions, cause positive and negative secondary ions to be emitted from the sample surface. Mass spectrometry analysis of these secondary ions reveals information about the chemical composition of the upper layers of a surface. The mass of secondary ions is determined by their time of flight. The results of this method are qualitative in nature.

The measuring principle is that primary ions which hit the surface penetrate it to some degree and collide with atoms of the sample several times. The transfer of energy in this process leads to subsequent collisions, which can cause emission of particles at the surface. Neutral particles are not detected, but charged species are. The secondary ions can be polyatomic, which provides additional insight into the chemical nature of the surface [231].

The experiment was carried out using an Ion-Tof device, using Bi^{3+} as primary ion with an energy of 30keV and an analysis current of 0.25pA. The size of the analysis area was approximately $200x200\mu m^2$.

3.4.2 Fluorescence microscopy

For further quantification of surface-bound peptide, peptides (RGD, BMP and both together) modified with the fluorescent group Fluorescein isothiocyanate (FITC) were grafted to glass surfaces as described in the section on materials preparation and examined using fluorescence microscopy. Images were acquired using a LEICA DM5500B epifluorescence microscope at a magnification of 2.5x (NA 0.07), 10x (NA 0.25) or 40x (NA 1.03, oil immersed) and different exposition times (650ms and 1500ms). Data was acquired with MetaMorph®software visualised with a Leica Microsystems filter and evaluated using the freeware program ImageJ.

The relationship between measured fluorescence and peptide quantity was established using a calibration curve. Aqueous solutions of fluorescent RGD and BMP were prepared at concentrations between 10^{-6} mol/L and 10^{-5} mol/L from a 10^{-3} mol/L stock solution in DMSO. Drops of these solutions (1 μL) were deposed onto an ultrasound-cleaned PET surface, and their fluorescence was measured. The difference between PET and glass was accounted for by subtracting the background in either case. Using the linear regression equation of fluorescence as a function of peptide quantity and the average fluorescences of the prepared homogeneous materials, the density of peptide on the glass surfaces was calculated by converting the remaining fluorescence into peptide quantities per mm^2 by applying the following equation:

$$\rho = \frac{f - b}{a * A}$$

Where f is the fluorescence measured on a surface of the area A, and a and b are the slope and y-intercept of the linear calibration curve. ρ is the peptide density on the surface.

3.4.3 UV/Vis-Absorption

After the immobilisation of peptides onto helices, the peptide density on nanohelices was confirmed by measuring the UV/Vis-absorption of flourescence-labelled peptide grafted helices in suspension. *L*-helices functionalised with FITC-modified fluorescent RGD- and BMP-peptide and *D*-helices modified with fluorescent BMP were prepared according to the protocol in the section ”Synthesis”. After peptide grafting, the helix samples were washed by adding 2mL of water, mixing by sonication and centrifuging to remove the water. This process was repeated until the washing water appeared uncoloured, the water was kept. The absorbance of suspensions of functionalised helices and unfunctionalised helices and washing liquid was measured in aqueous suspension at wavelengths between 350nm and 750nm with a Cary 300scan UV-Vis Spectrophotometer (CBMN Bordeaux) and a Molecular devices SpectraMax M5 (School of Pharmacy, University of Waterloo).

3.5 Biological characterisation

Cell culture of bone marrow derived hMSCs (procured from LONZA, Switzerland) took place in a BSL-2 laboratory at Bordeaux University. Cells were cultured at 37°C and 5% CO_2 (v/v) and in minimum essential medium (Alpha-MEM, Gibco) contaning 10% FBS (v/v) and 1% penicillin/streptomycin. Cells at low passage numbers (2 to 4) were seeded at 10^4 cells/cm^2. During the first eight hours of culture, experiments were carried out without serum.

3.5.1 Immunofluorescence

hMSCs were seeded on ethanol-sterilised substrates of different types (cf. Figure 3.7) and cultivated for four weeks. In order to assess the differentiation behaviour of cells on materials with or without helices functionalised or not with peptide(s), hMSCs cultured thereon were stained with Runx2 and OCN. After four weeks of culture, the cells were fixed with 4% PFA for 15 minutes at 4°C, using 400μL of fixation solution per glass slide. The samples were washed three times with PBS and permeabilised with a 0.5% aqueous Triton X-100 solution for 15 minutes at 4°C, followed by three washing steps with PBS. Nonspecific binding sites were saturated by treatment with BSA (1% in PBS) for 30 minutes at room temperature, followed by washing with PBS. In the case of Runx2, the permeabilisation was carried out with cold methanol instead of Triton X-100 in order to improve permeabilisation of the nucleus, where the marker Runx2 is located. The samples were incubated with the appropriate primary antibodies (10 μg/mL in 1% BSA/PBS) at 4°C overnight and washed with three changes of PBS for five minutes each. Incubation with the secondary antibodies (dilution factor 400, in 1% BSA/PBS) took place for one hour at room temperature in the dark, followed by three PBS washing steps. The samples were mounted with Antifade DAPI mounting gel and stored in the dark at 4°C.

The following antibodies/stains were used (AF stands for AlexaFluor®):

- Runx2 Primary: D1L7F Rabbit
- Runx2 Secondary: AF goat anti-rabbit
- OCN primary: FL-100 Santa Cruz 30044
- OCN secondary: AF 647 goat anti-rabbit
- DAPI

The localisation of the staining agents inside the cells is shown by examples in Figure 3.11. At least 50 images for OCN and 30 images for Runx2 at 40x magnification were taken per culturing condition. The exposition time was kept constant for each marker. Fluorescences were calculated per cell. For OCN, the intensity in the entire cell was calculated; for Runx2, only the intensity in the nucleus. The microscope specifications were stated in the previous section.

Image treatment and statistics

In the case of Runx2, acquired images of marked cells were evaluated by measuring the cumulative fluorescence and subtracting the background, i.e. the product of measured cell area and average grey value outside the cell. To quantify the expression of OCN, fluorescence values were obtained by setting a triangular threshold using the freeware program ImageJ and measuring only the area inside the cell which is above this threshold, called region of interest. Again, the background was subtracted. Prior to calculating the mean and standard deviations of the per-cell fluorescences, outliers were removed by calculating the interquartile range of a dataset and

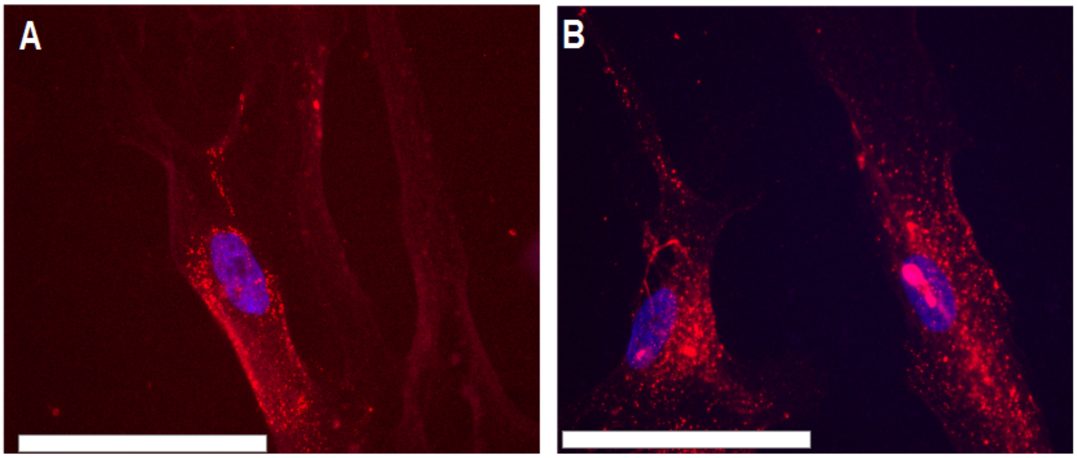

Figure 3.11: Examples of fluorescence images: (A) with DAPI- and Runx2-staining (as used in [212]), (B) with DAPI- and OCN-staining. Scaling bars 100μm.

eliminating values which had a difference to the mean which was higher than this range. Statistical significance between different culturing conditions was determined using two-tailed t-tests. For the identification of cell populations which are positive for a given cell marker, an appropriate fluorescence level as positivity criterion was identified by the shape of the histograms describing the distribution of fluorescence values. Not all of the cells were assigned to positive/negative populations, which is why the percentages of the positive and negative populations do not add up to 100%. For all experimental conditions, it was verified that the positive and negative population of any sample were significantly different (t-test, p-value lower than 0.05).

3.5.2 Proteomics

Ten cell samples of three different culturing conditions were prepared for proteomic analysis: Cells on bare glass, surface-bound silica-helices and surface-bound BMP-functionalised silica helices were chosen for this method. For this experiment, about 270μL of protein solution was used per sample, the concentration being 0.57mg/mL (bare glass), 1.92mg/mL (grafted helices) and 0.93mg/mL (grafted BMP-modified helices) as determined by absorbance measurements. After washing with PBS, the cells were scraped off their substrates, collected, centrifuged and the sediment was washed with 600μL PBS. The washing step with centrifugation was repeated three times. An aqueous extraction buffer containing TRIS-Hydrochloride (10mM, pH 7.4-8), Antiprotease and Phosstop (Roche) was added to the residue. After 30-40 minutes under ice cooling, the samples were alternatingly sonicated for 15 seconds and cooled with ice for 3 minutes; this was repeated three times. Sodium dodecyl sulfate was added to reach a concentration of 4%, followed by four sonicating/cooling cycles. The samples were vortexed for 1 minute and centrifuged at 16000-20000rpm. The supernatant was stored at -80°C.

10μg aliquots were reduced with DTT (10mM) at 56°C for 40 minutes, alkylated with TAA (20mM) at room temperature in the dark for 30 minutes, and reduced with DTT again (21mM) at room temperature for five minutes. The protein solutions were trypsinated twice with 0.2μg and 0.1μg Trypsine per aliquot at 37°C, once overnight and once for three hours.

The separation of digested peptides was performed by reverse phase chromatography using a nanoACQUITY two-dimensional ultra performance LC (Waters, Milford, MA) coupled to a Q Exactive Plus Hybrid Quadrupole-Orbitrap mass spectrometer (Thermo Fisher Scientific) equipped with a nanospray source. The configuration of the 2D-nanoUPLC system was a reversed phase pH 10 and reversed phase pH 3-based two dimension separation. The first dimension separation was made on an X-Bridge BEH C18 5 μm column (300 μm x 50 mm). The trap column Symmetry C18 5μm (180 μm x 20 mm) and analytical column BEH C18 1.7 μm (75 μm x 250 mm) (Waters Corp., USA) were used after an online dilution to lower pH values. The samples were loaded at 2 μL/min (20 mM Ammonium formate solution adjusted to pH 10) on the first column and subjected to three isocratic elution steps (13.3%, 19% and 65% ACN). Each eluted fraction was desalted on the trap column after a ten times online dilution to pH 3 and subsequently separated on the analytical column; flow rate 250 nL/min, solvent A (0.1% formic acid in water) and solvent B (0.1% formic acid in acetonitrile) with a linear gradient: 0 min, 99% A; 5 min, 93% A; 140 min, 65% A. The total run time for each of the fractions was 180 min. The mass spectrometer method is a TopN-MSMS method where N was set to 12, meaning that the spectrometer acquires one Full MS spectrum, selects the 12 most intense peaks in this spectrum (singly charged precursors excluded) and make a Full MS2 spectrum of each of these 12 compounds. The parameters for MS spectrum acquisition are: Mass range from 400 to 1750 *m/z*, Resolution of 70000, AGC target of 1e6 or Maximum injection time of 50 ms. The parameters for MS2 spectrum acquisition are: Isolation Window of 2.0 m/z, Collision energy (NCE) of 25, Resolution of 17500, AGC target of 1e5 or Maximum injection time of 50 ms. MaxQuant software (version 1.5.2.8) was used to analyze raw mass spectrometric files. The following parameters were selected: Methionine oxidation as variable modifications and cysteine carbamidomethylation as fixed variation. MS/MS spectra were searched against the Uniprot human database (version 2015-04). Seven amino acids were the minimum peptide length and at least two peptides per protein were required for identification, including at least one unique peptide and one razor peptide. The precursor mass tolerance was set at 4.5 ppm (main search). Finally, Perseus software (version 1.5.0.15) was used to perform further downstream statistical/bioinformatic analyses of the MaxQuant processing results.

Chapter 4

Results and Discussion

This chapter covers three topics: First, results concerning the synthesis of nanohelices and ways to tune their morphological properties are shown. Next, experiments to validate the characteristics of biomaterials for cell biology studies are elaborated on. Namely, the presence and quantity of bioactive peptides on materials and helices, and of helices on materials are to be evaluated. Lastly, the outcomes of cell culture studies are presented in the form of immunofluorescence and proteomics.

4.1 Helices

The Materials and Methods chapter described the synthesis of silica nanohelices based on 16-2-16-*L*-tartrate. In this section, we are going to explore the morphological control of the chiral ribbons. By varying different parameters, we try to tune the following properties:

1. Handedness control: left- or right handed (*D*- or *L*) helices
2. Diameter control
3. Pitch control
4. Length control

5. Bioactivity control

4.1.1 Handedness control

As it was previously described, gemini *L*-tartrate forms right handed helices and gemini *D*-tartrate forms left-handed helices. It should be noted that as *L*-tartaric acid is the natural enantiomer, suppliers like Sigma-Aldrich provide it in a higher default purity than the unnatural *D*-form, which may be reflected in experimental outcomes. For example, the *D*-helices in image 4.1 (b) show a slightly less regular morphology than their *L*-counterparts (a). Despite this subtle difference, synthesis of D-helices using the respective tartaric acid turned out to be feasible.

As TEM images represent a projection of an object on a plane, they can demonstrate the regular morphology of *L*- and *D*-helices, but not their handedness. This information can be found in SEM images like Figure 4.1 (c), which confirms that *L*-helices are right-handed, and *D*-helices are left-handed. In addition to the SEM experiments, AFM images of *L*- and *D*-helices were acquired at high magnification. The results are shown in Figure 4.2.

As the AFM images show, chiral features are not equally visible in all helices; some appear to have a band structure where it is hard to discern any orientation to the left or right. However, most helices were found to have a clearly visible helix shape. A possible reason for the difficulty to see chiral morphology on some helices might be the AFM method itself: Whether or not a helix groove is accurately represented in AFM images could depend on whether it is aligned with or perpendicular to the cantilever trajectory. Each image pair shows a helix the sense of rotation of which is clearly visible.

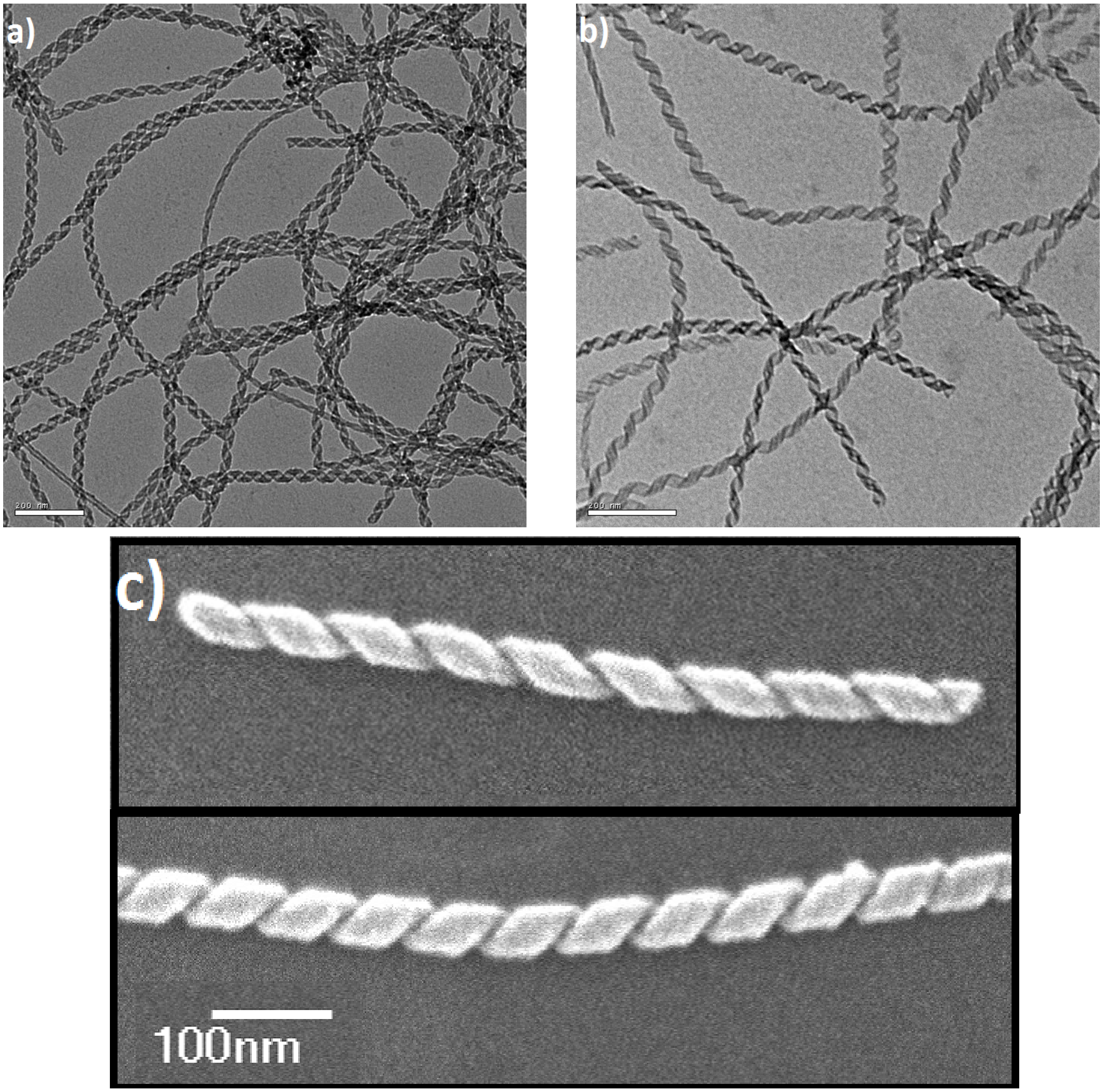

Figure 4.1: TEM images of silica helices with a) *L*- and b) *D*-orientation, scale bars represent 200nm. c): SEM images of *L*- and *D*-helix (top and bottom). Scale bar represents 100 nm.

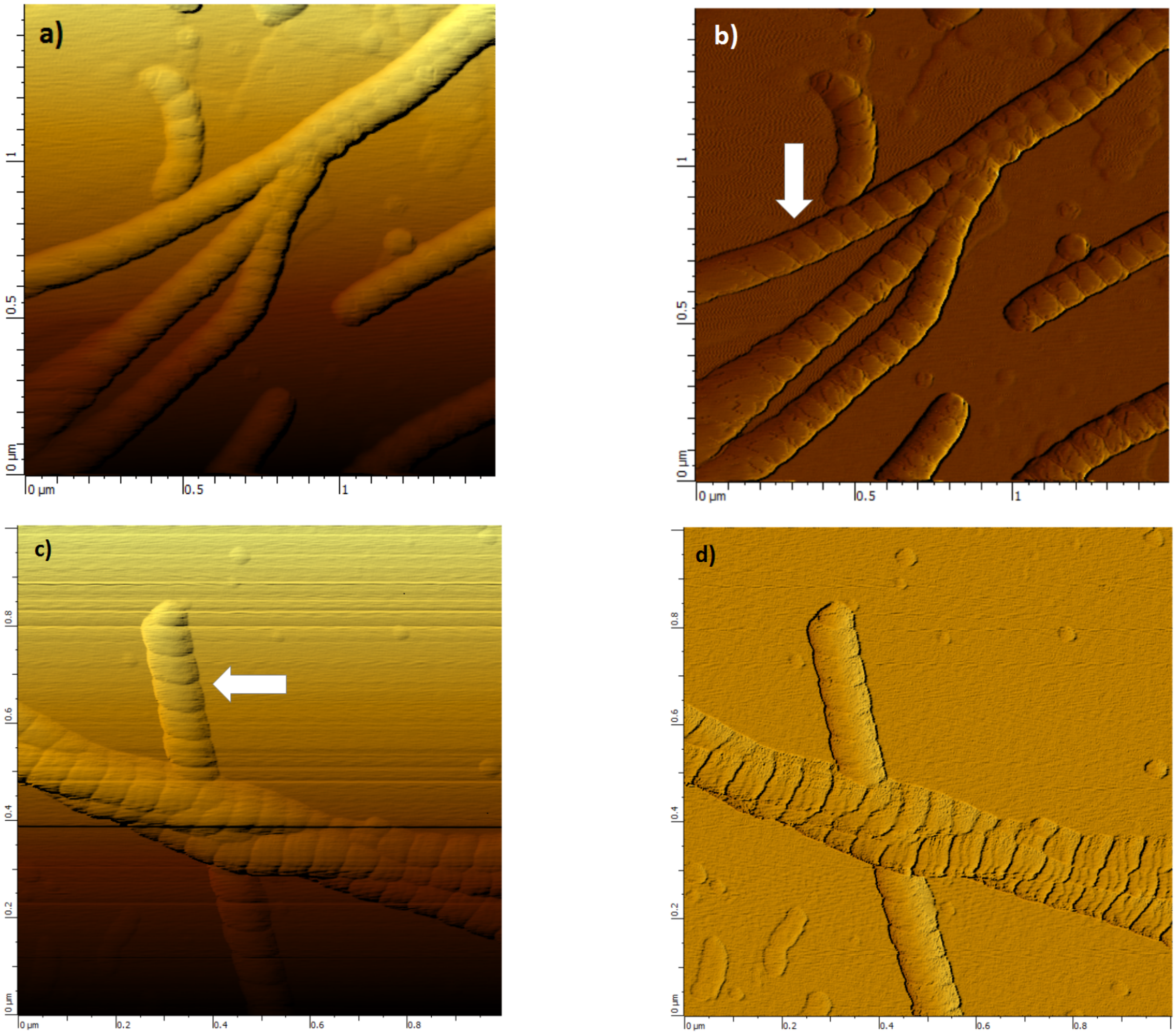

Figure 4.2: AFM images of helices. a and b: *L*, c and d: *D*, a and c: height, b and d: magnitude). A white arrow indicates where the handedness is visible.

4.1.2 Diameter and pitch

TEM images of helix variations were acquired to compare their geometrical parameters, namely their diameters and pitches or period lengths, to those of unfunctionalised 16-2-16-*L*-helices.

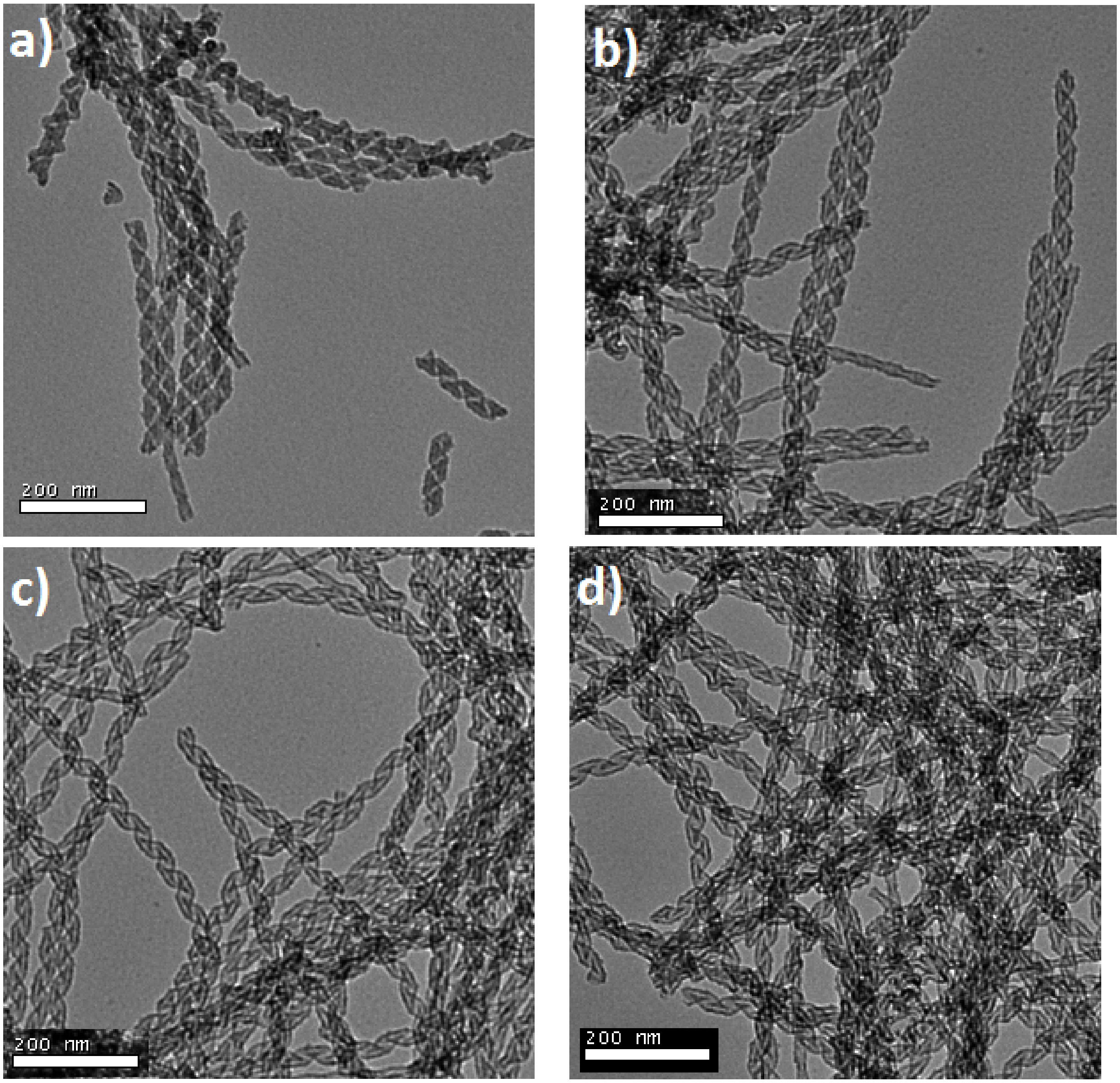

Figure 4.3: TEM images of silica helices: a) unfunctionalised, b) APTES-functionalised, c) functionalised with RGD- and d) BMP-peptide. Scale bars represent 200nm.

The TEM images of silica helices at different stages of functionalisation (Figures 4.3) were compared to determine whether the chemical modifications of their surfaces had an impact on their morphological characteristics. As the images show, no such effect can be seen.

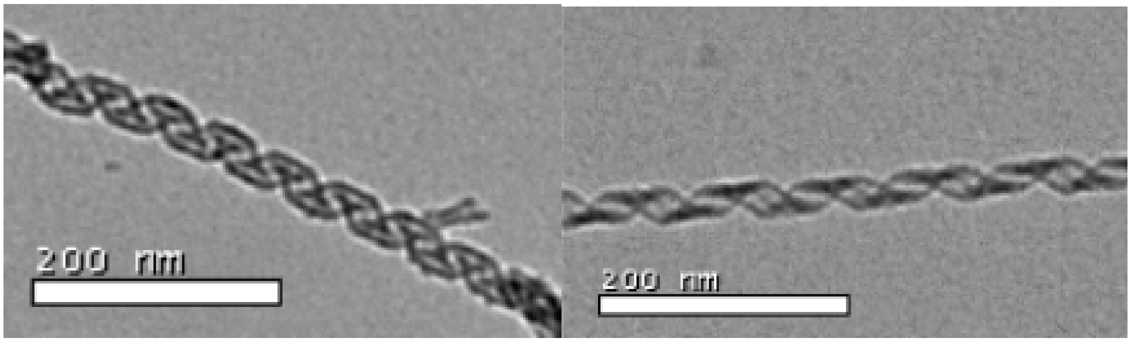

Figure 4.4: TEM images of 16-2-16 (left) and 18-2-18 (right) gemini silica helices.

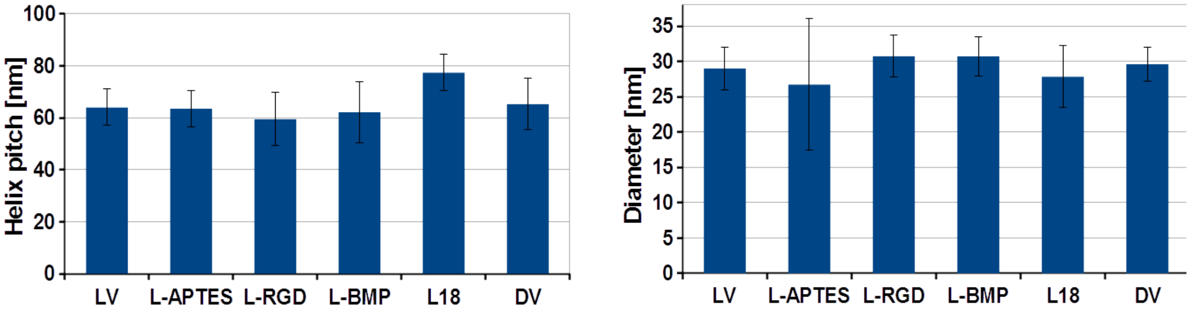

Figure 4.5: Pitches and diameters of (from left to right): *L*-helices (LV), *L*-helices modified with APTES (L-APTES), RGD (L-RGD) and BMP (L-BMP), 18-2-18 helices (L18), and *D*-helices (DV).

As image 4.4 shows, helices assembled from 18-2-18 gemini *L*-tartrate resemble the 16-2-16 helices in morphology, but exhibit slight differences in size. Close examination of the images shows a thin line of unknown origin along each ribbon. These helices have a larger helical pitch than the 16-2-16 type, as shown in Figure 4.5. 20-2-20 helices with an even longer aliphatic tail have been shown to have a diameter around 40nm and a pitch length of about 75nm [200]. This shows that an increased length of the gemini surfactant's tail results in higher helix diameters and can thus be used to tune their nanomorphology. Further increase of tail length and diameter is difficult because beyond 20-2-20, the ageing time for nanohelices rises substantially.

Two geometric parameters - helix diameter and period length - were measured to detect differences between helix variants. The data shown in Figure 4.5 (n=50) quantitatively compares the helical pitch (i.e. period length) and helix diameter of different types of helices with an *ee* of 1.0. Enantiomeric 16-2-16-*L*-helices were found to have a diameter of 29±3nm and a pitch of 64±7nm.

Percentage of D	0	5	10	20	40	50
Enantiomeric excess of L	1.0	0.9	0.8	0.6	0.2	0

Table 4.1: Table of different enantiomeric excesses of *L*-enantiomer used in this study.

The results confirm that there is no significant difference between unfunctionalised and functionalised helices, both regarding pitch and diameter. This demonstrates that helix morphology does not change due to peptide functionalisation, which is an important insight for the interpretation of cell experiments. The diameter and pitch of helices also does not show significant changes depending on chiral orientation (*L* or *D*). As the data shows, *L*-18-2-18 gemini helices have a significantly higher pitch (77±5nm) than their 16-2-16 counterpart, while the diameter decreases insignificantly.

As it was previously shown by the group, a continuous tuning of helix pitches can be achieved by variation of the enantiomeric excess of counterion tartrate. The enantiomeric excess is defined as

$$ee = \frac{[L] - [D]}{[L] + [D]},$$

where $[L]$ and $[D]$ are the amounts of *L*- and *D*-enantiomer. In this work, *L*-tartrate was treated as the main enantiomer to which a defined quantity of the opposite *D*-tartrate was added (cf. Table 4.1).

In a first attempt, gemini *D*-tartrate was synthesised and mixed with gemini *L*-tartrate in the desired ratio. In other words, the mixing of enantiomers took place in solid phase as surfactants having opposite enantiomers of tartrate as counterions were mixed after the completion of the synthesis. Figure 4.6 shows examples of the results: Instead of a homogeneous sample of helices the pitch of which increases with decreasing enantiomeric excess, inhomogeneous helix batches with a wide range of pitches were obtained. Very heterogeneous mixtures of tightly wound helices, twisted ribbons with much larger pitches or even flat bilayers were observed. Lowering the enantiomeric excess increased the proportion of these unwound helices, but did not change the morphological homogeneity of the nanomaterials (Figure 4.6, e) and f)).

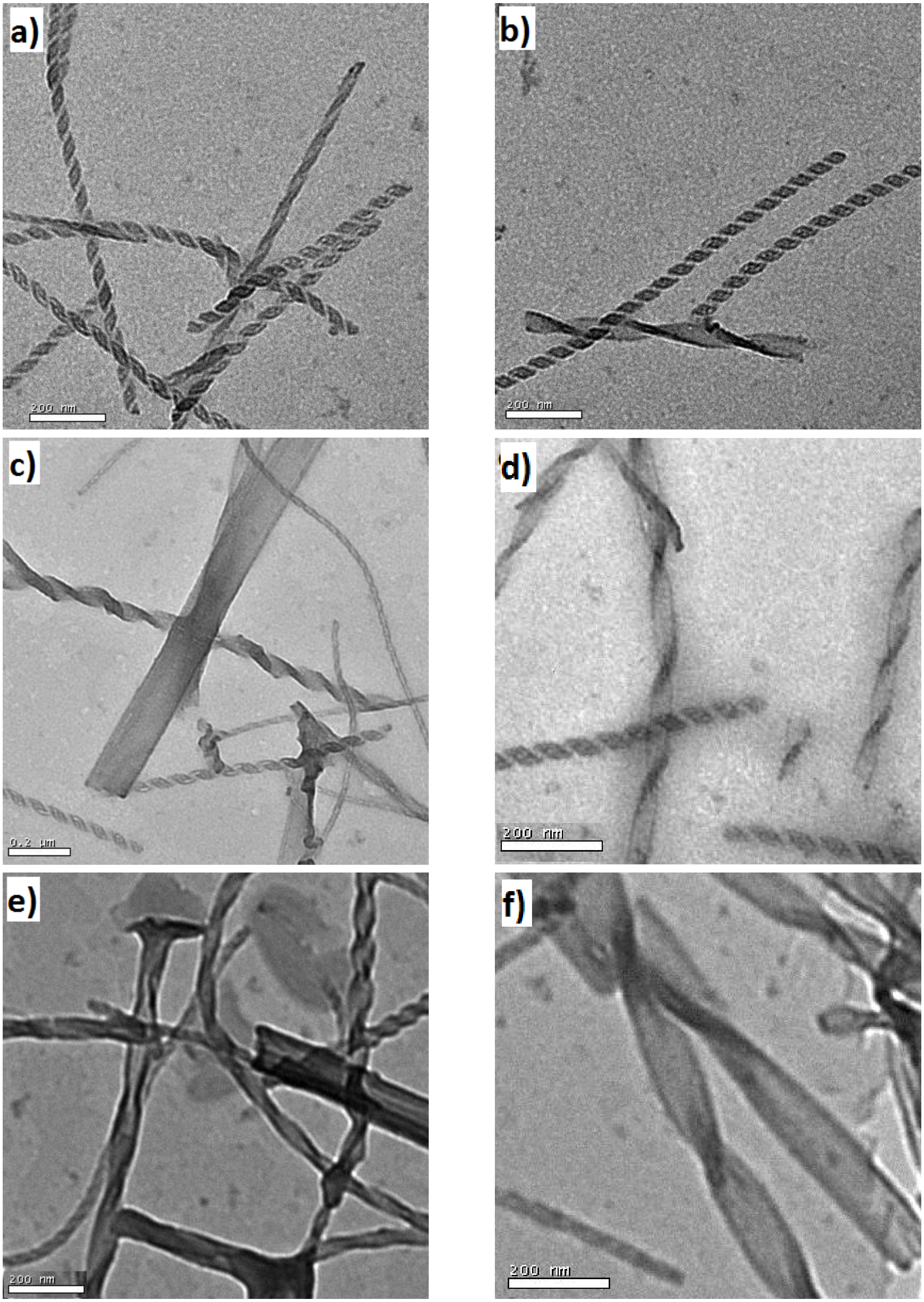

Figure 4.6: TEM images of silica helices, made with 5% (a and b), 10% (c and d) and 15% (e and f) *D*-gemini surfactant, mixed as powders (*ee* 0.9, 0.8 and 0.7). Scale bars 200nm.

In order to achieve a more homogeneous pitch distribution, the suspensions of gemini tartrate with *ee* below 1 were subjected to an enhanced mixing procedure at the beginning of the gemini gel ageing: The process of dissolving the gemini tartrate in an ultrasound bath for 5 minutes and heating the solution to 60°C for 15-20 minutes was repeated three times instead of once. The resulting helices were examined by TEM. As exhibited in Figure 4.7, a similar overall tendency as in the previous experiment can be observed: Nanoribbons of different morphologies form, and as the enantiomeric excess increases, we observe less helices and more twisted or flat ribbons. The polydispersity of helix pitches can at best be mitigated, but not removed by the intensified mixing protocol, as the following pages and Figure 4.12 will show in more detail. Further modification in the gemini tartrate preparation is required.

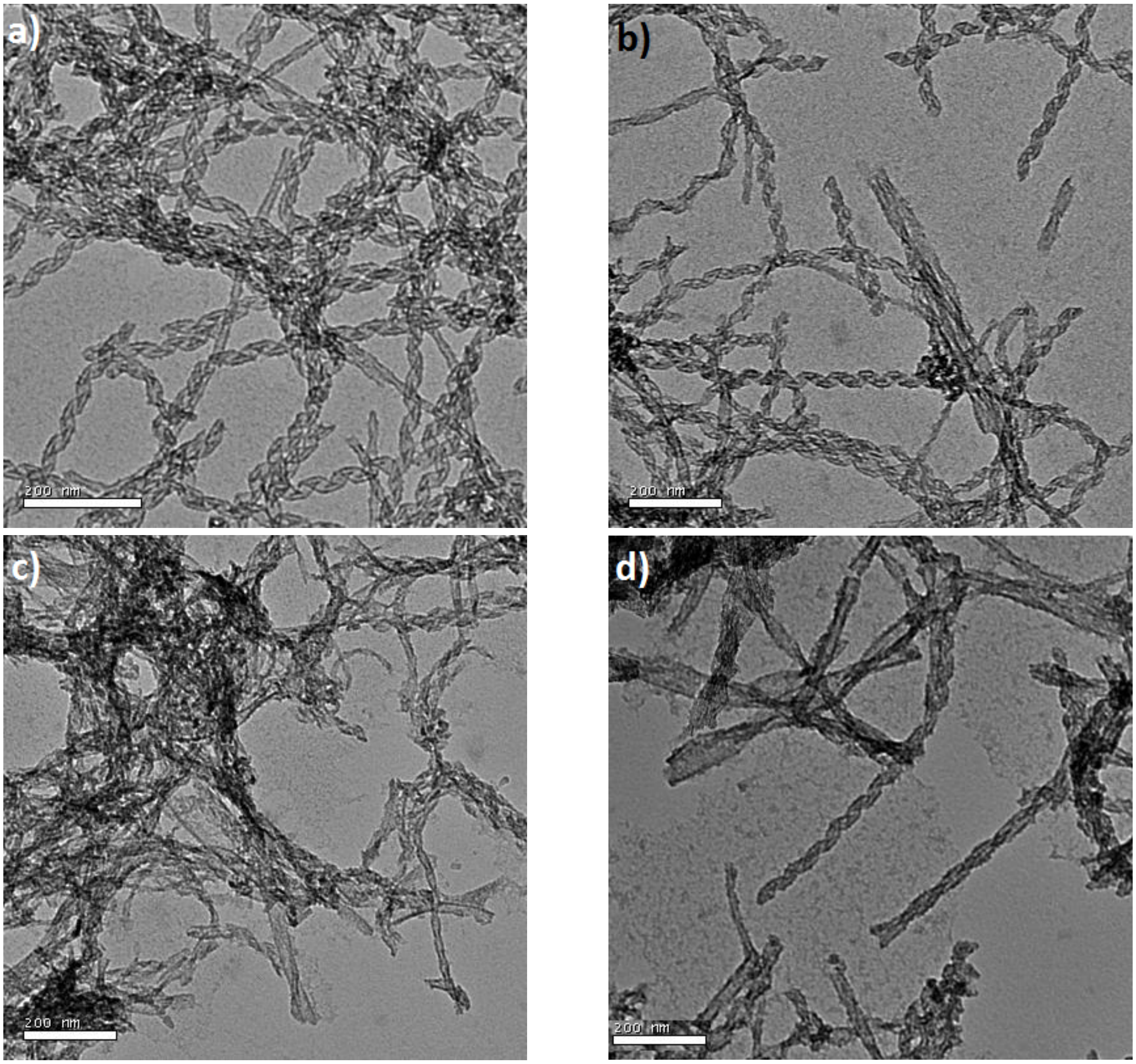

Figure 4.7: TEM images of silica helices, made with 0% (a), 5% (b), 7.5% (c) and 10% (d) *D*-gemini surfactant, mixed as powders, with improved mixing (*ee* of 1.0, 0.9, 0.85 and 0.8). Scale bars represent 200nm.

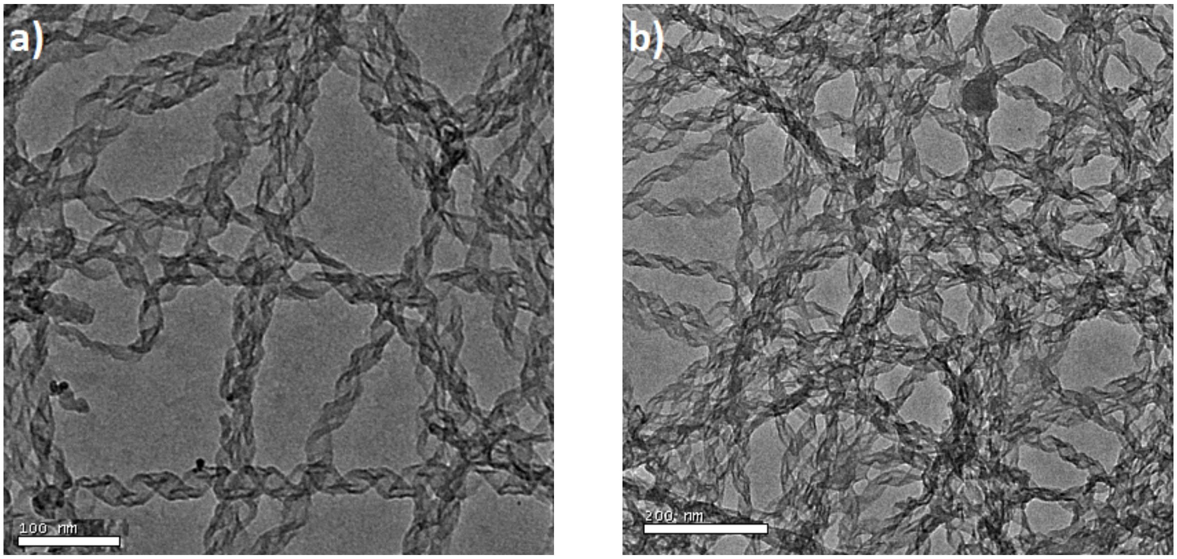

Figure 4.8: TEM images of silica helices, made with 5% *D*-gemini surfactant, mixed during synthesis (*ee* 0.9). Scale bar represents 100nm (a) and 200nm (b).

As mixing of gemini tartrate powders has proven insufficient to obtain monodisperse helix samples, a third method was applied: Instead of combining gemini tartrate powders of opposite chirality in a desired ratio, gemini tartrate was synthesised from gemini acetate using tartaric acid solution of a defined enantiomeric excess. This means that the *ee* was adjusted in the course of the synthesis, not after it. Helices of an enantiomeric excess of 0.9 were fabricated this way. As Figure 4.8 shows, homogeneous batches of helices could be obtained this way. It can be seen with the naked eye that their morphology is not as tightly wound than that of helices with an *ee* of 1.0.

The impact of the *D/L* enantiomer composition on helix shape was investigated further. Gemini tartrate with varied enantiomeric excesses were synthesised according to the most advanced procedure (i.e. by adding the gemini acetate to tartaric acid solutions of a defined enantiomeric excess). The ageing time was set to two days. TEM measurements were carried out at the Department of Biology at Waterloo University. As the enantiomeric excess decreases, the helix pitch increases so drastically that many helices do not show any helical features any more, so pitch and diameter are no longer suitable for quantitative characterisation of these nanoobjects.

At ee=0.9 (Figure 4.9), nearly all observed nanoobjects have regular helical morphologies, resembling those made with enantiomerically pure tartrate. The same is true for ee=0.8, basically all ribbons exhibit a helical morphology. The morphology of helices shows an abrupt change at ee=0.6 (Figure 4.9, e and f): Most nanoribbons have a twisted ribbon morphology with a much higher pitch compared to enantiomeric helices. Some ribbons show a tendency to twist, but the feature is not persistent over the length of the ribbon; some objects even feature no twist whatsoever. This trend continues for ee=0.2 (Figure 4.10), where only very few ribbons show any helical shape at all, and most of them are just long, flexible-looking ribbons without any defined morphology. As expected, nanomaterials with an ee of 0 exhibit no helical features either. They are also different from the ee=0.2 samples in that they appear flatter without a lot of bending and folding, and the widths of the objects vary substantially.

The images show that gemini tartrate made with tartaric acid of ee$<$1 results in the formation of helices of a better homogeneity regarding helix morphology compared to helices obtained by mixing enantiomerically pure *L*- and *D*-tartrate as powders. However, a certain degree of polydispersity is still observed in these samples.

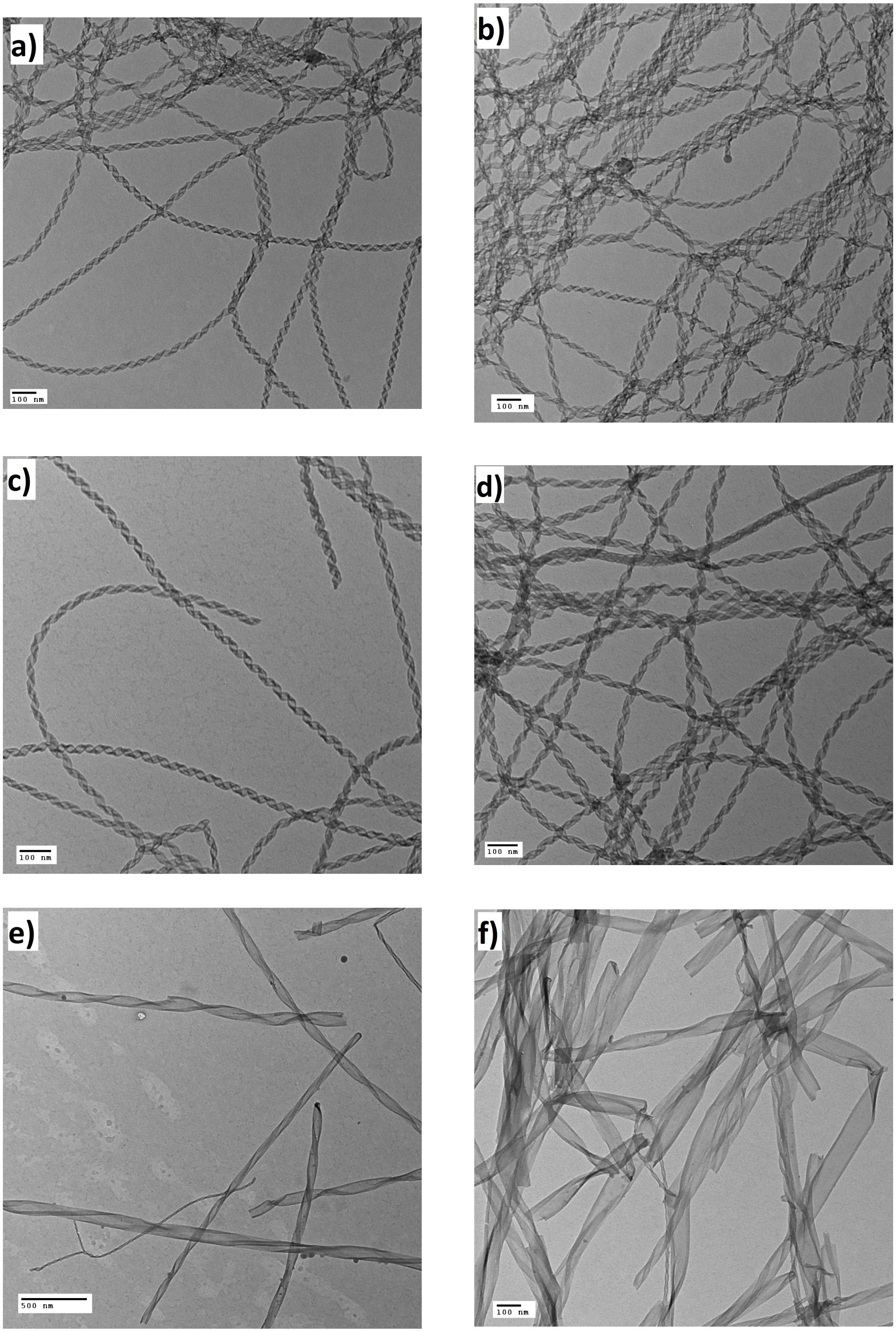

Figure 4.9: TEM images of silica gemini helices with an ee of 0.9 (a and b), 0.8 (c and d) and 0.6 (e and f).

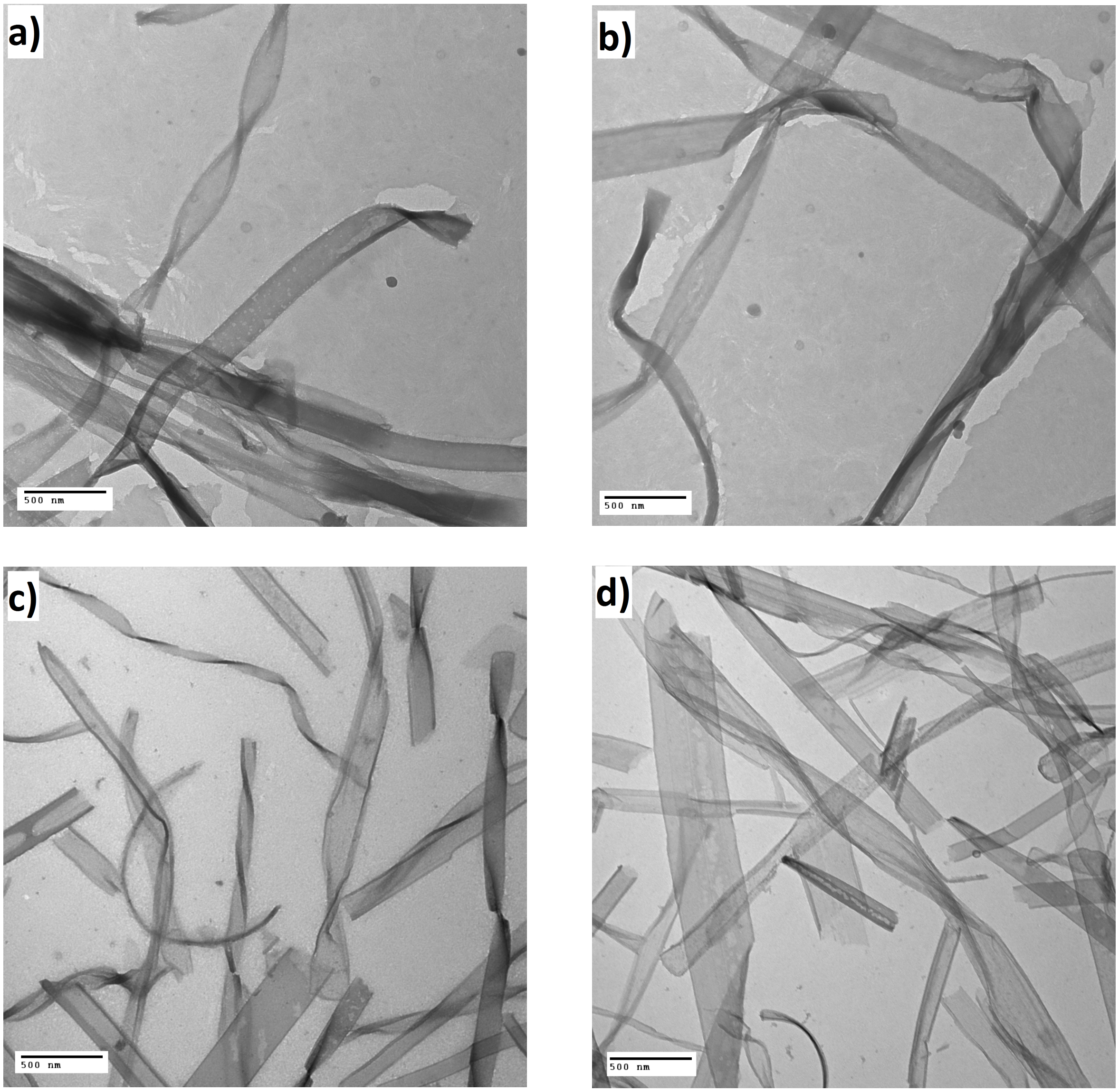

Figure 4.10: TEM images of silica gemini helices with an ee of 0.2 (a and b) and 0.0 (c and d).

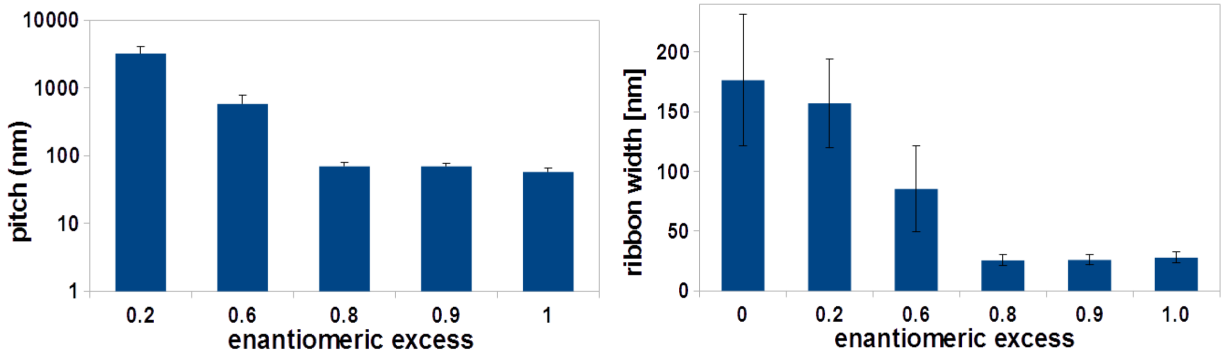

Figure 4.11: Pitches and ribbon widths of nanoobjects as a function of enantiomeric excess. Helix pitches are shown in logarithmic scale. The standard deviation of the pitch for an *ee* of 0.2 represents the expected minimum error. 50 helices per condition were measured.

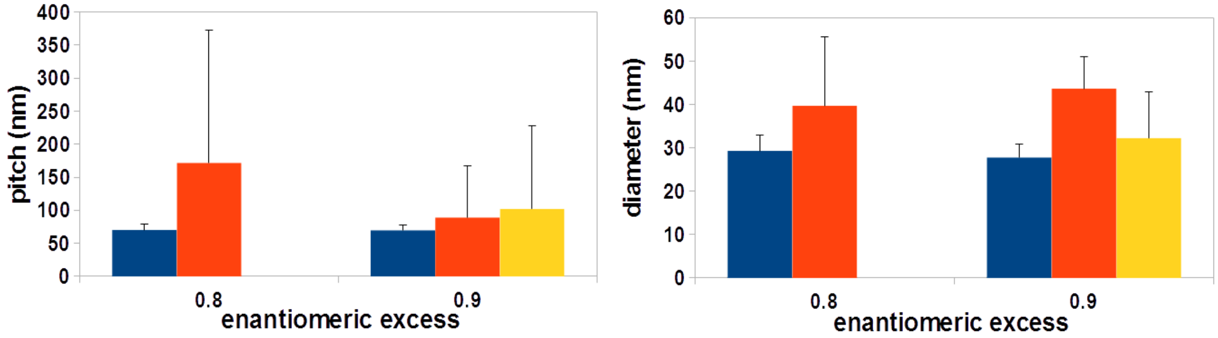

Figure 4.12: Comparison of pitches and diameters of helices made using different methods: mixed at the powder stage (red), with improved mixing (yellow) and with mixed tartaric acid (blue). The number of measured helices was 50 for the blue columns and 30 for the others.

The development of helix pitch and diameter as a function of *ee* is shown in Figure 4.11: The graphs show that at an *ee* of 0.6, both values exhibit a strong increase. For *ee*s lower than 0.6, the number of helices which exhibit periodic features is so low that average pitch and diameter could not be obtained, as one can see in Figure 4.10. Comparison between the data obtained with different preparation methods (Figure 4.12) show that with the most recent preparation method, the standard deviations of the helix pitch is much smaller than they were with the previous protocols. The standard deviation of the diameters shows the same tendency.

4.1.3 Length control

After their assembly and silica transcription, nanohelices are obtained as a heterogeneous suspension with macroscopic aggregates. The product is homogenised by ultrasound cutting: A silica helix suspension (synthesised from 5 μmol of gemini tartrate) is freezedried for two days and resuspended in 2 mL of organic solvent (1:1 ethanol and isopropanol). After ultrasound treatment as described in the Materials and Methods section, no more aggregates could be seen with the naked eye, the suspension appeared homogeneous and opaque. Due to the absence of aggregates, it can be pipetted easily.

The appearance of cut helices depends on the solvent that is used (cf. Figure 4.13, left). In polar solvents like water or ethanol, helices are damaged by the ultrasonic treatment. In DMSO, DMF, pyridine and trifluoroethanol, helices were fragmented and dispersed fairly well with little damage. In acetonitrile, the nanohelices are disentangled, but showed little fragmentation. In the apolar solvents hexane and toluene, helices aggregate, which is probably caused by residual water that remained on the surface of the nanoribbons despite the transfer in another solvent. The attraction between them makes the helices stick together as bundles [206].
The effect of sonication power on helix length was examined in trifluoroethanol at a concentration of 1 mg of helix in 1 mL of solvent (cf. Figure 4.13, right). As the results show, sonicating at higher power (up to 130W) leads to a narrower length distribution with a maximum at shorter lengths: At 26W, a broad range of helix lengths which extends beyond 2 μm is found; at 104 W and 130 W, nearly all helices exhibited a length of less than 1 μm. The morphology of the individualised helices was not substantially damaged. The results were published in ACS Nano [206].

As mentioned above, helices were damaged when fragmented in water. In an effort to circumvent this problem, silica helices were freeze-dried prior to resuspension and ultrasound treatment. The drying consolidates the bonds of silica and makes the helices more resistant to damage induced by sonication in polar media. The tendencies regarding the effect of solvent choice

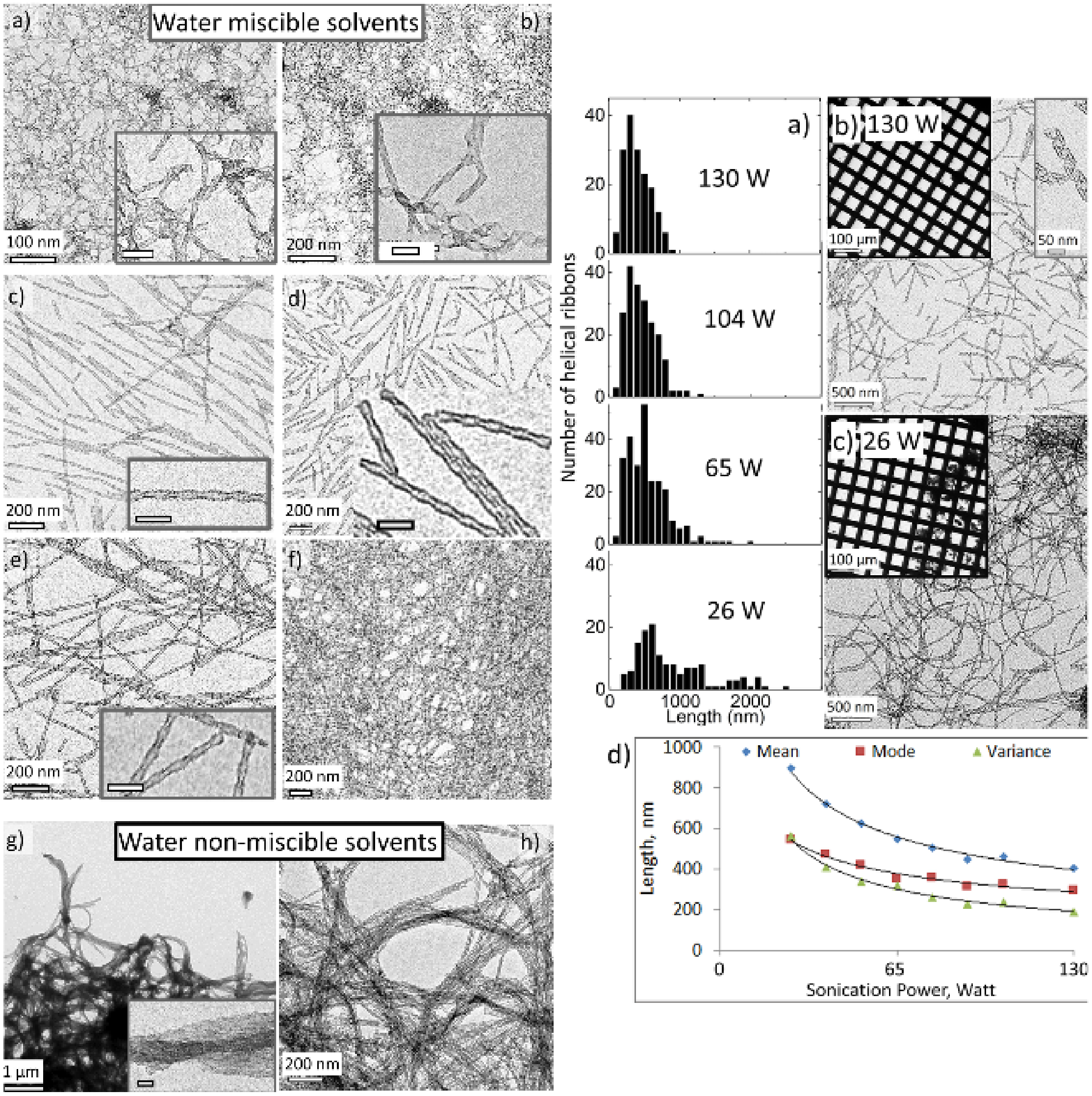

Figure 4.13: Left side: Silica twisted ribbons after ultrasound cutting in the following solvents: (a) water, (b) ethanol, (c) DMSO, (d) DMF, (e) pyridine, (f) acetonitrile, (g) hexane and (h) toluene. Scaling bars correspond to 50 nm. Right side: (a) Histograms showing the length distribution of helices (n>150) at four different sonication power settings. (b) TEM images at different magnifications of helices cut at 130W (c) and 26 W. (d) development of mean, mode and variance of helix length as a function of sonication power. One notices a steady decrease of mean length as power increases. Images from [206].

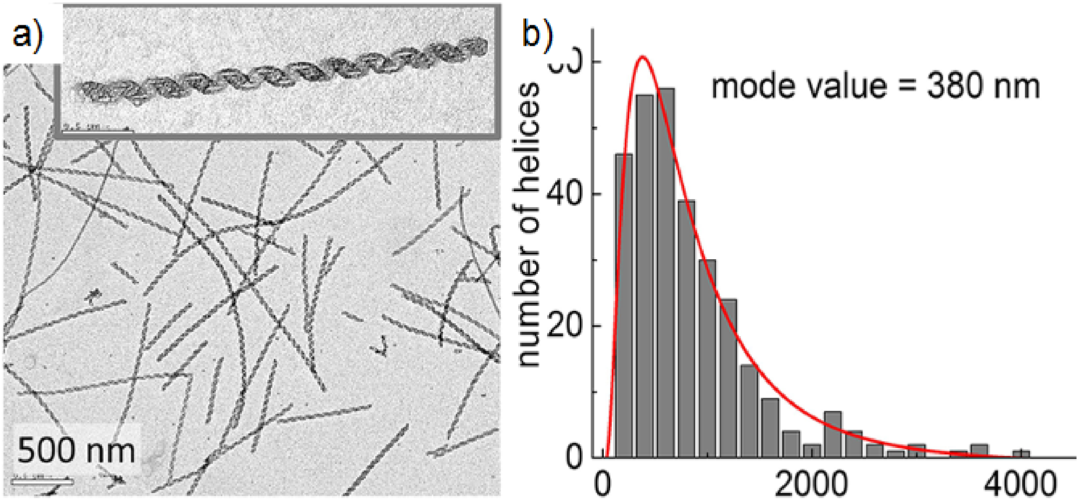

Figure 4.14: (a) TEM image of nanohelices redispersed in water after drying; 1.25mg/mL. (b): Length distribution of helices after ultrasound treatment [206].

on the appearance of individualised helices as described above also apply to freezedried helices, only the deformation in polar media did not take place. When dispersing helices in water, the pH influences dispersion behaviour. At high pH (<8), the silica surface is deprotonated and therefore negatively charged, which results in electrostatic repulsion between helices, which decreases their tendency to aggregate. At lower pH, stronger aggregation takes places because the silica surface is protonated and the repulsion does not take place.

Figure 4.15 shows TEM images of uncut and cut helices. Figure 4.14 (b) shows the lengths distribution of helices after cutting. A comparison to uncut helices is difficult, because most of them are so long that their beginning and end is usually not in the same picture on an appropriate magnification range.

Although the helices after the dispersion process are conveniently individualised, this state could not be maintained for the use of helices in cell biology experiments, because during the following functionalisation and immobilisation steps, helices reaggregate.

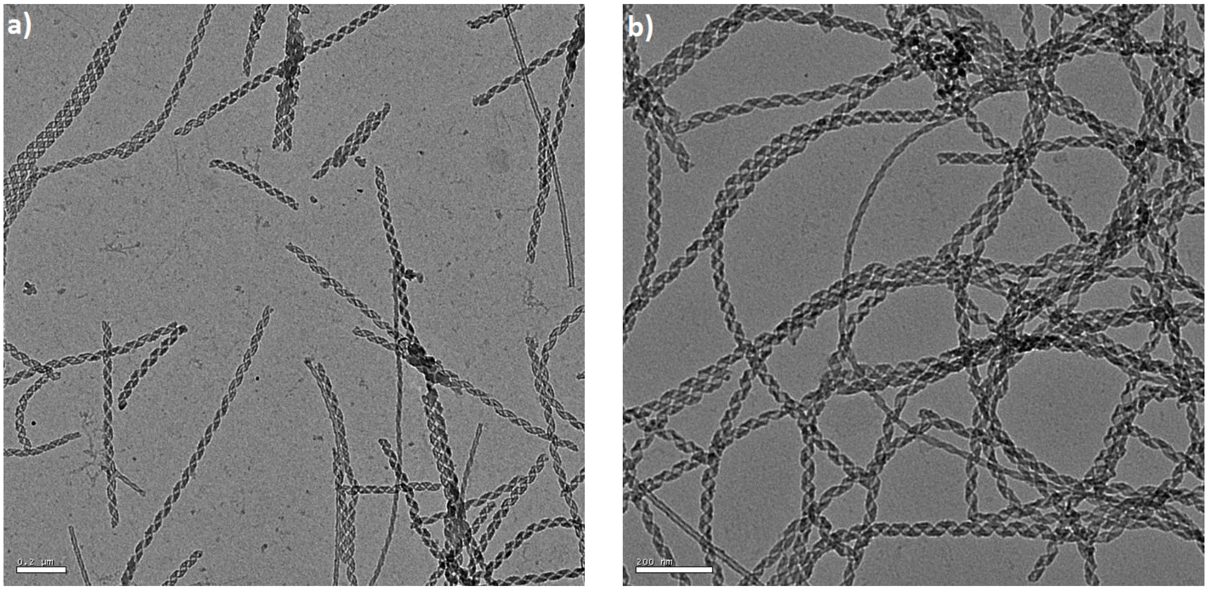

Figure 4.15: TEM images of cut and uncut silica helices.

4.1.4 Functionalisation

As shown earlier in Figures 4.3 and 4.5, the morphology of silica helices is not significantly affected by peptide functionalisation. In order to assure the correct grafting of bioactive peptides onto silica helices, fluorescence labelled peptides modified with a FITC moiety were used. UV/Vis absorption spectra of suspensions of helices with and without fluorescent peptide modification were taken. For these experiments, the base helix concentration is 2.5 mg/mL. After the reaction between SMP-functionalised helices and peptides, the washing water was kept to ensure that no more peptide could be removed from the helices by washing. FITC has an absorption maximum around 495nm. As Figures 4.16 a), c) and d) show, the suspensions with fluorescent peptide grafted helices which were washed with water all exhibit a visible absorption peak at this wavelength. (Samples needed to be diluted to avoid exceeding the operative range of the instrument.) Helix suspensions without peptides show no sign of this peak. The water which had been used to wash the helices after peptide attachment shows a decrease of this peak in the case of RGD; in the case of BMP, the peak even disappears after the first washing step. This shows that fluorescent peptide is present on the helices, and that the vast majority of the helix-bound peptide remained on the helices during the washing steps.

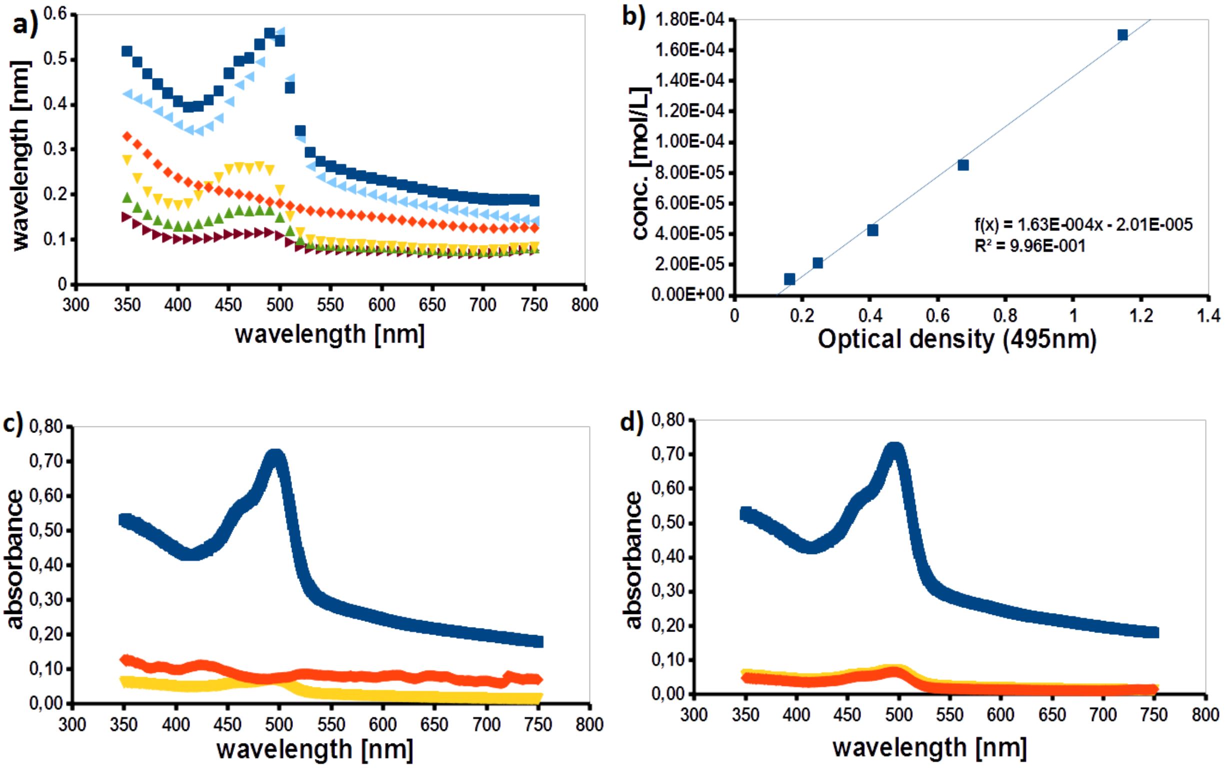

Figure 4.16: Optical density as a function of wavelength λ [nm]. a) dark blue: RGD-*L*-helices after washing with water, red: Silica helices, yellow: peptide solution that was used for peptide grafting, after the end of the reaction and removal of the helices, green and purple: Washing solutions (first and second washing step), light blue: suspension of BMP-modified *L*-helices for comparison. b) Correlation curve of fluorescent RGD-peptide concentration in water and optical density at 495 nm. c) Blue: Absorbance of BMP-modified *L*-helices, red: Absorbance of unfunctionalised *L*-helices, yellow: washing water. d) Same spectra as in c), but for *D*-helices.

Figure 4.16 a) shows that RGD- and BMP-functionalised *L*-helices exhibit the same absorbance at 495 nm, Figures 4.16 c) and d) show that the same is true when comparing left- and righthanded BMP-functionalised helices. This shows that the peptide grafting on helices does not change depending on peptide or chiral orientation.

In order to obtain quantitative results, we measured the OD of the RGD-FITC-modified helix suspension (Figure 4.16 a)) and the ODs of fluorescent RGD-peptide solutions at different concentrations (Figure 4.16, b)) at 490nm. With the latter, a regression curve to correlate OD with peptide concentration was established. By inserting the absorption of a helix suspension (250 mg/L) into the equation of the linear regression curve, we determined that its OD corresponds to that of a peptide solution at 46.5 μmol/L. Division of these two values shows that the amount of peptide on helices is 0.186 μmol per miligram of nanohelices. It is not known at this point if this is the maximal density, or if it could be further increased by changes in the reaction conditions.

In order to compare the helix densities on homogeneous materials and helix-grafted materials, the peptide quantity per miligram of helix must be converted into a value per area of a helix-grafted glass surface. One can work with the assumption that immobilised helices form a single layer on the surface, and that they are positioned side by side and aligned. This is not overly far-fetched because only the top layer of helices can be in contact with cells seeded onto them. Jiaji Cheng reported the thickness of the silica ribbons to be 3 nm [200], and we found a helix diameter of 29 nm in this study. The density of amorphous silica is 2.2 g/cm^3. If one approximates the helices as hollow cylinders, one can use the aforementioned values to calculate that 1 mm^2 of idealised helix monolayer consists of 74.4 ng of silica. Bearing in mind that the peptide density on helices is 0.186 μmol/mg and that only the peptides facing upwards are in contact with the cells, one can calculate that this corresponds to a peptide quantity of 6.9 pmol/mm^2, which is about 4.2 molecules per nm^2. This rather high value suggests that not all the peptides are covalently grafted, but random adsorption of peptides forming disordered layers has probably taken place.

4.2 Nanohelix synthesis: Discussion

We have developed a method to fragment (inorganic) silica nanohelices [206]. Freeze-drying was used to consolidate the helices prior to the process, and sonication power and choice of solvent were shown to influence the shape of the resulting nanomaterials. This proved helpful for the rest of the project as it provided a homogeneous helix suspension which is important for the preparation of helix-grafted surfaces. Homogeneous nanohelices are both better to characterise at the nanoscale (because their length is short enough to measure) and more manageable at the macroscale (because fragmented helices form more homogeneous aqueous suspensions, which makes any further operations on them easier). For the immobilisation of silica helices onto surfaces, this treatment is beneficial because cut helices are less likely to entangle, which has the potential to result in more homogeneous surfaces.

Furthermore, silica helices with different pitches were successfully synthesised by varying the enantiomeric excess of the tartaric acid which was used in the synthesis of chiral gemini surfactants. The tuning of the periodicity of gemini surfactant based organic twisted ribbons by changing the enantiomeric excess had previously been performed by Reiko Oda *et al.* [197]. The present study aimed at developing a procedure to apply this approach to silica helices while achieving a low polydispersity of period length for these materials. Three protocols were tried, and an approach where the enantiomeric excess is adjusted during the gemini tartrate synthesis rather than after it was deemed the most successful. This method yielded silica helices with low pitch polydispersity for enantiomeric excesses of at least 0.8. For *ee*=0.6, the pitch and its polydispersity both increased strongly, and for lower excesses (*ee*=0.2 and *ee*=0.0), the vast majority of nanoobjects exhibited little or no chiral features. A study by Brizard *et al.* [232] also investigates the impact of enantiomeric excess on chiral nanomaterials, but it is about organic twisted ribbons rather than inorganic helices. It was shown that these twisted ribbons also exhibit a increase in twist pitch as the enantiomeric excess changes over a range from 1.0 to 0.2. Our results show that unlike organic twisted ribbons, silica helices exhibited no periodicity for enantiomeric excesses under 0.6.

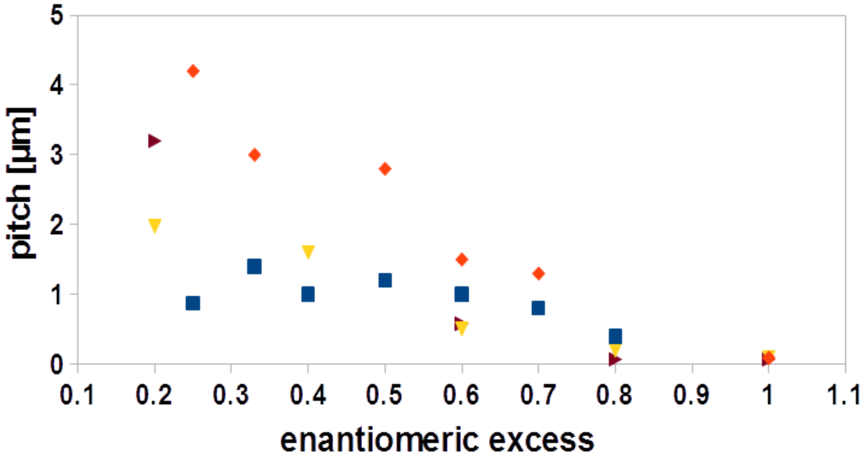

Figure 4.17: Twist pitch as a function of enantiomeric excess, for the following nanostructures: silica helices (dark triangles), organic helices (orange and yellow, measured by members of the Oda research group) and twisted ribbons after two hours of ageing (blue).

Figure 4.17 shows how the results of the present study compare to similar experiments: The development of twist pitch of silica helices resembles the observations made with organic ribbons and helices. The pitches of the present studies lie between those found in 2000 by Reiko Oda and recently by Jie Gao. The figure also shows that organic twisted ribbons with a short ageing time of only two hours exhibit a higher twist pitch for high enantiomeric excesses, but as the excess decreases, the pitch hardly increases.

In the context of the application of silica nanohelices for cell culture experiments, this technique is very practical because it provides an easy way of tuning the periodicity of nanohelices, which makes it possible to explore the effect of this parameter on cell behaviour. Finally, the results show that the morphology of helices does not change upon peptide modification. This is important for cell culture experiments because when the surface chemistry of nanomaterials is altered, other properties like helix morphology should not change.

The quantification of peptide on helices has shown that adsorption is very likely to have taken place because of the elevated peptide density.

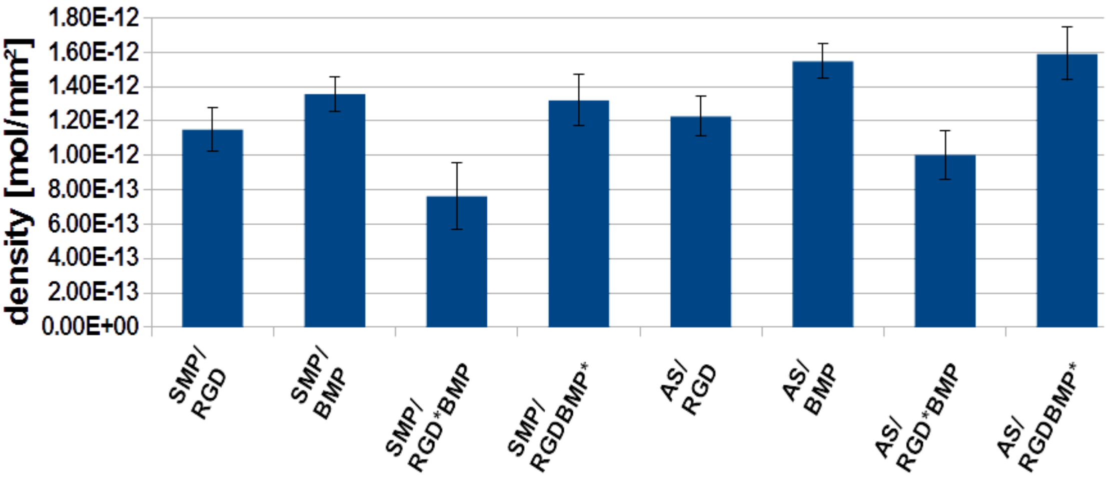

Figure 4.18: Densities of surface grafted peptides in pmol/mm^2, for all linker/peptide combinations. Images taken at 1500ms exposition time.

4.3 Physicochemical Characterisation

4.3.1 Peptide grafting onto glass surfaces

The purpose of the fabrication of homogeneous peptide-grafted materials is to provide a reference to compare to cell behaviour on peptide functionalised helices. In order to validate the grafting of peptides onto the glass substrates, two techniques were used: Firstly fluorescence microscopy using fluorescent-labelled peptides to quantify the density of grafted peptides on glass surfaces, and secondly XPS to provide information on elemental composition and chemical bonding states of materials.

Fluorescence microscopy

The grafting of RGD- or/and BMP-peptide onto glass surfaces was monitored through fluorescence microscopy. Substrates modified with FITC-functionalised peptide(s) prepared according to the procedure described in the last chapter were observed at 650ms and 1500ms exposition time. Both linkers (SMP and AS) are compared (Fig. 4.18). The fluorescence per surface unit is measured for surfaces functionalised with RGD, BMP and both peptides, only one of them bearing the FITC moiety. In the following, the fluorescent species in binary peptide substrates is labelled with

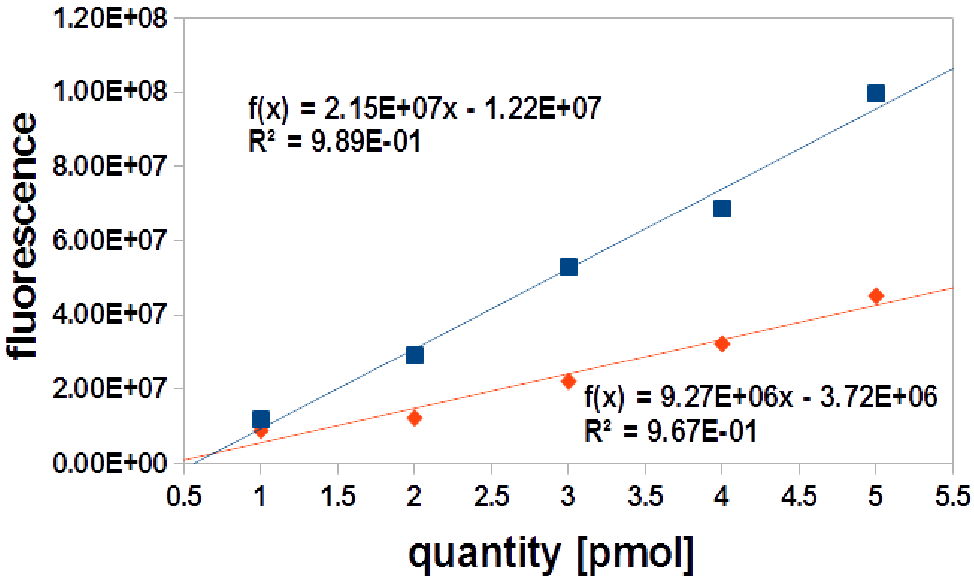

Figure 4.19: Standard curves for RGD (blue) and BMP (orange), showing the fluorescence (a.u.) of known quantities of peptide (in pmol).

	RGD	BMP	RGD*BMP	RGDBMP*
SMP [pmol/mm^2]	1.2 ± 0.12	1.4 ± 0.10	0.7 ± 0.19	1.3 ± 0.15
AS [pmol/mm^2]	1.2 ± 0.12	1.5 ± 0.10	1.0 ± 0.14	1.5 ± 0.15
SMP [/mm^2]	$6.9 \cdot 10^{11} \pm 0.7 \cdot 10^{11}$	$8.1 \cdot 10^{11} \pm 0.6 \cdot 10^{11}$	$4.6 \cdot 10^{11} \pm 1.2 \cdot 10^{11}$	$8.0 \cdot 10^{11} \pm 0.9 \cdot 10^{11}$
AS [/mm^2]	$7.4 \cdot 10^{11} \pm 0.7 \cdot 10^{11}$	$9.3 \cdot 10^{11} \pm 0.6 \cdot 10^{11}$	$6.0 \cdot 10^{11} \pm 0.8 \cdot 10^{11}$	$9.6 \cdot 10^{11} \pm 0.9 \cdot 10^{11}$

Table 4.2: Densities of surface grafted peptides in pmol/mm^2 and molecules per mm^2, for all linker/peptide combinations. If two peptides are grafted together, an asterisk indicates which one is fluorescence-labelled.

an asterisk behind it, i.e. RGD*BMP or RGDBMP*. For example, RGD*BMP means that the peptides RGD and BMP were grafted together, but only RGD is FITC-modified. The measured fluorescence levels are converted into peptide densities as described in the materials and methods chapter (Figure 4.19).

The results of these experiments are displayed in Figure 4.18. All average fluorescences of peptide grafted materials were significantly higher than the background fluorescence of glass, which indicates that the peptide immobilisation did indeed take place.

The calculated densities for RGD-only and BMP-only surfaces were above 1 pmol/mm^2 for both linkers, the values for BMP being higher than those for RGD (Table 4.2). For all peptides, the

samples with the linker AS showed slightly higher fluorescence than the same peptide(s) grafted with SMP, which indicates that AS might permit grafting at a higher yield.
The samples with RGD and BMP grafted together exhibit the same tendency in all cases: Binary samples with fluorescent RGD exhibit a slightly lower fluorescence than surfaces featuring only RGD, whereas binary samples where BMP is the fluorescent species are closer to the corresponding substrate where BMP is the only peptide.

Variation of the exposure time between 650ms and 1500ms does not have an impact on the observed trends, but it can change the signal-to-noise ratio. 1500ms was chosen as exposition time for the results presented in this section because it permitted the highest signal-to-noise ratio without incurring saturation.
Fluorescence images (Figure 4.20) of peptide-grafted materials show that the distribution of peptides is homogeneous at the length scale that is relevant for cell culture experiments.

XPS

The purpose of the XPS examination of peptide-functionalised materials is to confirm the grafting of organic matter on the surfaces, and to compare the composition of the functionalised materials to the chemical composition of the grafted peptides. Four spots on one material of each type were measured using XPS to identify the atomic composition using peak areas. The experiment was carried out with all intermediates of the pepide grafting process (Figure 3.10), and using both available linkers (SMP and AS, cf. Fig. 3.5 on page 73). The materials are cleaned glass (MV), APTES-functionalised glass (APTES), SMP-functionalised glass (SMP), succinic anhydride functionalised glass (AS), RGD or BMP grafted via SMP (SMP/RGD and SMP/BMP) and the same peptides, grafted via succinic anhydride (AS/RGD and AS/BMP)(peptide structural formulae cf. Fig. 3.4, page 72). For six elements, the average atomic percentages obtained by XPS are as shown in Table 4.3:

Sodium, silicon and oxygen are among the usual constituents of Borosilicate glass, the latter

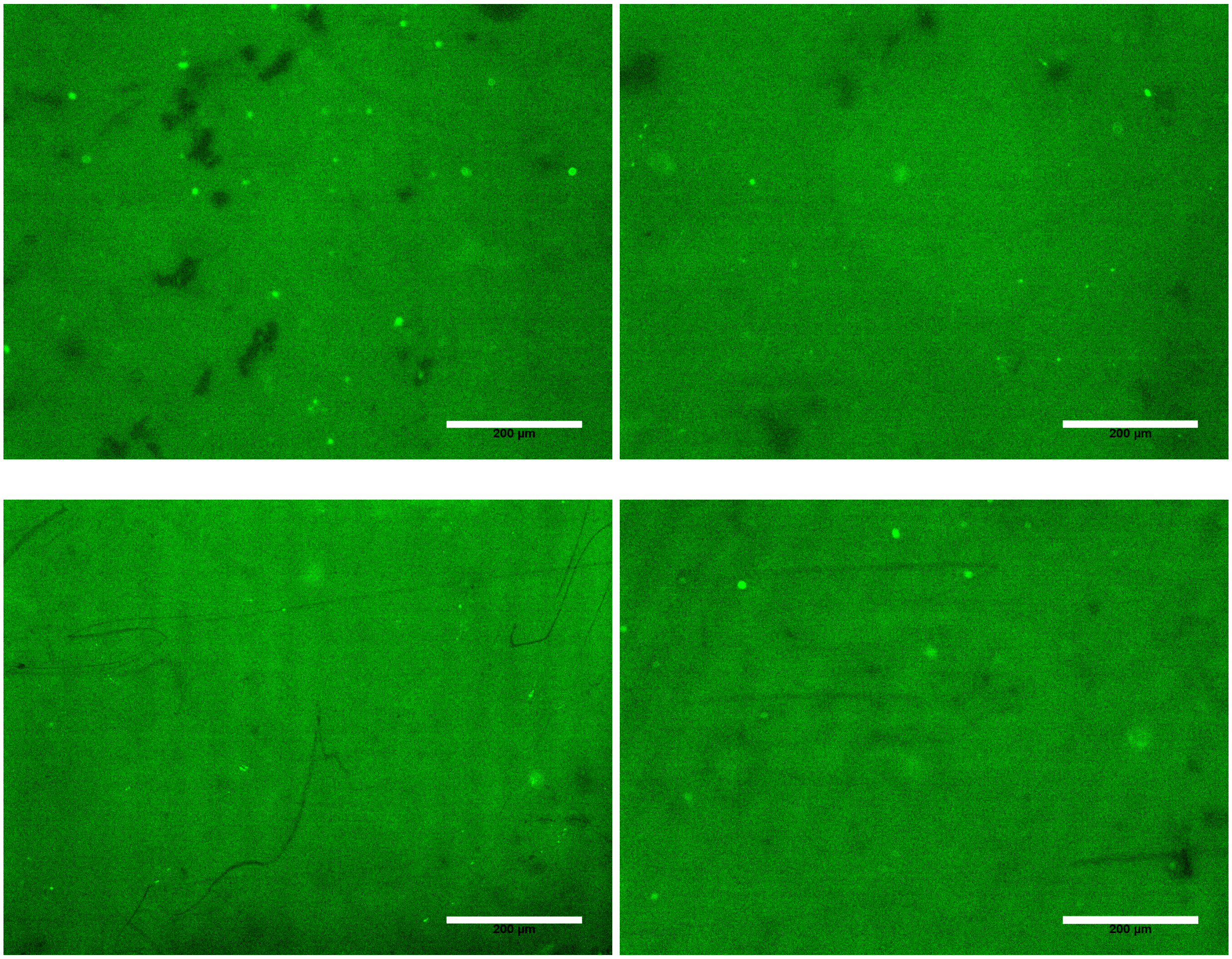

Figure 4.20: Fluorescence images of FITC-modified RGD (left) and BMP (right) grafted onto glass surfaces using SMP (top) and AS (bottom) as crosslinker; 650 ms exposition time. The distribution of fluorescence is sufficiently homogeneous. White bars respresent 200μm.

	MV	APTES	SMP	AS	SMP/RGD	SMP/BMP	AS/RGD	AS/BMP
C	7.9	39.1	26.4	41.7	20.0	22.5	38.9	47.4
N	0.3	3.3	3.3	6.3	2.3	3.2	5.7	7.8
Na	0.6	0.2	0.3	0.1	0.2	0.2	0.0	0.0
O	58.0	32.9	42.1	30.2	48.9	46.6	35.5	28.7
S	0.1	0.4	0.0	0.0	0.0	0.0	0.4	0.2
Si	33.1	24.1	27.9	21.7	28.6	27.5	19.5	15.9

Table 4.3: XPS atomic percentages of carbon, nitrogen, sodium, oxygen, sulphur and silicon in different materials.

	MV	APTES	SMP	AS	SMP/RGD	SMP/BMP	AS/RGD	AS/BMP
C	-	64	61	61	58	64	57	64
O	-	18	26	28	23	19	23	19
N	-	9	9	5	17	16	17	15
Si	-	9	4	6	1	0	2	1
S	-	-	-	-	1	1	1	1

Table 4.4: Calculated atomic fractions (in percent) of carbon, oxygen, nitrogen, silicon and sulphur at different states of functionalisation, assuming 100 % yield. The percentages were obtained by counting the atoms of different elements of the grafted moieties at all stages of the functionalisation process.

two of them are also parts of the molecules bound to the surface. The relative abundance of these three elements thus does not provide direct information about the presence of grafted compounds, but as the XPS method only analyses the specimen's surface with a limited penetration depth, a decreasing quantity of these elements might suggest an increasingly thick layer of other compounds on the glass.

When glass substrates come into contact with air, they will immediately adsorb contaminants [233] which appear in the results as unintended occurrence of oxidised and unoxidised carbon. As Table 4.3 shows, a bare glass surface exhibits a carbon content of 7.9 at.%. Here this pollution was minimised by storing the specimens under vacuum (5.3 mPa) whenever possible prior to the experiment, but it could not be removed entirely (cf. Landoulsi *et al.*, [233]). The interpretation of these results is greatly facilitated by comparing the obtained data with the atomic compositions of the surface-bound moieties. These theoretical percentages are calculated by assuming an idealised yield of 100% for all coupling reactions. Carbon, oxygen, nitrogen, silicon and sulphur are of interest for this comparison. As the actual yields of the grafting reactions may be less than quantitative, the changes in atomic percentages in the course of the grafting process are likely to be smaller than expected. By counting the atoms in the surface-bound compounds, one obtains Table 4.4:

It needs to be noted that these values do not represent absolute quantities. The bare glass reference surface features 7.9% of carbon, which can be attributed to the pollution which inevitably occurs when glass samples are exposed to air. The carbon percentage rises to 39.1% after APTES treatment due to the C-chain of the Silane. The expected value was 64%. For all following functionalisation steps involving AS, the carbon percentage remains on a level close the one of APTES, which is in agreement with the calculated values (Table 4.4). However, the carbon content in SMP-modified materials (with and without peptide) is much lower, namely between 20% and 30%. This result is unexpected, as a decrease in carbon content to this extent following SMP functionalisation cannot be explained by low yield. The carbon content remained roughly the same on AS materials (i.e. 42%at.), which was not expected either. Following the APTES functionalisation, the relative nitrogen content increases by a factor of 11, from 0.3% (MV) to 3.3% (APTES), as expected due to the amine group (-NH_2) in APTES: A theoretical nitrogen percentage of 9% had been calculated. After the linker introduction, the nitrogen percentage ought to remain the same (9%) for SMP and decrease to 6% for AS. The value for SMP remains at 3.3% as it was for APTES. This percentage is less than theoretically calculated, but the tendency is in agreement with the theory. The percentage for AS increases to 6.3% for unknown reasons. This value is very close to the calculated value of 6%, but the nitrogen percentage was expected to decrease rather than increase after AS-modification. For AS-bound peptides, the nitrogen content is higher than for those bound via SMP, which again might indicate a lower yield for SMP. Moreover, the N content for BMP materials is higher than for the RGD-materials with the same linker, although they were expected to be 16-17% for both peptides.

Overall, the nitrogen percentages on all peptide-grafted materials are lower than predicted, but this discrepancy can be explained with the presence of carbon contaminations as outlined above, and a yield of less than 100% for the peptide grafting step, which results in a smaller quantity of nitrogen on the surface. Sulphur can be found on MV- and APTES-samples (0.1% and 0.4%). This might be the case due to the cleaning procedure of glass slides prior to functionalisation, which involves Piranha treatment (cf. Materials and Methods). Therefore, residues of sulphuric acid may leave traces of sulphur on the samples after washing processes. The contamination disappears after crosslinker introduction. Samples with RGD and BMP bound using AS exhibited a sulphur content of 0.4% and 0.2%, and no sulphur could be detected for peptides grafted via SMP. This

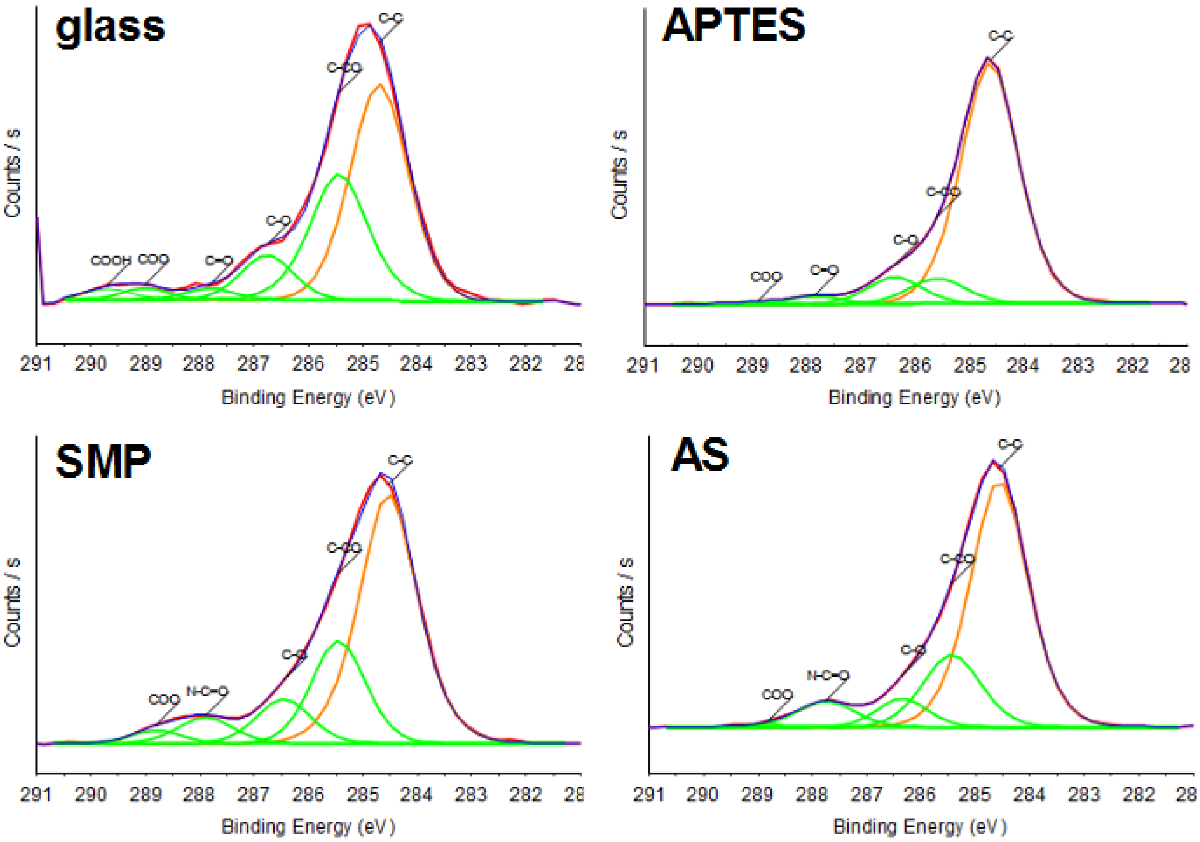

Figure 4.21: XPS C1s high-resolution spectra of bare glass, APTES, SMP, and AS-modified materials.

might mean that the peptide grafting yield with AS binding is higher than for SMP, which matches the observation that higher nitrogen contents were observed for AS than for SMP. As the atomic percentage of sulphur on peptide-modified samples was expected to be lower than 2% (cf. Figure 4.4), the low sulphur content does not mean that the peptide grafting was unsuccessful.

In order to gain further insight into the chemical situation on the materials surface, one out of the four examined spots per specimen was selected and its C1s and N1s XPS spectrum was fitted to identify their components. The C1s spectrum was split up into components that are attributed to C/O or C/N bondings which cause slight changes in the energy at which they appear in the spectrum (Figures 4.21 and 4.22). They are fitted so that the sum of all partial peaks matches the shape of the peak that was experimentally obtained. The same fitting procedure was carried out with the N1s spectrum (Figures 4.23 and 4.24). In the case of nitrogen peak fitting, the components

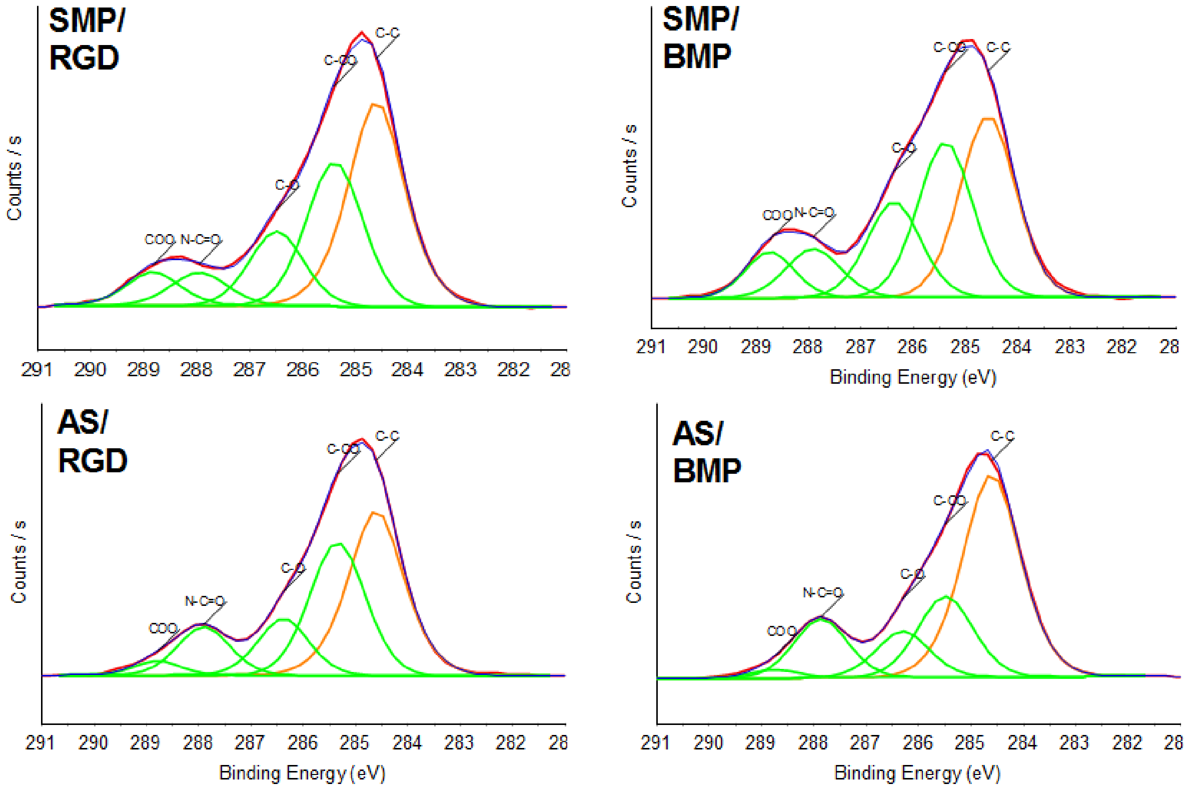

Figure 4.22: XPS C1s high-resolution spectra of materials modified with SMP/RGD, SMP/BMP, AS/RGD and AS/BMP.

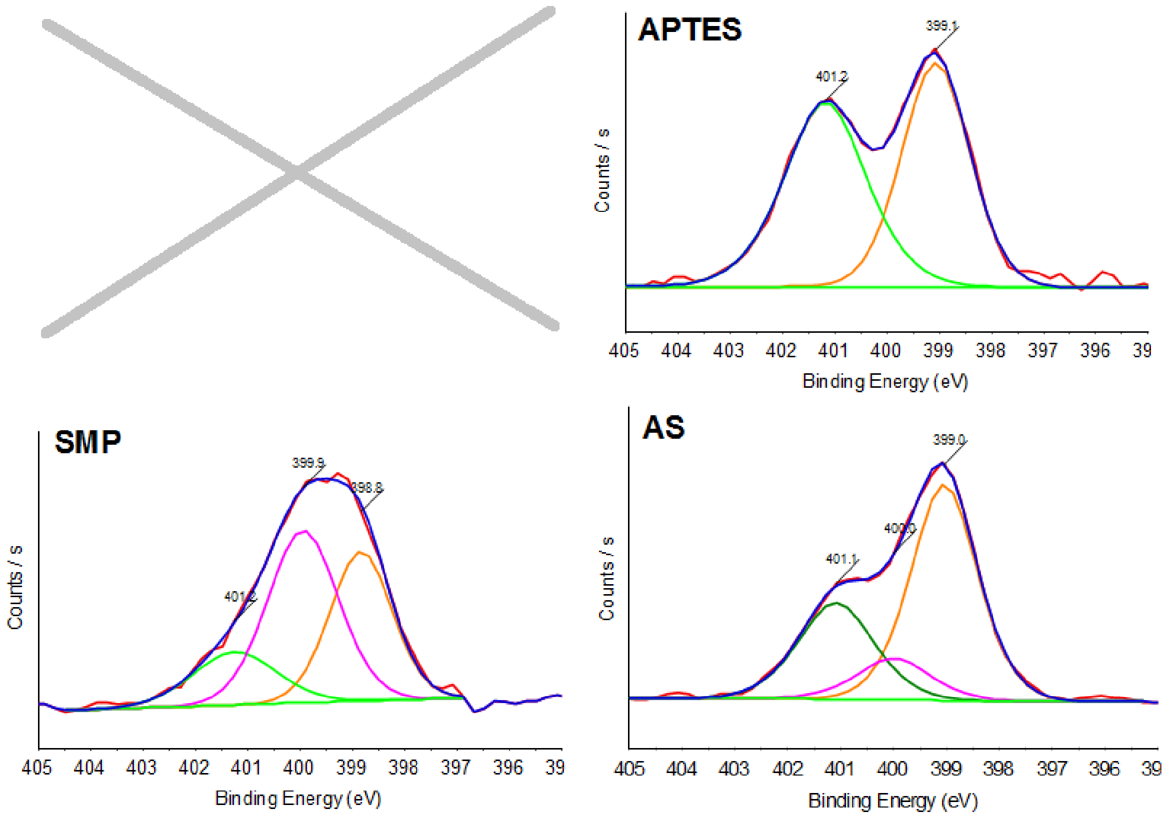

Figure 4.23: XPS N1s high-resolution spectra of APTES, SMP, and AS-modified materials. Due to the low amount of nitrogen atoms on bare glass, the procedure was not performed for this sample.

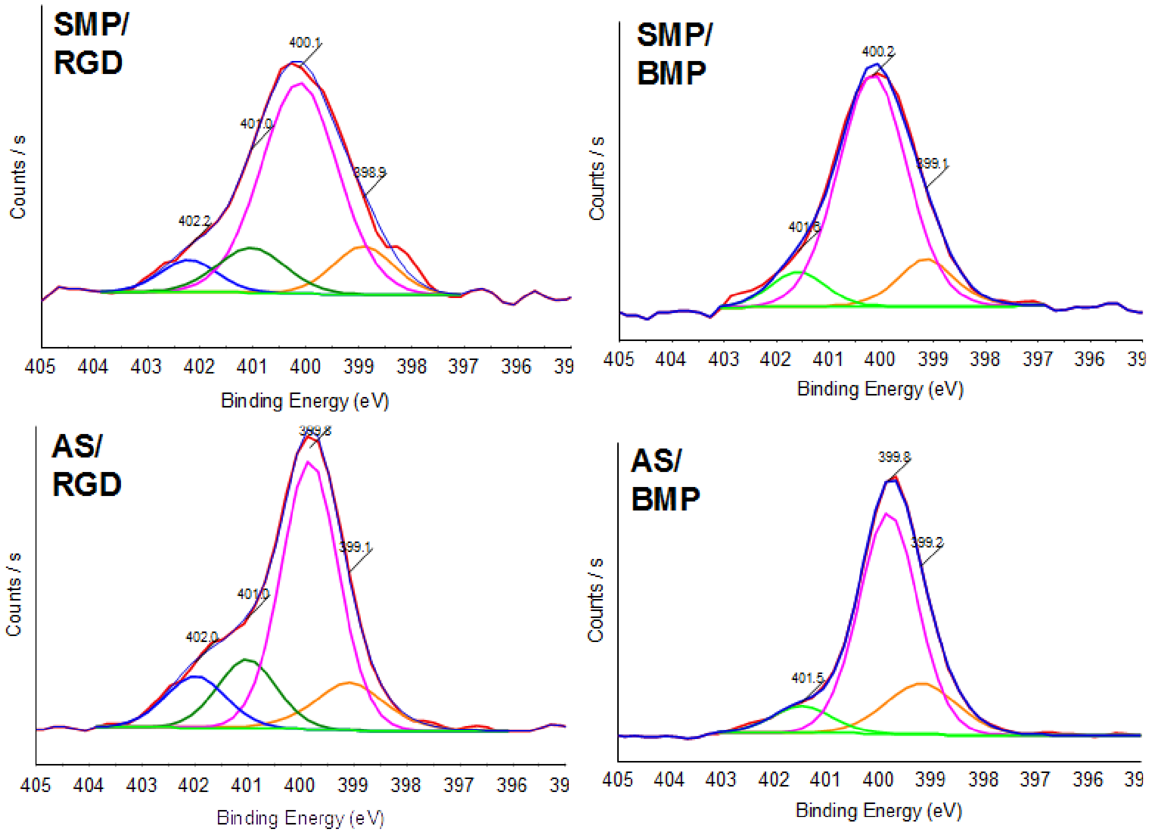

Figure 4.24: XPS N1s high-resolution spectra of materials modified with SMP/RGD, SMP/BMP, AS/RGD and AS/BMP.

	MV	APTES	SMP	AS	SMP/RGD	SMP/BMP	AS/RGD	AS/BMP
C-C	53	80	60	67	43	35	41	53
C-CO	31	8	22	19	31	30	32	20
C-O	10	8	9	7	14	18	13	11
C=O	2	3	0	0	0	0	0	0
N-C=O	0	0	6	7	6	9	11	14
COOR	2	1	3	0	6	8	3	2
COOH	2	0	0	0	0	0	0	0

Table 4.5: Percentages of different carbon peak components obtained by fitting C1s spectra for each sample. The lines represent different functional groups / chemical environments of carbon atoms.

	MV	APTES	SMP	AS	SMP/RGD	SMP/BMP	AS/RGD	AS/BMP
C-C	-	67	20	29	25	40	26	41
C-CO		33	50	43	41	31	39	30
C-O	-	-	-	-	7	6	8	7
C=O	-	-	-	-	-	-	-	-
N-C=O	-	-	30	14	22	21	19	19
COOR	-	-	-	-	-	-	-	-
COOH	-	-	-	14	5	2	8	3

Table 4.6: Expected relative distribution of chemical environments of carbon atoms according to the molecular structures of grafted moieties.

are assigned as follows (Table 4.7, from low to high binding energy): N bound to carbon (C-N, 399 eV), N bound to Carbon and an electron-drawing group (C-N=O, 400 eV), protonated N (N$^+$, 401 eV) and N in an electron-drawing environment (N$^+*$, 402 eV). The assignments are based on considerations by Iucci, who assigned the 400eV peak to unprotonated amine groups in peptides [234].

The proportions of components resulting from the C1s fittings are shown in Table 4.5. Carbon atoms bearing amine groups (C-NH$_2$) appear in XPS spectra in the same region as those vicinal to

	BE	APTES	SMP	AS	SMP/RGD	SMP/BMP	AS/RGD	AS/BMP
C-N	399 eV	50	36	58	12	13	13	20
C-N=O	400 eV	0	47	13	67	77	59	71
N$^+$	401 eV	50	17	29	13	10	16	9
N$^+*$	402 eV	-	-	-	8	-	12	0

Table 4.7: Percentages of different nitrogen components obtained by fitting N1s spectra for each sample, BE stands for binding energy.

a C-atom with an O-substituent, thus they can be found in the peaks labelled as ”C-CO”.

Amide and alcohol moieties (-N-C=O and C-OH) are of interest here because they appear at specific stages of the functionalisation process. In theory, amide groups (-N-C=O) should appear after the introduction of the crosslinkers, and alcohol groups (-CH_2-OH) are expected to occur after peptide grafting (cf. Table 4.6). Amide groups behave as predicted, whereas C-OH moieties seem to exist on all examined surface types. However, they are more abundant on peptide-grafted materials compared to substrates without peptide. The behaviour of -N-C=O groups suggests that the binding of the linkers did take place, and the increase of C-O groups provides some evidence of successful peptide grafting. In the case of peptides grafted via AS, a further increase of -N-C=O-groups after peptide grafting suggests that at least with this linker, peptide grafting was successful.

The most common environments for carbon atoms according to the experimental results are C-C and C-CO, i.e. first neighbours of C-O bonds. The C-C component increases in intensity from 4.2 at.% (MV) to 31.3 at.% (APTES), suggesting the successful establishment of the self-assembled layer. According to the molecular structures, C-C should be much more abundant on APTES samples than on peptide materials (which is the case), and the amounts of C-C and C-CO should be more similar for the peptide grafted materials (which is mostly the case). The C-CO-peak increases in size after the crosslinker reactions (5.8 at.% for SMP and 7.9 at.% for AS opposed to 3.1 at.% for APTES) due to the higher number of O-substituted carbon atoms.

Several functional groups, like esters (COOR), do not occur in the calculated values, but did appear in the experimental results, their percentages being higher for SMP-grafted materials than for those with AS. The reason for this might be carbon contamination and the increasing complexity of the grafted entities, e.g. carbon atoms can have more than one oxygen-containing substituent: This could make carbon atoms appear in the spectrum at higher binding energies.

Surprisingly, the nitrogen signal for APTES (Figure 4.23) consists of two components of similar area, one at 399.1 eV assigned to -NH_2 bondings, the other at 401.2 eV. A possible reason for this can be found in previous studies [235], [236]: By bending the C-chains of APTES, its amine groups (-NH_2) can come into contact with the glass surface, which does not result in covalent bonds, but gives rise to a component at higher binding energy. Alternatively, the nitrogen peak might be split due to the -NH_2 groups being protonated or not [234]. Either way, this situation might reduce the availability of amine groups for linker molecules and therefore decrease the yield of the following reactions. The split of the N1s peak becomes less visible when linkers and peptides are introduced 4.24. After introduction of the peptides, the relative proportion of the C-N component decreases strongly compared to all other samples (Fig. 4.7), whereas the C-N=O component at around 400 eV rises. This shows that peptides are covalently bound to the surface.

Interestingly, only samples with RGD-peptide feature a component at 402 eV (Fig. 4.24). This shows the presence of a strongly oxidised nitrogen moiety, possibly the arginine side chain of the RGD-peptide. BMP also contains arginine, but as BMP consists of more amino acids than RGD, its relative proportion is low. If these considerations are correct, this 402 eV N1s component provides strong evidence of the presence of RGD.

ToF-SIMS

Four samples were selected for ToF-SIMS examination: One bare, cleaned glass surface, one modified with APTES and one functionalised with each peptide, RGD and BMP, both using SMP as linker. The ToF-SIMS data of these samples are shown in Tables 4.8 and 4.9.

On all surfaces, secondary ion signatures which are characteristic of polydimethylsiloxane (PDMS) can be found. This polymer is part of none of the chemicals used in the materials preparation process, but its presence in vacuum grease and its ability to spread over surfaces make it a well-known contaminant in ToF-SIMS experiments. The $(SiO)_X$OH-anion, which is typical for glassy surfaces, also appeared on all surfaces. For unknown reasons, peaks that match the antioxidant Irgafos 168 and lauryl sulfate - probably originating from contaminants - were found on the APTES sample. The identification of lauryl sulfate on the APTES-material is equally unexpected.

		Mass (u)	MVd	APTES	S/R	S/B
elements						
	Na+	23.0	760.8	60.6	367.8	624.4
	Mg+	24.0	1.8	0.4	0.7	2.1
	Al+	27.0	1.4	0.5	1.0	2.7
	Si+	28.0	67.8	64.3	49.6	51.9
	K+	39.0	13.5	1.0	43.5	8.0
	Ca+	40.0	0.5	0.6	1.9	3.4
	Cr+	51.9	0.1	0.9	0.5	0.2
	Fe+	55.9	0.6	0.2	0.5	0.6
	Ni+	57.9	0.1	0.1	0.0	0.0
	Cu+	62.9	0.3	0.5	0.9	2.3
	Sn+	119.9	0.2	0.3	0.5	1.0
amino acids						
Glycine	CH4N+	30.0	25.4	61.2	22.6	58.8
Alanine	C2H6N+	44.1	27.3	19.9	15.3	82.6
Serine	C2H6NO+	60.0	nd	nd	3.7	25.9
Proline	C4H8N+	70.1	11.3	9.4	17.2	115.1
Valine	C4H10N+	72.1	42.8	27.5	9.9	45.7
(Iso)leucine	C5H12N+	86.1	6.7	1.3	2.5	47.4
Lysine	C5H13N2+	101.1	1.7	nd	nd	nd
Glutamic acid	C4H8NO2+	102.1	nd	nd	nd	1.8
Methionine	C4H10NS+	104.1	2.1	1.9	nd	nd
Phenylalanine	C8H10N+	120.1	3.2	1.3	3.3	3.0
Tyrosine	C8H10NO+	136.1	0.7	nd	1.3	6.8
Polysiloxane	Si2C5H15O+	147.1	597.9	814.3	524.5	482.6

Table 4.8: Normalised intensities of selected fragments in the ToF-SIMS spectra; cationic species. The examined samples are MVd (cleaned bare glass), APTES, S/R (RGD-peptide grafted using SMP) and S/B (BMP-peptide grafted using SMP).

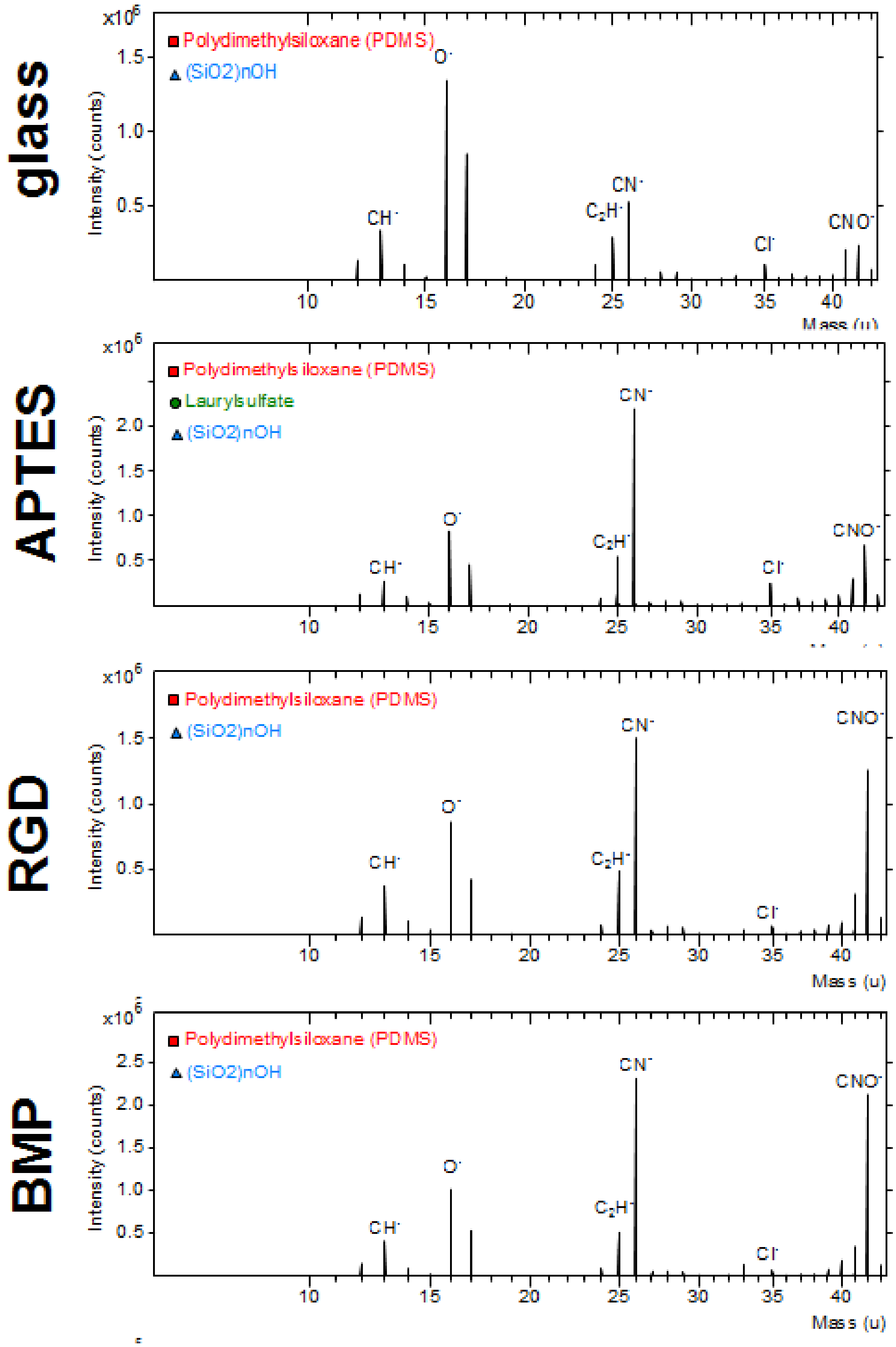

Figure 4.25: Extracts from the ToF-SIMS mass spectra displaying fragments with low molecular weight.

		Mass (u)	MVd	APTES	S/R	S/B
elements	C-	12.0	58.1	43.7	45.7	48.0
	O-	16.0	506.3	281.6	288.5	343.3
	S-	32.0	8.7	2.1	1.8	4.2
N-containing	CN-	26.0	247.4	814.2	570.5	765.2
signals	CNO-	42.0	128.3	310.2	832.8	563.4
	NO2-	46.0	4.3	28.7	12.2	12.2
	NO3-	62.0	5.1	69.5	32.1	54.9
Sulphates	SO3-	80.0	475.5	216.7	64.7	122.5
	HSO4-	97.0	660.4	460.2	75.1	46.6
(SiO2)xOH	SiHO3-	77.0	199.6	157.1	78.1	107.9
	Si2O5H-	136.9	115.9	78.5	40.8	67.6
	Si3O7H-	196.9	55.6	37.2	21.9	37.2

Table 4.9: Normalised intensities of selected fragments in the ToF-SIMS spectra; anionic species. The examined samples are MVd (cleaned bare glass), APTES, S/R (RGD-peptide grafted using SMP) and S/B (BMP-peptide grafted using SMP).

Some peaks at low molecular weight (Figure 4.25) are of interest to the verification of peptide grafting because the corresponding fragments contain both carbon and nitrogen. It is useful to use the peaks of $(SiO)_X OH$ as a reference to compare their height, because this fragment is related to glass and should therefore appear in similar quantities on all materials. Amongst the anions, the species CN^- and CNO^- exhibit a higher (absolute) intensity for APTES, RGD and BMP than for bare glass. At the same time, the (absolute) intensities of $(SiO)_X OH$-related peaks is lower for APTES, RGD and BMP than for bare glass. However, this trend cannot be observed for the anionic organic nitrogen-free fragments C_2H^- and CH^-, maybe because they are partly due to PDMS or other organic contaminations which are present on all samples. Interestingly, the CN^- and CNO^--peaks are of similar size on peptide-grafted samples, whereas CN^- is much higher than CNO^- for APTES.

On a different note, sulphate peaks (SO_3^- and HSO_4^-) appear with the highest intensity on bare glass, and their size decreases for APTES and even further for peptide grafted materials. Their existence can be ascribed to the cleaning of the glass slides with sulphuric acid prior to functionalisation.

The observations so far match what one would expect in view of the molecular structures of the grafted moieties, but the normalised intensities (Tables 4.8 and 4.9) reveal additional information: The intensities of nitrogen-containing signals confirm what was said above, because the number of -CN-groups increases after introduction of APTES, and -CNO-groups appear after pepide functionalisation. On the cationic side, certain organic species are typical for a given amino acid, but their specificity varies between the fragments. Contrary to our expectations, some amino acids appear to occur on bare glass more frequently than on the RGD-grafted sample. In addition to that, the amino acids found on the RGD-grafted specimen do not match the sequence of this peptide. The amino acid signal intensities for BMP are higher than those of RGD as expected due to the higher length of BMP. The detection of glycine on the APTES sample might be explained with its similarity to the molecular structure of APTES.

In view of the conflicting conclusions from the cationic and the anionic spectrum, it is difficult to decide which one is more reliable: Normally, the amino acid related fragments are considered more reliable than small nitrogen-containing species because of their higher complexity and thus specificity, but some amino acid fragments are known to be not very specific either. For example, the fragments of Glycine and Alanine are formed by many nitrogen-containing compounds.

The presence of PDMS can be problematic if a siloxane layer covers other compounds and makes them invisible to ToF-SIMS.

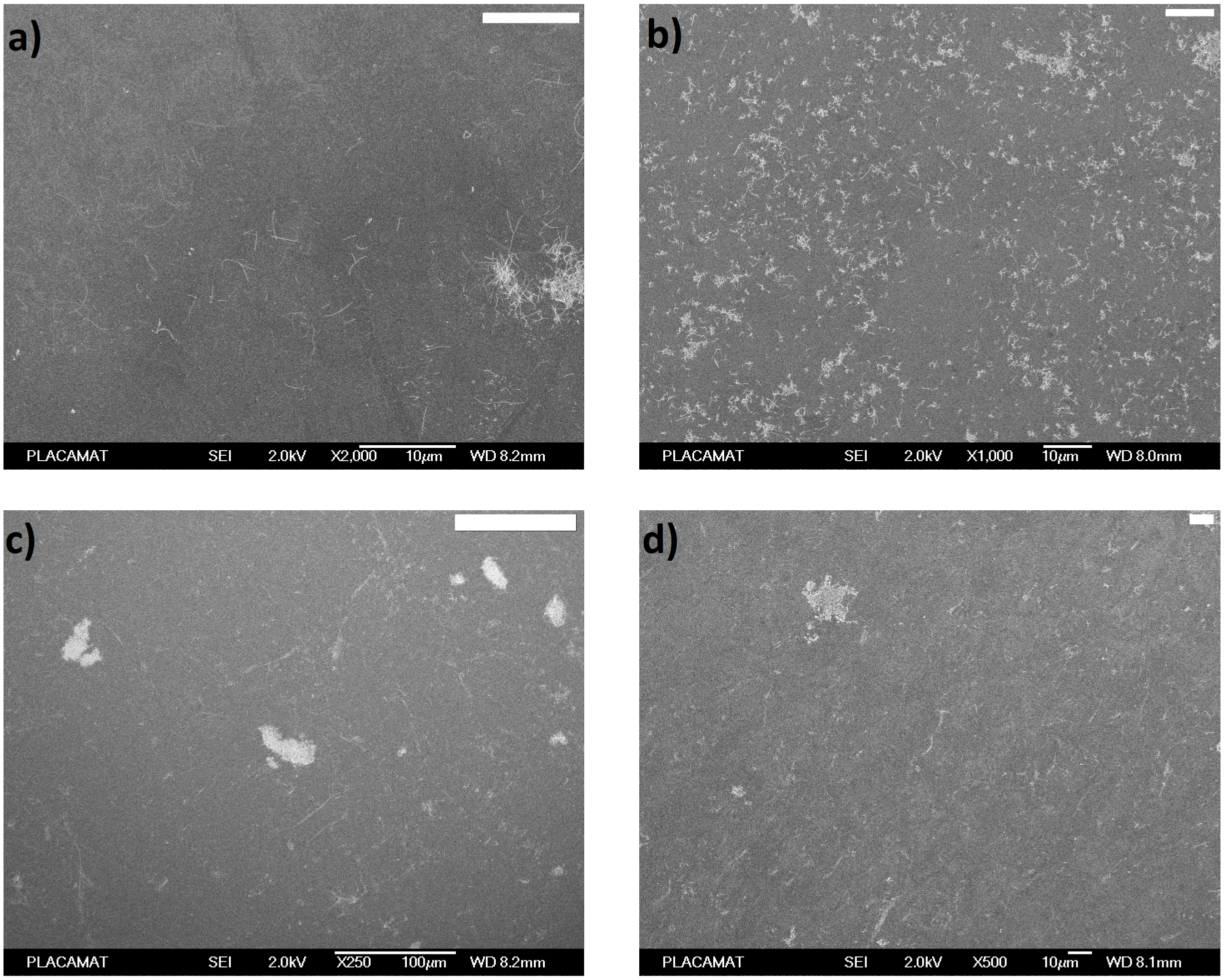

Figure 4.26: SEM images of peptide-modified surface-grafted silica helices: a) Cut and grafted once for one day; b) cut and grafted three times for one, three and three days; c) uncut and grafted once for one day; d) uncut and grafted three times for one, three and three days. White scaling bars represent 10μm (a,b and d) and 100 μm (c).

4.3.2 Helix surfaces

After grafting of silica helices onto glass surfaces, the degree of surface coverage was estimated using SEM images. The images obtained by this method also permitted the evaluation of helix morphology after their immobilisation onto surfaces. A suitable helix grafting time was found by comparing the outcomes of different grafting procedures:

Figure 4.26 shows the quantity of helices on the surface, visible in white. The results show that the surface coverage after one single 24h-grafting step is very low, both for cut and uncut helices (a and c). The amount of immobilised helices could be increased by adding helix suspension to

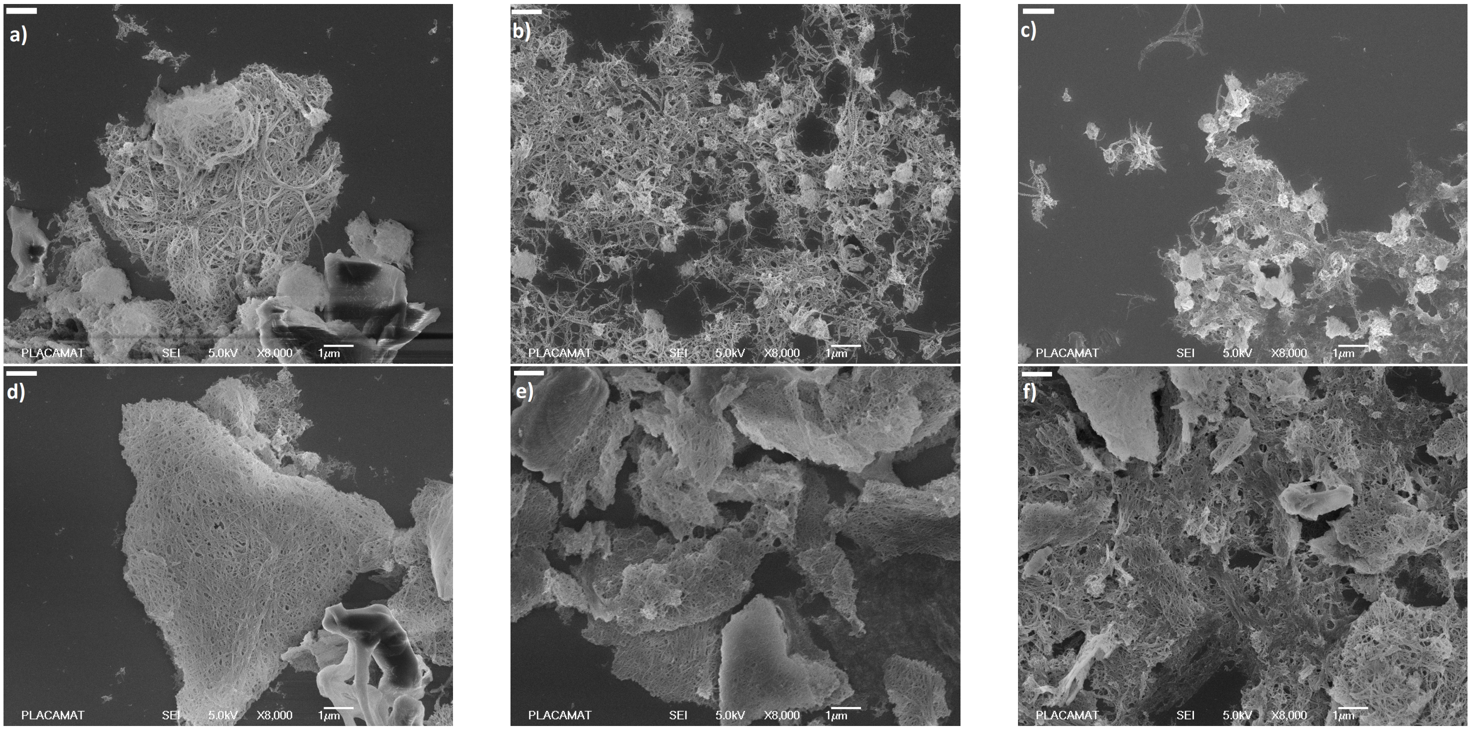

Figure 4.27: SEM images of surface-grafted helices, 8000x magnification, *L*- and *D*-helices with and without peptide functionalisation: a) *L* without peptide, b) *L* with RGD, c) *L* with BMP, d) *D* without peptide, e) *D* with RGD, f) *D* with BMP. The scaling bars in the top left corners represent 1μm.

the prepared substrates three times, the reaction time being one day for the first addition and three days for the second and third (b and d). This approach increased the surface coverage for uncut helices, but the amount of helices on the surfaces remained low. Therefore, the number of grafting steps was increased to five, each one lasting 24 hours. SEM images of the surfaces obtained by this method are shown in images 4.27 and 4.28.

Figure 4.29, which shows a surface-grafted nanohelix at high magnification, shows that after their immobilisation to glass surfaces, the helices still exhibit a nanoperiodic morphology. The helices thus still possess the collagen-mimicking geometrical property which is required for their use in cell culture experiments. SEM images of immobilised helices on the surfaces (Figures 4.27 and 4.28) show that the nanomaterials are not evenly distributed, but tend to form islands of high helix density, whereas other regions are scarcely covered. Apart from these islands, large round

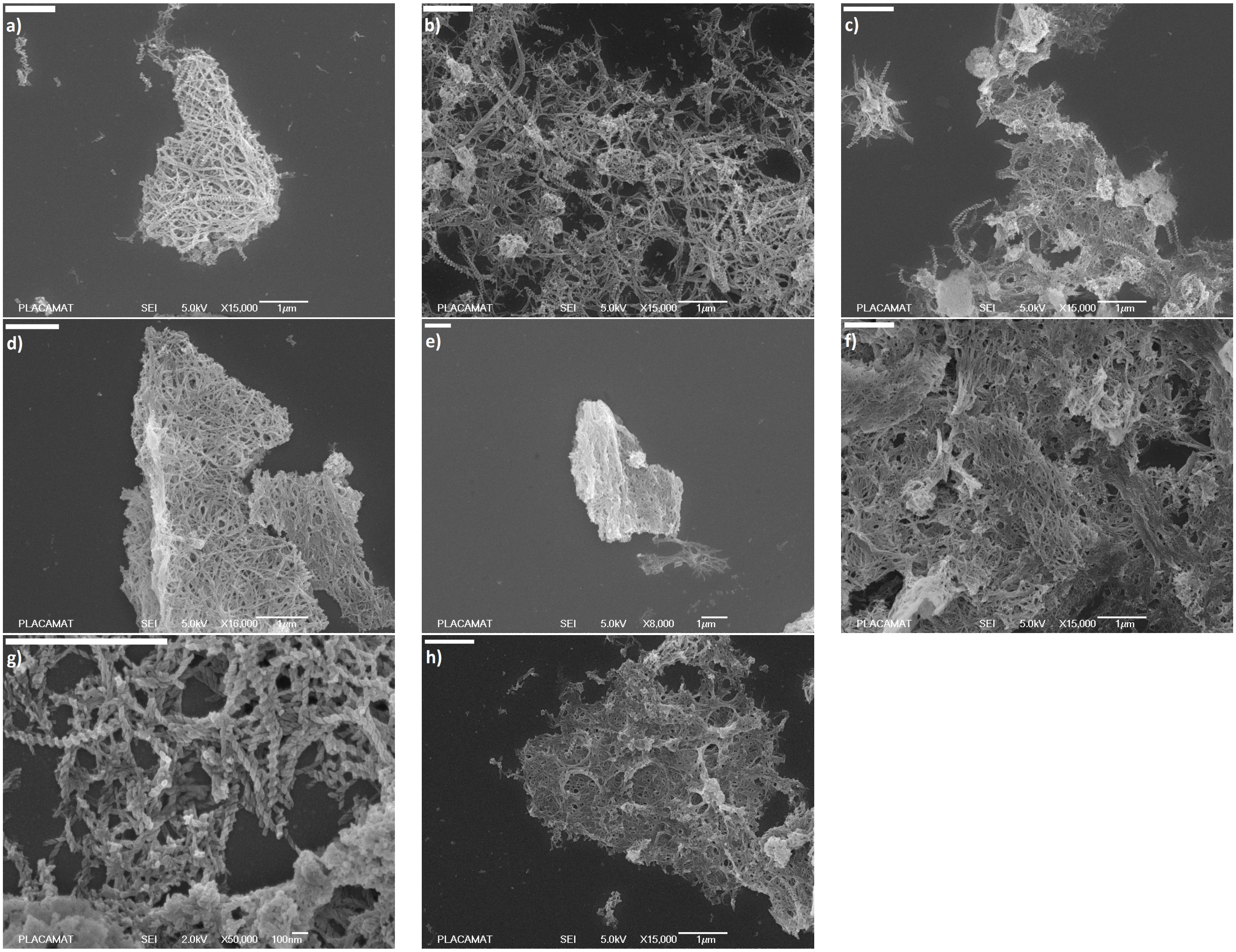

Figure 4.28: SEM images of surface-grafted *L*- and *D*-helices, 8000x-16000x magnification. a) *L* without peptide, b) *L* with RGD, c) *L* with BMP, d) *D* without peptide, e) *D* with RGD, f) *D* with BMP, g) *L* with RGD and BMP, h) *D* with RGD and BMP. The scaling bars in the top left corners represent 1μm.

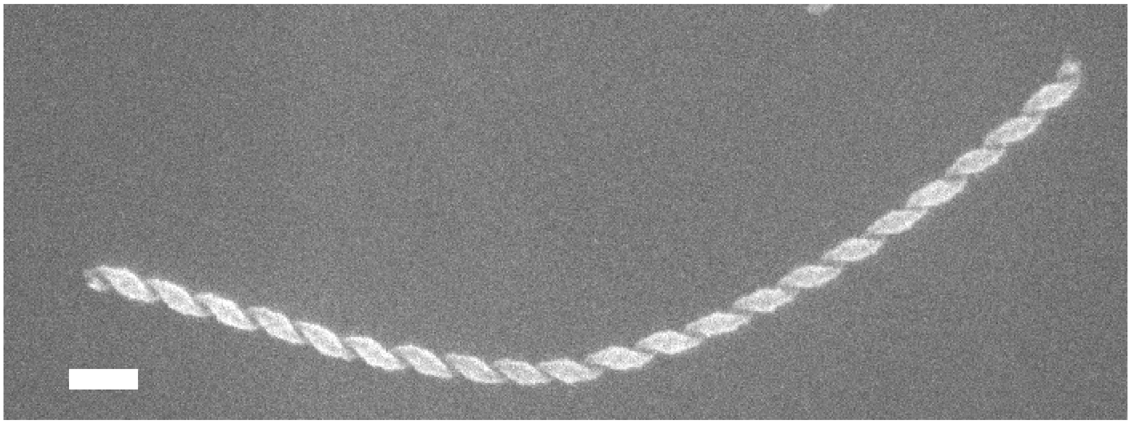

Figure 4.29: Close-up SEM image of a surface-grafted silica nanohelix; scaling bar represents 100nm.

objects were found in several pictures; these might arise from the aggregation of helices. Not all nanoobjects are regular helices, some are deformed helices or aggregates (which appear as white spots in the SEM images).

As it would be helpful to know the percentage of surface which is covered by helices, the different grey values in low magnification SEM images were exploited to estimate the covered fraction. Using only pictures with a magnification of less than 1000x, a grey value threshold was set to selectively measure the surface of the darker, uncovered regions of the images. Using this method, it was determined that the percentages of the surface that is covered varies between the samples on a range from 9% to 29%.

4.4 Materials characterisation: Discussion

As mentioned in the introductory chapter, a key idea of (bone) tissue engineering related research is to find materials which control (stem) cell behaviour and differentiation by setting appropriate cues to steer them in the desired direction. In the present work, we deal with materials featuring two potentially relevant properties at once: bioactive peptide functionalisation and collagen-mimicking, periodic morphology. Hence it is necessary to compare the effect of these materials to reference samples which feature only one of these properties in order to identify the factor that is responsible for the observed effect. Therefore, materials with peptides homogeneously grafted to their surface, and samples with non-functionalised helices were prepared.

Both of the techniques that were used to verify the presence of the peptides RGD and BMP on glass surfaces have their particular strengths: Fluorescence microscopy permits the selective quantification of peptide on the surface, whereas XPS yields information about the chemical composition of the surface at all stages of the functionalisation process. The use of two methods instead of one improves the reliability of the results.

The preparation of the nanobiomaterials is a multistep process involving a variety of experimental parameters like the choice of reagents, solvents, reaction time and temperature, peptide and helix concentration, etc. These factors can impact the amount and distribution of peptides and helices on the final materials.

The results from XPS measurements confirm that reactions with the borosilicate glass surface have taken place. The formation of a self-assembled APTES layer can be fairly safely assumed due to the increase in relative nitrogen content. Nitrogen atoms are equally present on the peptide functionalised samples. The high-resolution study of carbon and nitrogen peaks provides several details which point to the presence of peptides, namely the increase of carbon atoms in C-O groups, nitrogen atoms with electron-drawing substituents, and the presence of a unique high-energy peak component for RGD-grafted materials provide strong evidence of the attachment of peptides. Furthermore, the grafting of BMP peptide is confirmed by the appearance of sulphur, and the appearance of amide groups confirms the successful grafting of the crosslinkers.

Comparison to XPS experiments in other studies shows that results within this order of magnitude are not surprising: Bilem *et al.* [106] grafted the same peptides to glass surfaces using a linker similar to SMP. He obtained carbon percentages that increased from 10% for bare glass to 25% and 39% for grafted RGD and BMP. Our values are similar in all cases except for BMP, where the carbon content is lower (22.5% with SMP). The nitrogen percentages in the present study (2.3% for RGD, 3.2% for BMP) are similar to those in [106] (2.9% for RGD, 5.9% for BMP), except after BMP grafting, where our percentage of nitrogen is lower in the case of SMP, but not in the case of AS. One must bear in mind that not only the crosslinker SMPB which was used in the cited study might perform differently from SMP, but the experiments were also carried out with peptides bearing fluophore moieties which contain additional nitrogen atoms. It is conceivable, for example, that the longer spacer of SMPB facilitates the binding of peptides. Furthermore, the results obtained by Zhe Cheng [237] (nitrogen content 5.6% for a peptide modified material) are similar to our findings - again, the experimental setups were not identical, e.g. because the peptide had a different sequence and included TAMRA (carboxytetramethylrhodamine), a nitrogen-containing fluophore.

Similar statements can be made when comparing the results of this study to those in [235]. In both studies, the appearance of nitrogen in the XPS results shows the presence of amine groups on the surface.

Iucci *et al.* [234] also grafted RGD on glass using APTES, albeit using a different crosslinker, and presented the ratios between different elements as obtained by XPS. In his study, the C/Si ratios for glass, APTES-modified glass and RGD-grafted glass were 0.65, 0.7 and 1.0 respectively, compared to 0.24, 1.6 and 0.7 (with SMP) /or 2.0 (with AS) in our work. The N/Si ratio was 0.0, 0.06 and 0.13 for bare glass, APTES and RGD; compared to 0.01, 0.14 and 0.08 (with SMP) or 0.29 (with AS) in the present study. In comparison to these results, it appears that with the methods used herein, a lower level on carbon contamination and a higher yield for the grafting reactions with APTES and AS/RGD was achieved in our experiments. High-resolution analysis of N1s peaks shows the same phenomenon in both studies: The nitrogen peak after APTES functionalisation consists of two discrete components, which are less discernable after completion of peptide grafting. This demonstrates that the chemical environment of nitrogen changes after the introduction of crosslinkers, even though the atomic percentage remains roughly stable.

Apte *et al.* adsorbed a 14- and 15-AS peptide onto self-assembled monolayers [238]. Due to the different method of applying peptide to the surface, the results are not directly comparable to ours, but the nitrogen content can be juxtaposed in both studies: Depending on peptide and surface

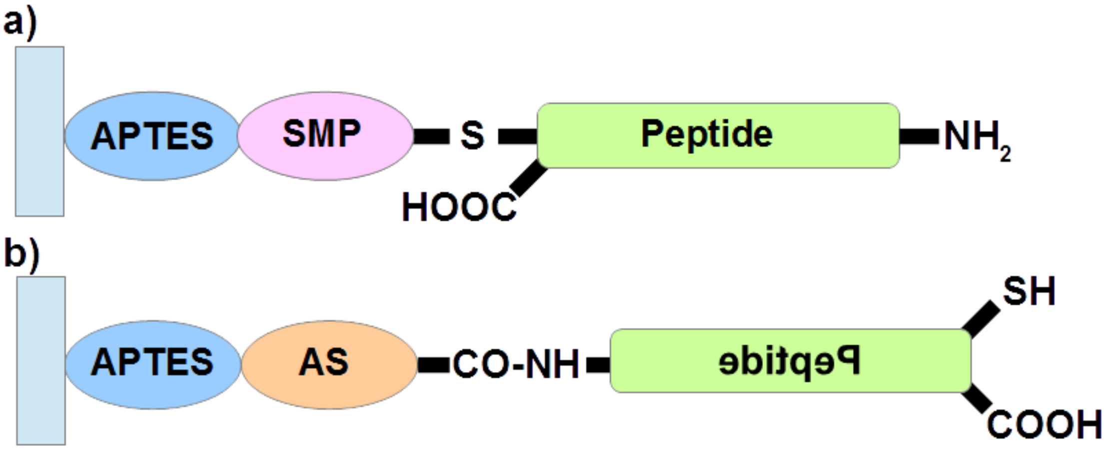

Figure 4.30: Diagram showing how the orientation of grafted peptides depends on the chosen crosslinker, SMP (a) or AS (b): If SMP is used, the N-terminus faces away from the surface. In the case of a), the peptide binds to SMP *via* the thiol groups of the amino acid cystein.

type, [238] the nitrogen percentages of a monolayer were found to be between 8-9%. This value is higher than our nitrogen percentages, which can be explained by the easy formation of thick peptide layers by adsorption.

Briefly, the comparison of the XPS results of the present study to other studies show that the obtained results are in the same order of magnitude as the findings of others. Our results suggest that of the two peptide binding techniques used in this study, AS permits a higher peptide density:

It is indeed clear that the nitrogen and sulphur content of the peptide materials grafted with AS as crosslinker is closer to the theoretical values than those crosslinked with SMP. This might suggest that the binding *via* AS is more effective than *via* SMP. Regardless of whether or not this is the case, a change of crosslinker is not a viable option for this project because of the orientation of the peptides: If RGD and BMP were bound to helices using AS, but to glass slides using SMP, these surfaces would not be comparable in that the peptide would have different termini facing upwards (as shown in Fig. 4.30); and if AS was used as crosslinker for all reactions, the peptide grafting to helices might saturate all binding sites and make it impossible to immobilise the nanomaterials to surfaces. Therefore, the use of SMP was continued in this study.

The results of the ToF-SIMS experiment showed rather clearly that the BMP-peptide was successfully attached. As to the RGD-peptide, the situation is less clear because nitrogen-containing organic compounds were found, but could not be identified as composed of amino acids. The reason for this might be the shorter length of RGD compared to BMP: Assuming both peptides were grafted at similar densities, the amount of amino acids is higher for BMP, so it is easier to detect. The appearance of anionic nitrogen-containing fragments indicates successful grafting of APTES and peptides. The fact that CNO-fragments appear on peptide materials in higher numbers than on the APTES-samples provides further evidence of successful peptide grafting. Lastly, the decreasing relative intensity of peaks that are assigned to glass suggests that in the course of the reaction steps, the glass substrate is covered by an increasingly thick organic layer.

Fluorescence microscopy images of FITC-modified peptide materials provide a more quantitative view of the amount of grafted peptide. The results show that both RGD and BMP were successfully grafted to the glass surfaces, because the fluorescence of these materials were higher than that of unfunctionalised substrates. However, the quantification of grafted peptide showed different peptide densities for RGD and BMP: Whilst the density is around 1.4 ± 0.1 pmol/mm^2 for SMP-grafted BMP, it reached 1.2 ± 0.1 pmol/mm^2 for SMP-grafted RGD. When both peptides are grafted together, BMP appears to be found in higher quantities than RGD as well (0.7 pmol/mm^2 for RGD, 1.3 pmol/mm^2 for BMP, grafted together using SMP). This means that the number of molecules per mm^2 is between $4.6\cdot10^{11}$ and $9.6\cdot10^{11}$ molecules per mm^2, which corresponds to $4.6\cdot10^{-}3$ to $9.6\cdot10^{-}3$ molecules per square Ångström. It will be shown in the following that these values resemble the peptide densities found in other studies. From a steric point of view, the density per square Ångström does not suggest that a multilayer of adsorbed peptide was formed. Fluorescence microscopy images show that inhomogeneities in the peptide coverage exist, but do not occur frequently.

The findings seem to suggest that when both peptides are grafted simultaneously, BMP binds better than RGD. This observation is surprising at the first glance, because due to the lower molecular weight of RGD, one would assume that it binds to the surface more quickly. Perhaps other reasons like steric hindrance due to the peptide secondary structure play a role in the reaction speed: If the folding of the peptide diminishes the accessibility of the thiol group, the reaction might be slowed down. If the rate-determining step for the surface immobilisation is the reaction between peptide and crosslinker, it would be remarkable that the trend is the same for both crosslinkers although they bind to different functional groups.

The peptide densities obtained herein are in the range of values that were found for RGD on (PET substrates) by Chollet *et al.* [239]. Moore *et al.* [240] assumed that when an RGD-peptide and BMP2 are grafted to glass together via click chemistry, the densities of both peptides on the glass will be equal. The thiol-ene-reaction used herein to immobilise peptides is also a click reaction, and indeed the peptide densities were similar, yet not equal. Bilem *et al.* [106] grafted the same peptides to glass using a similar linker and obtained 1.8 pmol/mm^2 for RGD and 2.2 pmol/mm^2 for BMP. These values are higher than the ones in the present study, but they exhibit the same tendency. Similarly, He *et al.* [241] grafted an RGD- and a BMP-peptide together and measured their densities as a function of peptide concentration in solution for the grafting reaction. Their experimental setup differs from ours, but they also observed higher densities of BMP compared to RGD as long as the peptide solution was dilute enough to not saturate the binding sites. It seems that it is not abnormal that BMP is detected in higher quantities than RGD.

The peptide grafting densities of 1.2pmol/mm^2 and 1.4pmol/mm^2 for SMP-grafted RGD and BMP, respectively, lie between the density obtained by Zhe Cheng [237] (0.2-0.4 molecules per mm^2) and Ibrahim Bilem [106] (1.8pmol/mm^2 for RGD and 2.2pmol/mm^2 for BMP). Both of the cited studies used grafting procedures similar to ours, but different in several details. One might hypothesise that SMPB, the crosslinker used by Bilem *et al.*, is more effective than the SMP we used: The spacer arm of SMPB is twice as long, which makes it more likely to provoke an immune response [242], but increases the mobility of the maleimido group.

Comparison with further literature suggests that the quantity of peptide is sufficient for BMP to have an osteogenic effect [240]. According to Massia and Hubbel [243] and Rezania and

Healey [244], the achieved RGD density is also sufficient to enhance cell adhesion. Concerning the relative peptide density, the fluorescence microscopy results suggest that BMP is slightly more abundant, which is compatible with the XPS results. However, the large discrepancy between SMP-and AS-based peptide grafting we observed by XPS could not be found using microscopy. For the continuation of the discussion, this issue is not relevant because peptides are only grafted using SMP for reasons explained earlier.

Wright, Peaden and Lee [245] have determined the density of hydroxyl groups on the surface of borosilicate glass to be about 2.8 per nm^2, which is 4.7pmol/mm^2. Considering that this is the highest density of peptides on the surface which one can possibly achieve with our method, the final yield is fairly high considering the number of reaction steps.

It was shown by fluorescence images that the peptide is distributed over the surfaces in a sufficiently homogeneous manner.

UV/Vis-experiments described in section 4.1 on page 106 have demonstrated that the peptides were successfully grafted onto silica helices and their density per weight unit of silica was determined. An estimation of the peptide density on a surface with immobilised, peptide-grafted helices suggested that the peptide density on helix-grafted surfaces is of the same order of magnitude as the density of homogeneous peptide materials. By comparing the peptide densities on homogeneous materials and silica helices, one can estimate that the peptide densities on peptide-functionalised materials with or without helices are in the same order of magnitude.

To summarise the results about homogeneous materials characterisation, it was shown that peptides were successfully grafted to glass surfaces. XPS atomic percentages showed that APTES and AS-bound peptides were covalently attached. In high-resolution analysis, amine and alcohol peaks indicated that SMP-bound peptides are also present, and in the case of RGD, the existence of a high-energy component in the N1s spectrum provides evidence of its presence. For BMP, the grafting can even be confirmed by the atomic percentages.

ToF-SIMS demonstrated that BMP was grafted successfully. The findings for RGD were ambiguous, possibly due to its shorter length. The results from XPS, ToF-SIMS and fluorescence microscopy all suggest that the grafting of BMP has a higher yield than that of RGD, the only detail that does not fit into this picture is the amount of silicon oxide peaks in the ToF-SIMS data, which implies that the glass of the RGD-sample is covered by a thicker layer than that of BMP.

4.4.1 Helix immobilisation

SEM observation of surface-grafted nanohelices has shown that the vital morphological features - diameter and helical periodicity - are still present in the helices after graftig them onto the surface. The procedure of helix immobilisation was optimised by increasing the number of times helices were deposited onto the surface. We succeeded in improving the degree of surface coverage: By applying helix suspension to the appropriately prefunctionalised substrates five times for 24 hours each, surface coverage was greatly improved and is now between 9% and 29%, but unfortunately this helix grafting onto glass surfaces is not homogeneous and the differences between the samples are very large.

The lack of nanohelices on the surfaces indicates an issue with the immobilisation process. Its first step - the APTES grafting - is unlikely to be the source because the APTES binding to glass is an established procedure [246] [212], and the repeated thermal treatment after each functionalisation step does not damage the APTES layer: It was shown that it can withstand temperatures of up to 285°C [247]. In addition to that, the successful peptide grafting that was demonstrated by XPS and fluorescence microscopy implies that the silane layer was still present at this step. A more plausible potential impediment for covalent helix attachment could be the properties of the nanomaterials themselves. Whilst there are many studies involving covalent attachment of nanoparticles onto surfaces (e.g. [248], [249], [250]), studies about nanofibre grafting are few and far between by comparison. Perhaps the low mobility of high aspect ratio materials in colloidal suspension prevents them from sedimenting and covering the surface efficiently. Ceylan *et al.* [148] attached peptide amphiphile nanofibres to metal surfaces by relying on the adhesive force of 3,4-

dihydroxy-*L*-phenyl alanine. Unlike us, they let the fibre solution dry after depositing them onto the substrates. Their fibres formed homogeneous, continuous layers which were stable to washing with 10x PBS for two days and surfactant treatment with sodium dodecyl sulfate under mechanical shearing.

Sargeant *et al.* [251] bound self-assembled peptide amphiphile nanofibres covalently onto APTES-modified nickel-titanium surfaces using the same EDC/NHS coupling reaction as we used in our grafting reaction. As their fibres are composed of carboxyl-terminated amphiphiles, they can react directly with the amine groups on the surface using EDC/NHS, whereas our experimental setup required AS as linker. One difference between their grafting approach and ours is the method how the nanomaterials are deposited onto the surfaces: In their work, the EDC/NHS solution was added to the substrates after casting the nanofibres onto the surfaces and letting the samples dry. In our study, pretreated samples were immersed in nanohelix suspension without letting them dry; perhaps this difference in the experimental procedure leads to the different helix immobilisation performance.

Another factor which might play a role was discussed in [252]: In this paper, which describes the attachment of microtubes on silanised surfaces, it was argued that the opposite charges on the peptide tube surface facilitate the adhesion of the microobjects on the surface. In our case, AS-functionalised glass substrates might still feature unreacted APTES amine groups, depending on the yield of the AS reaction. Translating their arguments to our setup means that the presence of positively charged, protonated amine groups on the surface of both helices and glass slides could create a repulsion between nanomaterials and surface, which would be an additional obstacle for helix attachment.

The literature shows that the immobilisation of nanomaterials on surfaces can be a complicated undertaking: Pichavant *et al.* grafted polymer NPs with COOH-groups on the surface onto APTES-functionalised titanium surfaces and reported that several grafting steps were necessary [249]. As in the publication [250], NPs were coupled to an APTES-modified surface using NHS and DCC (dicyclohexylcarbodiimide), whereas in the present study, the carbodiimide EDC was used along with NHS. Other studies required only one grafting step, but their experimental systems were fundamentally different: For example, Kvítek *et al.* relied on the affinity of thiols to gold to graft gold NPs onto thiol-terminated glass surfaces at a concentration of 50mg/L in one reaction during 24 hours. Other studies ([253], [254], [255]) succeeded in grafting polymer or inorganic NPs onto surfaces in a matter of hours, using NP solutions of 3-10 mg/mL. This shows that the nanomaterial concentration used in this work was in the same order of magnitude as in other studies. The difference in grafting behaviour of NPs and the nanohelices used herein is probably due to the low mobility of high aspect ratio nanomaterials in suspension, and the resulting lack of contact between helices and glass surface.

Correspondingly, the discrepancy between these findings and the results of [212] might be explained with the use of fragmented helices: The uncut nanohelices which Das and Zouani used are prone to forming large aggregates, which one might suppose to sediment more easily than dispersed helices and therefore enable a higher surface coverage.

In summary, silica nanohelices were attached to glass surfaces, but the degree of surface coverage exhibited disparities between individual samples. Possible reasons for these drawbacks were proposed. The suboptimal characteristics of the nanobiomaterials surfaces must be taken into account when interpreting the results of cell biology experiments.

4.5 Cell biology

4.5.1 Immunofluorescence

Using fluorescence microscopy, fixated and stained cells (as described in section 3.5 and depicted in Figure 3.11) after four weeks of culture were localised and observed. At least 50 images for OCN and 30 for Runx2 were acquired per culture condition. The program ImageJ permits the quantification of cumulative grey values (i.e. the overall fluorescence) in a desired area. The fluorescence associated with OCN was measured over the entire area of each cell. In the case of Runx2, the marker is located inside the nucleus, so only the fluorescence detected within each

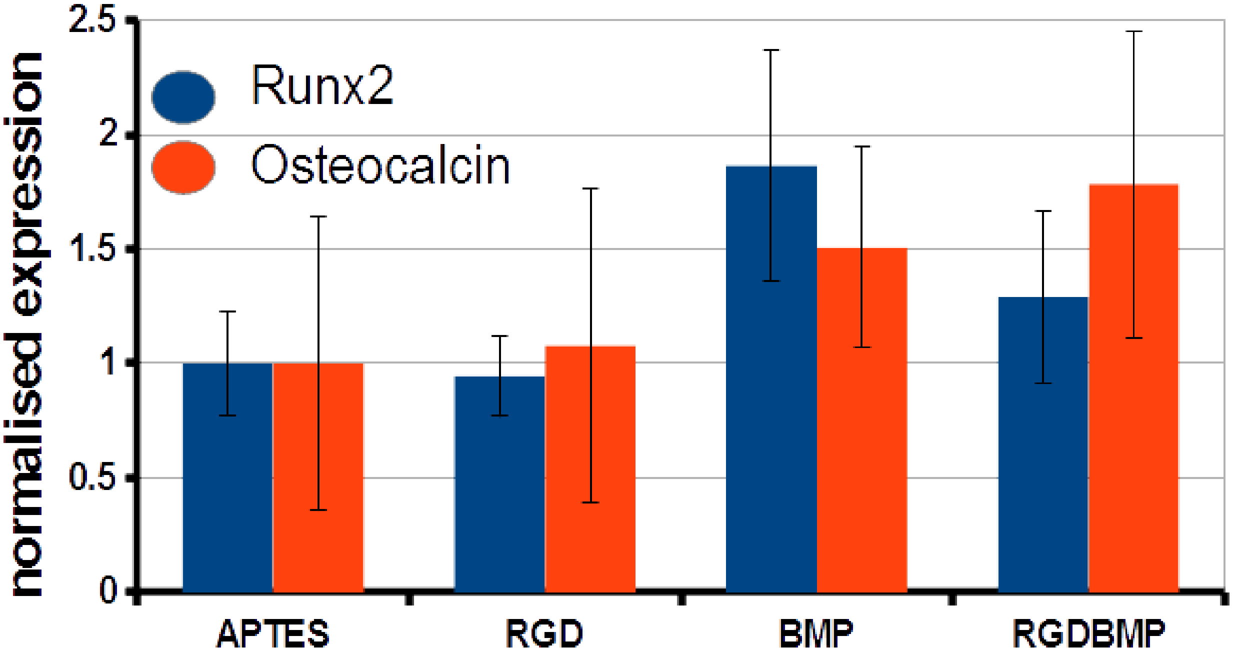

Figure 4.31: Immunofluorescence data of Runx2 and OCN per cell for homogeneous materials (without helices); arbitrary units. Columns from left to right: Glass modified with APTES, RGD, BMP and RGD and BMP together.

cell's nucleus was taken into account. This was achieved by identifying the precise area of the nucleus in the image taken at 461nm, taking advantage of the DAPI staining. The identified area of the nucleus indicated where to measure in the Runx2-stained images.

The fluorescence values for both markers are shown in Figures 4.31 and 4.32. Tables 4.10 and 4.11 show statistical significances between the samples in Figures 4.31 and 4.32.

The fluorescence data for Runx2 show a strong increase on a homogeneous BMP-surface, relative to APTES. (APTES-modified surfaces are used as reference for the peptide materials because all other samples were also functionalised with APTES). These data match the expectation that BMP should have a strong osteoinductive effect, as previously shown in the research of our group. The value obtained for RGD and BMP grafted together is not significantly higher than for APTES. Comparing *L*- and *D*-helices shows that *D*-helices without peptide functionalisation, with RGD- and with RGD/BMP-functionalisation exhibit higher Runx2-fluorescence than *L*-helices with the same functionalisations. BMP-functionalised *L*-helices have a higher Runx2-

	APTES	RGD	BMP	RGDBMP	LV	LR	LB	LRB	DV	DR	DB	DRB
APTES	▨	-	***	-	-				-			
RGD		▨	***	-		-				-		
BMP			▨	*			**				***	
RGDBMP				▨				**				-
LV					▨	-	*	-	***			
LR						▨	*	-		***		
LB							▨	-			-	
LRB								▨				***
DV									▨	-	-	*
DR										▨	-	*
DB											▨	***
DRB												▨

Table 4.10: Statistical significances (by t-test) for the Runx2 fluorescence data in Figure 4.31. (*) : p-value <0.05; (**) : p-value <0.01; (***) : p-value <0.001; minus sign: no statistical significance.

expression than the other *L*-helix samples. Among the *D*-helices, the ones functionalised with both peptides show a higher abundance of the marker than the other *D*-helix samples. None of the *D*-helix samples exhibited a significantly higher fluorescence than homogeneous surfaces with the same surface chemistry; in the case of BMP-helices, the expression was even lower. *L*-helices functionalised with BMP and RGD/BMP express less Runx2 than the homogeneous BMP- and RGD/BMP-samples, respectively. None of the helix-grafted samples exhibited a higher Runx2 expression than homogeneously grafted BMP.
Furthermore, another cell biology experiment with hMSCs cultivated with or without *D*- or *L*-helices with or without peptide functionalisation was carried out. The marker osteocalcin (OCN) was stained, because it is a late osteogenic marker.

Figure 4.31 shows that the expression of the osteogenic marker OCN is increased by homogeneous grafting of the peptide BMP, and this effect is even more visible for RGD and BMP grafted together. RGD-materials exhibit almost the same fluorescence as APTES, and the obtained value is equally lower than those for BMP and RGD/BMP.
Cells on *L*-helices without peptide or with BMP-functionalisation exhibit significantly higher

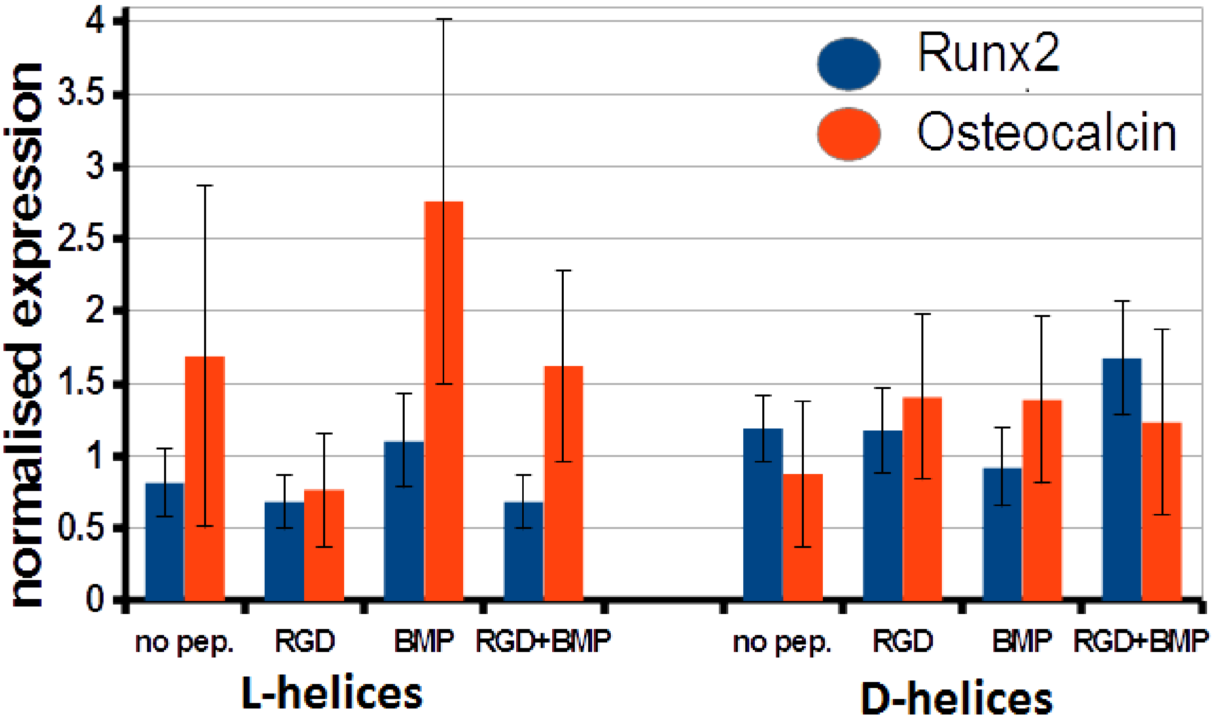

Figure 4.32: Average Runx2 and OCN-fluorescences per cell (a.u.) on helix-grafted materials. Samples from left to right: *L*-helices without peptide, with RGD, BMP and RGD/BMP together; *D*-helices without peptide, with RGD, BMP and RGD/BMP together.

	APTES	RGD	BMP	RGDBMP	LV	LR	LB	LRB	DV	DR	DB	DRB
MV	-	-	***	***								
APTES		-	***	***	***				-			
RGD			***	***		-				-		
BMP				*			***				-	
RGDBMP								-				***
LV						***	***	-	***			
LR							***	***		***		
LB								***			***	
LRB												-
DV										**	**	**
DR											-	-
DB												-
DRB												

Table 4.11: Statistical significances (by t-test) for the OCN fluorescence data in Figure 4.32. (*) : p-value <0.05; (**) : p-value <0.01; (***) : p-value <0.001; minus sign: no statistical significance.

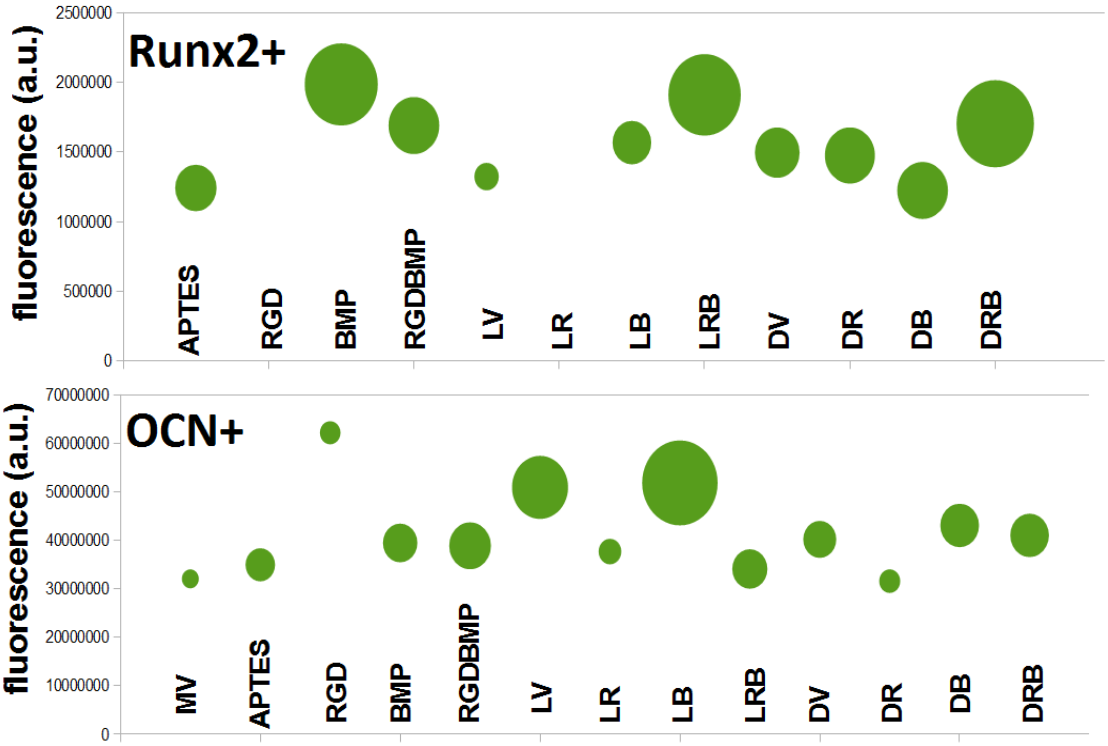

Figure 4.33: Bubble charts of cells that are positive for Runx2 and OCN. Samples from left to right: Bare glass (not for Runx2); modified with APTES, RGD, BMP and RGD/BMP together; *L*-helices with: nothing, RGD, BMP and RGD/BMP together; *D*-helices with: nothing, RGD, BMP and RGD/BMP together.

OCN marker fluorescence than cells on bare glass. For *D*-helices, this is not the case; in fact, *D*-helix samples modified with both peptides exhibit lower OCN expression than homogeneous RGD/BMP-samples. *L*-helix samples without peptide and with BMP exhibit higher fluorescence than *D*-helix samples with the same functionalisation, but RGD-modified *D*-helix samples show a higher OCN expression than the corresponding *L*-helix sample. OCN abundance on samples with *L*-helices is lowest for RGD-functionalisation, and highest for BMP-functionalisation. *D*-helix samples without peptide functionalisation show less OCN than the other *D*-samples.

As an alternative to the representation as average per-cell fluorescence, the marker expression can be depicted as subpopulations of cells which are positive or negative for a given marker, as described in the materials and methods chapter. The results are shown in Figures 4.33. Each bubble represents the subpopulation of a sample that is considered positive for a given marker. The size of the bubble represents the percentage of cells that belongs to this subpopulation, its position on the vertical axis represents its fluorescence from the respective marker.

The results show details that can not be seen in other representations: For example, the difference in Runx2-expression between *L*- and *D*-helices functionalised with both peptides (Figure 4.32) is not visible in the positive population (Figure 4.33). The data show that samples with a high percentage of positive cells often feature a high average fluorescence of these cells: In the Runx2-data, this is the case for cells on homogeneously grafted BMP and on *L*- and *D*-helices modified with RGD and BMP together. Among the osteocalcin data, *L*-helices with BMP-functionalisation and without peptide exhibit the highest percentages of OCN-positive cells, and relatively high average OCN fluorescences. The OCN expression on these samples appears to be stronger than on the corresponding homogeneous materials.

4.5.2 Proteomics

For better clarity, the results of proteomic experiments will be presented along with the discussion of the immunofluorescence experiments (Section 4.6.1, page 148).

4.6 Biology: Discussion

According to the state of research in the literature, BMP-modified substrates are expected to have an osteogenic effect [256]. Bilem *et al.* [106] found that BMP and RGD grafted to surfaces together show a cooperative osteoinductive effect, *i. e.* both peptides together caused a stronger expression of osteogenic markers than both peptides separately. Based on the findings of Das, Zouani *et al.* [212], one could assume that RGD-functionalised silica nanohelices seem to promote osteogenic commitment, and conjecture that this effect might even be generalised to all nanohelices of this type. The present study aims at investigating this alleged effect and exploring the impact of helix variants, with some changes to the experimental setup: The cell culture time is increased from four days to four weeks, and the helices used in this work were fragmented before surface immobilisation.

As expected, in our results, BMP-surfaces were shown to increase Runx2 expression substantially, and OCN to a lesser extent. However, a cooperative effect of samples featuring both BMP and RGD could only be found in the case of OCN, but not in the mean fluorescence results for Runx2. On the other hand, a high percentage of cells on helices featuring both peptides is Runx2-positive. As Runx2 and OCN are markers which are expressed at early and late stages of osteogenic differentiation, respectively, this inconsistency might be explained with a difference in progress of osteoblastic commitment; however, the original study on the cooperative effect of RGD and BMP on stem cell fate [106] featured Runx2 data.

When examining *L*- and *D*-helices as a whole, they exhibited no systematically different behaviour compared to samples without helices in terms of osteogenic differentiation: Although for both markers and both helix handednesses, there are individual samples which deviate significantly from the homogeneous reference sample, the differences in marker expression point in different directions for different samples. Therefore, this obervation does not permit drawing conclusions regarding the effect of helix-functionalised nanomaterials on hMSC differentiation in general. The idea of a strong stimulation of osteogenic induction by helices alone could thus not be corroborated. As to the comparison between *L*- and *D*-helices, the situation is the same: Although there are significant differences between cells in different conditions, there is no trend which is consistent throughout all samples. Hence a difference in osteogenesis between the two chiral orientations cannot be proven at this point.

In nature, we observe a number of enantioselective processes, e.g. enzyme-catalised reactions, and the existence of supramolecular helical chirality, e.g. in right-handed nucleic acids and right-handed protein α-helices. This leads to the question how cells react to supramolecular chirality [257]. The possible reasons why no effect of the helices used herein could be found are manifold; for example, the size of the nanohelices and their features might not be ideal.

The next question to treat is the effect of bioactive functionalisation of helices. The marker expressions of cells cultured on helices functionalised with RGD, BMP or RGD and BMP exhibited differences to samples with unfunctionalised helices, but these discrepancies were not consistent across the experiments and handednesses. Samples grafted with BMP-modified *L*-helices exhibit higher quantities of both osteogenic markers than samples with unfunctionalised *L*-helices, an observation which does not apply to *D*-helices.

One notices that the standard deviations of the fluorescences is high, sometimes more than half of the mean. According to Sigal *et al.* [258], the normal characteristic variability of protein expression between human cells is 15%-20% of the mean, this is partly because proteins expression can depend on the stage of the cell cycle [259]. For biomaterials with BMP-functionalisation, it is not surprising that the standard deviations are higher than this because the cells are not expected to have all the same phenotype. Control materials (unfunctionalised or with APTES) should have lower standard deviations, which is not always the case; this might indicate that even on the control materials, cells could partly have undergone cell differentiation.

According to our findings regarding peptide density on helices (4.1.4, page 105), we estimate that the peptide density on homogeneously grafted materials and helix-covered substrates is of the same order of magnitude. However, it is nonetheless possible that helices on peptide materials are exposed to smaller quantities of bioactive peptide than those on homogeneous peptide materials, because the imobilised helices do not cover the entire surface.

When reflecting on possible reasons for these inconsistent results, the first thing that comes to mind is the variability of helix surface coverage between different samples. As discussed in the previous section, the degree of surface coverage exhibited large disparities between the samples, which means that cells cultivated on scarcely grafted materials may only be exposed to a small amount of helices, and the degree of exposure may vary from sample to sample. In this case, the properties of a sample with few helices would resemble those of APTES-substrates and the cells would behave accordingly. This issue can easily lead to false negatives, but not to false positives: Cells on helix-grafted materials can behave as if they were on an APTES substrate, but there is no reason for cells to exhibit an increased level of osteoblastic marker expression despite the absence of osteogenic cues. In other words, one might argue that the data points which indicate a higher expression of osteoblast markers in cells cultivated on helices are still valid, even if other data points point in the opposite direction. On the other hand, this issue makes it hard to compare between the effect of different helix-grafted materials.

This being said, the immunofluorescence results seem to suggest that helices- especially those with BMP-functionalisation- might have an effect on osteogenic hMSC differentiation.

Das and Zouani [212] found an enhancing effect of RGD-grafted nanohelices on hMSC osteogenic differentiation. Our results did not show this effect with RGD-helices. Their work was carried out using uncut silica helices, which might be the reason behind the different performance of helix surface immobilisation, and the cell response might also be influenced by this factor. In addition to that, in the cell culture experiments by Das and Zouani, hMSCs were cultivated on the biomaterials for only four days, as opposed to four weeks in the present study. It is conceivable that nano-biomaterials have an effect on cell fate which causes elevated levels of osteoblastic markers in the first days after seeding, but the effect fades in the following weeks. As [74] demonstrates, the expression of a number of osteoblast markers including Runx2 and OCN does not follow a linear development during osteogenesis, but increases more or less strongly at earlier or later stages of cell differentiation. We used one early and one late marker of osteogenic differentiation in order to cover most stages of osteogenic differentiation. Nonetheless, it is possible that the impact of nanohelices on stem cell fate is only measurable in a certain time window after hMSC seeding.

In a project similar to ours, Ceylan *et al.* [148] examined the effect of bioactive nanofibres on hMSC fate and found an increase in calcium deposition, but no data about the effect of unfunctionalised fibres was shown.

This leaves us with the question whether the mere morphology of nanofibres and -helices is to be expected to induce osteogenic differentiation. Based on section 2.1.3, one can summarise that surface roughness at the nanoscale increases cytoskeletal tension of adherent hMSCs, which in turn stimulates differentiation of hMSC into osteoblasts. This surface roughness can be, for example, increased by the presence of electrospun nanofibres [260]. Therefore, one would expect that silica nanohelices have a comparable effect.

Whether the collagen-mimicking periodic morphology alone is a factor that promotes osteogenesis is a more difficult question. To the best of our knowledge, no other study explored the effect of periodicity or handedness in a comparable set-up. Concerning the nanoperiodicity, one could argue that high aspect-ratio nanomaterials with periodic grooves have a higher specific surface area and roughness than those smooth fibres, so if their impact on stem cell fate is in any way different from the effect of non-periodic fibres, one would expect them to increase cytoskeletal tension and therefore stimulate osteogenic commitment. This applies to nanohelices both with and without functionalisation, as they both feature periodic morphology, as shown in section 4.1.2. The idea that right- and lefthanded helices might have different influences on stem cells is based on the fact that most amino acids exist naturally as *L*-enantiomer and often form right-handed α-helices. Due to the lack of comparability between helix-grafted samples, our study cannot provide a conclusive answer to the question of whether stem cells respond differently to nanohelices of different handednesses. An answer to the question whether nanohelix periodicity alone has an effect cannot be answered with our experimental setup because of the lack of non-periodic reference materials.

4.6.1 Proteomics

The proteome of cellular lysate of cells cultivated on bare glass (MV), grafted helices (LV) and BMP-functionalised grafted helices (LB) was investigated. The obtained data were analysed in three different ways: Firstly, the most conspicuous differentially expressed proteins were examined for a possible specificity for a relevant phenotype; secondly, previously published proteomic comparisons between MSCs and osteoblasts are juxtaposed to our results to identify proteins of importance, and thirdly, the online database STRING was used to find proteins which are usually associated with those found in this experiment. The STRING search permitted the identification of protein groups amongst the overexpressed proteins which commonly occur together.

Generally, a protein in our data was only considered overexpressed if its expression differed at least by the factor 2 between two conditions, and if a sufficient number of peptide fragments of this protein was found. In the following, the symbols $<$ and $>$ are used to show that a protein is more/less strongly expressed in one of the aforementioned experimental conditions compared to another condition in the results of this study.

Two proteins were identified as particularly interesting because they were differentially expressed between all conditions: Vimentin (MV>LB>LV) and Complement C3 (LB>MV>LV). The significance of vimentin for osteogenic differentiation is difficult to define: Park *et al.* [261] used it as a marker to identify MSCs, but a recent study [262] claims that its expression increases during osteogenic differentiation, and a third publication [263] showed that the vimentin content in the secretome of MSCs remains constant during osteogenic differentiation. It is therefore hard to draw conclusions regarding the phenotype of the cells, but its role as a cytoskeletal component in mesenchymal cells and the fact that it is involved in the inhibition of osteogenic differentiation [264] might indicate that it is linked to hMSCs. Complement C3 might be relevant for osteogenesis because it was shown that its deficiency hinders bone fracture healing [265], but this effect seems not be due to a direct impact on cell differentiation but rather because Complement C3 attracts and recruits hMSCs [266]. A connection to osteogenic commitment of hMSCs could not be found. A STRING search of vimentin and complement c3 did not reveal any connections to other differentially expressed proteins.

The results of three proteomic studies [267–269] on hMSCs undergoing chemically induced osteogenic differentiation were compared to the results of this study. Two of them listed Annexin A1 (LB>LV) and other Annexins as upregulated during osteogenesis. Moreover, Filamin-A (MV>LB>LV), Heat shock protein 70kDa (LB>LV) and Gelsolin (LB>MV) were identified as overexpressed. This means that four of the proteins which were found to be upregulated according to literature were overexpressed in LB, and one in MV. This could indicate that cells cultured on BMP-functiomalised helices have a higher degree of osteoblastic differentiation than those on bare glass. Differential expression of osteoblast marker proteins which are typically used for immunofluorescence, e.g. Runx2, was not detected.

All of the aforementioned proteins appear to be underexpressed in the sample LV. This could mean that cells on silica helices exhibit a much less osteoblastic character than the others, or that this discrepancy is an artifact caused by abundant contaminants in the LV-sample. The latter viewpoint is supported by the increased amounts of likely contaminants (albumin, trypsin and cuticular keratin proteins) in this sample.

Another study [263] investigated not the proteome, but the secretome (i.e. not the proteins contained in the cells, but those secreted by them) of MSCs before and after osteogenic differentiation. Some proteins including Fibronectin (MV>LB) were shown to be downregulated. The upregulated proteins in [263] included Calponin and Caldesmon (MV>LB). These secretomic results of [263] cannot be directly compared to our proteomic finding, but may serve as a starting point for further investigations.

The STRING research revealed a pair of related proteins all of which are found in higher quantities in MV than in LB: TGM2 was shown to be involved in cell-matrix interactions through association with Fibronectin [270]. As these two proteins experience the strongest overexpression in MV compared to LB, they are of particular interest. Kubo *et al.* [271] showed that TGM2 is selectively expressed in MSCs as opposed to osteoblasts (and other cells). This might mean that cells cultivated on bare glass have more stem cell-like characteristics than those cultivated on BMP-functionalised helices.

It needs to be noted that our study involved only one lysate sample per experimental condition, which is why the results need to be interpreted with caution.

The proteomics experiments have primarily an exploratory character to discover potential leads for later research. Only one replica of each cell culture material could be fabricated, so the statistical significance is limited. Our results showed a number of proteins which can be associated with osteogenic differentiation were more abundant in cells cultivated on BMP-modified helices, compared to bare glass samples. This finding is consistent with the results of immunofluorescence experiments. Unfortunately, there is doubt about the meaningfulness of the data regarding unfunctionalised silica helices. Moreover, strongly differentially expressed proteins without a clear connection to cell lineage were found. Especially Vimentin and the lack of certainty about its role in hMSCs on nanobiomaterials leave much room for future research.

Chapter 5

Conclusion and Perspectives

The first part of this work dealt with the synthesis of nanomaterials. We have shown that by varying the enantiomeric excess of gemini surfactant tartrate, we can obtain silica helices of different period lengths. For high enantiomeric excesses, the helices were morphologically homogeneous. This tunable nanoperiodicity may be helpful in future studies which aim at investigating the role of the band structure of collagen. Furthermore, we have shown how these nanohelices and bioactive peptides can be used to prepare bio-nanomaterials, featuring both the aforementioned periodicity and bioactive cues. We used several analytical methods, including XPS, electron microscopy and fluorescence microscopy, to ascertain that the properties of the materials were in accordance with our expectations. The results of this study show that althought individual bio-nanomaterial samples increased osteogenic differentiation of hMSCs, nanohelices were not shown to have a reproducible effect on osteogenic commitment. Moreover, the data do not indicate that the impact of these materials on stem cells depends on nanohelix handedness. Due to the variability between the bio-nanomaterials, it is conceivable that a possible effect of nanohelices with or without bioactive functionalisation was concealed by lacking exposure of cells to these materials. The fact that increased osteogenic differentiation was found in a few individual samples points to this explanation. In any case, a statement about the extent of this effect as a function of the choice of bioactive functionalisation cannot be made with the current data, and an osteoinductive effect of collagen-mimicking nanohelices in general cannot be proven at this point.

The question whether any effect of silica nanohelices on stem cell fate is due to their periodic, chiral structure remains to be answered because we could not compare the influence of nanohelices to the effect of similar nanomaterials without collagen-mimicking morphology. For further research on this topic, it would be interesting to perform the experiment shown here both with silica nanohelices and nanotubes, which can be prepared by increasing the ageing time of nanohelices. These tubes resemble silica nanohelices in everything except for the lack of helix shape, hence they could be used to determine whether the collagen-mimicking morphology is the reason for a possible osteogenic effect of the bio-nanomaterials. With the results obtained in this study, it is not possible to ascertain whether any impact on cells of nanohelices is linked to their periodic structure. If it turns out that the collagen-mimicking morphology does indeed have an effect on stem cell fate, the next step would be to perform cell culture experiments with cells on nanohelices of varying period length (¿64nm). This would make it possible to investigate whether the well-defined periodicity of collagen 1 is recognised by cells. As we have shown, the helix pitch can be tuned by making small changes to the gemini surfactant synthesis.

Future work on this topic should firstly focus on the optimisation of the surface immobilisation procedure of nanohelices, because the preparation of helix-grafted materials appeared to be a major challenge in this work. One possible way to increase the amount of grafted helices is a quantitative approach: Increasing the concentration of helices and the number or duration of grafting steps might improve the effectiveness of the helix grafting process. Alternatively, other parameters could be tweaked. For example, if the helices are fragmented longer or at higher amplitude, the resulting nanomaterials are expected to be shorter than the ones used herein, resulting in higher mobility in a liquid medium and perhaps easier reaction with functionalised surfaces. Moreover, the question whether or not the glass slides should be shaken during the might be worth an investigation. As explained in the discussion, it would be interesting to determine the yield of the reactions between AS and surface-bound APTES (e.g. using ninhydrin to quantify amine groups) to find out whether electrostatic repulsion between helices and surface might be an issue. Finally, one could try to carry out the EDC/NHS-immobilisation of helices onto the surface with a different solvent.

As shown in the discussion, other researchers succeeded in covalently immobilising high aspect ratio nanomaterials onto surfaces using protocols in the course of which the nanomaterial suspension is left to dry on the substrate. Application of a similar strategy might resolve the issue of surface coverage insufficiency and variability, and thus enable direct comparisons between different bio-nanomaterial variants. This opens up the possibility not only to compare the perfomances of helix handednesses and biofunctionalisatons in terms of osteogenic induction, but also to investigate the importance of helical morphology. Concerning the cell culture experiments, the question remains which combination of culture time and osteogenic markers is most appropriate to detect an effect on cell differentiation. As the osteoinductive stimulus of nano-biomaterials might be weaker than the induction with an osteogenic medium, I could be best to rely on both early and late osteogenic markers to cover more stages of osteoblast development. Based on the findings from the proteomics experiment, it might be of interest to study the role of other proteins in determination of stem cell fate, such as vimentin and annexin A1.

Bibliography

[1] Glenn Dickson, Fraser Buchanan, David Marsh, Eileen Harkin-Jones, Uel Little, and Mervyn McCaigue. ”Orthopaedic tissue engineering and bone regeneration”. *Technology and Health Care*, 15:57–67, 2007.

[2] Patrick P Spicer, James D Kretlow, Simon Young, John A Jansen, Kurtis Kasper, and Antonios G Mikos. ”Evaluation of bone regeneration using the rat critical size calvarial defect”. *Nature Protocols*, 7:1918–1929, 2012.

[3] Alistair Brydone, Dominic Meek, and Sarah E. Maclaine. ”Bone grafting, orthopaedic biomaterials, and the clinical need for bone engineering”. *Proc. Inst. Mech. Eng. H*, 224:1329–1343, 2010.

[4] European project reborne. `www.reborne.org`. 22. 2. 2017.

[5] Reinhard Gruber, Hannjörg Koch, Bruce A. Doll, Florian Tegtmeier, Thomas A. Einhorn, and Jeffrey O. Hollinger. ”Fracture healing in the elderly patient”. *Experimental Gerontology*, 41:1080–1093, 2006.

[6] Rebecca E. McMahon, Lina Wang, Roman Skoracki, and Anshu B. Mathur. ”Development of nanomaterials for bone repair and regeneration”. *J. Biomed. Res. Part B*, 101:387–397, 2013.

[7] Elise F. Morgan and Jenny Lei. ”Toward Clinical Application and Molecular Understanding of the Mechanobiology of Bone Healing”. *Clinic. Rev. Bone Miner. Metab.*, 13:256–265, 2015.

[8] K.D. Hankenson, G. Zimmerman, and R. Marcucio. ”Biological perspectives of delayed fracture healing”. *Injury*, 45S:8–15, 2014.

[9] Edgar Dahl. ”Xenotransplantation - Chancen, Risiken und Alternativen”, July.

[10] Frank ANtwerpes and Agnes Christine Podlewski. ”Xenotransplantation”, July.

[11] Mohamadreza Baghaban Eslaminejad and Faezeh Faghihi. ”Mesenchymal Stem Cell-Based Bone Engineering for Bone Regeneration”. *Regenerative Medicine and Tissue Engineering - Cells and Biomaterials*, 2010.

[12] Anindita Chatterjea, Gert Meijer, Clemens van Blitterswijk, and Jan de Boer. ”Clinical Application of HumanMesenchymal Stromal Cells for Bone Tissue Engineering”. *Stem Cells International*, 2010:1–12, 2010.

[13] Raymond Pollock, Ilhan Alcelik, Chandra Bhatia, Graham Chuter, Kiran Lingutla, Chakravarty Budithi, and Manoj Krishna. ”Donor site morbidity following iliac crest bone harvesting for cervical fusion: a comparison between minimally invasive and open techniques”. *Eur. Spine J.*, 17:845852, 2008.

[14] Susmita Bose, Mangal Roy, and Amit Bandyopadhyay. ”Recent advances in bone tissue engineering scaffolds”. *Trends Biotechnol.*, 30:564–554, 2012.

[15] Yukie Aizawaa, Shawn C. Owena, and Molly S. Shoicheta. ”Polymers used to influence cell fate in 3D geometry: New trends”. *Progress in Polymer Science*, 37:645–658, 2012.

[16] Azizeh-Mitra Yousefi, Paul F. James, Rosa Akbarzadeh, Aswati Subramanian, Conor Flavin, and Hassane Oudadesse. ”Prospect of Stem Cells in Bone Tissue Engineering: A Review”. *Stem Cells International*, 2016.

[17] Nasrin Shadjou and Mohammad Hasanzadeh. ”Silica-based mesoporous nanobiomaterials as promoter of bone regeneration process”. *J. Biomed. Mater. Res. Part A*, 103:3703–3716, 2015.

[18] Ami R. Amini, Cato T. Laurencin, and Syam P. Nukavarapu. ”Bone Tissue Engineering: Recent Advances and Challenges”. *Crit. Rev. Biomed. Eng.*, 40:363–408, 2012.

[19] Ivan Marcos-Campos, Darja Marolt, Petros Petridis, Sarindr Bhumiratana, Daniel Schmidt, and Gordana Vunjak-Novakovic. ”Bone scaffold architecture modulates the development of mineralized bone matrix by human embryonic stem cells”. *Biomaterials*, 33:8329–8342, 2012.

[20] Sean V Murphy and Anthony Atala. ”3D bioprinting of tissues and organs”. *Nature Biotechnology*, 32:773–785, 2014.

[21] Betuül Çelebi, Maxime Cloutier, Rodrigo Balloni, Diego Mantovani, and Antonella Bandiera. ”Human Elastin-Based Recombinant Biopolymers Improve Mesenchymal Stem Cell Differentiation”. *Macromolecular Bioscience*, 12:1546–1554, 2012.

[22] Sriram Ravindran and Anne George. ”Biomimetic extracellular matrix mediated somatic stem cell differentiation: applications in dental pulp tissue regeneration”. *Frontiers in Physiology*, 6, 2015.

[23] Weiliang Zhong, Weiguo Zhang, Shouyu Wang, and Jianhua Qin. ”Regulation of Fibrochondrogenesis of Mesenchymal Stem Cells in an Integrated Microfluidic Platform Embedded with Biomimetic Nanofibrous Scaffolds”. *PLOS one*, 8, 2013.

[24] Shima Tavakol, Hadi Aligholi, Ali Gorji, Arezou Eshaghabadi, Elham Hoveizi, Behnaz Tavakol, Seyed Mahdi Rezayat, and Jafar Ai. ”Thermogel nanofiber induces human endometrial-derived stromal cells to neural differentiation: In vitro and in vivo studies in rat”. *J. Biomed. Mater. Res. Part A*, 102:4590–4597, 2014.

[25] Benjamin Holmes, Xiuqi Fang, Annais Zarate, Michael Keidar, and Lijie Grace Zhang. ”Enhanced human bone marrow mesenchymal stem cell chondrogenic differentiation in electrospun constructs with carbon nanomaterials”. *Carbon*, 97:1–13, 2016.

[26] Anita Shukla, John H. Slater, James C. Culver, Mary E. Dickinson, and Jennifer L. West. ”Biomimetic Surface Patterning Promotes Mesenchymal Stem Cell Differentiation”. *Applied Materials and Interfaces*, 2015.

[27] Cole A. DeForest and David A. Tirrell. ”A photoreversible protein-patterning approach for guiding stem cell fate in three-dimensional gels”. *Nature Materials*, 14:523–531, 2015.

[28] Mark W. Tibbitt and Kristi S. Anseth. ”Hydrogels as Extracellular Matrix Mimics for 3D Cell Culture”. *Biotechnology and Bioengineering*, 103:655–663, 2009.

[29] Peter Newman, Andrew Minett, Rutledge Ellis-Behnke, and Hala Zreiqat. ”Carbon nanotubes: Their potential and pitfalls for bone tissue regeneration and engineering”. *Nanomedicine: Nanotechnology, Biology, and Medicine*, 9:1139?1158, 2013.

[30] M. M. Stevens and J. H. George. ”Exploring and engineering the cell surface interface”. *Science*, 310, 2005.

[31] Junbin Shi, Malcolm M. Q. Xing, and Wen Zhong. ”Development of Hydrogels and Biomimetic Regulators as Tissue Engineering Scaffolds”. *Membranes*, 2:70–90, 2012.

[32] Michael Goldberg, Robert Langer, and Xingquiao Jia. ”Nanostructured materials for applications in drug delivery and tissue engineering”. *J. Biomater. Sci. Polymer Edition*, 18:241–268, 2007.

[33] Murat Guvendiren and Jason A. Burdick. ”Engineering synthetic hydrogel microenvironments to instruct stem cells”. *Current Opinion in Biotechnology*, 18:241–268, 2013.

[34] Jan Behring, Rdiger Junker, X. Frank Walboomers, Betsy Chessnut, and John A. Jansen. ”Toward guided tissue and bone regeneration: morphology, attachment, proliferation, and migration of cells cultured on collagen barrier membranes. A systematic review”. *Odontology*, 96:1–11, 2008.

[35] Julie Glowacki and Shuichi Mizuno. ”Collagen Scaffolds for Tissue Engineering”. *Biopolymers*, 89:338–344, 2008.

[36] Lian Cen, Wei Liu, Wenjie Zhang, and Yilin Cao. ”Collagen Tissue Engineering: Development of Novel Biomaterials and Applications”. *Pediatric Research*, 5:492–496, 2008.

[37] Wenfu Zheng, Wei Zhang, and Xingyu Jiang. ”Biomimetic Collagen Nanofibrous Materials for Bone Tissue Engineering”. *Advanced Engineering Materials*, 12:451–466, 2010.

[38] Rémi Parenteau-Bareil, Robert Gauvin, and François Berthod. ”Collagen-Based Biomaterials for Tissue Engineering Applications”. *Materials*, 3:1863–1887, 2010.

[39] Max R Salick, Brett N Napiwocki, Jin Sha, Gavin T Knight, Shahzad A Chindhy, Timothy J Kampa, Randolph S Ashton, and Wendy C Crone. ”Micropattern width dependent sarcomere development in human ESC-derived cardiomyocytes”. *Biomaterials*, 35:4454–4464, 2014.

[40] Dasong Liu, Mehdi Nikoo, Gökhan Boran, Peng Zhou, and Joe M. Regenstein. ”Collagen and Gelatin”. *Annu. Rev. Food Sci. Technol.*, 6:527–557, 2015.

[41] Roberta Tasso, Franco Fais, Daniele Reverberi, Federico Tortelli, and Ranieri Cancedda. ”The recruitment of two consecutive and different waves of host stem/progenitor cells during the development of tissue-engineered bone in a murine model”. *Biomaterials*, 31:2121–2129, 2010.

[42] Wenchuan Chen, Jun Liu, Navid Manuchehrabadi, Michael D.Weir, Zhimin Zhu, and Hockin H.K. Xu. ”Umbilical cord and bone marrow mesenchymal stem cell seeding on macroporous calcium phosphate for bone regeneration in rat cranial defects”. *Biomaterials*, 34:9917–9925, 2013.

[43] Kenneth M. Dupont, Kapil Sharmac, Hazel Y. Stevens, Joel D. Boerckel, Andrés J. García, and Robert E. Guldberg. ”Human stem cell delivery for treatment of large segmental bone defects”. *PNAS*, 107:3305–3310, 2009.

[44] Giuseppe Maria de Peppo, Iván Marcos-Campos, David John Kahler, Dana Alsalman, Linshan Shang, Gordana Vunjak-Novakovic, , and Darja Marolt. ”Engineering bone tissue substitutes from human induced pluripotent stem cells”. *PNAS*, 101:8680–8685, 2013.

[45] Cornel Iancu, Ioana R. Ilie, Carmen E. Georgescu, Razvan Ilie, Alexandru R. Biris, Teodora Mocan, Lucian C. Mocan, Florin Zaharie, Dana Todea-Iancu, Sergiu Susman, Dan Rus Ciuca, and Alexandru S. Biris. ”Applications of Nanomaterials in Cell Stem Therapies and the Onset of Nanomedicine”. *Particulate Science and Technology*, 27:562–574, 2009.

[46] Elke Eggenhofer, Franka Luk, Marc H. Dahlke, and Martin J. Hoogduijn. ”The life and fate of mesenchymal stem cells”. *Frontiers in Immunology*, 5, 2014.

[47] Elizaveta Kon, Giuseppe Filardo, Alice Roffi, Alessandro Di Martino, Mohammad Hamdan, Laura De Pasqual, Maria Letizia Merli, and Maurilio Marcacci. ”Bone regeneration with mesenchymal stem cells”. *Clinical Cases in Mineral and Bone Metabolism*, 9:2427, 2012.

[48] Azizeh-Mitra Yousefi, Paul F James, Rosa Akbarzadeh, Aswati Subramanian, Conor Flavin, and Hassane Oudadesse. ”Prospect of Stem Cells in Bone Tissue Engineering: A Review”. *Stem Cells International*, 2016.

[49] Imran Ullah, Raghavendra Baregundi Subbarao, and Gyu Jin Rho. ”Human mesenchymal stem cells - current trends and future prospective”. *Biosci. Rep.*, 35, 2015.

[50] L. Mazzini, F. Fagioli, R. Boccaletti, K. Mareschi, G. Oliveri, C. Olivieri, I. Pastore, R. Marasso, and E. Madon. ”Elongated Aggregates Formed by Cationic Gemini Surfactants”. *Langmuir*, 15:2384–2390, 1999.

[51] http://www.nature.com/scitable/topicpage/cell-differentiation-and-tissue-14046412.

[52] http://stemcells.nih.gov/info/basics/Pages/Default.aspx.

[53] Terhi J. Heino and Teuvo A. Hentunen. ”Differentiation of Osteoblasts and Osteocytes from Mesenchymal Stem Cells”. *Current Stem Cell Research Therapy*, 3:131–145, 2008.

[54] Amy M. DiMarino, Arnold I. Caplan, and Tracey L. Bonfield. ”Mesenchymal stem cells in tissue repair”. *Frontiers in Immunology*, 4, 2013.

[55] Thomas Schubert, Daela Xhema, Sophie Vériter, Michaël Schubert, Catherine Behets, Christian Delloye, Pierre Giannello, and Denis Dufrane. ”The enhanced performance of bone allografts using osteogenic-differentiated adipose-derived mesenchymal stem cells”. *Biomaterials*, 32:8880–8891, 2011.

[56] Dah-Ching Ding, Woei-Cherng Shyu, , and Shinn-Zong Lin. ”Mesenchymal Stem Cells”. *Cell Transplantation*, 20:5–14, 2011.

[57] Mark F. Pittenger, Alastair M. Mackay, Stephen C. Beck, Rama K: Jaiswal, Robin Douglas, Joseph D. Mosca, Mark A. Moorman, Donald W. Simonetti, Stewart Craig, and Daniel R. Marshak. ”Multilineage Potential of Adult Human Mesenchymal Stem Cells”. *Science*, 284:143–147, 1999.

[58] Ralf Hass and Anna Otte. ”Mesenchymal stem cells as all-round supporters in a normal and neoplastic microenvironment”. *Cell Communication and Signaling*, 10, 2012.

[59] O. O. Maslova. ”Current view of mesenchymal stem cells biology (brief review)”. *Biopolymers and Cell*, 28:190–198, 2012.

[60] M. F. Pittenger, A. M. Mackay andS. C. Beck andR. K. Jaiswal, R. Douglas, J. D. Mosca, M. A. Moorman, D. W. Simonetti, S. Craig, and D. R. Marshak. ”Multilineage potential of adult human mesenchymal stem cells”. *Science*, 284:143–147, 1999.

[61] Luca Dalle Carbonare, Giulio Innamorati, and Maria Teresa Valenti. ”Transcription Factor Runx2 and its Application to Bone Tissue Engineering”. *Stem Cell Rev. and Rep.*, 8:891–897, 2012.

[62] Paolo Bianco. ”“Mesenchymal” Stem Cells”. *Annu. Rev. Cell Dev. Biol.*, 30:677–704, 2014.

[63] Jifan Feng, Andrea Mantesso, Cosimo De Bari, Akiko Nishiyama, and Paul T. Sharpe. ”Dual origin on mesenchymal stem cells contributing to organ growth and repair”. *PNAS*, 108:6503–6508, 2011.

[64] Jessie R. Lavoie and Michael Rosu-Myles. ”Uncovering the secretes of mesenchymal stem cells”. *Biochimie*, 95:2212–2221, 2013.

[65] P. Mafi, S. Hindocha, R. Mafi, M. Griffin, and W.S. Khan. ”Adult Mesenchymal Stem Cells and Cell Surface Characterization - A Systematic Review of the Literature”. *The Open Orthopaedics Journal*, 5:253–260, 2011.

[66] Guiting Lin, Gang Liu, Lia Banie, Guifang Wang, Hongxiu Ning, Tom F. Lue, and Ching-Shwun Lin. ”Tissue Distribution of Mesenchymal Stem Cell Marker Stro-1”. *Stem Cells and Development*, 20, 2011.

[67] Hongxiu Ning, Guiting Lin, Tom F. Lue, and Ching-Shwun Lin. ”Mesenchymal stem cell marker Stro-1 is a 75kd endothelial antigen”. *Biochemical and Biophysical Research Communications*, 413:353–357, 2011.

[68] M. Bruderer, R.G. Richards, M. Alini, and M.J. Stoddart. ”ROLE AND REGULATION OF RUNX2 IN OSTEOGENESIS”. *European Cells and Materials*, 28:269–286, 2014.

[69] P.J. Miranda N. Selvamurugan S. Vimalraj, B. Arumugam. ”Runx2: Structure, function, and phosphorylation in osteoblast differentiation”. *International Journal of Biological Macromolecules*, 78:202–208, 2015.

[70] Aaron W. James. ”Review of Signaling Pathways Governing MSC Osteogenic and Adipogenic Differentiation”. *Scientifica*, 2013.

[71] Jianwen Wei, Junko Shimazu, Munevver P. Makinistoglu, Antonio Maurizi, Daisuke Kajimura, Haihong Zong, Takeshi Takarada, Takashi Iezaki, Jeffrey E. Pessin, Eiichi Hinoi, and Gerard Karsenty. ”Glucose Uptake and Runx2 Synergize to Orchestrate Osteoblast Differentiation and Bone Formation”. *Cell*, 161:1576–1591, 2015.

[72] Marina Panek, Inga Marijanović, and Alan Ivković. ”Stem cells in bone regeneration”. *Periodicum Biologorum*, 117:177–184, 2015.

[73] R Zohar, S Cheifetz, C A McCulloch, and J Sodek. ”Analysis of intracellular osteopontin as a marker of osteoblastic cell differentiation and mesenchymal cell migration”. *Eur. J. Oral Sci.*, 106:407–407, 1998.

[74] Liang Wang, Zheng yao Li, Yi peng Wang, Zhi hong Wu, and Bin Yu. ”Dynamic Expression Profiles of Marker Genes in Osteogenic Differentiation of Human Bone Marrow-derived Mesenchymal Stem Cells”. *Chin Med Sci J*, 30:108–113, 2015.

[75] E. Birmingham, G.L. Niebur, P.E. McHugh, G. Shaw, F.P. Barry, and L.M. McNamara. ”Osteogenic Differentiation Of Mesenchymal Stem Cells Is Regulated By Osteocyte And Osteoblast Cells In A Simplified Bone Niche”. *European Cells and Materials*, 23:13–27, 2012.

[76] Robert H. Christenson. ”Biochemical Markers of Bone Metabolism: An Overview”. *Clinical Biochemistry*, 30:593–593, 1997.

[77] Markus J Seibel. ”Biochemical Markers of Bone Turnover Part I: Biochemistry and Variability”. *Clin. Biochem. Rev.*, 26:97–122, 2005.

[78] Riko Nishimura, Kenji Hata, Takuma Matsubara, Makoto Wakabayashi, and Toshiyuki Yoneda. ”Regulation of bone and cartilage development by network between BMP signalling and transcription factors”. *J. Biochem.*, 151:247–254, 2012.

[79] T. Katagiri and N. Takahashi. ”Regulatory mechanisms of osteoblast and osteoclast differentiation”. *Oral diseases*, 8:147–159, 2002.

[80] Christian Frantz, Kathleen M. Stewart, and Valerie M. Weaver. ”The extracellular matrix at a glance”. *Journal of Cell Science*, 123:4195–4200, 2010.

[81] Michael W. King. 2016.

[82] Sameer Varma, Mohsen Botlani, Jeff R. Hammond, H. Larry Scott, Joseph P. R. O. Orgel, and Jay D. Schieber. ”Effect of intrinsic and extrinsic factors on the simulated D-band length of type I collagen”. *Proteins*, 83:1800–1812, 2015.

[83] Shyam Rele, Yuhua Song, Robert P. Apkarian, Zheng Qu, Vincent P. Conticello, and Elliot L. Chaikof. ”D-Periodic Collagen-Mimetic Microfibers”. *J. Am. Chem. Soc.*, 129:14780–14878, 2007.

[84] Gilberto Goissis, Silvana Vargas da Silva Maginador, and Virginia da Conceiç$\tilde{a}$o Amaro Martins. ”Biomimetic Mineralization of Charged Collagen Matrices: In Vitro and In Vivo Study”. *Artificial Organs*, 27:437–443, 2003.

[85] Alexander J. Lausch, Bryan D. Quan, Jason W. Miklas, and Eli D. Sone. ”Extracellular Matrix Control of Collagen Mineralization In Vitro”. *Advanced Functional Materials*, 23:49064912, 2013.

[86] Jing He, Bo Jiang, Yun Dai, Jianyuan Hao, Zongke Zhou, Zhili Tian, Fang Wu, and Zhongwei Gu. ”Regulation of the osteoblastic and chondrocytic differentiation of stem

cells by the extracellular matrix and subsequent bone formation modes”. *Biomaterials*, 34:6580–6588, 2013.

[87] Sarah Cartmell. ”Controlled Release Scaffolds for Bone Tissue Engineering”. *Journal of Pharmaceutical Sciences*, 98:430–441, 2009.

[88] Zhinong Huang, Pei-Gen Ren, Ting Ma, R. Lane Smith, and Stuart B. Goodman. ”Modulating osteogenesis of mesenchymal stem cells by modifying growth factor availability”. *Cytokine*, 51:305–310, 2010.

[89] Ahmad Oryan, Soodeh Alidadi, Ali Moshiri, and Amin Bigham-Sadegh. ”Bone morphogenetic proteins: A powerful osteoinductive compound with non-negligible side effects and limitations”. *Biofactors*, 40:459–481, 2014.

[90] G E Friedlaender, C R Perry, J D Cole, S D Cook, G Cierny, G F Muschler, G A Zych, J H Calhoun, A J LaForte, and S Yin. ”Osteogenic Protein-1 (Bone Morphogenetic Protein-7) in the Treatment of Tibial Nonunions”. *J. Bone Joint Surg. Am.*, 83A:151–158, 2001.

[91] Catriona Y Logan and Roel Nusse. ”The Wnt Signalin Pathway in Development and Disease”. *Annual Review*, 20:781–810, 2004.

[92] Longxiang Shen, Julie Glowacki, and Shuanhu Zhou. ”Inhibition of adipocytogenesis by canonical WNT signaling in human mesenchymal stem cells”. *Experimental Cell Research*, 317:1796–1803, 2011.

[93] Lu lu Zhang, Jing jin Liu, Fang Liu, Wen hua Liu, Yong shun Wang, Bin Zhu, and Bo Yu. ”MiR-499 induces cardiac differentiation of rat mesenchymal stem cells through wnt/β-catenin signaling pathway”. *Biochemical and Biophysical Research Communications*, 420:875–881, 2012.

[94] Wulin You, Lihong Fan, Dapeng Duan, Lei Tian, Xiaoqian Dang, Chunsheng Wang, and Kunzheng Wang. ”Foxc2 over-expression in bone marrow mesenchymal stem cells

stimulates osteogenic differentiation and inhibits adipogenic differentiation". *Mol. Cell. Biochem.*, 386:125–134, 2014.

[95] Jiamin Wu, Kewen Wu, Feng Lin, Qing Luo, Li Yang, Yisong Shi, Guanbin Song, and Kuo-Li Paul Sung. "Mechano-growth factor induces migration of rat mesenchymal stem cells by altering its mechanical properties and activating ERK pathway". *Biochemical and Biophysical Research Communications*, 441:202–207, 2013.

[96] Xinxin Xiang, Jing Zhao, Geyang Xu, Yin Li, and Weizhen Zhang. "mTOR and the differentiation of mesenchymal stem cells". *Acta Biochim. Biophys. Sin.*, 43:501–510, 2011.

[97] Jiahai Xu, Zhanghua Li, Yudong Hou, and Weijun Fang. "Potential mechanisms underlying the Runx2 induced osteogenesis of bone marrow mesenchymal stem cells". *Am. J. Transl. Res.*, 7:2527–2535, 2015.

[98] Amelia Ahmad Khalili and Mohd Ridzuan Ahmad. "A Review of Cell Adhesion Studies for Biomedical and Biological Applications". *Int. J. Mol. Sci.*, 16:18149–18184, 2015.

[99] L A Hidalgo-Bastida and S H Cartmell. "Mesenchymal stem cells, osteoblasts and extracellular matrix proteins: enhancing cell adhesion and differentiation for bone tissue engineering". *Tissue Eng. Part B Rev.*, 16:405–412, 2010.

[100] Brenda K. Mann, Annabel T. Tsai, Timothy Scott-Burden, and Jennifer L. West. "Modification of surfaces with cell adhesion peptides alters extracellular matrix deposition". *Biomaterials*, 20:2281–2286, 1999.

[101] Alireza Rezania and Kevin E. Healy. "Integrin Subunits Responsible for Adhesion of Human Osteoblast-like Cells to Biomimetic Peptide Surfaces". *Journal of Orthopaedic Research*, 17:615–623, 1999.

[102] Brenda K. Mann and Jennifer L. West. ”Cell adhesion peptides alter smooth muscle cell adhesion, proliferation, migration, and matrix protein synthesis on modified surfaces and in polymer scaffolds”. *J. Biomed. Mater. Res.*, 60:86–93, 2002.

[103] Mandana Veiseh, Omid Veiseh, Michael C. Martin, Fareid Asphahani, and Miqin Zhang. ”Short Peptides Enhance Single Cell Adhesion and Viability on Microarrays”. *Langmuir*, 23:4472–4479, 2007.

[104] Rachelle N. Palchesko, Jared D. Romeo, Kenneth A. McGowan, and Ellen S. Gawalt. ”Increased osteoblast adhesion on physically optimized KRSR modified calcium aluminate”. *J. Biomed. Mater. Res. Part A*, 100A:1229–1238, 2012.

[105] Martin Schuler, Douglas W. Hamilton, Tobias P. Kunzler, Christoph M. Sprecher, Michael de Wild, Donald M. Brunette, Marcus Textor, and Samuele G. P. Tosatti. ”Comparison of the Response of Cultured Osteoblasts and Osteoblasts Outgrown From Rat Calvarial Bone Chips to Nonfouling KRSR and FHRRIKA-Peptide Modified Rough Titanium Surfaces”. *Journal of Biomedical Materials Research Part B: Applied Biomaterials*, 91B:517–527, 2009.

[106] I Bilem, P Chevallier, L Plawinski, ED Sone, MC Durrieu, and G Laroche. ”RGD and BMP-2 mimetic peptide crosstalk enhances osteogenic commitment of human bone marrow stem cells.”. *Acta Biomater.*, 36:132–142, 2016.

[107] Sun-Mi Kim, Ji-Ung Jung, Jae-Sung Ryu, Jung-Woo Jin, Hyo-Jung Yang, Kisung Ko, Hyung-Keun You, Kyu-Yong Jung, and Young-Kug Choo. ”Effects of gangliosides on the differentiation of human mesenchymal stem cells into osteoblasts by modulating epidermal growth factor receptors”. *Biochemical and Biophysical Research Communications*, 371:866–871, 2008.

[108] Caixia Xu, Zebin Zheng, LiMing Fang, Naru Zhao, Zihong Lin, Tangzhao Liang, Zhichen Zhai, and Jiaan Zhou. ”Phosphatidylserine enhances osteogenic differentiation in human

mesenchymal stem cells via ERK signal pathways". *Materials Science and Engineering C*, 33:1783–1788, 2013.

[109] Andreas Zablotni, Olga Dakischewa, Katja Trinkaus, Sonja Hartmann, Gabor Szalay, Christian Heiss, and Katrin Susanne Lips. "Regulation of acetylcholine receptors during differentiation of bone mesenchymal stem cells harvested from human reaming debris". *International Immunopharmacology*, 29:119–126, 2015.

[110] Rajat K. Das and Omar F. Zouani. "A review of the effects of the cell environment physicochemical nanoarchitecture on stem cell commitment". *Biomaterials*, 35:5278–5293, 2014.

[111] Daniel J Kelly and Christopher R Jacobs. "The Role of Mechanical Signals in Regulating Chondrogenesis and Osteogenesis of Mesenchymal Stem Cells". *Birth Defects Research C*, 90:75–85, 2010.

[112] Adam J. Engler, Shamik Sen, H. Lee Sweeney, and Dennis E. Discher. "Matrix Elasticity Directs Stem Cell Lineage Specification". *Cell*, 126:677–689, 2006.

[113] Seyed Jamaleddin Mousavi and Mohamed Hamdy Doweidar. "Role of Mechanical Cues in Cell Differentiation and Proliferation: A 3D Numerical Model". *PLOS one*, 2012.

[114] Akon Higuchi, Qing-Dong Ling, Yung Chang, Shih-Tien Hsu, and Akihiro Umezawa. "Physical Cues of Biomaterials Guide Stem Cell Differentiation Fate". *Chemical Reviews*, 113:32973328, 2013.

[115] Akon Higuchi, Qing-Dong Ling, Yung Chang, Shih-Tien Hsu, and Akihiro Umezawa. "Physical Cues of Biomaterials Guide Stem Cell Differentiation Fate". *Chemical Reviews*, 113:32973328, 2013.

[116] TomBongiorno, JacobKazlow, Roman Mezencev, Sarah Griffiths, Rene Olivares-Navarrete, John F McDonald, Zvi Schwartz, Barbara D Boyan, Todd C McDevitt, and Todd

Sulchek. ”Mechanical stiffness as an improved single-cell indicator of osteoblastic human mesenchymal stem cell differentiation”. *Journal of Biomechanics*, 47:2197–2294, 2014.

[117] Andrew J Steward and Daniel J Kelly. ”Mechanical regulation of mesenchymal stem cell differentiation”. *Journal of Anatomy*, 227:717–731, 2015.

[118] Jeroen Eyckmans and Christopher S. Chen. ”Sticky mechanical memory”. *Nature Materials*, 13:542–543, 2014.

[119] Masakazu Yamada, Takahisa Anada, Taisuke Masuda, Teruko Takano-Yamamoto, and Osamu Suzuki. ”Effect of mechanical stress on differentiation of mouse mesenchymal stem cells seeded into an octacalcium phosphate?gelatin scaffold”. *Sensors and Actuators B: Chemical*, 220:125–130, 2015.

[120] Runguang Li, Liang Liang, Yonggang Dou, Zeping Huang, Huiting Mo, Yaning Wang, and Bin Yu. ”Mechanical stretch inhibits mesenchymal stem cell adipogenic differentiation through TGFβ1/Smad2 signaling”. *Journal of Biomechanics*, 48:3665–3671, 2015.

[121] Michael Levin and Mark Mercola. ”The compulsion of chirality: toward an understanding of leftright asymmetry”. *Genes and development*, 12:763769, 1998.

[122] Qiangying Yi, Xiantao Wen, Li Li, Bin He, Yu Nie, Yao Wu, Zhirong Zhang, and Zhongwei Gu. ”The chiral effects on the responses of osteoblastic cells to the polymeric substrates”. *European Polymer Journal*, 45:1970–1978, 2009.

[123] Xuan Wang, Kai Ye, Zhenhua Li, Ce Yan, and Jiandong Ding. ”Adhesion, proliferation, and differentiation of mesenchymal stem cells on RGD nanopatterns of varied nanospacings”. *Organogenesis*, 9:280–286, 2013.

[124] Weili Wei, Can Xu, Nan Gao, Jinsong Ren, and Xiaogang Qu. ”Opposing enantiomers of tartaric acid anchored on a surface generate different insulin assemblies and hence contrasting cellular responses”. *Chemical Science*, 5:4367, 2014.

[125] Alexandre Cunha, Omar Farouk Zouani, Laurent Plawinski, Ana Maria andBotelho do Rego, Amélia Almeida, Rui Vilar, and Marie-Christine Durrieu. ”Human mesenchymal stem cell behavior on femtosecond laser-textured Ti-6Al-4V surfaces”. *Nanomedicine*, 10:725–739, 2015.

[126] Alexandre Cunha. *”Multiscale femtosecond laser surface texturing of titanium and titanium alloys for dental and orthopaedic implants”*. PhD thesis, Université de Bordeaux and Téchnico Lisboa, 2015.

[127] Lesley Y. Chan, William R. Birch, Evelyn K.F. Yim, and Andre B.H. Choo. ”Temporal application of topography to increase the rate of neural differentiation from human pluripotent stem cells”. *Biomaterails*, 34:382–392, 2013.

[128] Rajeswari Ravichandran, Radhakrishnan Sridhar, Jayarama Reddy Venugopal, Subramanian Sundarrajan, Shayanti Mukherjee, and Seeram Ramakrishna. ”Gold Nanoparticle Loaded Hybrid Nanofibers for Cardiogenic Differentiation of Stem Cells for Infarcted Myocardium Regeneration”. *Macromolecular Bioscience*, 14:515–525, 2014.

[129] Pei-Leun Kang, Chih-Hao Chen, Shu Ying Chen, Yi-Jhen Wu, Chia Yun Lin, Feng-Huei Lin, and Shyh Ming Kuo. ”Nano-sized collagen I molecules enhanced the differentiation of rat mesenchymal stem cells into cardiomyocytes”. *J. Biomed. Mater. Res. Part A*, 101:2808–2816, 2013.

[130] Giulio Abagnale, Michael Steger, Vu Hoa Nguyen, Nils Hersch, Antonio Sechi, Sylvia Joussen, Bernd Denecke, Rudolf Merkel, Bernd Hoffmann, Alice Dreser, Uwe Schnakenberg, Arnold Gillner, and Wolfgang Wagner. ”Surface topography enhances differentiation of mesenchymal stem cells towards osteogenic and adipogenic lineages”. *Biomaterials*, 61:316–326, 2015.

[131] Elisa Migliorini, Jelena Ban, Gianluca Grenci, Laura Andolfi, Alessandro Pozzato, Massimo Tormen, Vincent Torre, and Marco Lazzarino. ”Nanomechanics Controls Neuronal Precursors Adhesion and Differentiation”. *Biotechnol. Bioeng.*, 110:23012310, 2013.

[132] Wenxin Geng, Dongyang Ma, Xingrong Yan, Liangqi Liu, Jihong Cui, Xin Xie, Hongmin Li, and Fulin Chen. ”Engineering tubular bone using mesenchymal stem cell sheets and coral particles”. *Bioch emical an dBiophysical Research Com munications*, 433:595?601, 2013.

[133] Alongkorn Pimpin and Werayut Srituravanich. ”Review on Micro- and Nanolithography Techniques and their Applications”. *Engineering Journal*, 16, 2012.

[134] Rong Peng, Xiang Yao, and Jiandong Ding. ”Effect of cell anisotropy on differentiation of stem cells on micropatterned surfaces through the controlled single cell adhesion”. *Biomaterials*, 32:8048–8057, 2011.

[135] Xuan Wang, Shiyu Li, Ce Yan, Peng Liu, and Jiandong Ding. ”Fabrication of RGD Micro/Nanopattern and Corresponding Study of Stem Cell Differentiation”. *Nano Letters*, 15:1457–1467, 2015.

[136] Kai Ye, Xuan Wang, Luping Cao, Shiyu Li, Zhenhua Li, Lin Yu, and Jiandong Ding. ”Matrix Stiffness and Nanoscale Spatial Organization of Cell-Adhesive Ligands Direct Stem Cell Fate”. *Nano Letters*, 15:4720–4729, 2015.

[137] Rebecca Medda, Arne Helth, Patrick Herre, Darius Pohl, Bernd Rellinghaus, Nadine Perschmann, Stefanie Neubauer, Horst Kessler, Steffen Oswald, Jürgen Eckert, Joachim P Spatz andAnnett Gebert, and Elisabetta A Cavalcanti-Adam. ”Investigation of early cell surface interactions of human mesenchymal stem cells on nanopatterned β-type titanium-niobium alloy surfaces”. *Interface Focus*, 4, 2013.

[138] Sébastien G Ricoult, Jennifer S Goldman, David Stellwagen, David Juncker, and Timothy E Kennedy. ”Generation of microisland cultures using microcontact printing to pattern protein substrates”. *Journal of Neuroscience matters*, 208:10–17, 2012.

[139] A G Castaño, V Hortigüela, A Lagunas, C Cortina, N Montserrat, J Samitier, and E Martínez. ”Protein patterning on hydrogels by direct microcontact printing: application to cardiac differentiation”. *RCS Advances*, 4:29120–29123, 2014.

[140] Julie A Phillippi, Eric Miller, Lee Weiss, Johnny Huard, Alan Waggoner, and Phil Campbell. ”Microenvironments Engineered by Inkjet Bioprinting Spatially Direct Adult Stem Cells Toward Muscle- and Bone-Like Subpopulations”. *Stem Cells*, 26:127–134, 2008.

[141] Somayeh Ebrahimi-Barough, Abbas Norouzi Javidan, Hoshangh Saberi, Mohammad Tghi Joghataei, Reza Rahbarghazi, Esmaeil Mirzaei, Faezeh Faghihi, Sadegh Shirian, Armin Ai, and Jafar Ai. ”Evaluation of Motor Neuron-Like Cell Differentiation of hEnSCs on Biodegradable PLGA Nanofiber Scaffolds”. *Mol. Neurobiol.*, 52:1704–1713, 2015.

[142] Wojtek Tutak, Sumona Sarkar, Sheng Lin-Gibson, Tanya M. Farooque, Giri Jyotsnendu, Dongbo Wang, Joachim Kohn, Durgadas Bolikal, and Carl G. Simon Jr. ”The support of bone marrow stromal cell differentiation by airbrushed nanofiber scaffolds”. *Biomaterials*, 34:2389–2398, 2013.

[143] Ke Cheng and William S Kisaalita. ”Exploring Cellular Adhesion and Differentiation in a Micro-/Nano-Hybrid Polymer Scaffold”. *Biotechnol. Prog.*, 26:838–846, 2010.

[144] K. Wingate, W. Bonani, Y. Tan, S. J. Bryant, and W. Tan. ”Compressive elasticity of three-dimensional nanofiber matrix directs mesenchymal stem cell differentiation to vascular cells with endothelial or smooth muscle cell markers”. *Acta Biomaterialia*, 8:1440–1449, 2012.

[145] Koshiro Sonomoto, Kunihiro Yamaoka, Hiroaki Kaneko, Kaoru Yamagata, Kei Sakata, Xiangmei Zhang, Masahiro Kondo, Yukichi Zenke, Ken Sabanai, Shingo Nakayamada,

Akinori Sakai, and Yoshiya Tanaka. ”Spontaneous Differentiation of Human Mesenchymal Stem Cells on Poly-Lactic-Co-Glycolic Acid Nano-Fiber Scaffold”. *PLOS One*, 11:1–15, 2016.

[146] Shreyas Shah, Perry T. Yin, Thiers M. Uehara, Sy-Tsong Dean Chueng, Letao Yang, and Ki-Bum Lee. ”Guiding Stem Cell Differentiation into Oligodendrocytes Using Graphene-Nanofi ber Hybrid Scaffolds”. *Materials Views*, 26:3673–3680, 2014.

[147] Girish Kumar, Michael S. Waters, Tanya M. Farooque, Marian F. Young, and Carl G. Simon Jr. ”Freeform fabricated scaffolds with roughened struts that enhance both stem cell proliferation and differentiation by controlling cell shape”. *Biomaterials*, 33:4022–4030, 2012.

[148] Melike Sever, Busra Mammadov, Mustafa O Guler, and Ayse B Tekinay. ”Tenascin-C Mimetic Peptide Nanofibers Direct Stem Cell Differentiation to Osteogenic Lineage”. *Biomacromolecules*, 15:4480–4487, 2014.

[149] Kazuto Fukunaga, Hiroshi Tsutsumi, and Hisakazu Mihara. ”Self-Assembling Peptide Nanofibers Promoting Cell Adhesion and Differentiation”. *Peptide Science*, 100, 2013.

[150] Shumeng Bai, Hongyan Han, Xiaowei Huang, Weian Xu, David L. Kaplan, Hesun Zhu, and Qiang Lu. ”Silk scaffolds with tunable mechanical capability for cell differentiation”. *Acta Biomaterialia*, 20:22–31, 2015.

[151] Lauren S. Sefcik, Rebekah A. Neal, Stephanie N. Kaszuba, Anna M. Parker, Adam J. Katz andRoy C. Ogle, and Edward A. Botchwey. ”Collagen nanofibres are a biomimetic substrate for the serum-free osteogenic differentiation of human adipose stem cells”. *Journal of Tissue Engineering and Regenerative Medicine*, 2:210–220, 2008.

[152] Anna M. Lipski, Christopher J. Pino, Frederick R. Haselton, I.-Wei Chen, and V. Prasad Shastri. ”The effect of silica nanoparticle-modified surfaces on cell morphology,cytoskeletal organization and function”. *Biomaterials*, 29:3836–3846, 2008.

[153] Shuhua Liu and Mingyon Han. ”Synthesis, Functionalization and Bioconjugation of Monodisperse, Silica-coated Gold Nanoparticles: Robust Bioprobes”. *Advanced Functional Materials*, 15:961?967, 2005.

[154] Bo Wang, Qing Cai, Shen Zhang, Xiaoping Yang, and Xuliang Deng. ”The effect of poly (L-lactic acid) nanofiber orientation on osteogenic responses of human osteoblast-like MG63 cells”. *Journal of the mechanical behaviour of biomedical materials*, 4:600–609, 2011.

[155] Elisabeth H. C. van Manen, Weibo Zhang, X. Frank Walboomers, Betsy Vazquez, Fang Yang, Wei Ji, Na Yu, Daisy J. Spear, John A. Jansen, and Pamela C. Yelick. ”The influence of electrospun fibre scaffold orientation and nano-hydroxyapatite content on the development of tooth bud stem cells in vitro”. *Odontology*, 102:14–21, 2014.

[156] V. Bayati, L. Altomare, M. C. Tanzi, and S. Farè. ”Adipose-derived stem cells could sense the nano-scale cues as myogenic-differentiating factors”. *J. Mater. Sci: mater. Med.*, 24:2439–2447, 2013.

[157] Seon Namgung, Ku Youn Baik, Juhun Park, and Seunghun Hong. ”Controlling the Growth and Differentiation of Human Mesenchymal Stem Cells by the Arrangement of Individual Carbon Nanotubes”. *ACSnano*, 5:73837390, 2011.

[158] Akhil Patel, Shilpaa Mukundan, Wenhu Wangand Anil Karumuri, Vinayak Sant, Sharmila M. Mukhopadhyay, and Shilpa Sant. ”Carbon-based hierarchical scaffolds for myoblast differentiation: Synergy between nano-functionalization and alignment”. *Acta Biomaterialia*, 32:77–88, 2016.

[159] Xingjie Zan, Sheng Feng, Elizabeth Balizan, Yuan Lin, and Qian Wang. ”Facile Method for Large Scale Alignment of One Dimensional Nanoparticles and Control over Myoblast Orientation and Differentiation”. *ACSnano*, 7:8385–8396, 2013.

[160] Vipuil Kishore, Whitney Bullock, Xuanhao Sun, William Scott Van Dyke, and Ozan Akkus. ”Tenogenic differentiation of human MSCs induced by the topography of electrochemically aligned collagen threads”. *Biomaterials*, 33:2137–2144, 2012.

[161] Milton J. Rosen and Joy T. Kunjappu. *”Surfactants and Interfacial Phenomena”*. Wiley, 2012.

[162] S. K. Hait and S. P. Moulik. ”Gemini surfactants: A distinct class of self-asembling molecules”. *Current Science*, 82:1101–1111, 2002.

[163] Fredric M. Menger and Jason S. Keiper. ”Gemini surfactants”. *Angew. Chem. Int. Ed.*, 39:1906–1920, 2000.

[164] Amelia M. Lapeñ a, Adam F. Gross, and Sarah H. Tolbert. ”Examining the Role of Surfactant Packing in Phase Transformations of Periodic Templated Silica/Surfactant Composites”. *Langmuir*, 21:470–480, 2005.

[165] Martin In and Raoul Zana. ”Phase Behavior of Gemini Surfactants”. *Journal of Dispersion Science and Technology*, 28:142–154, 2007.

[166] Anthony J. Kirby, Patrick Camilleri, Jan B. F. N. Engberts, Martin C. Feiters, Roeland J. M. Nolte, Olle Söderman, Mark Bergsma, Matthew L. Fielden Paul C. Bell, Cristina L. García Rodríguez, Philippe Guédat, Andreas Kremer, Caroline McGregor, Christele Perrin, Gaël Ronsin, and Marcel C. P. van Eijk. ”Gemini Surfactants: New Synthetic Vectors for GeneTransfection”. *Angew. Chem. Int. Ed.*, 42:1448–1457, 2003.

[167] Honggang Cui, Matthew J. Webber, and Samuel I. Stupp. ”Self-Assembly of Peptide Amphiphiles: From Molecules to Nanostructures to Biomaterials”. *Peptide Science*, 94, 2009.

[168] Mikhail A. Voronin, Dinar R. Gabdrakhmanov, Ravil N. Khaibullin, Irina Yu. Strobykina, Vladimir E. Kataev, Bulat Z. Idiyatullin, Dzhigangir A. Faizullin, Yuriy F. Zuev, Lucia Ya.

Zakharova, and Alexander I. Konovalov. ”Novel biomimetic systems based on amphiphilic compounds with a diterpenoid fragment: Role of counterions in self-assembly”. *Journal of Colloid and Interface Science*, 405:125–133, 2013.

[169] Qing He, Yu-Fei Ao, Zhi-Tang Huang, and De-Xian Wang. ”Self-Assembly and Disassembly of Vesicles as Controlled by Anionπ Interactions”. *Angew. Chem. Int. Ed.*, 54:11785–11790, 2015.

[170] H. Christopher Fry, Jamie M. Garcia, Matthew J. Medina, Ulises M. Ricoy, David J. Gosztola, Maxim P. Nikiforov, Liam C. Palmer, , and Samuel I. Stupp. ”Self-Assembly of Highly Ordered Peptide Amphiphile Metalloporphyrin Arrays”. *J. Am. Chem. Soc.*, 134:1464614649, 2012.

[171] Arijit Ghosh, Mark Haverick, Keith Stump, Xiangyu Yang, Michael F. Tweedle, and Joshua E. Goldberger. ”Fine-Tuning the pH Trigger of Self-Assembly”. *J. Am. Chem. Soc.*, 134:36473650, 2012.

[172] Jingnan Luo and Yen Wah Tong. ”Self-Assembly of Collagen-Mimetic Peptide Amphiphiles into Biofunctional Nanofiber”. *ACS Nano*, 5:77397747, 2011.

[173] Naoya Kobayashi, Keiichi Yanase, Takaaki Sato, Satoru Unzai, Michael H. Hecht, and Ryoichi Arai. ”Self-Assembling Nano-Architectures Created from a Protein Nano-Building Block Using an Intermolecularly Folded Dimeric de Novo Protein”. *J. Am. Chem. Soc.*, 137:1128511293, 2015.

[174] Yihua Loo, Shuguang Zhang, and Charlotte A.E. Hauser. ”From short peptides to nanofibers to macromolecular assemblies in biomedicine”. *Biotechnology Advances*, 30:593–603, 2012.

[175] Yuefei Wang, Wei Qi, Renliang Huang, Xuejiao Yang, Mengfan Wang, Rongxin Su, and Zhimin He. ”Rational Design of Chiral Nanostructures from Self-Assembly of a Ferrocene-Modified Dipeptide”. *JACS*, 137:7869–7880, 2015.

[176] Munenori Numataa and Seiji Shinkai. ”Supramolecular wrapping chemistry by helix-forming polysaccharides: a powerful strategy for generating diverse polymeric nano-architectures”. *Chem. Commun.*, 47:19611975, 2011.

[177] Yoshiko Kira, Yutaka Okazaki, Tsuyoshi Sawada, Makoto Takafuji, and Hirotaka Ihara. ”Amphiphilic molecular gels from x-aminoalkylated L-glutamic acid derivatives with unique chiroptical properties”. *Amino Acids*, 39:587–597, 2010.

[178] María J. Clemente, Pilar Romero, Joseé L. Serrano, Juliette Fitremann, and Luis Oriol. ”Supramolecular Hydrogels Based on Glycoamphiphiles: Effect of the Disaccharide Polar Head”. *Chem. Mater.*, 24:3847–3858, 2012.

[179] Christoph Boettcher, Holger Stark, and Martin van Heel. ”Stacked bilayer helices: a new structural organization of amphiphilic molecules”. *Ultramicroscopy*, 62:133–139, 1996.

[180] Naomi Sakai, Yuko Kamikawa, Masayuki Nishii, Toru Matsuoka, Takashi Kato, and Stefan Matile. ”Dendritic Folate Rosettes as Ion Channels in Lipid Bilayers”. *JACS*, 128:2218–2219, 2006.

[181] Fátima García, Julia Buendía, and Luis Sánchez. ”Supramolecular Ribbons from Amphiphilic Trisamides Self-Assembly”. *The Journal of Organic Chemistry*, 76:6271–6276, 2011.

[182] Stefania Bonazzi, Massimo Capobianco, Monica Miranda De Morais, Anna Garbesi, Giovanni Gottarelli, Paolo Marhi, Maria Grazia Ponzi Bassi, Gian Piero Spada, and Luisa Tondelli. ”Four-Stranded Aggregates of Oligodeoxyguanylates Forming Lyotropic Liquid Crystals: A Study by Circular Dichroism, Optical Microscopy, and X-ray Diffraction”. *JACS*, 113:5809–5916, 1991.

[183] Paolo Mariani, Claude Mazabard, Anna Garbesi, and Gian Piero Spada. ”A Study of the Structure of the Lyomesophases Formed by the Dinucleoside Phosphate d(GpG). An Approach by X-ray Diffraction and Optical Microscopy”. *JACS*, 111:6369–6373, 1989.

[184] Iartin Gellert, Marie N. Lipsett, and David R. Davies. ”Helix Formation By Guanylic Acid”. *Proc. N. A. S.*, 48:2013–2018, 1962.

[185] Željko Tomović, Joost van Dongen, Subi J. George, Hong Xu, Wojciech Pisula, Philippe Leclè re, Maarten M. J. Smulders, Steven De Feyter, E. W. Meijer, and Albertus P. H. J. Schenning. ”Star-Shaped Oligo(p-phenylenevinylene) Substituted Hexaarylbenzene: Purity, Stability, and Chiral Self-assembly”. *JACS*, 129:16190–16196, 2007.

[186] Damei Ke, Ailing Tang, Chuanlang Zhan, and Jiannian Yao. ”Conformation-variable PDI@b-sheet nanohelices show stimulus-responsive supramolecular chirality”. *Chem. Commun.*, 49:4914, 2013.

[187] Zheng Ren and Pu-Xian Gao. ”A review of helical nanostructures: growth theories, synthesis strategies and properties”. *Nanoscale*, 6:9366, 2014.

[188] Manashi Nath and B. A. Parkinson. ”Superconducting MgB_2 Nanohelices Grown on Various Substrates”. *J. Am. Chem. Soc.*, 129:11302–11303, 2007.

[189] Hongwei Lv, Lisha Li, Yin Zhang, Zhishen Chen, Meiyu Sun, Tiankai Xu, Licheng Tian, Man Lu, Min Ren, Yuanyuan Liu, and Yulin Li. ”Union is strength: matrix elasticity and microenvironmental factors codetermine stem cell differentiation fate”. *Cell Tissue Res.*, 361:657–669, 2015.

[190] John G. Gibbs, Andrew G. Mark, Tung-Chun Lee, Sahand Eslami, Debora Schamelab, and Peer Fischer. ”Nanohelices by shadow growth”. *Nanoscale*, 6:9457, 2014.

[191] Qin Yu, Lizhen Liu, Yanping Duan, Yan Wang, Xiaobo Xuan, Liping Zhou, and Wei Liu. ”Wnt/β-catenin signaling regulates neuronal differentiation of mesenchymal stem cells”. *Biochemical and Biophysical Research Communications*, 439:297–302, 2013.

[192] Colin Nuckolls, Thomas J. Katz, and Louis Castellanos. ”Aggregation of Conjugated Helical Molecules”. *JACS*, 118:3767–3768, 1996.

[193] Colin Nuckolls, Thomas J. Katz, Gail Katz, Peter J. Collings, and Louis Castellanos. ”Synthesis and Aggregation of a Conjugated Helical Molecule”. *JACS*, 121:79–88, 1999.

[194] Yuanyuan Shang, Yibin Li, Xiaodong He, Shanyi Du, Luhui Zhang, Enzheng Shi, Shiting Wu, Zhen Li, Peixu Li, Jinquan Wei, Kunlin Wang, Hongwei Zhu, Dehai Wu, and Anyuan Cao. ”Highly Twisted Double-Helix Carbon Nanotube Yarns”. *ACS Nano*, 7:14461453, 2013.

[195] Alicja Bachmatiuk, Felix Börrnert, Volker Hoffmann, Dirk Lindackers, Jarrn-Horng Lin, Bernd Büchner, and Mark H. Rümmeli. ”Hydrogen-induced self-assembly of helical carbon nanostructures from ethanol over SiO_2 catalysts”. *Journal of Applied Physics*, 109:094317–1, 2011.

[196] L. Dai, X. J. Huang, L. X. Dong, Q. Zhangd, and L. Zhang. ”Mechanically tough, elastic and stable rope-like double nanohelices”. *Nanoscale*, 6:9436, 2014.

[197] R. Oda, I. Huc, M. Schmutz, S. J. Candau, and F. C. MacKintosh. ”Tuning bilayer twist using chiral counterions”. *Nature*, 399:566–569, 1999.

[198] Damien Berthier, Thierry Buffeteau, Jean-Michel Lé ger, Reiko Oda, and Ivan Huc. ”From Chiral Counterions to Twisted Membranes”. *JACS*, 124:13486–13494, 2002.

[199] Reiko Oda, Franck Artzner, Michel Laguerre, and Ivan Huc. ”Molecular Structure of Self-Assembled Chiral Nanoribbons and Nanotubules Revealed in the Hydrated State”. *J. Am. Chem. Soc.*, 130:14705–14712, 2008.

[200] Jiaji Cheng. *”Fine-tuned Silica Nanohelices as Platforms for Chiral Organization of Gold Nanoparticles : Synthesis, Characterization and Chiroptical Analysis”*. PhD thesis, Bordeaux University, 2015.

[201] Thomas Delclos, Carole Aimé, Emilie Pouget, Aurélie Brizard, Ivan Huc, Marie-Hélène Delville, and Reiko Oda. ”Individualized Silica Nanohelices and Nanotubes: Tuning

Inorganic Nanostructures Using Lipidic Self-Assemblies". *Nano Letters*, 8:1929–1935, 2008.

[202] Naoya Ryu, Yutaka Okazaki, Kana Hirai, Makoto Takafuji, Shoji Nagaoka, Emilie Pouget, Hirotaka Ihara, and Reiko Oda. "Memorized chiral arrangement of gemini surfactant assemblies in nanometric hybrid organicsilica helices". *Chem. Commun.*, 52:5800, 2016.

[203] Aurélie Brizard, Carole Aimé, Thomas Labrot, Ivan Huc, Damien Berthier, Franck Artzner, Bernard Desbat, and Reiko Oda. "Counterion, Temperature, and Time Modulation of Nanometric Chiral Ribbons from Gemini-Tartrate Amphiphiles". *J. Am. Chem. Soc.*, 129:3754–3762, 2007.

[204] C. Jeffrey Brinker and George W. Scherer. *"Sol-Gel Science"*. Elsevier, 1990.

[205] Rumi Tamoto, Nicolas Daugey, Thierry Buffeteau, Brice Kauffmann, Makoto Takafuji, Hirotaka Iharad, and Reiko Oda. "*In situ* helicity inversion of self-assembled nano-helices". *Chem. Commun.*, 51:3518, 2015.

[206] Yutaka Okazaki, Jiaji Cheng, Dmytro Dedovets, Gregor Kemper, Marie-Hé lène Delville, Marie-Christine Durrieu, Hirotaka Ihara, Makoto Takafuji, Emilie Pouget, and Reiko Oda. "Chiral Colloids: Homogeneous Suspension of Individualized SiO2 Helical and Twisted Nanoribbons". *ACS Nano*, 8:6863–6872, 2014.

[207] R. Aelion, A. Loebel, F., and Eirich. "Hydrolysis of Ethyl Silicate". *J. Am. Chem. Soc.*, pages 5705–5712, 1950.

[208] R. K. Iler. "The Chemistry of Silica: Solubility, Polymerization, Colloid and Surface Properties, and Biochemistry". *J. Am. Chem. Soc.*, pages 5705–5712, 1950.

[209] Dmytro Dedovets. *"Cationic gemini amphiphiles : from chiral organic self-assembly towards functional composite micro- and nanomaterials"*. PhD thesis, Université de Bordeaux, 2014.

[210] Robert M. Pasternack, Sandrine Rivillon Amy, and Yves J. Chabal. ”Attachment of 3-(Aminopropyl)triethoxysilane on Silicon Oxide Surfaces: Dependence on Solution Temperature”. *Langmuir*, 24:12963–12971, 2008.

[211] Nesrine Aissaoui, Latifa Bergaoui, Jessem Landoulsi, Jean-François Lambert, and Souhir Boujday. ”Silane Layers on Silicon Surfaces: Mechanism of Interaction, Stability, and Influence on Protein Adsorption”. *Langmuir*, 28:656665, 2012.

[212] Rajat K. Das, Omar F. Zouani, Christine Labrugère, Reiko Oda, and Marie-Christine Durrieu. ”Influence of Nanohelical Shape and Periodicity on Stem Cell Fate”. *ACS Nano*, 7:3351–3361, 2013.

[213] E. De Giglio L. Sabbatini, S. Colucci, and G. Zambonini. ”Synthesis, analytical characterization, and osteoblast adhesion properties on RGD-grafted polypyrrole coatings on titanium substrates”. *J. Biomater. Sci. Polymer Edn*, 11:1073–1083, 2000.

[214] Arthur W Miller and John F Robyt. ”Sodium cyanoborohydride in the immobilization of proteins to glutaraldehyde activated aminoalkyl silica”. *Biotechnology and Bioengineering*, 25:2795–2800, 1983.

[215] Graziella El Khoury, Emmanuelle Laurenceau, Vincent Dugas, Yann Chevolot, Yves Mérieux, Marie-Christine Duclos, Eliane Souteyrand, Dominique Rigal, Jean Wallach, and Jean Pierre Cloarec. ”Acid deprotection of covalently immobilized peptide probes on glass slides for peptide microarrays”. *Proceedings of the 29th Annual International Conference of the IEEE EMBS*, 2007.

[216] Paola Brun, Michele Scorzeto, Stefano Vassanelli, Ignazio Castagliuolo, Giorgio Palù, Francesca Ghezzo, Grazia M.L. Messina, Giovanna Iucci, Valentina Battaglia, Stefano Sivolella, Andrea Bagno, Giovanni Polzonetti, Giovanni Marletta, and Monica Dettin. ”Mechanisms underlying the attachment and spreading of human osteoblasts: From

transient interactions to focal adhesions on vitronectin-grafted bioactive surfaces". *Acta Biomaterialia*, 9:61056115, 2013.

[217] Frederic Murschel, Benoit Liberelle, Gilles St-Laurent, Mario Jolicoeur, Yves Durocher, and Gregory De Crescenzo. "Coiled-coil-mediated grafting of bioactive vascular endothelial growth factor". *Acta Biomaterialia*, 9:68066813, 2013.

[218] Namrata Dixit, Jenifer K. Settle, Qiang Ye, Cindy L. Berrie, Paulette Spencer, and Jennifer S. Laurence. "Grafting MAP peptide to dental polymer inhibits MMP-8 activity". *J. Biomed. Mater. Res. Part B*, 103:324331, 2015.

[219] Vincent Rerat, Vincent Pourcelle, Sabrina Devogue, Bernard Nysten, and Jacqueline Marchand-Brynaert. "Surface Grafting on Poly(ethylene terephthalate) Track-Etched Microporous Membrane by Activation with Trifluorotriazine: Application to the Biofunctionalization with GRGDS Peptide". *Journal of Polymer Science*, 48:195208, 2010.

[220] Jessie Peyre, Vincent Humblot, Christophe Meéthivier, Jean-Marc Berjeaud, and Claire-Marie Pradier. "Co-Grafting of AminoPoly(ethylene glycol) and Magainin I on a TiO2 Surface: Tests of Antifouling and Antibacterial Activities". *Journal of Physical Chemistry B*, 116:1383913847, 2012.

[221] Lina Xua, Jianhui Liaoa, Lan Huanga, Danlin Oub, Zhirui Guoa, Haiqian Zhanga, Cunwang Gea, Ning Gua, and Juzheng Liu. "Surface-bound nanoparticles for initiating metal deposition". *Thin Solid Films*, 434:121–125, 2003.

[222] Shekhar Agnihotri, Soumyo Mukherji, and Suparna Mukherji. "Immobilized silver nanoparticles enhance contact killing and show highest efficacy: elucidation of the mechanism of bactericidal action of silver". *Nanoscale*, 5:7328, 2013.

[223] Ondřej Kvítek, Marek Bot, and Václav Švorčík. "Gold nanoparticles grafting on glass surface". *Applied Surface Science*, 258:8991 8995, 2012.

[224] Zdenka Novotna, Alena Reznickova, Ondrej Kvitek, Nikola Slepickova Kasalkova andZdenka Kolska, and Vaclav Svorcik. ”Cells adhesion and growth on gold nanoparticle grafted glass”. *Applied Surface Science*, 307:217–223, 2013.

[225] Timothy D. Sargeant, Mukti S. Rao, Chung-Yan Koh, and Samuel I. Stupp. ”Covalent functionalization of NiTi surfaces with bioactive peptide amphiphile nanofibers”. *Biomaterials*, 29:1085–1098, 2008.

[226] Frank Balzer, Christian Röthel, Horst-Guünter Rubahn, Arne Luützen, Juürgen Parisi, Roland Resel, and Manuela Schiek. ”Thin Film Phase and Local Chirality of Surface-Bound MOP4 Nanofibers”. *J. Phys. Chem. C*, 120:7653–7661, 2016.

[227] the editors of E.B. Electron microscopy, 2011.

[228] C B Prater, H J Butt, and P K Hansma. ”Atomic force microscopy”. *Nature*, 345:839–840, 1990.

[229] Emanuel Heindl. ”Rasterkraftmikroskopie (atomic force microscopy AFM)”. *Regensbrug University*, 2003.

[230] Charles C Chusnei and D Wayne Goodman. *”X-Ray Photoelectron spectroscopy”*. Academic Press, 2002.

[231] Alfred Benninghoven. ”Chemical Analysis of Inorganic and Organic Surfaces and Thin Films by Static Time-of-Flight Secondary Ion Mass Spectrometry (TOF-SIMS)”. *Angew. Chem. Imt. Ed. Engl.*, 33:1023–43, 1994.

[232] Aurélie Brizard, Carole Aimé, Thomas Labrot, Ivan Huc, Damien Berthier, Franck Artzner, Bernard Desbat, and Reiko Oda. ”Counterion, Temperature, and Time Modulation of Nanometric Chiral Ribbons from Gemini-Tartrate Amphiphiles”. *J. Am. Chem. Soc.*, 129:3754–3762, 2007.

[233] Jessem Landoulsi, Michel J. Genet, Sandrine Fleith, Yetioman Touréd, Irma Liascukiene, Christophe Méthivier, and Paul G. Rouxhet. ”Organic adlayer on inorganic materials: XPS analysis selectivity to cope with adventitious contamination”. *Applied Surface Science*, 383:71–83, 2016.

[234] G. Iucci, C. Battocchio, M. Dettin, F. Ghezzo, and G. Polzonetti. ”An XPS study on the covalent immobilization of adhesion peptides on a glass surface”. *Solid State Science*, 12:1861–1865, 2010.

[235] M. C. Porté-Durrieu, C. Labrugère, F. Villars, F. Lefebvre, S. Dutoya, A. Guette, L. Bordenave, and C. Baquey. ”Development of RGD peptides grafted onto silica surfaces: XPS characterization and human endothelial cell interactions”. *Journal of Biomedical Materials Research*, 46:368–375, 1999.

[236] Stéphane Pallu, Chantal Bourget, Reine Bareille, Christine Labrugere, Michel Dard, Andreas Sewing, Alfred Jonczyke, Michel Vernizeau, Marie Christine Durrieu, and Joelle Amédée-Vilamitjana. ”The effect of cyclo-DfKRG peptide immobilization on titanium on the adhesion and differentiation of human osteoprogenitor cells”. *Biomaterials*, 26:69326940, 2004.

[237] Zhe (Annie) Cheng. *”Biological Multi-Functionalization and Surface Nanopatterning of Biomaterials”*. PhD thesis, Université de Bordeaux, 2013.

[238] Julia S. Apte, Galen Collier, Robert A. Latour, Lara J. Gamble, and David G. Castner. ”XPS and ToF-SIMS Investigation of α-Helical and β-Strand Peptide Adsorption onto SAMs”. *Langmuir*, 26:3423–3432, 2010.

[239] C Chollet, C Chanseau, M Remy, A Guignandon, R Bareille, C Labrugre, L Bordenave, and M. C. Durrieu. ”The effect of RGD density on osteoblast and endothelial cell behavior on RGD-grafted polyethylene terephthalate surfaces”. *Biomaterials*, 30:711–720, 2009.

[240] N.M. Moore, N.J. Lin, N.D. Gallant, and M.L. Becker. ”Synergistic enhancement of human bone marrow stromal cell proliferation and osteogenic differentiation on BMP-2-derived and RGD peptide concentration gradients”. *Acta Biomaterialia*, 7:2091–2100, 2011.

[241] Xuezhong He, Junyu Ma, and Esmaiel Jabbari. ”Effect of Grafting RGD and BMP-2 Protein-Derived Peptides to a Hydrogel Substrate on Osteogenic Differentiation of Marrow Stromal Cells”. *Langmuir*, 24:12508–12516, 2008.

[242] Thermofisher scientific company website. `www.thermofisher.com`. 24. 3. 2017.

[243] S.P Massia and J.A. Hubbell. ”An RGD spacing of 440 nm is sufficient for integrin alpha V beta 3-mediated fibroblast spreading and 140 nm for focal contact and stress fiber formation.”. *J Cell Biol*, 114:1089–1100, 1991.

[244] A. Rezania and K.E. Healy. ”The effect of peptide surface density on mineralization of a matrix deposited by osteogenic cells.”. *J Biomed Mater Res*, 15 52:595–600, 2000.

[245] B. W. Wright, P. A. Peaden, and M. L. Lee. ”Determination of Surface Hydroxyl Concentration on Glass and Fused Silica Capillary Columns”. *Chromatographia*, 15:584–586, 1982.

[246] A. Simon, T. Cohen-Bouhacina, M. C. Porté, J. P. Aimé, and C. Baquey. ”Study of Two Grafting Methods for Obtaining a 3-Aminopropyltriethoxysilane Monolayer on Silica Surface”. *Journal of Colloid and Interface Science*, 251:278–283, 2002.

[247] Dang Viet Quang, T. Alan Hatton, and Mohammad R. M. Abu-Zahra. ”Thermally Stable Amine-Grafted Adsorbent Prepared by Impregnating 3-Aminopropyltriethoxysilane on Mesoporous Silica for CO_2 Capture”. *Ind. Eng. Chem. Res.*, 55:7842–7582, 2016.

[248] L. Pichavant, H. Carrie, M.N. Nguyen, L. Plawinski, M.-C. Durrieu, and V. Heroguez. ”Vancomycin Functionalized Nanoparticles for Bactericidal Biomaterial Surfaces”. *Biomacromolecules*, 17:1339–1346, 2016.

[249] Loïc Pichavant, Gilles Amador, Cédric Jacqueline, and Marie-Christine Durrieu Brigitte Brouillaud, Valérie Héroguez. ”pH-controlled delivery of gentamicin sulfate from orthopedic devices preventing nosocomial infections”. *Journal of Controlled Release*, 162:373–381, 2012.

[250] Minh Ngoc Nguyen, Thomas Lebarbe, Omar F. Zouani, Loïc Pichavant, Marie-Christine Durrieu, and Valérie Hérogeuz. ”Impact of RGD Nanopatterns grafted onto Titanium on Osteoblastic Cell Adhesion”. *Biomacromolecules*, 13:896–904, 2012.

[251] Timothy D. Sargeant, Mukti S. Rao, Chung-Yan Koh, and Samuel I. Stupp. ”Covalent functionalization of NiTi surfaces with bioactive peptide amphiphile nanofibers”. *Biomaterials*, 29:1085–1098, 2008.

[252] L. Pichavant, H. Carrie, M.N. Nguyen, L. Plawinski, M.-C. Durrieu, and V. Heroguez. ”Matthew P. Nicholas and Lu Rao and Arne Gennerich”. *Methods Mol. Biol.*, 1136:137–169, 2014.

[253] Shilpi Chaudhary, Tripta Kamra, Khan Mohammad Ahsan Uddin, Olesia Snezhkova, H. Surangi N. Jayawardena, Mingdi Yan, Lars Montelius, Joachim Schnadt, and Lei Ye. ”Controlled short-linkage assembly of functional nano-objects”. *Applied Surface Science*, 300:22–28, 2014.

[254] Tripta Kamra, Shilpi Chaudhary, Changgang Xu, Niclas Johansson, Lars Montelius, Joachim Schnadt, and Lei Ye. ”Covalent immobilization of molecularly imprinted polymer nanoparticles using an epoxy silane”. *Journal of Colloid and Interface Science*, 445:277–284, 2015.

[255] Samer Doughan, Yi Han, Uvaraj Uddayasankar, and Ulrich J. Krull. ”Solid-Phase Covalent Immobilization of Upconverting Nanoparticles for Biosensing by Luminescence Resonance Energy Transfer”. *ACS Applied Materials and Interfaces*, 6:14061–14068, 2014.

[256] O. F. Zouani, C. Chollet, B. Guillotin, and M.-C. Durrieu. ”Differentiation of pre-osteoblast cells on poly(ethylene terephthalate) grafted with RGD and/or BMPs mimetic peptides.”. *Biomaterials*, 31:8245–53, 2010.

[257] David W. Green, Jong-Min Lee, Eun-Jung Kim, Dong-Joon Lee, and Han-Sung Jung. ”Chiral Biomaterials: From Molecular Design to Regenerative Medicine ”. *Advanced Materials Interfaces*, 3:1500411, 2016.

[258] Alex Sigal, Ron Milo, Ariel Cohen, Naama Geva-Zatorsky, Yael Klein, Yuvalal Liron, Nitzan Rosenfeld, Tamar Danon, Natalie Perzov, and Uri Alon. ”Variability and memory of protein levels in human cells”. *Nature*, 444:643–646, 2006.

[259] Mohammad Soltani, Cesar A. Vargas-Garcia, Duarte Antunes, and Abhyudai Singh. ”Intercellular Variability in Protein Levels from Stochastic Expression and Noisy Cell Cycle Processes”. *PLoS Comput Biol*, 12, 2016.

[260] Xiaokun Wang, Jingxian Zhu, Ling Yin, Shize Liu, Xin Zhang, Yingfang Ao, and Haifeng Chen. ”Fabrication of electrospun silicatitania nanofibers with different silica content and evaluation of the morphology and osteoinductive properties”. *J Biomed Mater Res Part A*, 100:3511–3517, 2012.

[261] Bong-Wook Park, Eun-Ju Kang, June-Ho Byun, Myeong-Gyun Son, Hyun-Joon Kim, Young-Sool Hah, Tae-Ho Kim, B. Mohana Kumar, Sun-A Ock, and Gyu-Jin Rho. ”In vitro and in vivo osteogenesis of human mesenchymal stem cells derived from skin, bone marrow and dental follicle tissues”. *Differentiation*, 83:249–259, 2012.

[262] Yin-Quan Chen, Yi-Shiuan Liu, Yu-An Liu, Yi-Chang Wu, Juan C. del Álamo, Arthur Chiou, and Oscar K. Lee. ”Bio- chemical and physical characterizations of mesenchymal stromal cells along the time course of directed differentiation”. *Scientific Reports*, 6:31547, 2016.

[263] Jung-Min Kim, Jaeyoon Kim, Yun-Hee Kim, Kyong-Tai Kim, Sung Ho Ryu, Taehoon G. Lee, and Pann-Ghill Suh. ”Comparative Secretome Analysis of Human Bone Marrow-Derived Mesenchymal Stem Cells During Osteogenesis”. *J. Cell. Physiol.*, 228:216224, 2013.

[264] Na Lian, Tonghui Lin, Wenguang Liu, Weiguang Wang, Lingzhen Li, Stephanie Sun, Jeffry S. Nyman, and Xiangli Yang. ”Transforming Growth Factor β Suppresses Osteoblast Differentiation via the Vimentin Activating Transcription Factor 4 (ATF4) Axis”. *Journal of Biological Chemistry*, 287:35975–84, 2012.

[265] Christian Ehrnthaller, Markus Huber-Lang, Per Nilsson, Ronny Bindl, Simon Redeker, Stefan Recknagel, Anna Rapp, Tom Mollnes, Michael Amling, Florian Gebhard, and Anita Ignatius. ”Complement C3 and C5 Deficiency Affects Fracture Healing”. *PLoS one*, 8, 2013.

[266] Ingrid U Schraufstatter, Sophia K Khaldoyanidi, and Richard G DiScipio. ”Complement activation in the context of stem cells and tissue repair”. *World J Stem Cells*, 7:1090–1108, 2015.

[267] Ai-Xia Zhang, Wei-Hua Yu, Bao-Feng Ma, Xin-Bing Yu, Frank Fuxiang Mao, Wei Liu, Jia-Qing Zhang, Xiu-Ming Zhang, Shu-Nong Li, Ming-Tao Li, Bruce T. Lahn, and Andy Peng Xiang. ”Proteomic identification of differently expressed proteins responsible for osteoblast differentiation from human mesenchymal stem cells”. *Mol Chem Biochem*, 304:167–179, 2007.

[268] Dun Hong, Hai-Xiao Chen, Hai-Qiang Yu, Yong Liang, Carrie Wang, Qing-Quan Lian, Hai-Teng Deng, and Ren-Shan Ge. ”Morphological and proteomic analysis of early stage of osteoblast differentiation in osteoblastic progenitor cells”. *Experimental Cell Research*, 316:22912300, 2010.

[269] M.S. Giusta, H. Andrade, A.V. Santos, P. Castanheira, L. Lamana, A.M.C. Pimenta, and A.M. Goes. ”Proteomic analysis of human mesenchymal stromal cells derived from adipose tissue undergoing osteoblast differentiation”. *Cytotherapy*, 12:478–490, 2010.

[270] I. Cardoso, E.C. Østerlund, J. Stamnaes, R. Iversen, J.T. Andersen, T.J. Jørgensen, and L.M. Sollid. ”Dissecting the interaction between transglutaminase 2 and fibronectin”. *Amino Acids*.

[271] Hiroshi Kubo, Masakazu Shimizu, Yuji Taya, Takeshi Kawamoto, Masahiko Michida, Emi Kaneko, Akira Igarashi, Masahiro Nishimura, Kazumi Segoshi, Yoshihito Shimazu, Koichiro Tsuji, Takaaki Aoba, and Yukio Kato. ”Identification of mesenchymal stem cell (MSC)-transcription factors by microarray and knockdown analyses, and signature molecule-marked MSC in bone marrow by immunohistochemistry”. *Genes to Cells*, 14:407–424, 2009.